NATIONAL ACADEMY OF SCIENCES OF UKRAINE

SPACE RESEARCH IN UKRAINE

2016—2018

Report
to COSPAR

The Report Prepared by the Space Research Institute
of NAS of Ukraine and SSA of Ukraine

Scientific Editor O. FEDOROV

KYIV • AKADEMPERIODYKA • 2018

UDK 001.891(15)
BBK 22.6
S78

SRI NASU-SSAU
Space Research Institute
of National Academy of Sciences of Ukraine
and State Space Agency of Ukraine
Ukraine
03187, Kyiv
40, bd 4/1, Acad. Glushkov av.
http://www.ikd.kiev.ua

NASU
National Academy of Sciences of Ukraine
Ukraine
01601, Kyiv 30
54, Volodymyrska St.
http://www.nas.gov.ua

Space research in Ukraine. 2016–2018 / Ed. O. Fedorov. — K.:
S78 Akademperiodyka, 2018. — 164 p.
ISBN 978-966-02-8590-3

Ukrainian report to COSPAR summarizes the results of space research performed during the years 2016—2018. This edition presents the current state of Ukrainian space science in the following areas: astronomy, Earth exploration and near-Earth space research, life sciences, space technologies and materials science. A number of papers are dedicated to the creation of scientific instruments for perspective space missions. Considerable attention paid to applied research of space monitoring of the Earth. The collection is the Ukrainian report to COSPAR.

The collection can be useful for a wide range of readers, interested in space research.

UDK 001.891(15)
BBK 22.6

ISBN 978-966-02-8590-3

CONTENTS

Space Astronomy and Astrophysics

Near Earth Space Research

Space Biology

Earth Observation from Space

Space Technologies and Materials Sciences

FOREWORD

The publication represents the main results of research and development in exploration and utilization of space, performed by leading Ukrainian institutions in the years 2016—2018. The collection is the Ukrainian report to COSPAR, issued in Ukrainian and English every two years. This edition includes review papers dedicated to priorities of the Program on Space Research of the National Academy of Sciences of Ukraine (NASU) and the National Space Program.

The collection sections includes, in the main, review articles in the following scientific areas: Space Astronomy and Astrophysics, Near Earth Space Research, Space Biology, Earth Observation from Space, Space Technologies and Materials Sciences.

Scientific direction "Space Astronomy and Astrophysics" represents work of Institute of Radio Astronomy of the NASU (IRA NASU) specialists in collaboration with France, Austria, USA, Japan colleagues and other Ukrainian participants on the results of Jupiter radio emission studies using high-sensitivity Ukrainian radio telescopes for the JUNO space mission ground support. Low-frequency multi-antenna synchronous ground-space observations have been carried out, data processing methods of various astronomical instruments have been developed, which will allow deeper study the physical processes of Jupiter radio emission generation, its natural satellites, the solar system planets and to search for the exoplanets radio emission.

The second section of the collection includes the fundamental and applied research of Ukrainian scientific schools in studying the processes and interactions in the Earth's "atmosphere - ionosphere - magnetosphere" system. The article of Space Research Institute (SRI) of NASU and SSAU experts is devoted to the disclosure of the physical nature of the mechanisms for energy transfer from Earth's surface into the ionosphere through the acoustic channel; the theoretical description of the infrasonic signal spreading from the ground source through the atmosphere is developed. In the framework of the scientific background development of space weather forecasting service a new model of local geomagnetic disturbances, suitable for implementation in operational practice (SRI NASU-SSAU, the Main Center of Special Monitoring of SSA of Ukraine) was obtained.

Some of articles on the study of nonstationary processes in near-Earth space are represented by Kharkiv physicists. The IRA NASU scientists and their Polish colleagues discuss the diagnosis and visualization methods of ionospheric heterogeneities with high spatial and temporal rate resolution using geostationary and low-orbit satellites data; the work of the Institute of Ionosphere NASU and MESU specialists continues multiyear systemic theoretical and experimental geospace studies over Ukraine using ground-based ionospheric observatory data. The description of the collection, processing and dissemination information system of the space experiment "Ionosat-Micro" data, created in the framework of the national ionospheric project "Ionosat" using the Ukrainian satellite "Microsat-M" is given (SRI NASU-SSAU). New approach to the simulation of magnetized particles diffusion in low-frequency waves propagating in the near-space is proposed (Bogolyubov Institute for Theoretical Physics of NASU).

The next series of articles represents the Ukrainian activity in space biology (institutes of the National Academy of Sciences of Ukraine, Taras Shevchenko National University of Kyiv, National Botanical Garden of NASU). The results of the research in plant biology at the cellular, molecular and tissue levels in simulated microgravity are presented. The search for new approaches to testing the properties of substrates adequate to requirements of space planting had been conducted, an original biological experiment at the nanosatellite to find out the adaptive potential of plants under the space flight conditions on the visual observation parameters was proposed, the neurotoxicity assessment of inorganic analogue of Martian dust with different content of carbon nanoparticles was performed.

The next section of the collection is devoted to research in the field of satellite Earth observations. A multi-level Deep Learning approach for land cover and crop types classification on Big Data from different sources (optical and radar remote sensing satellites) was proposed by SRI NASU-SSAU specialists in co-authorship with other Ukrainian and foreign participants. The scientists of the Scientific Centre for Aerospace Research of the Earth of NASU have worked out the methods of space monitoring of the winter wheat crops state in the forest-steppe zone of Ukraine, of the dangerous condition of the air basin in the industrial centers ecosystems, of the erosion hazard for soil cover in Ukraine, the search for hydrocarbon deposits on the sea shelf, etc.

Series of articles on the current results of theoretical and experimental research on space technology, the creation of devices, materials and systems completes the collection. In the National Technical University of Ukraine "Kyiv Polytechnic Institute" within the framework of the international space project QB50 the nanosatellite PolyITAN-2-SAU, which was launched into orbit has been designed. This nanosatellite is the part of the scientific network for the Earth's thermosphere studying. The E.O. Paton Electric Welding Institute of NASU substantiated the possibility of creating the solid welded thin-walled structures of a convertible volume with acceptable technological and geometric characteristics, optimized for application in space conditions. A pilot sample of an integrated universal navigation complex with high characteristics based on fiber-optic gyroscopes and pendulum accelerometers for using in aircraft control systems has been developed in the RPE HARTRON-ARKOS LTD. Among the results of the work are the radiation tests of materials and devices of space designation by electronic accelerator (Institute of Electron Physics of NASU, Yuzhnoye State Design Office, Lutsk National Technical University), technical solutions for the creation of thermal protection systems (Frantsevich Institute for problems of materials science of NASU, E.O. Paton Electric Welding Institute of NASU, SRI NASU-SSAU), new effective methods and algorithms for controlling the spacecrafts orientation (SRI NASU-SSAU).

In general, the presented review illustrates the current Ukrainian possibilities in different areas of space research and utilization. Some of the results were obtained in the framework of international projects, programs and grants, including Horizon 2020, the most of the results had been reported at the annual Ukrainian Conference on Space Research, international seminars and conferences.

The collection is intended for space research specialists and readers interested in space research.

JUPITER RADIO EMISSION STUDIES AT UTR-2, URAN AND GURT WITHIN THE FRAME OF JUNO SPACE MISSION GROUND SUPPORT

V. Zakharenko[1], S. Yerin[1], O. Konovalenko[1], A. Brazhenko[2], B. Cecconi[3], P. Zarka[3], H. Rucker[4], M. Panchenko[5], M. Imai[6], A. Lecacheux[4], V. Ryabov[7], G. Litvinenko[1], I. Bubnov[1], O. Ulyanov[1], M. Sidorchuk[1], S. Stepkin[1], V. Koliadin[1], V. Melnik[1], V. Dorovskyy[1], O. Stanislavsky[1], O. Khristenko[1], P. Tokarsky[1], N. Kalinichenko[1], O. Reznichenko[1], V. Lisachenko[1], V. Bortsov[1], G. Kvasov[1], I. Vasylieva[1], A. Skoryk[1], A. Shevtsova[1], K. Mylostna[1], R. Vashchishin[2], A. Frantsuzenko[2], O. Ivantyshin[8], A. Lozinsky[8]

[1] Institute of Radio Astronomy NAS of Ukraine (IRA NASU)
[2] Poltava gravimetrical observatory of Institute of Geophysics NAS of Ukraine (PGO IGP NASU)
[3] LESIA, Observatoire de Paris, Meudon, France
[4] OAW Commission for Astronomy, Austria
[5] Space Research Institute (SRI), Austria
[6] University of Iowa, USA
[7] Future University Hakodate, Japan
[8] Karpenko Physico-Mechanical Institute NAS of Ukraine (PMI NASU)

Space research missions made a great contribution to Solar system planets studies. However, the long-term experience shows that the most effective way of exploration is a combination of using the equipment at spacecraft and high-sensitive astronomical instrumentation on Earth or near-earth orbit (for example Hubble space telescope). It applies most to low-frequency radio band (10–100 MHz) due to low directivity of spacecraft antennas on one hand and the fact that parameters of receivers and recording devices on spacecraft are strictly limited in compare to ground-based instruments on the other hand. A good example of successful joint space- and ground-based observations was identification of lightning in Saturn atmosphere registered at UTR-2 radio telescope using data of simultaneous observations with Cassini spacecraft (Zakharenko et al., 2011, 2012). It resulted in the discovery of the fine time structure of Saturn lightning thanks to UTR-2 high sensitivity and high temporal resolution of receiving equipment (Konovalenko et al., 2013, Mylostna & Zakharenko, 2013; Mylostna et al., 2014).

In 2016 Juno spacecraft started orbiting Jupiter. Its research program is planned for more than 30 rotations around the planet with a period of about 53.5 earth days. The spacecraft carries a great number of research equipment, which operate in almost all ranges of electromagnetic spectrum and will give much valuable information for scientific studies of Jupiter. However, the big data volume to be transferred from the spacecraft to Earth during closest flybys to the planet's surface (< 5000 km) and the restrictions of communication link do not allow doing nonstop observations because of impossibility of full observation data set transferring. This means that the results of ground-based observations will be used not only for confirmation of Juno spacecraft observational data, but also will contain much more information about Jovian radio emission and physical processes that originate it. The common data timeslots will allow deep study of the generation processes and the relations of various factors influencing the emission.

A dense ionosphere of Jupiter, its strong magnetic field, gravitational interaction with close natural moons (Io and others) originate the intense sporadic emission at frequencies below 40 MHz which has been studied for more than 50 years. Thanks to polar spacecraft orbit, which approaches so-called current tubes of Io, Europe and Ganymede, the moons whose interaction with Jupiter is the origin of sporadic emission (Zarka et al., 2016), the Juno observational data will be of great value for science.

Multiantenna low-frequency observations with distant radio telescopes provide non-stop Jupiter studies irrespective of earth rotation as well as better results in overcoming such hindering factors as local radio frequency interference (RFI) and local inhomogeneity of earth ionosphere. Synchronous joint observations are being done at different continents using LWA (the USA), NDA, NenuFAR (France) and others. However the highest sensitivity is provided by Ukrainian radio telescopes UTR-2, URAN and GURT (Konovalenko et al., 2016). Therefore it is critically important to carry all observation sessions in accordance with Juno mission ground support program to prepare data for further joint using with results of observations in other spectral ranges and to create databases of observations and to store the data on servers for research.

Low-frequency radio telescopes of Juno ground support team

Juno mission ground radio support in low-frequency range is provided by:

France:
- Nançay Decameter Array (NDA), France,
- LOFAR (ref.), station FR606,
- NenuFAR.

Ukraine:
- UTR-2, GURT (IRA NASU),
- URAN-2 (Megn et al., 1997, 2003) (PGO of S.I. Subbotin IGF, NASU),
- URAN-3 (G.V. Karpenko PMI NASU).

The USA:
- LWA1, New Mexico,
- Owens valley LWA (OLWA),

Japan:
- Iitate & Zao instruments of Tohoku University,
- Fukui Institute of Technology,
- University of Electronics and Communication,
- Kochi University.

Juno low-frequency receiving system includes monopole antenna of single linear polarization and series-parallel radio spectrometer WAVES, which operates in wide frequency range (0.01–40 MHz). According to predefined sequence the central frequency of digital receiver is tuned to a value in the range and a 3 MHz band is digitized. The full record cycle of the entire operating frequency range varies in the range from 30 seconds up to several minutes (depending on distance to Jupiter and observation program). The spectrometer has an option of on-line data FFT calculation. The decision on the type of data to transfer to Earth (spectra or raw output data – ADC samples) is made by mission control center.

The receiving systems of Ukrainian radio telescopes ensure high sensitivity and RFI immunity (Zakharenko et al., 2016). The digital receivers provide non-stop data recording over the entire observation session (6–8 hours) with maximal time resolution (15 ns for UTR-2 and up to 6.25 ns for GURT).

A large effective area of UTR-2 radio telescope allows varying time and frequency resolution in wide ranges. It makes possible to detect the shortest and narrow-band details of S-type (bursts with time scales of milliseconds), L-type (long-term radio emission intensity grows) and other recently discovered (Ryabov at al., 2017; Litvinenko et al., 2016) burst types (LS-bursts, absorption bursts, zebra-structures). Another feature is much more flexible data processing in new digital receivers of these radio telescopes.

Multiantenna low-frequency observations

Multiantenna observations have many advantages even in compare to very efficient but single radio telescope. It is clearly noticeable in low-frequency radio range, where manmade RFI (for example short-wave broadcasting radio stations) are many orders higher even than the signal of such a strong source like Jupiter. Another factor of observation results distortion is parameters variation of ionosphere above the radio telescope, which result in substantial variations of amplitude and phase of received signal.

Simultaneous observations with multiple instruments allows reliable differentiation of useful signal on the background of interference even for quite unusual signal shapes on dynamic spectra. Fig. 1 shows Jupiter observations data from UTR-2 (upper panel) and URAN-2 (lower panel) radio telescopes obtained on August 27, 2016. Io-controlled storms took place a day before and a day after of the time indicated. It is the reason why the short intense bursts shown in Fig. 1 cannot be assigned to well-known S-bursts class, which is traditionally associated with Io.

Development of metadata format and joining European astronomical data sharing system VESPA

For further joint using of received data we need to adapt data record format (current data formats of digital receivers need to be converted to commonly accepted standard formats like FITS of CDF), as well as, provide all additional information which is crucial for unambiguous interpretation of measurements. This kind of information like variables used and their units, ranges of parameters variations, observation modes, selected parameters of receiving equipment, is usually referred as "metadata". The metadata must briefly and at the same time fully describe the conditions of observations.

Collaboration with other radio telescopes and various instruments based on various physical principles of data acquisition (optical cameras, magnetic fields sensors, etc.) needs more common description of obtained observational data. The work on common data representation formats has been done for decades in observatories of many countries. Thanks to collaboration with European colleagues, the IRA NASU team decided to join to powerful European-developed system of data collecting and data access provider VESPA (Virtual European Solar and Planetary Access). VESPA allows collecting of data in all accessible electromagnetic spectrum ranges and data of particle detectors, etc., for comprehensive studies of physical processes and phenomena on the planets of Solar system and beyond.

The VESPA virtual observatory provides an access to data from measuring devices of spacecrafts, radio telescopes, ground-based facilities of astronomical data and models of various objects and media (for example model of Jupiter magnetic field), which allow studying the astronomical phenomena in vast range of their manifestations.

For description of observations data files from UTR-2, URAN and GURT radio telescope we developed a type of metadata tables with all necessary information. From the variety of parameters provided by VESPA developers for various receiving systems, we picked those, which fully describe data

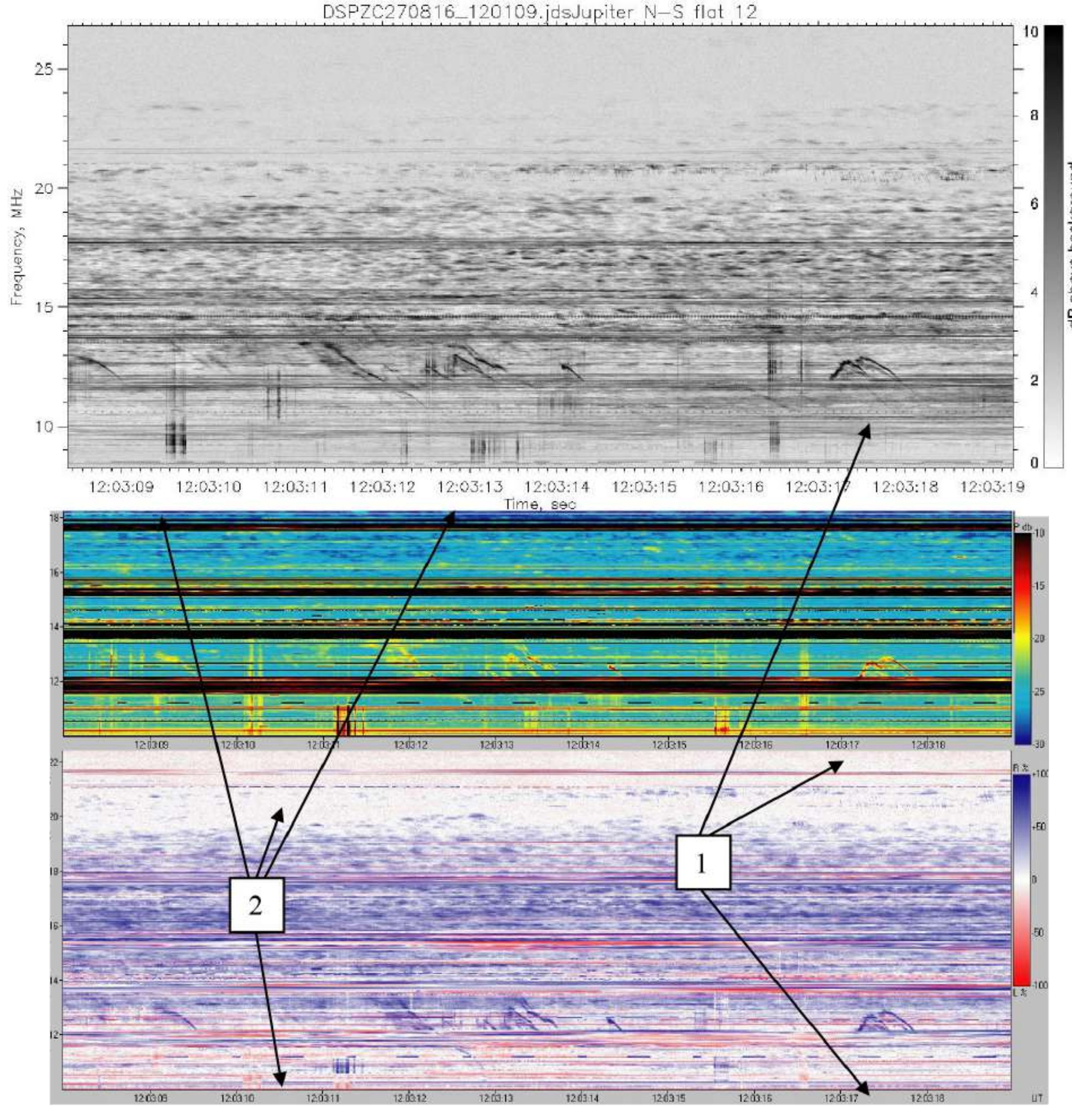

Fig. 1. Dynamic spectra of Jupiter observations with UTR-2 (upper panel) and URAN-2 (lower panel). Simultaneous arrival and the spectral shape indicate unambiguously the cosmic origin of the signal (1). Local RFI (2) markedly differ at different radio telescopes. Polarization data from URAN-2 (lower part of lower panel) indicates the high level of circular polarization (blue color) for short intense bursts. This feature is typical for well-known S-bursts

type from our radio telescopes (telescope name, beam number, receiver name, data storing mode, resolution, etc.). The description of each file have 33 fields listed in Table. Each field has its name, type of variable in terms of SQL database, formats and examples of typical values.

Metadata fields of Table are arranged in a single line for each data file in the SQL table on VESPA server and is used for selection and fast data analysis or preview. It is useful for selection of simultaneously recorded data from all available receivers and instruments, especially for time of Juno spacecraft maximal approach to Jupiter, or for finding and downloading of data files with other time slots being under study.

Thanks to collaboration with Paris observatory (Observatoire de Paris, France) and Future University Hakodate (Japan) it became possible to implement a server where an archive of UTR-2, URAN and GURT observation data are stored. This server is included to extensive European VESPA database. All data of preparatory observation sessions for ground Juno support as well as data received during approaches of spacecraft to Jupiter surface are stored on servers of research institutions? and after finish of VESPA software testing will be indexed by VESPA service and become available for processing by all interested researchers.

Simultaneous observations at UTR-2 and GURT

Unique close location of two instruments with different parameters – UTR-2 and GURT radio telescopes in the same S.Y. Braude observatory, makes possible to broad the potential of observations. UTR-2 has dipoles of single linear polarization (east-west dipole axis direction) and GURT sections have dipoles of two linear polarizations (southwest-northeast and the orthogonal one). It gives more possibilities for RFI differentiation using joint data processing, because signals coming from phased array side lobes (which dramatically differ for two telescopes) will have notably different frequency characteristics. Moreover, it becomes possible to implement short-base interferometer to combine the advantages of both radio telescopes: large effective area of UTR-2 and two linear polarizations of GURT.

Increasing of effective area of synthesized radio telescope in compare to effective area of small antenna, which is a part of it, is achieved because the total effective area of two antennas in correlation mode is a geometric mean value of effective areas of these antennas. Relative position of UTR-2 and GURT dipoles (45° angle rotation of UTR-2 dipoles to GURT dipoles of each linear polarization) results in presence of information from two orthogonal polarizations of GURT subarray in a signal from UTR-2 single polarization. Therefore, for UTR-2 effective area (A_e) of 70 000 m^2 and GURT subarray of 350 m^2 the total A_e will be 4500 m^2, which is equal to effective area of 14 GURT subarrays. Moreover, the interferometer allows eliminating the galactic background noise, which is uncorrelated and strong enough at decameter waves.

Multiantenna polarization studies are made with URAN-2, URAN-3 and GURT. Fig. 2 shows

Metadata file fields and its parameters

№	Field name	Type (SQL)	Format and typical values (? – any value in this position)	Description and ***example***
1	granule_uid	Text	File name	File name (.adr, .jds) ***20160501_120000.jds***
2	granule_gid	Text	5char – telescope name (UTR-2, GURT1, URAN1...URAN4) + 3char beam number (b01...b05...b99) – for URAN always b1" + 2char – receiver name (rA...rD...rZ) + 2char – mode (SP, WF, CR) spectra, ADC samples, correlation All fields separated with "_"	Groups according to telescope name, beam number, receiver name, observation mode ***UTR-2_b03_rD_SP***
3	obs_id	Text	8char Date of observations [+6char start time +6char stop time +?char object] All fields separated with "_"	***20160501_120000_230000_Jupiter*** ***20160501_070123_081212_Saturn***
4	dataproduct_type	Text	2char Output data arrangement in numerated list	Standard: ***ds*** = dynamic spectrum ***ts*** = time series (waveform)

5	target_name	Text	?char	***Jupiter*** ***Saturn*** ***Uranus***
6	target_class	Text	?char Type of object from numerated list	***Planet*** ***Stat*** ***Interplanetary media***
7	time_min	double	Start time in Julian days, UTC	***2457628.0234606***
8	time_max	double	Stop time in Julian days, UTC	***2457628.0248495***
9	time_exp_max	double	Integration time, seconds	***0.02***
10	spectral_range_min	double	Lower bound of frequency range, Hz	8×10^6
11	spectral_range_max	double	Upper bound of frequency range, Hz	33×10^6
12	spectral_resolution_max	double	Spectral resolution, Hz	4×10^3
13	instrument_host_name	Text	Standard radio telescope name	***UTR-2*** ***GURT*** ***URAN1…URAN4***
14	instrument_name	Text	Standard instrument (receiver) name	***A…E…Z***
15	measurement_type	Text	Data type (spectra, correlation, ADC samples)	***sp, cr, wf***
16	processing_level	Integer	Committee on Data Management and Computation (CODMAC) calibration level	***2***
17	creation_date	Date (ISO-8601 String)	Time of data creation YYYY-MM-DDThh:mm:ss±hh:mm	***2016-08-27T12:33:47±00:00***
18	modification_date	Date (ISO-8601 String)	Time of the last data change YYYY-MM-DDThh:mm:ss±hh:mm	***2016-08-27T12:33:47±00:00***
19	release_date	Date (ISO-8601 String)	Date and time of data publication YYYY-MM-DDThh:mm:ss±hh:mm	***2016-08-27T12:33:47±00:00***
20	service_title*	Text	Service title	***Juno*** ***Saturn***
21	access_url	Text	Data URL (register sensitive)	***http://…20160501_120000.jds***
22	access_format	Text	File format	***.jds*** ***.adr***
23	access_estsize	Integer	Approximate file volume. kBytes	***2 048 000***
24	data_access_url	Text	If data stored separately	***http://…20160501_120000.jds***
25	access_md5	Text	MD5 check sum	
26	thumbnail_url	Text	Icon URL (not more than 256x256 pixels, .png)	***http://…20160501_120000.png***
27	file_name	Text	File name	
28	target_region	Text	Region of interest	***Atmosphere*** ***Magnetosphere*** ***Etc.***
29	feature_name	Text	Secondary name	***IoA_DAM***
30	bib_reference	Text	Bibcode, doi, URL…	***DOI…***
31	ra	double	Right Ascension h.h чи h:m:s	***10.45632***
32	dec	double	Declination, deg	***15.34746***
33	publisher	Text	Right holder	***IRA_NASU***

observations data after preliminary processing for each linear polarization and their sum.

Prospects of further studies in the frame of Juno mission ground support. Detection of new types of emission

Radio emission in Jupiter-Io system (Io-controlled emission) has been known since 1964 and it is a result of Io tube Alfven waves with Jupiter magnetic field. Ultraviolet emission near Jupiter poles from the feet of Io, Ganymede, and Europa tubes has been known since 2002 from the observations of Hubble space telescope. In case of Ganymede, which has its own magnetic field, it is believed that they interact through reconnection of the moon and Jupiter magnetic fields. Emission of Jupiter-Ganymede interaction (Ganymede-controlled emission) has been searched for the last two decades but only inconsistent results has been obtained.

In works (Zarka et al., 2016; Marques et al., 2017) the processing of observations database from NDA radio telescope resulted in clear detection and parameters measurement of such emission. The observations done in the frame of Juno mission

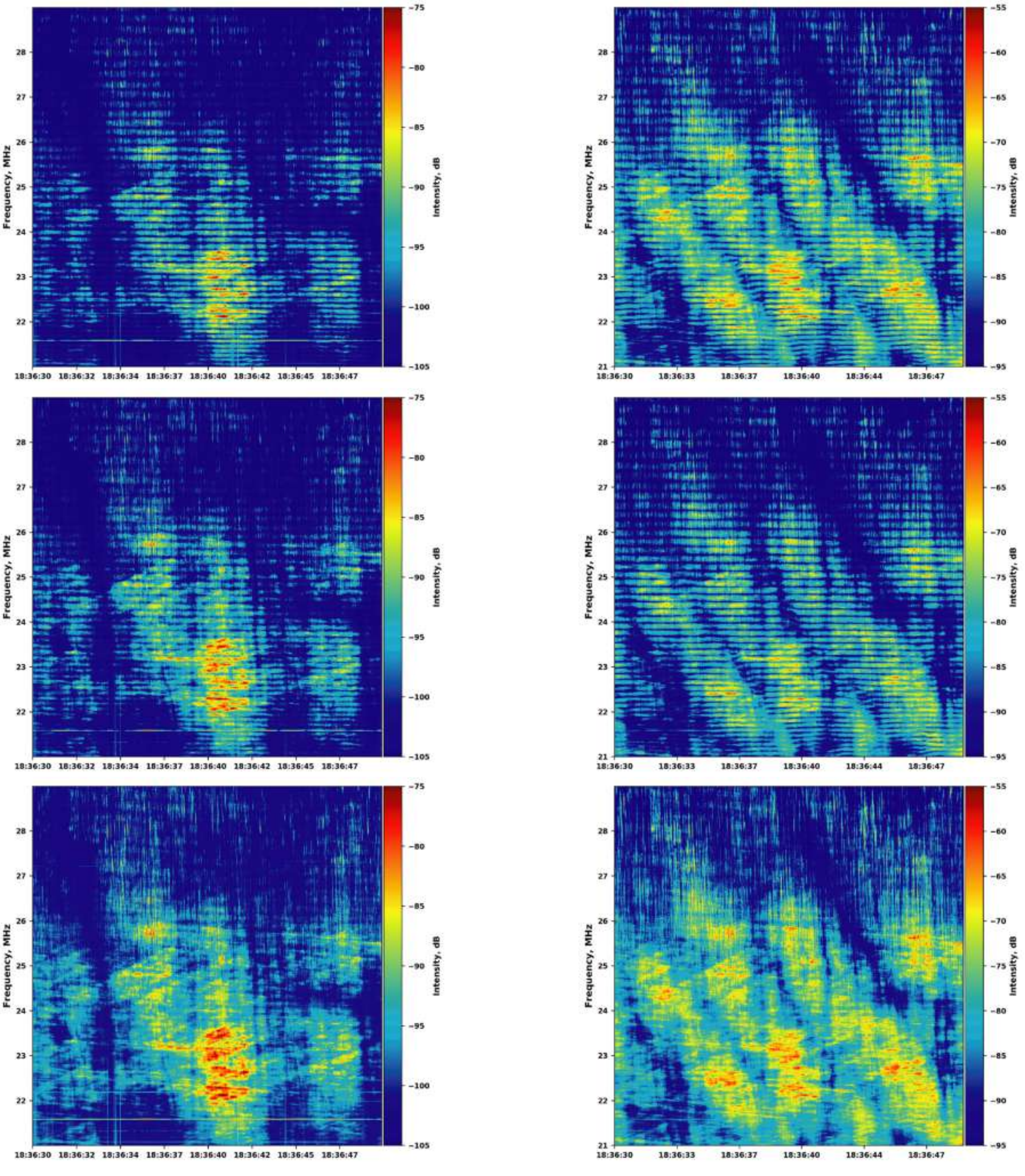

Fig. 2. Decameter radio emission of Jupiter simultaneously received on May 18, 2017 at GURT subarray (left column) and URAN-2 radio telescope (right column). Two linear polarizations of radio emission are shown in upper two rows, and the sum of the two polarization is shown in the bottom row

ground support project and preliminary results of their processing, additionally extend the set of phenomena which require substantial upgrade of emission physical models of the system of Jupiter and its moons. The possibility of any preset time and frequency resolution in addition to possibility of long-term non-stop wideband signal recording results in significant increasing of astrophysical phenomena spectral picture details contrast and provides unprecedented opportunity to study short bursts and more precise detection of distinctive features between different types of Jupiter decametric radio emission.

We mentioned above that new wideband long-term observations with high sensitivity and resolution allow detecting the types of radio emission which are unidentified or has not been deeply studied before. Some of them (Ryabov et al., 2014) manifest themselves as an interaction of various emission types but have noticeable differences. Bursts of first type (LS-bursts, or superposition of L and S type bursts) have substantially lower frequency drift rate than ordinary quasi-linear drifting S-bursts and they often appear in the same frequency band where L-type emission takes place. One can assume that LS as well as some of L-type bursts originates from the same source. The bursts of the second type, which are formed by wideband frequency modulation, when observed with insufficient time resolution, can seem to be S-bursts with very steep negative (or even positive) drift rates. The nature of modulation itself has not been studied well yet. The obvious presence of Ganymede-controlled emission, and therefore the medium of its origin, results in the task of search and study the interaction of various areas of short bursts generation and manifestation of these effects in various types of emission.

Fig. 3 shows the example of "crossing" of bursts with different properties. In the upper panel the absorption bursts appear on the background of zebra-structure. These bursts and the bursts in 23–24 MHz range (LS-bursts) have a frequency drift of 4–5 MHz/s, which probably is caused by common properties of generation areas or they originate in the same spatial area. In the lower panel another type of zebra-structure behavior is shown: the change of modulation from horizontal to vertical, which is similar to features of modulated S-bursts.

To conclude, the above described multiantenna synchronous ground- and space-based observations allow much deeper studies of physical processes of Jupiter and its closest moons radio emission generation. It is essential for studies of Jupiter itself, Solar system planets as well as for searches of "Hot Jupiters" type of exoplanet's radio emissions. Moreover, the developed methods and techniques of various radio astronomy instruments data processing will be of great demand for further astronomical and space studies.

REFERENCES

1. *Zakharenko V.V., Mylostna K.Y., Fischer G., Konovalenko A.A., Zarka P., Griebmeier J.M., Ryabov B.P., Vavriv D.M., Ryabov V.B., Rucker H.O., Ravier P.* Identification of Saturn lightnings recorded by the UTR-2 radio telescope and Cassini spacecraft // Radio Physics and Radio Astronomy. – 2011. – V. 15. – No. 4. – P. 361–369.
2. *Zakharenko V., Mylostna C., Konovalenko A., Zarka P., Fischer G., Grießmeier J.M., Litvinenko G., Rucker H., Sidorchuk M., Ryabov B., Vavriv D.* Ground-based and spacecraft observations of lightning activity on Saturn// Planetary and Space Science. – 2012. – V. 61 (1). – P. 53–59.
3. *Konovalenko A.A., Kalinichenko N.N., Rucker H.O., Lecacheux A. et al.* Earliest recorded ground-based decameter wavelength observations of Saturn's lightning during the giant E-storm detected by Cassini spacecraft in early 2006 // Icarus. – 2013. – V. 224. – No. 1. – P. 14–23.
4. M*ylostna K., Zakharenko V., Konovalenko A., Kolyadin V., Zarka P., GrieBmeier J.M., Litvinenko G., Sidorchuk M., Rucker H., Fischer G.* Study of Saturn electrostatic discharges in a wide range of time scales // Odessa astronomical publications. – 2013. – V. 26 (2). – P. 251–253.
5. *Mylostna K.Y., Zakharenko V.V., Konovalenko A.A. et al.* Fine time structure of lightnings on Saturn // Radio Physics and Radio Astronomy. – 2014. – V. 19. – No. 1. – P. 10–19 (in Russian).
6. *Zarka P., Soares-Marques M., Louis C. et al.* Discovery of the radio emission from the Ganymede-Jupiter interaction / The "SF2A week", June 14–17, 2016, Lyon, France.
7. *Konovalenko A., Sodin L., Zakharenko V., Zarka P. et al.* The modern radio astronomy network in Ukraine: UTR-2, URAN and GURT // Experimental Astronomy. – 2016. – V. 42. – Iss. 1. – P. 11–48.
8. *Konovalenko A.A., Yerin S.M., Bubnov I.M., Tokarsky P.L. et al.* Astrophysical studies with small low-frequency radio telescopes of new generation // Radio Physics and Radio Astronomy. – 2016. – V. 21 (2). – P. 83–132.
9. *Megn A.V., Braude S.Y., Rashkovskiy S.L. et al.* URAN system of the decametric interferometers // Radio Physics and Radio Astronomy. – 1997. – V. 2. – No. 4. – P. 385–401.
10. *Megn A.V., Sharykin N.K., Zakharenko V.V., Bulatsen V.G., Brazhenko A.I., Vashchishin R.V.* Decameter wavelength radio telescope URAN-2 // Radio Physics and Radio Astronomy. – 2003. – V. 8 (4). – P. 345–357.
11. *Zakharenko V., Konovalenko A., Zarka P., Ulyanov O. et al.* Digital receivers for low-frequency radio telescopes UTR-2, URAN, GURT // Journal of Astronomical Instrumentation. – 2016. – V. 5(04). – P. 1641010-1–1641010-19.

12. *Litvinenko G.V., Shaposhnikov V.E., Konovalenko A.A., Zakharenko V.V., Panchenko M., Dorovsky V.V. et al.* Quasi-similar decameter emission features appearing in the solar and jovian dynamic spectra // Icarus. – 2016. – V. 272. – P. 80–87.

13. *Marques M.S., Zarka P., Echer E., Ryabov V.B., Alves M.V., Denis L., Coffre A.* Statistical analysis of 26 yr of observations of decametric radio emissions from Jupiter // Astronomy & Astrophysics. – 2017. – V. 604. – 18 p.

14. *Ryabov V.B., Zarka P., Hess S. et al.* Fast and slow frequency-drifting millisecond bursts in Jovian decameter radio emissions // Astronomy & Astrophysics. – 2014. – V. 568. – P. A53–A64.

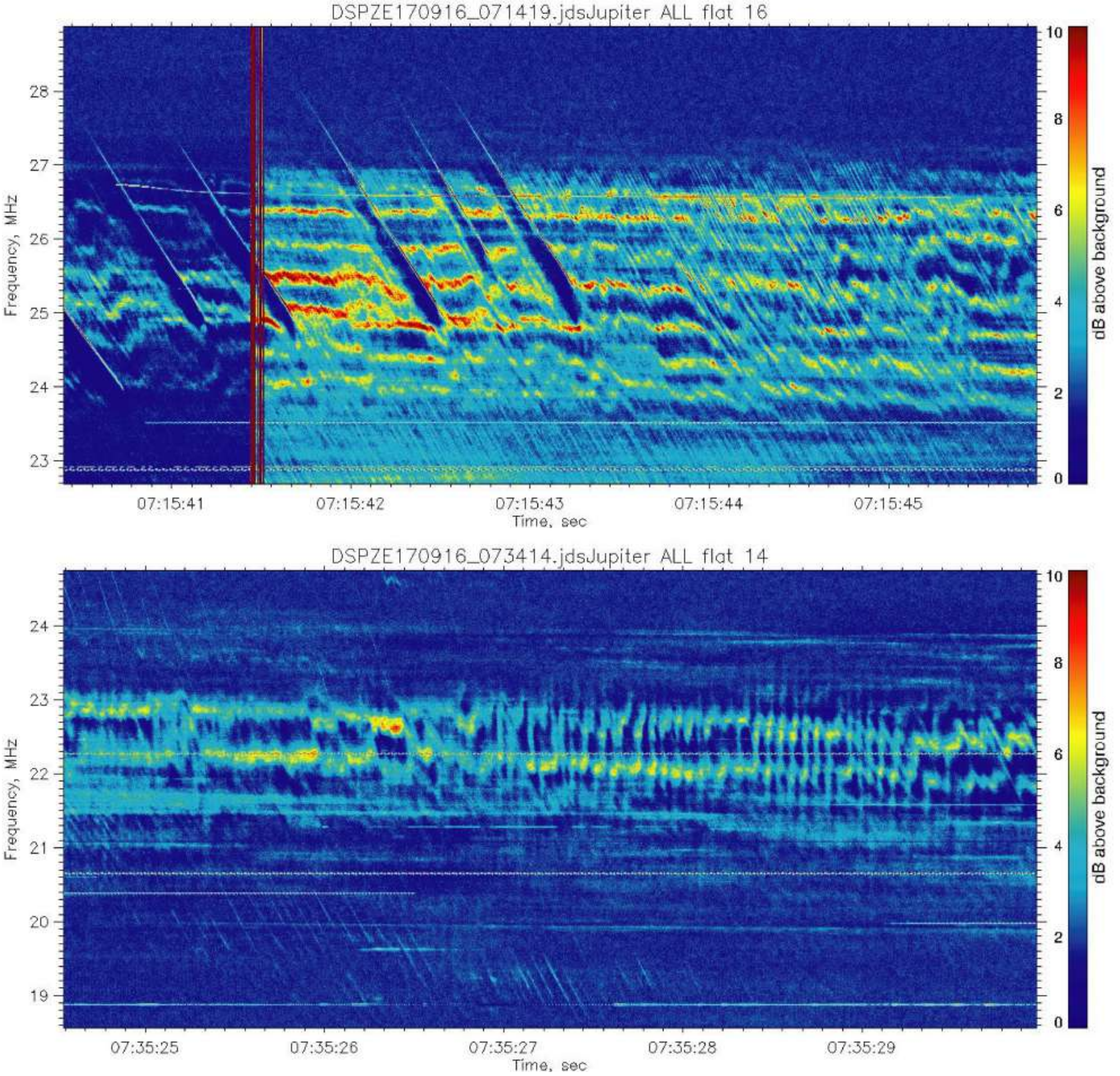

Fig. 3. Observations of Jupiter on September 17, 2016. The upper panel shows a complex combination of various emission types, which become known recently. In the central part of the spectrum the absorption burst masks zebra-structure. Also the LS-bursts with frequency drift rate of 4–5 MHz/s are present on the spectrogram (in the range 23–24 MHz). The lower panel demonstrates the example of unusual fast change of zebra-structure modulation direction from horizontal to vertical

THE INFLUENCE OF INFRASOUND ON THE IONOSPHERE: SOME FEATURES OF THE IONOSPHERIC RESPONSE TO THE SIGNAL OF A GROUND-BASED ACOUSTIC RADIATOR

Yu. Selivanov, Yu. Rapoport, O. Cheremnykh
Space Research Institute of NAS of Ukraine and SSA of Ukraine (SRI NASU-SSAU)

By today, we all have a definite answer to the question "Can earthquakes (or volcano eruptions) affect the state of the ionosphere?" The answer is "Yes" and it is substantiated both experimentally and theoretically in a number of publications (see reviews in [1, 2]). But the obvious answer to the question "Is this always the case?" is "Not always". And it is much more difficult to explain what the experimental conditions should be under which the ionosphere reaction manifests itself in some way. Thus, we may consider the ground-level sources in accordance with the effectiveness of their impact on the ionosphere and talk about the optimal conditions that ensure the appearance of the ionosphere reaction. For example, in [3] based on the analysis of publications over the period of 1965–2013, which reported on registration of wave-like traveling ionospheric disturbances after earthquakes, have shown that the magnitude of the earthquakes really having a wave response in the ionosphere was no less than 6.5. It is clear that the term effectiveness is not always associated with huge energy release (as in the case of a nuclear explosion) to impact the ionosphere. Our studies over the years have been devoted to the search for a key to the effective impact in the case of the low-frequency (LF) acoustic source.

The problem of the interaction of LF acoustic waves of natural or artificial origin with the Earth's ionosphere is becoming more and more important due to the increasing activity on the development of means to foresee such dangerous natural phenomena as powerful cyclones, earthquakes [1, 2, 3, 4], volcanic eruptions and various man-made disasters [5, 6, 7]. However, it should be noted that all these papers are devoted, mainly, to the study of the influence of infrasound on the Earth's ionosphere from uncontrolled sources, mainly of natural origin.

In contrast, we studied the effect of programmable infrasound signal from an artificial acoustic source on the Earth's ionosphere. This was the case with the active ground-space experiment conducted by the Space Research Institute of NAS and SSA of Ukraine (SRI NASU-SSAU), the Lviv Center of the SRI NASU-SSAU and the Karpenko Physical-Mechanical Institute of NAS of Ukraine (FMI NASU) in November, 2013. The schemes of experiment and the results obtained are described in detail in a number of publications [1, 4, 8]. The results of controlled experiments on the effect of specifically formed infrasonic waves from the powerful technical radiator on the upper layers of the atmosphere and ionosphere can be used as a basis for flexible and adaptive modeling the impact on the ionosphere of infrasound from both natural sources of danger, and man-made disasters. In addition, as noted in [1, 8], we draw attention to the fundamental nature of such studies, given the importance of determining such a minimum signal power that still produces a measurable ionosphere response (figuratively speaking, the "guaranteed signal delivery"). The task of optimizing the propagation of the acoustic signal to the ionosphere has already begun to be considered, but in a slightly different aspect – as the search for optimal atmospheric parameters to reduce energy losses along the way to the ionosphere [9]. Also, in our studies, it turned out that among the parameters at the expense of which it is possible to optimize the propagation of an acoustic signal to the ionosphere, the statistical distribution of its initial phase characteristics should also be considered. One of the positive effects of such a study may be the methodology for assessing "the effectiveness with respect to the impact on the ionosphere" of natural and man-made acoustic sources.

Parametric acoustic radiator and its mathematical model

Here we give a short description of the ground-based controlled acoustic radiator [1, 8], which is located in the Lviv Center of the SRI NASU-SSAU and was used in the experiments of 2013. Structurally, the facility consists of a chamber with two rotors inside and a vertical horn. The sound generation is carried out by the bodies attached to the ends of each of the rotors and having their linear speed in the transonic range. In this case, a weak shock wave (acoustic impulse) is formed in front of the body and a turbulent trace - behind it. From the chamber with rotors, pulses enter into a vertical horn with a height of 8 meters. At a pulse repetition frequency of 600 Hz, the effective wavelength (the distance between pulses) is of the order of 0.5 m. At a level of acoustic pressure at the upper cutoff of the horn, equal to 165 dB, the amplitude value of the excess pressure is about 3.6 kPa, which is comparable with the excess pressure in the shock wave of a supersonic aircraft and leads to the manifestation of nonlinear effects. To provide a reasonable compromise between the power of the ground-based acoustic source (the radiation efficiency is higher at high frequencies) and the reaching of ionospheric heights (the maximum height is greater at low frequencies), the designers of the system developed a scheme in which the initial generation was performed at the frequencies of nonlinear waves (acoustic impulses) 600 and 625 Hz in packets with a duration of 60 s and with a pause between them of 60 s, which corresponds to rectangular amplitude modulation. Further, according to estimates, a "parametric antenna", radiating near the difference frequency (25 Hz) and with almost the same amplitude modulation, would be formed at the altitudes of the lower atmosphere, in the region of overlapping of two slightly different nonlinear waves. When the waves with frequencies of 600 and 625 Hz reach the height of the decay due to nonlinear effects, the secondary complex (25 Hz with rectangular modulation) should continue to move up to its own decay height. After this, as shown in a number of works, a signal similar in shape to the modulating envelope (rectangular) will propagate further ("atmospheric detection") [10]. This signal according to our calculations based on the MSISE2000 model should reach ionospheric heights approximately 4.5 minutes after the start of the generation. Also, as shown by the analysis performed in [1], this choice of waveform makes it largely "non-natural", different from most known acoustic signals of natural phenomena such as lightning discharges.

The first version of the working model of the process of parametric generation and propagation of acoustic waves in a realistic atmosphere to the heights of the ionosphere was developed by the authors just after our experiment in 2013. It was based on information used in the preparation and planning of the experiment and on the preliminary analysis of its results. In 2016, the model was improved using the large array of results obtained by research groups headed by Prof. S.O. Soroka (Lviv Center of the SRI NASU-SSAU) and Prof. V.V. Koshovy (FMI NASU) in the 1990s and 2000s. This version of the model was presented in the paper [1] in 2017.

The model is constructed on the basis of the Khokhlov-Zabolotskaya equation [1] for the vertical component of the material velocity of the acoustic wave with the addition of the initial and boundary conditions. The nonlinear model describes the vertical propagation of a transversely bounded acoustic beam of finite amplitude in a gravitationally stratified non-isothermal atmosphere.

In the model, we consider two beams of acoustic waves, radiated by a ground-based sound generator. These beams are then transformed into atmospheric acoustic-gravity waves, which have parameters that enable them to penetrate to the altitudes of the ionospheric E and F regions where they influence the electron concentration of ionosphere that, in turn, leads to observable effects. Acoustic waves are generated by the ground-based parametric sound generator (PSG) at the two close frequencies. The main idea of the experiment is to design the output parameters of the PSG to build a cascade scheme of nonlinear wave frequency downshift transformations to provide the necessary conditions for its vertical propagation and to enable penetration to ionospheric altitudes. The PSG generates the sound waves of frequencies f_1, f_2 (in the experiment $f_1 = 600$ Hz, $f_2 = 625$ Hz) and large amplitudes V (in the experiment $V = 100 \ldots 420$ m/s). Each of these waves is modulated with the frequency $f_{mod} = 0.016$ Hz. The novelty of the proposed analytical-numerical model is due to simultaneous accounting for nonlinearity, diffraction, losses, and dispersion and effectively a two-stage transformation: (1) of the initial acoustic waves to the acoustic wave with the difference frequency $\Delta f = f_2 - f_1$ in the altitude ranges $(0 - 0.1)$ km, in the strongly nonlinear regime and (2) of the acoustic wave with the difference frequency to atmospheric acoustic-gravity waves (AGW) with the modulational frequency in the altitude ranges (0.1–20) km, which then reach the altitudes of the ionospheric E and F regions, in a practically linear regime. The main result of the experimental study and the simulation based on the proposed model is to demonstrate an increase in transparency of the ionosphere for the electromagnetic waves in HF (MHz) and VLF (kHz) ranges, due to the impact on the ionosphere from the AGW, transformed from the sound waves, excited by the PSG, launched by the ground-based sound radiator.

Here it is important for us that the region of parametric frequency conversion turned out to be located relatively low (~ 100 m), as is the region of decay of acoustic waves with a difference frequency (~ 20 km). We have obtained from modeling that the resulting acoustic-gravity waves enter the ionosphere with a frequency of about the initial modulation frequency. The detailed description of the model, as well as the results of using it in the analysis of the experiment conducted in 2013, is given in the article [1].

The model improvements

The model of radiation and propagation in the atmosphere of an infrasonic signal from a ground-based generator described above have been improved in several directions.

Firstly, we have improved the model to allow setting a certain distribution of random initial phases for generated acoustic waves to use in the study of upward propagation of noise-like infrasonic radiation.

Secondly, it was accepted that the ultimate goal of developing our model for description of acoustic packets propagation from a ground-based parametric generator up to the ionosphere should be the possibility of obtaining operational information: the data obtained at the output of the model should provide the basis for the immediate interpretation of satellite measurements and operational correction of experimental procedure in the course of its implementation.

Multifractal analysis of ground-space acoustic experiments

In the period for which we report we have been engaged in the search for fast and at the same time informative methods for analyzing satellite data. We proceeded from the idea expressed by one of the co-authors of our paper [8] (L.V. Kozak) in 2015: for the analysis of acoustically disturbed ionospheric regions, three independent approaches should be considered: the analysis of the probability density function for the measured parameters fluctuations, the analysis of the excess and the analysis of structural functions of high orders. This allows us to determine the presence or absence of heterogeneity in the investigated environment and compare the observed values with existing models. Already having the experience of modeling the situation of acoustic experiments, we note that the idea of finding boundaries between regions of the ionosphere with different statistical properties of fluctuations turned out to be fruitful. In our experiments, where in many cases we are forced to measure some "trace" of ionospheric acoustic excitation, such approach is quite reasonable. Therefore, we adapted for our analytic purposes a multifractal approach, which is based on the analysis of structure functions of various orders. It was implemented using the "wavelet leaders" method [11] in a sliding window.

This procedure was used in the study of the space-time distribution of the ionospheric plasma response in the vicinity of the selected orbits of the research micro-satellites Demeter (2005) and Chibis-M (2013) by the data of on-board equipment and related information.

In order to have an idea of the form in which the ionospheric disturbances from the acoustic effect will be "perceived" by the satellites, we have used the results of the papers [7, 12]. So, in particular, for the case of an acoustic wave from a weak ground-based explosion, the paper [7] presents the following ionospheric effects: (1) in the acoustic range of the spatial-temporal scales, the level of the natural ionospheric turbulence is considerably lower than for the internal gravity waves range, and therefore the effects of the man-made sources will be more pronounced; (2) the acoustic front generates a small-scale turbulent structure; (3) at the heights of the sporadic Es-layer, one could observe the fragmentation of the inhomogeneities into typical spatio-temporal scales of ~ 2–10 km and 1–2 s; (4) the plasma turbulization was also detected in the lower part of the F-layer.

Also, according to [7], in the satellite Aureol-3 fly-by over the explosion field line "a noisy spot" was detected with a low-frequency (50—5000 Hz) electrostatic turbulence. When the satellite crossed the explosion flux tube, an increased level of noise was observed (at distances within 200 km) in the frequency range 0.1—1 kHz. The magnetic, components of these oscillations were negligible and the perturbations could thus be considered as electrostatic. According to measurements, the oscillations near the explosion flux tube persisted up to 35 min after the explosion.

The analysis of records of satellite measurements of low-frequency variations of electric and magnetic fields in the ionosphere at altitudes of 420 km (Chibis-M) and 710 km (Demeter) made it possible to detect several passages of satellites through localized excitation areas that differ from the environment by another spatial-temporal variability in the multifractal sense.

Proceeding from the analysis of the spatial-temporal relations that existed during experiments we interpreted the found events as candidates for excitations caused by the action of acoustic radiation of a ground-based acoustic generator.

As an example, we propose the results of an analysis based on the multifractal singularity spectra. It was applied to fragment of dataset No. 1 (Fig. 1), recorded by on-board scientific instrumentation of the Demeter microsatellite during a series of ground-space experiments in 2005. During the experiments, the microsatellite Demeter measured the variations of the ionospheric electric and magnetic fields in the vicinity of the orbit during the flight over the operating ground acoustic radiator of the Lviv Center, SRI. So far, these data sets have not been analyzed in detail. The fragment was recorded during the passage of the microsatellite over Lviv almost in the south direction. Guided by the above considerations, we expected to obtain a change in the nature of the fluctuations of the electric field somewhere south of Lviv. Indeed, for the multifractal singularity spectrum, working in a sliding window, we obtained a pronounced jump (increase) in the argument of the maximum of the singularity spectrum just in this region.

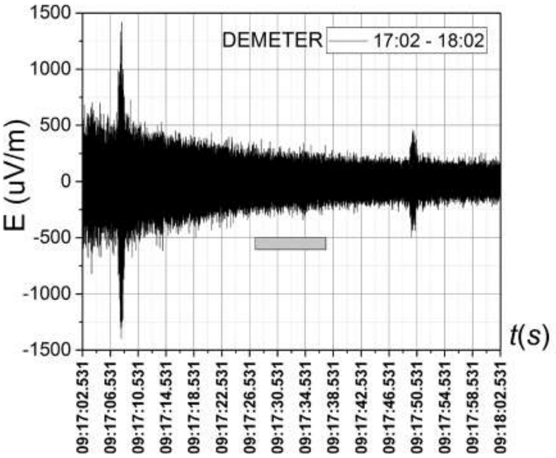

Fig. 1. Detail of dataset № 1, microsatellite Demeter (France), May 12, 2005, the vertical component of electric field in the very low frequency (VLF) band, beginning – 09:17:02.531 UT, ending – 09:18:02.537 UT. The passage over the generator (Lviv city) – from 09:17:27.531 UT to 09:17:37.531 UT, horizontal gray line allocates this period of time

Now we are considering the improvement of our program for finding the multifractal spectrum of the singularity as a problem with good prospects.

Propagation of noise-like infrasonic radiation to ionospheric heights through a nonlinear atmosphere

A theoretical description of the propagation of noise-like infrasonic radiation to ionospheric heights through a nonlinear atmosphere is developed. It is established that mutually incoherent low-frequency acoustic modes with close frequencies penetrate from the earth's surface to ionospheric heights significantly more efficiently than wave with the same total input intensity.

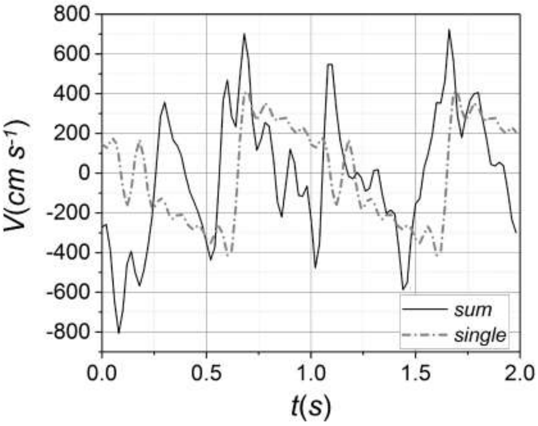

Fig. 2. Comparison of the intensities, at altitude Z = 90 km, of the sum of mutually incoherent waves (solid curve) and a single coherent wave with the same initial (at altitude Z = 0 km) intensity (dash-dotted curve)

To verify this statement, we modified our model (1) to describe incoherent waves. The problem was studied in a simple model in which 9 incoherent sine waves with frequencies distributed in the interval (0.8 ... 1.3) Hz and one wave with a frequency of 1 Hz with an initial intensity (at the generator output) equal to the total intensity of the first 9 waves were considered.

In order to compare the intensities for both curves (Fig. 2), we took the ratio of the integrals of the squared amplitudes of the signals over the time interval under consideration. The ratio turned out to be of the order of 1.7 in our numerical experiments. This indicates that our specially prepared signal, when moving up, toward the ionosphere, loses energy more slowly than the initially monochromatic signal of finite amplitude. We consider this scheme as a potentially new basis for influence on the ionosphere.

Note that the problem discussed above has to do with such an actually existing, but insufficiently investigated, class of ground- and underground-level sources, as "mosaic sources". Acoustic sources of this class can, for example, exist in some period before earthquakes. At the same time, the question remains whether they are more effective with regard to the ionosphere than the traditionally considered localized sources.

Conclusions

1. Specific steps have been identified to transform the radiation model and the subsequent propagation of the programmed acoustic signal of the ground parametric generator into an operational means to support experiments on the acoustic influence on the ionosphere.
2. The analysis of records of satellite measurements of low-frequency variations of electric and magnetic fields in the ionosphere at altitudes of 420 km (Chibis-M) and 710 km (Demeter) made it possible to detect several passages of satellites through localized excitation areas that differ from the environment by another spatial-temporal variability in the multifractal sense.
3. A theoretical description of the propagation of noise-like infrasonic radiation on ionospheric heights through a nonlinear atmosphere is developed. It is established that mutually incoherent low-frequency acoustic modes with close frequencies penetrate from the earth's surface to ionospheric heights significantly more efficiently than the wave with the same total input intensity.

Acknowledgement

The authors would like to acknowledge Grimalsky, V.V. (Autonomous University of State Morelos, Cuernavaca, Mexico) for productive cooperation in research.

REFERENCES

1. *Rapoport Y.G., Cheremnykh O.K., Koshovy V.V., Melnik M.O., Ivantyshyn O.L., Nogac R.T., Selivanov Y.A., Grimalsky V.V., Mezentsev V.P., Karataeva L.M., Ivchenko V.M., Milinevsky G.P., Fedun V.N., and Tkachenko E.N.* Ground-based acoustic parametric generator impact on the atmosphere and ionosphere in an active experiment // Annales of Geophysicae. – 2017. – V. 35. – P. 53–70. DOI:10.5194/angeo-35-53-2017.

2. *Zettergren M.D., Snively J.B.* Ionospheric response to infrasonic-acoustic waves generated by natural hazard events // Journal of Geophysical Research: Space Physics. – 2015. – V. 120. – No. 9. – P. 8002–8024.

3. *Perevalova N.P, Sankov V.A., Astafyeva E.I., Zhupityaeva A.S.* Threshold magnitude for Ionospheric TEC response to earthquakes // Journal of Atmospheric and Solar-Terrestrial Physics. – 2014. – V. 108. – P. 77–90. DOI: 10.1016/j.jastp.2013.12.014.

4. *Rapoport Yu.G., Cheremnykh O.K., Selivanov Yu.A., Grimalsky V.V., Ivchenko V.N., Milinevsky G.P., Tkachenko E.N., Melnik M.O., Mezentsev V.P., Karataeva L.M., Nogach R.T.* Ionosphere as a Sensitive Indicator of Powerful Processes in the Lower Atmosphere / Lithosphere, Artificial Acoustic Influence and Space Weather / Electromagnetic Effects of the Earthquakes an Volcanoes EMSEV 2014 Workshop. Book of Abstracts. – September 22–26, 2014, Konstancin Jeziorna, Poland. – P. 133–135.

5. *Blanc E., Rickel D.* Nonlinear wave fronts and ionospheric irregularities observed by HF sounding over a powerful acoustic source // Radio Science. – 1989. – V. 24. – No. 3. – P. 279–288.

6. *Blanc E.* Interaction of an acoustic wave of artificial origin with the ionosphere as observed by vertical HF sounding at total reflection levels // Radio Science. –1984. – V. 19. – No. 2. – P. 653–664.

7. *Pokhotelov O.A., Pilipenko V.A., and Fedorov E.N., Stenflo L., Shukla P.K.* Induced Electromagnetic Turbulence in the Ionosphere and the Magnetosphere // Physica Scripta. – 1994. – V. 50. – P. 600–605.

8. *Cheremnykh O.K.,. Grimalsky V.V , Ivantyshyn O.L., Ivchenko V.M., Kozak L.V., Koshovy V.V., Mezentsev V.P., Melnik M.O., Nogach R.T., Rapoport Yu.G., Selivanov Yu.A., Zhuk I.T.* Experimental and theoretical research of artificial acoustic modification of the atmosphere and ionosphere // Space Science and Technology. – 2015. – V. 21. – No. 1. – P. 48–53. DOI:10.15407/knit2015.01.048 (in Ukrainian).

9. *Petrukhin N.S., Pelinovsky E.N. & Batsyna E.K.* Reflectionless propagation of acoustic waves through the Earth's atmosphere // Jetp Lett. – 2011. – V. 93. – P. 564. DOI:10.1134/S0021364011100110.

10. *Krasnov V.M., and Kuleshov Yu.V.* Variation of Infrasonic Signal Spectrum during Wave Propagation from Earth's Surface to Ionospheric Altitudes // Acoust. Phys. – 2014. – V. 60. – P. 19–28.

11. *Serrano E., Figliola A.* Wavelet Leaders: A new method to estimate the multifractal singularity spectra // Physica A. – 2009. – V 388. – P. 2793–2805.

12. *Koshovy V.V.* Radiophysical and Radio Astronomical Diagnostics of Ionospheric Effects Induced by a Ground-Based Infrasonic Transmitter (Preliminary Results) // Radiophysics and Quantum Electronics. – 1999. – V. 42. – No. 8. – P. 691–703.

LOCAL GEOMAGNETIC FORECAST

D. Vlasov[1], A. Parnowski[1, 2]

[1] Space Research Institute of NAS of Ukraine and SSA of Ukraine (SRI NASU-SSAU)

[2] Main Center of Special Monitoring of SSA of Ukraine (MCSM SSAU)

For the first time, we achieved a useful forecast model of local geomagnetic perturbations suitable for transition to an operational product. The lead time is 3 hours.

Most space weather events affect the geomagnetic field by altering the pattern of magnetospheric currents. These changes are measured at the ground level by magnetic observatories around the globe. The changes of the geomagnetic field vary at different locations due to a complex geometry of magnetospheric currents. At this time, geomagnetic variations are analyzed through the use of planetary geomagnetic indices. As the name suggests, these indices are based on data collected from all around the globe. This makes them unsuitable for most practical applications where local dynamics is of essence. There were several attempts at constructing regional and local geomagnetic indices, yet none of them received broad acceptance.

We focused instead on predicting the components of geomagnetic field directly measured at any given magnetic observatory. The main advantage of such an approach is the possibility to use predicted values in the same way as measured values, i.e. they can be seamlessly integrated into existing services.

The scientific background of the prediction method was described in the articles [1, 2]. Since then, we introduced some technical improvements to our algorithm which allowed us to produce slightly more accurate models in significantly less time, so one model is now produced in several hours rather than several days using the same hardware. Otherwise, we mostly reused the code of AFFECTS geomagnetic forecast tool [3], so the models produced with our new software are fully compatible with the AFFECTS geomagnetic forecast service [4].

The predictive models were trained using the NASA OMNI2 database or archived L1 data depending on the intended cadence, and archived measurements of the magnetic observatory in question. We found that the training sample should cover at least one solar cycle to produce useful predictive models. Results are further improved if using deeper archives.

Though still a work in progress, this research already yielded forecast models with 3 hours lead time and a positive skill score (defined as relative reduction of mean square error). In Figs. 1–3 we demonstrate the performance of these models during the St. Patrick's Day storm of 2013 for the Boulder (*BOU*) magnetic observatory. In Table we list statistical scores of these models and our earlier 3-hour D_{st} forecast as a reference. It provides data on prediction efficiency (*PE*), Pearson's correlation coefficient (*r*), and skill score defined as relative reduction of mean square error (*SS*).

Of course, the accuracy of the local geomagnetic forecast is lower than that of a planetary index due to unaccountable factors such as local electromagnetic emissions produced by factories, railways, power lines etc., which are averaged out in planetary indices. Still, the listed values of skill score are high enough for practical applications.

Statistical scores of the 3-hour geomagnetic forecast

IMO	Component	*PE*, %	*r*, %	*SS*, %
BOU	X	83	85	16
	Y	80	84	14
	Z	80	83	10
D_{st} (for reference)		85	92	35

The authors are grateful to the Space Physics Data Facility (SPDF) and the National Space Science Data Center (NSSDC) for the free online OMNI2 catalogue, the World Data Center for

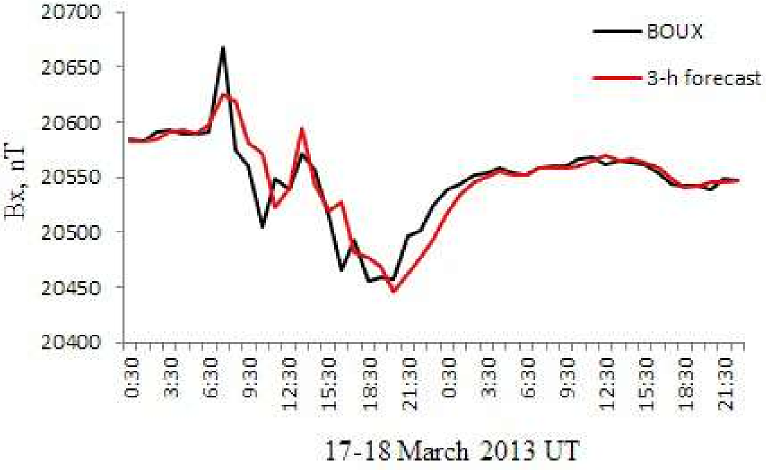

Fig. 1. 3-hour forecast of northward (X) component at Boulder magnetic observatory on 17–18 March 2013

Fig. 2. 3-hour forecast of eastward (Y) component at Boulder magnetic observatory on 17–18 March 2013

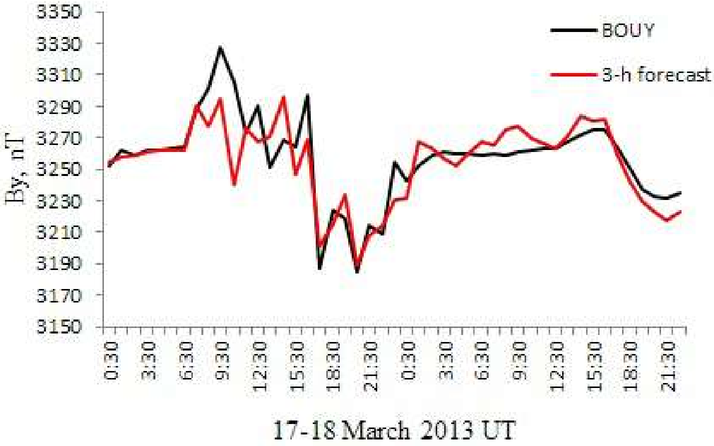

Fig. 3. 3-hour forecast of vertical (Z) component at Boulder magnetic observatory on 17–18 March 2013

Geomagnetism (WDC-B) at Kyoto University for the free online catalogue of geomagnetic indices and observatories operated by the U.S. Geological Survey (USGS, geomag.usgs.gov).

REFERENCES

1. *Parnowski A.* Regression modeling method of space weather prediction // Astrophysics & Space Science. – 2009. – V. 323, Iss. 2. – P. 169–180. – DOI: 10.1007/s10509-009-0060-4. – [arXiv:0906.3271].

2. *Parnowski A.* Regression modelling of geomagnetic activity // Journal of Physical Studies. – 2011. – V. 15, Iss. 2. – Ref. 2002. Available at: http://physics.lnu.edu.ua/jps/2011/2/abs/a2002-8.html.

3. *Parnowski A., Polonska A., Semeniv O., Yatsenko V., Cheremnykh O., Salnikov N., Kremenetsky I., Kuntsevich V.* Provision of software tool for forecasting indices // AFFECTS Deliverable 4.1. – 2012. Available at: http://www.affects-fp7.eu/uploads/media/AFFECTS_Deliverable_Report_D4.1.pdf.

4. *Semeniv O.V., Polonska A.Yu., Parnowski A.S.* Operational geomagnetic forecast service // Bulletin of Taras Shevchenko National University of Kyiv. Astronomy. – 2014. – V. 51. – P. 23–24.

USING TOTAL ELECTRON CONTENT VARIATIONS MAPS CREATED FROM DATA OF GLOBAL NAVIGATION SATELLITE SYSTEM FOR DIAGNOSTICS OF PLASMA INHOMOGENEITIES

Y. Zanimonskiy[1], Yu. Yampolski[1], G. Nykiel[2], M. Figurski[2]

[1] Institute of Radio Astronomy NAS of Ukraine (IRA NASU)

[2] Gdansk University of Technology, Poland

GNSS terrestrial receivers can provide a huge amount of information about the ionosphere and magnetosphere. Primary data, in the form of RINEX-files, accumulated over a period of fifteen years at thousands of world-wide stations are used for insignificant percentage. This publication presents some results of data processing for more than six hundred GNSS stations in Central Europe for a few days preceding the geomagnetic storm on March 17, 2015 and after it. Obtained, much unexpected results, we hope, will allow us to take a fresh look at the possibilities of GNSS methods for studying the upper layers of the atmosphere and give a new impetus to these works.

The magnitude of the total electron content (TEC) along the «satellite-receiver» line of sight is calculated from the primary data and is the basis for further transformations and applications, in particular, for calculating corrections in geodetic solutions, for constructing space-time ionospheric models, and so on.

TEC is an integral quantity that depends on the distribution of electron concentration along the line of sight. In order to evaluate the nature of this distribution, the data from several space-apart stations recording signals from several satellites simultaneously should be involved. The methods of tomography make it possible not only to construct a regional model of the ionosphere, but also to estimate in a number of cases the distribution of the electron density in the lower magnetosphere at altitudes of up to several thousand kilometers.

Global maps are widely used; continental, regional and local ionospheric maps are known, representing the spatial distribution of the TEC of the corresponding parts of the globe. Recently, several papers have been published in which the TEC spatial pattern is represented on a set of sub ionospheric points for the rays of the view of dozens of satellites to hundreds and thousands of stations.

The recently developed method of orthogonal projection of TEC variations [1–4] allows us to visualize TEC disturbances on a continental scale with the real spatial resolution of about 50 km. Now it is possible to determine not only such "classical" parameters as the spatial period and the speed of movement, but also the location and size of the region occupied by the travelling ionospheric disturbances (TIDs).

In the case of simultaneous observation of two satellites, it is also possible to estimate the height of localization of inhomogeneities. However, with the use of one GPS system, which is currently implemented, such an opportunity occurs several times a day for several tens of minutes. Far from always at these times, the events of interest to us in the ionosphere take place.

This paper presents some aspects and results of the first stage of processing the array of TEC variation maps obtained from the data of approximately six hundred GNSS receivers in Central Europe accumulated during a geomagnetic storm. The main goal of the work, which started late in 2015 and has been continued until recently, is to develop the methods for studying the plasma environment of the Earth using such maps. Some quantitative parameters of ionospheric disturbances, determined earlier, have already been published [3–5], some are given in this paper and some are still waiting for publication.

During the life cycle of the geomagnetic storm, considered on the example of the storm on March 17, 2015, the TEC variation maps show a very diverse process in the upper atmosphere. Before the storm beginning and after its end, there is a random spatial picture, against which quite regularly, several times a day, there occur quasi-wave TIDs. Fig. 1 shows the map constructed from the data of one GPS satellite (SV09) with averaging of seven consecutive

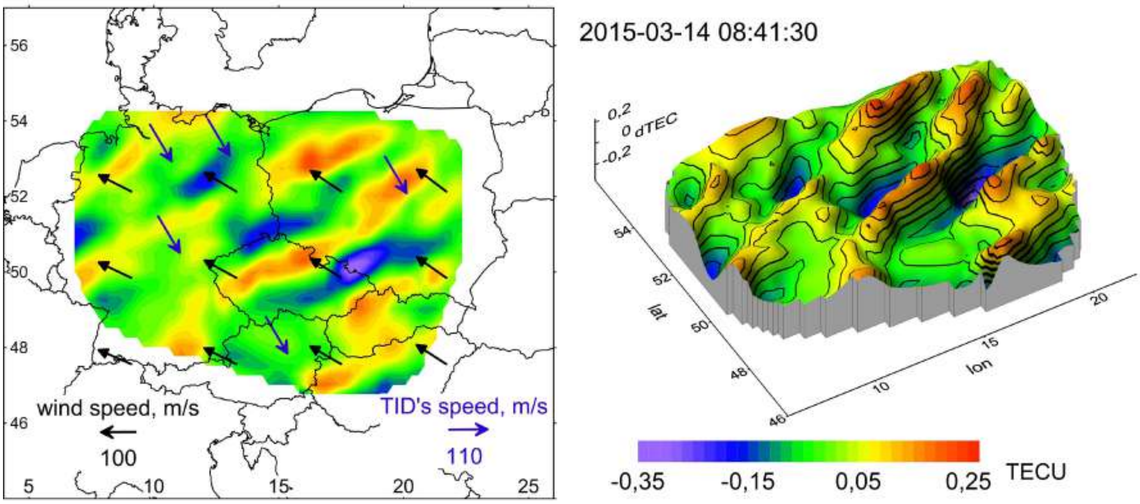

Fig. 1. Map (left) and 3D surface (right) of the spatial distribution of TEC variations (dTEC) during the TID passage under quiet geomagnetic conditions

maps from 08 h 40 m to 08 h 43 m on March 14, 2015. In addition, the averaging was carried out with the spatial shift of each map in the displacement direction so that the wave variations were added in phase, and the noise, respectively, randomly.

Fig. 1 shows the black and blue arrows. The first of these (black ones) show the direction and speed of thermospheric wind at the height of the F2 ionospheric layer maximum. We have used the horizontal wind model (HWM-07), which is a commonly used and available in the MATLAB software package. The second (blue ones) show the TID direction and speed estimated for the obtained TEC variation models. To characterize the detected structures, spatial autocorrelation functions (ACFs) were constructed for map segments including wavy zones. The size of the segments ranged from the entire map to one period of the undulating structure. It is supposed that the structure spatial size corresponds to the size of the segment of the most variable ACF that consequently will be used in the subsequent analysis. It will be observed that the possibility for determining the size of the TID zone appears to be due to the described visualization method usage.

The movement of inhomogeneities occurred to the southeast (azimuth of 143°) at the speed of about 110 m/s. The spatial period is estimated at 250 km, the most pronounced part of the quasi-wave perturbation occupies an area of about $8 \cdot 10^5$ square kilometers, the amplitude of TEC variations is estimated at 0.15 TECU, the lifetime is not less than one and a half hours. Probably, the moving ionospheric irregularities can be a consequence of the thermospheric wind [3], however, the study of this connection is of particular interest.

At the storm main phase, the maps show fast displacements of areas with the TEC increased or decreased value, and the nature of movements differs significantly for the northern and southern parts of the maps [5]. At present, the complex nature of the reaction of the ionosphere and, apparently, of the lower magnetosphere to geomagnetic disturbances in the storm main phase, does not allow clear interpretation of the cause-effect relationships of sources and observed phenomena. Maps obtained during the geomagnetic storm active phase were analyzed in a special way. We investigated the sequences of maps using the methods of general scene analysis, based on dividing each picture into regions representing different or differently changing structures. The two zones with different parameters of motion of inhomogeneities can be selected (Fig. 2).

Fig. 3 shows the changes in the profiles of TEC variations along the lines **A**-**A'** and **B**-**B'** which represent the directions with minimal transformations of spatial patterns for about a dozen minutes. Disturbances in the main phase of the storm are characterized by TEC variations being an order of magnitude greater than in the quiet days. The zone with the most intense TEC variations was located to the north of 52° N. Disturbances apparently were moving with the speed near 1 km/s being significantly higher than the speed of sound. (Fig. 3 **1**). Thus, the effect of moving is most likely linked to spatial and temporal changes in the flow of an ionizing agent, creating some surplus as against the quiet conditions of electron concentration, and its variations, too.

To the south of 52° N, the TEC variations are of lower intensity, they change their space form more

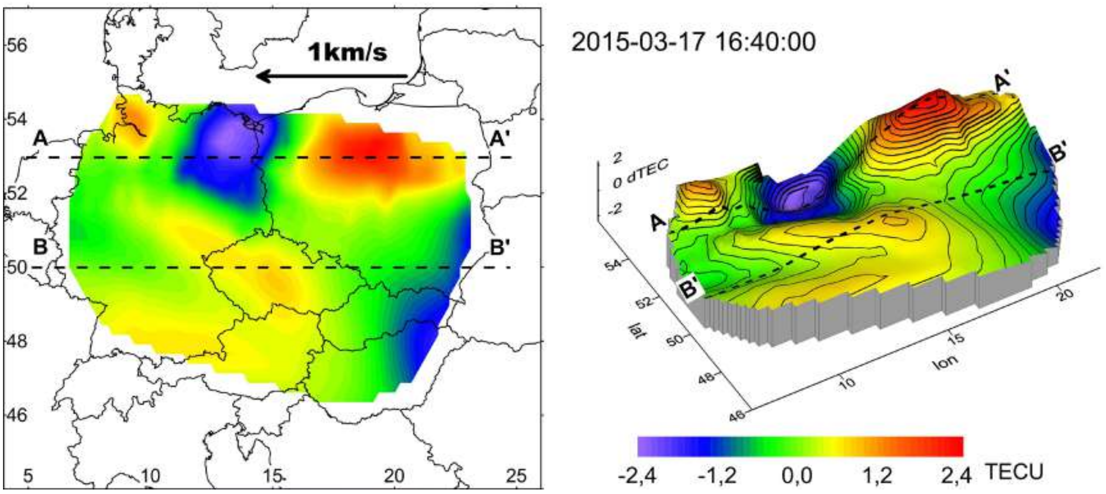

Fig. 2. Map (left) and 3D-image (right) of TEC variations over an investigated region during the geomagnetic storm active phase on 17 March 2015 at 16 h 40 m

rapidly and therefore it is not possible to reliably measure the speed of their movement (Fig. 3 **2**).

Conclusions

Here in this paper, a technique based on the data of the dense continental-wide network of GNSS receivers for the visualization of processes in the ionosphere, being the source of variations of the total electron content between satellites and ground receivers, is presented. The possibility to build maps of TEC variations with the resolution of tens of kilometers with the temporal rate of tens of seconds is demonstrated. This allows us to analyze the structure and temporal evolution of mesoscale ionospheric irregularities.

Our statistics of the quiet ionosphere processes is still small. Nevertheless, it is shown that undulating TIDs occur regularly in the ionosphere at approximately the same time of day and are likely related to the thermospheric wind at ionospheric heights. The measured parameters of TIDs are consistent with the literature data. For the first time, the duration of the existence and the area occupied by a stable TID were estimated.

On the maps obtained during the unique event of the geomagnetic storm on 17 March 2015, the TEC variations form very peculiar structures with the dynamics essentially different from the dynamics of ionospheric processes on quiet days. For the first time, we were able to determine the quantitative TID parameters simultaneously on two parts of the TEC variation map over the Central Europe. During the geomagnetic storm in the ionosphere above the Central Europe, a sharp latitudinal boundary of the increase in intensity of TEC variations during the storm main phase, located at approximately 52°N, was found. The level of TEC variations northwards of this boundary exceeds the background values by more than an order of magnitude. At this time, the main direction of the motion of aperiodic inhomogeneities was from east to west with a supersonic velocity of about 1 km/s.

Further studies of visualized structures at different phases of geomagnetic storms are very intensive and yield interesting results, which discussion is beyond the scope of this publication. Taking into account the existence and intensive development of dense networks of GNSS receivers in different regions of the globe and the simplicity of the proposed method for the visualization of TEC variations with high space-time resolution, this approach can be used for a more detailed investigation of ionospheric processes on a planetary scale.

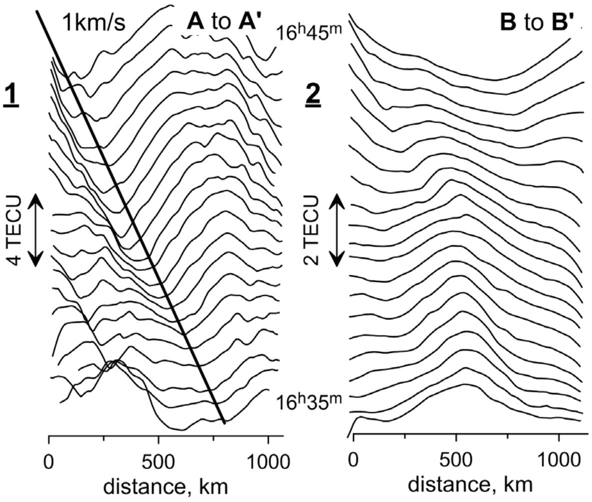

Fig. 3. Profiles of TEC variations, in the zones with (**1**) and without (**2**) active travelling disturbances, along the lines **A**-**A'** and **B**-**B'** in Fig. 2 on 17 March 2015, shown in the form of «waterfall». The thick line shows the trajectory of disturbances

REFERENCES

1. *Zanimonskiy Y.M., Nykiel G., Paznukhov A.V., Figurski M.* Modeling of TEC Variations Based on Signals from Near Zenith GNSS Satellite Observed by Dense Regional Network / Proceedings of the 2016 International Technical Meeting of The Institute of Navigation, Monterey, California, 2016. – P. 585–590.

2. *Zanimonskiy Y.M., Nykiel G., Figurski M., Yampolski Y.M.* Modeling of the travelling ionospheric disturbances. Case study of ASG-EUPOS network / Geophysical Research Abstracts, EGU General Assembly 2016, 17–22 April, 2016, Vienna, Austria. – V. 18. – P. 17484.

3. *Nykiel G., Figurski M., Koloskov A.V., Olijnyk A.Y., Zanimonskiy Y.M.* Measurements of TID's parameters based on dense national GNSS networks in Central Europe / EUREF-2016 Symposium, May 25–27, 2016, San Sebastian, Spain. Available at: http://www.euref.eu/symposia/2016SanSebastian/p-04-04-Nykiel.pdf.

4. *Nykiel G., Figurski M., Yampolski Yu.M., Zanimonskiy Y.M.* Continental-wide maps of TEC variations as a tool for monitoring of ionosphere. Status and prospects / EUREF-2017 Symposium, May 17–19, 2017, Wroclaw, Poland.

5. *Nykiel G., Zanimonskiy Y.M., Yampolski Yu.M., Figurski M.* Efficient Usage of Dense GNSS Networks in Central Europe for the Visualization and Investigation of Ionospheric TEC Variations // Sensors. – 2017. – V. 17. – Iss.10. – P. 2298. DOI: 10.3390/s17102298.

SEARCH OF THE CAUSAL RELATIONSHIP BETWEEN TEC VARIATIONS AND HIGH ENERGY ELECTRONS STREAMS ON THE EXAMPLE OF GEOMAGNETIC STORM ON MARCH 17, 2013

O. Dudnik, E. Zanimonskiy

Institute of Radio Astronomy NAS of Ukraine (IRA NASU)

Processes of radial and pitch-angle diffusion of high-energy particles in radiation belts on the jumps of the electric and magnetic fields of the Earth's magnetosphere are intensified during geomagnetic storms. Whilst during the main phase of the storm, which is determined by the time series of the D_{st}-index data, almost complete depletion of both electron radiation belts takes place, at the recovery phase processes of acceleration and intensification of particle fluxes play a predominant role. In some cases of the most severe storms, a gap between Van Allen inner and outer belts disappear: this spatial area is being filled with electrons of intensity values comparable to intensities in the outer radiation belt. At that, the energy spectrum of particles in a suddenly arising and short-lived belt is, as a rule, much wider than in a more stable inner radiation belt.

No less important physical processes take place inside the lower layers of the Earth's magnetosphere. Recent studies have shown the presence of significant fluctuations in the electron density in the Earth's plasmasphere during geomagnetic storms and, as a consequence, in variations of the Total Electron Content (TEC). The last one is being determined from the data of the Global Navigation Satellite System (GNSS).

We assume both processes are closely related to each other: non-stationary streams of high-energy particles with small pitch-angles at the altitudes of low Earth-orbiting satellites can affect the spatial distributions of TEC. In this work, we analyze dynamics of high energy electrons by using the database from the NOAA / POES patrol satellite and analyze maps of TEC variations above Central Europe during the geomagnetic storm on March 17, 2013 [1, 2].

Experimental data

Electron fluxes were recorded in several integral energy ranges from two mutually perpendicular directions by the MEPED (Medium Energy Proton Electron Detector) instrument, a part of the SEM-2 scientific equipment (Space Environment Monitor-2). The SEM-2 equipment, by-turn, is installed on board the low orbit spacecraft NOAA-15. The NOAA-15 is one of NOAA / POES / MetOp satellites, each of which flies around the Earth with a revolution period of $t_{cir} = 102$ min and with a quasi-circular solar-synchronous orbit at the altitude $h_{POES} \approx 850$ km. One of the two telescopes of the MEPED device captures particle streams from the "anti-Earth" direction, i.e. the axis of the solid angle of this telescope, into which the particles fall down, coincides with the line connecting the spacecraft with the center of the Earth. The second telescope registers particle fluxes from the horizontal direction, which has an inverse direction to the satellite's velocity vector. The electron fluxes are being measured in four energy ranges: E1 ($E_e > 40$ keV), E2 ($E_e > 130$ keV), E3 ($E_e > 287$ keV), and E4 ($E_e > 612$ keV).

Maps of TEC variations were constructed as results of processing the signals received from GNSS satellites located near zenith (with an elevation angle more than 70°). Data of about 600 terrestrial dual-frequency receivers were used. Each map with a spatial resolution of about 50 km has been calculated using a special algorithm of de-trending and with the further usage of the deviations of TEC from smoothed regional values [3–5]. Temporal interval between sequential maps is equal to 30 s, a step of the uniform grid by latitude and longitude is equal to 0.1°. Realization of the possibility to measure TEC in accordance with its direct

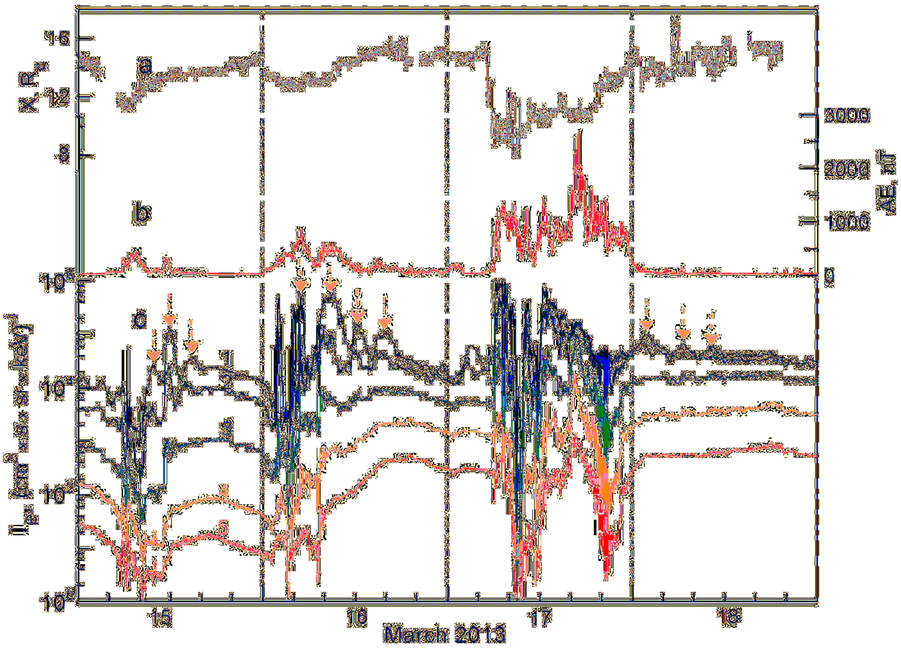

Fig. 1. 1-minute's data: *a* – magnetosphere bow shock nose location in the ecliptic plane; *b* – AE-index; *c* – spectral density of electron fluxes from the "anti-Earth" direction at geostationary orbit by the data of GOES-13 in 5 energy ranges: 1 – $E_e > 40$ keV, 2 – $E_e > 75$ keV, 3 – $E_e > 150$ keV, 4 – $E_e > 275$ keV, 5 – $E_e > 475$ keV for the period from March, 15 to March, 18 of 2013. Time scale is in UTC

determination eliminated a necessity to introduce model representations about ionosphere as a thin screen at a certain height.

Helio- and geophysical condition around storm of March 17, 2013

A long-drawn solar flare during time interval $\Delta t_2 \approx 06{:}46 - 09{:}35$ UTC with a maximum at $t_{max} = 07{:}58$ UTC on March 15, 2013, of M1.1 class in the X-ray range by the data of GOES-15 satellite was the source of enhanced fluxes of high energy particles of different species, and of Coronal Mass Ejection (CME). The front of CME shock, which is being characterized by a sharp and simultaneous increase of the solar wind (SW) velocity from $V_{SW1} \approx 450$ km/s to $V_{SW2} \approx 650$ km/s, and of SW density from $\rho_1 \approx 4$ part/cm^3 to $\rho_2 \approx 10 - 20$ part/cm^3, and of temperature from $T_1 \approx 1 \times 10^5$ °K to $T_2 \approx 7 \times 10^5$ °K, generated a strong geomagnetic storm with a sudden commencement SC at $t_{SC} \approx 06{:}02$ UTC and with a prolonged main phase which was lasting from $t_{mf1} \sim 10.30$ UTC to $t_{mf2} \sim 20.30$ UTC with a maximum value of $D_{st} = -132$ nT. It should be noted that solar flare of March 15 was geo-effective. It can be seen that on March 17 a strong compression of the magnetosphere has been observed: the position of bow shock decreased from $X_1 \approx 15\,R_e$ to $X_2 \approx 8\,R_e$ for a short time $\Delta t_3 \approx 05{:}06 - 08{:}24$ UTC (Fig. 1, *a*). This served as the development of a prolonged geomagnetic storm (Fig. 1, *b*).

The increase of electron, proton and ion fluxes in the near-Earth space with an insignificant count rate growth was recorded in the second half of March 15, and with a more significant gradient of growth at the end of March 16, according to the data of the ACE and WIND satellites at the Lagrangian point L1 in the system Sun-Earth. Particle fluxes in the interplanetary space reached their maximum in the first half of March 17. They served as a source of significant variations of the electron fluxes at the outer edge of the Van Allen outer belt according to measurements at GOES geostationary satellites. In addition, the processes of pitch-angle diffusion increased with a decrease of trapped particles content and with simultaneous replenishment of the belt due to injection of particles from the interplanetary space that was accelerated at the front of CME.

In Fig. 1, *c* vertical arrows indicate the peaks of the so-called "drift echo" of low energy ($E_e > 40$ keV) electrons and of intermediate energy electrons. The "drift echo" occurs as a result of injection processes of narrowly directed particle beams that are of impulse nature from the interplanetary magnetic field, of the capture of the particle beam parts by the Earth's magnetic field, followed by multiple azimuths drift around the Earth with returning to initial primary injection zone. Fig. 1, *c* also demonstrates that the energy spectrum of electrons injected from the outside has

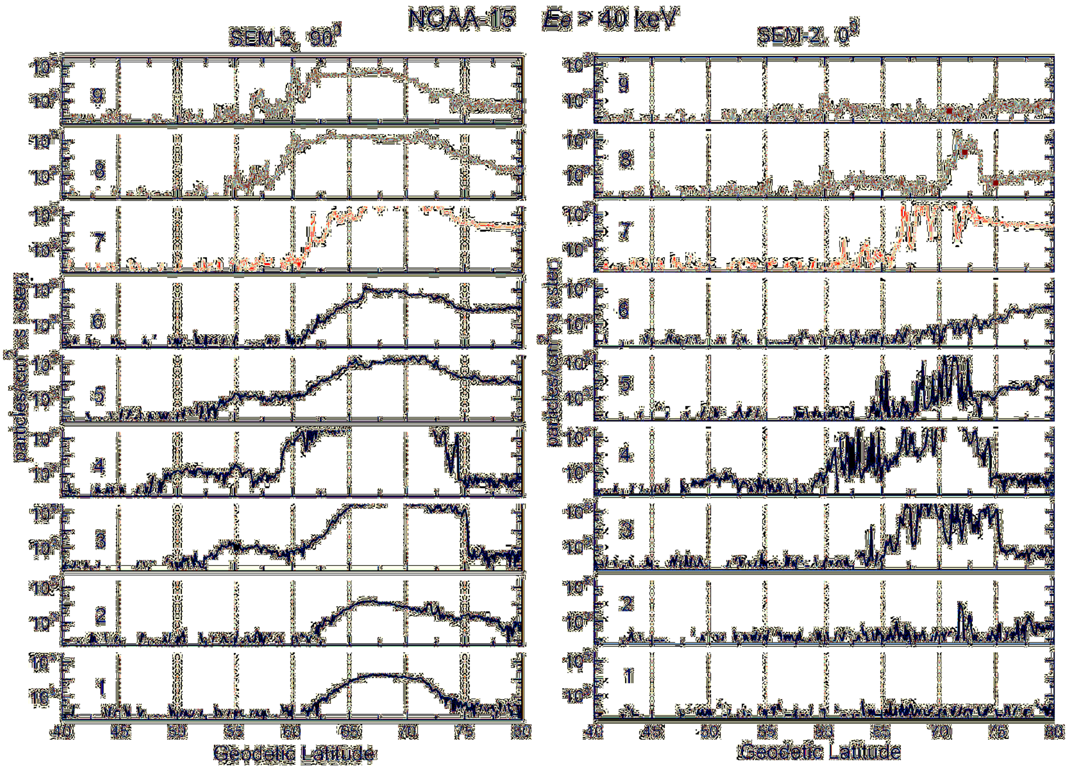

Fig. 2. Variations of the electron flux density with energies $E_e > 40$ keV in the Northern hemisphere in the interval of latitudes from $\varphi_1 = 40°$ to $\varphi_2 = 80°$N in the period from 15 to 18 March 2013 in the morning sector of local time above Europe from the horizontal (left panel) and vertical (right panel) of directions. Red color indicates variations of particles at the onset of the storm on March 17, while crimson color during the recovery phase on March 18. Explanations to the numbering of panels are given in Table

a falling down character, the upper energy limit of the particles does not exceed the value $E_e = 0.5$ MeV.

Dynamics of high energy electron fluxes in the Northern hemisphere

Enhanced fluxes of subrelativistic and relativistic electrons were detected at the end of March, 16 and during March, 17 according to the data of low Earth orbit satellite NOAA-15 at the Northern hemisphere at high latitudes in the region of open force lines of the geomagnetic field. Electrons of low and intermediate energies have got into the loss cone in the spatial region of the outer radiation belt in time the prolonged compression of the magnetosphere on March 16 and 17 (Fig. 1, *a*) and of the growth of AE-index (Fig. 1, *b*). The increase of the particle flux in the loss cone in the inner radiation belt zone was observed only in short intervals of pulse growth of SW velocity and density and in the main phase of the storm.

The profiles of radiation belts above the European continent at the observed period demonstrate the presence of pulsed vertical precipitations of electrons with energies $E_e > 40$ keV and $E_e > 130$ keV in the outer belt region at latitudes $\varphi \geq 60°$ (right-hand panels of Fig. 2 and 3); filling in some cases (profiles 3, 4 and 5 on the left panels of Fig. 2 and 3) of the gap between inner and outer belts by low energy electrons and sporadic variations of particle streams in the gap region at the recovery phase of geomagnetic storm (latitude range $55° \leq \varphi \leq 60°$); a slight increase of electron fluxes of both threshold energies (profiles 3, 4 and 5 on the left panels of Fig. 2 and 3) with the pitch-angles that are close to 90° in the inner belt region (latitude range $47° \leq \varphi \leq 55°$).

Registration of enhanced fluxes at low altitudes in the inner belt coincides with a significant increase of AE-index and electron fluxes with energies $E_e > 40$ keV at the geostationary orbit. Table shows time parameters of the profiles 1 – 9 in Fig. 2, 3.

Penetration of flare electrons with energies $E_e > 40$ keV from the interplanetary space onto low magnetosphere heights in the Northern hemisphere was recorded by the POES satellite at the end of March 16, and during March 17 at latitudes from 81° N up to latitudes of the projection of the outer radiation belt onto the Earth's surface (Fig. 4).

A significant part of particles immediately entered into the loss cone and was detected by sensors with view axis orienting in the direction of "anti-Earth" (Fig. 5). Injection of electrons onto outer belt region; accelerating processes and rapid radial diffusion

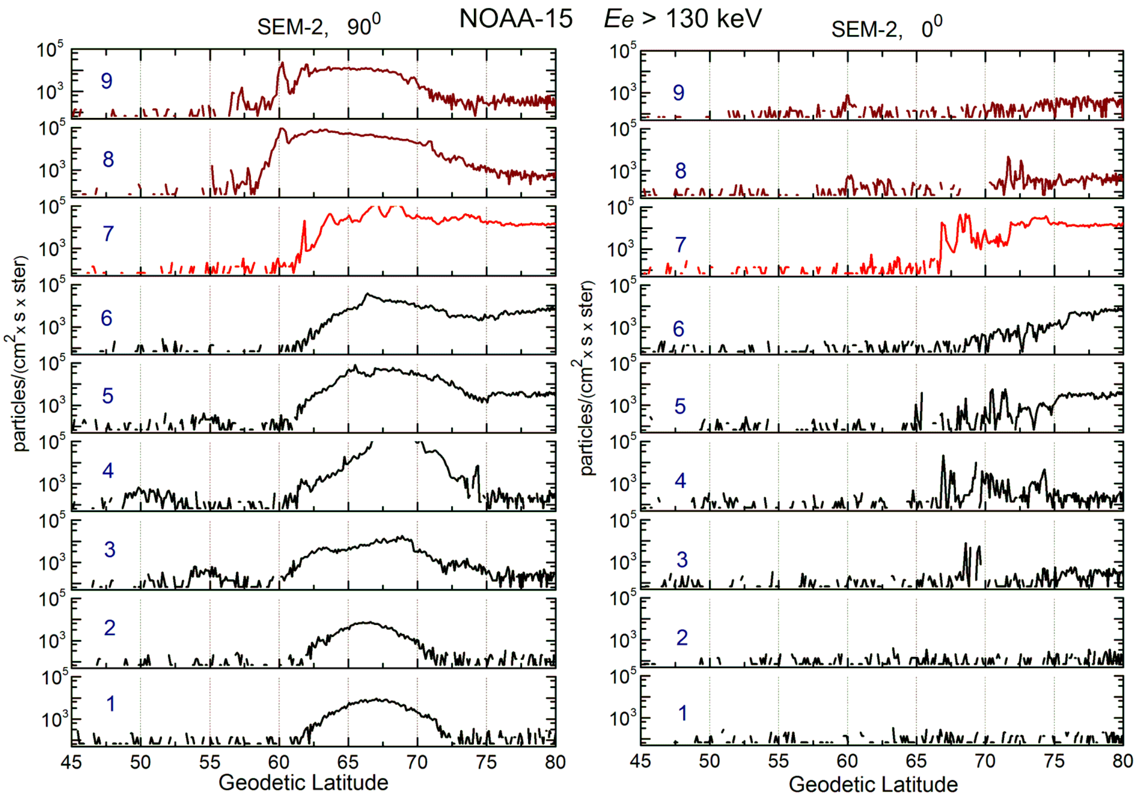

Fig. 3. The same as on Fig. 2 but for electrons with energies $E_e > 130$ keV

of outer belt particles downward to the inner part of magnetosphere; disappearance of the gap between belts, sharp increase of pulsed precipitating fluxes in the pre-dawn hours occurred during the main phase of the geomagnetic storm (right figure of panel *b*, Fig. 4) with the start of injection at $\Delta t_4 \approx 06{:}30-07{:}30$ UTC. Whilst in this temporal interval the lower boundary along the latitude of non-background quasi-trapped particle fluxes was observed at latitude $\varphi_1 \approx 52°$ N, then in the interval between $\Delta t_5 \approx 08{:}08-09{:}29$ UTC this boundary shifted to $\varphi_2 \approx 40°$ N, but in the time window from 11:10 to 11:30 UTC the lower boundary reached the minimum value of $\varphi_3 \approx 32°$ N.

Temporal intervals for registration of electron fluxes at the height of $h \approx 815$ km with energies $E_e > 40$ keV (Fig. 2) and $E_e > 130$ keV (Fig. 3) in the morning sector of local time above the Europe, and averaged within indicated intervals 1-minute's values of AE-, SYM-H-indices and of electron fluxes with energies $E_e > 40$ keV at geostationary orbit (EPS-MAGED / GOES-13) from the «anti-Earth» direction

№	Date March 2013	Temporal interval				Averaged values within interval		
		Start (80° N)		End (40° N)		AE	SYM-H	of electron fluxes with $E_e > 40$ keV at $h = 5.6\,R_e$
		UTC	LT	UTC	LT			
1	15	03h:35m	06h:35m	03h:46m	06h:46m	48	2	$7.6 \cdot 10^3$
2	15	05h:16m	08h:16m	05h:28m	08h:28m	80	5.2	$7.3 \cdot 10^3$
3	16	03h:11m	06h:11m	03h:22m	06h:22m	371	–23	$3.1 \cdot 10^3$
4	16	04h:52m	07h:52m	05h:03m	08h:03m	715	–18	$3.2 \cdot 10^5$
5	17	02h:46m	05h:46m	02h:57m	05h:57m	42	–10.5	$6.0 \cdot 10^4$
6	17	04h:27m	07h:27m	04h:38m	07h:38m	50	–8.5	$2.0 \cdot 10^4$
7	17	06h:08m	09h:08m	06h:19m	09h:19m	845	27	$8.1 \cdot 10^5$
8	18	04h:03m	07h:03m	04h:14m	07h:14m	77	–67	$5.3 \cdot 10^4$
9	18	05h:44m	08h:44m	05h:55m	08h:55m	30	–67	$5.1 \cdot 10^4$

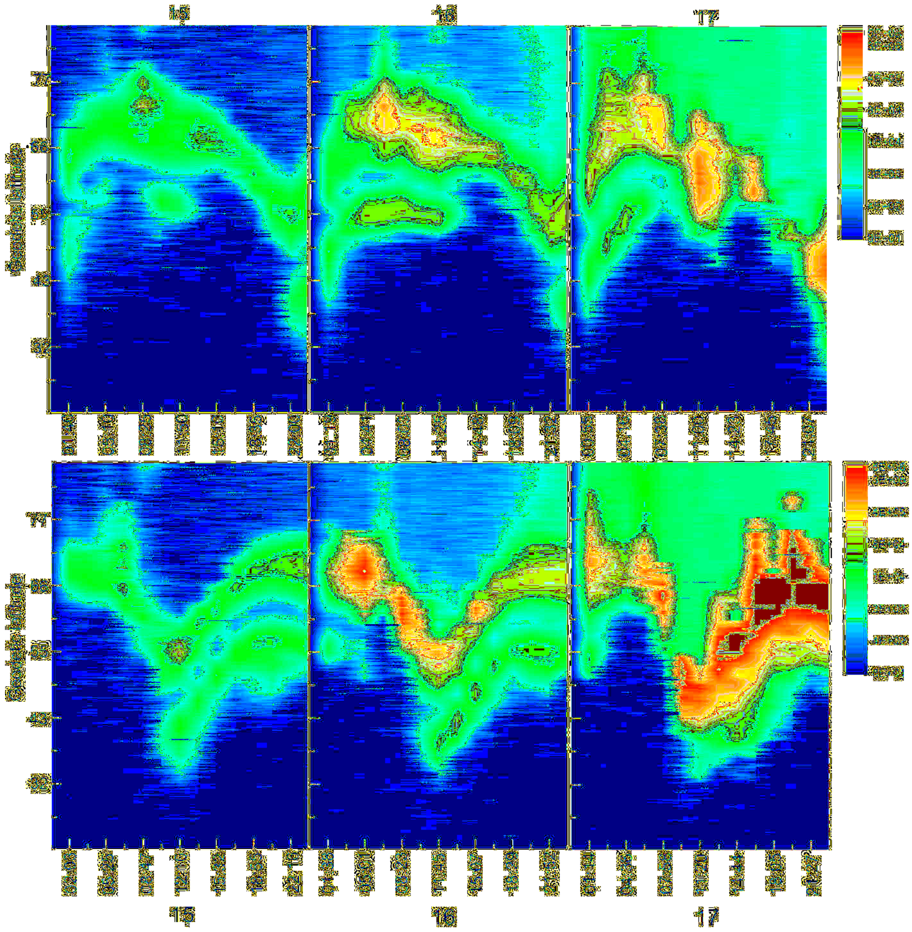

Fig. 4. Dynamics of electron fluxes with energies $E_e > 40$ keV in the Northern hemisphere in the interval of latitudes 20° – 80° N during the period from 15 to 17 March 2013 according to MEPED / SEM2 / POES data recorded from the horizontal direction at daytime (panel *a*) and in the pre-morning (panel *b*) hours of local magnetic time. Electron fluxes in the form of a 64-level color scale are represented in units of particles / (cm^2·s·ster). The time scale is in UTC

The southern latitude boundary of precipitating electrons that were measured from the "anti-Earth" direction has reached value $\varphi_4 \approx 42°$ N, and remained at this level within time interval $\Delta t_6 \approx$ 09:30 – 11:30 UTC on March 17, while on the previous day at similar time window the lower boundary reached the minimum value of $\varphi_5 \approx 52°$ N.

Features of TEC variations above Central Europe in the vicinity of the storm March 17, 2013

The dependence of the level of TEC variations vs. latitude at different phases of the storm is revealed. The conditional boundary, to the north of which the level of variation substantially increases, passes near 52° N parallel to the isolines of the geomagnetic field (Fig. 6). The position of the boundary at the onset of the storm changes insignificantly within few hours.

Electrons in plasmasphere make a noticeable contribution to TEC along the line of sight "GNSS satellite-terrestrial receiver". Earlier tomographic studies using GNSS signals have shown that the plasmaspheric electrons are concentrated into finger-like structures extending from the upper ionosphere to a height of several thousand kilometers and having transverse dimensions from 200 to 400 km (see [2] and therein referred literature). At the bottom of these structures, located at ionospheric heights, the electron concentration is higher than in neighboring regions and smoothly decreases to an altitude of about ten thousand kilometers, gradually increasing at high altitudes.

On maps above Central Europe during the storm, the quasi-periodical formations have been detected existing during 2 – 3 hours. Their direction changes during the satellite flight in accordance with the change of its angular coordinates (Fig. 6). Finger-like structure of variable density is being projected on the south of map in a form of a "tail" corresponding to increased electron concentration in the magnetosphere, and of the "head" with a high concentration of electrons in the ionospheric plasma in the north of the map.

We suppose that in high-altitude parts of the finger-like structures the signal of the GNSS satellite passes through the zone in which trapped and quasi-trapped electron fluxes are being concentrated near their mirror reflection points (Fig. 7). Accordingly, the increases of TEC in comparison with zones outside of structures, as well

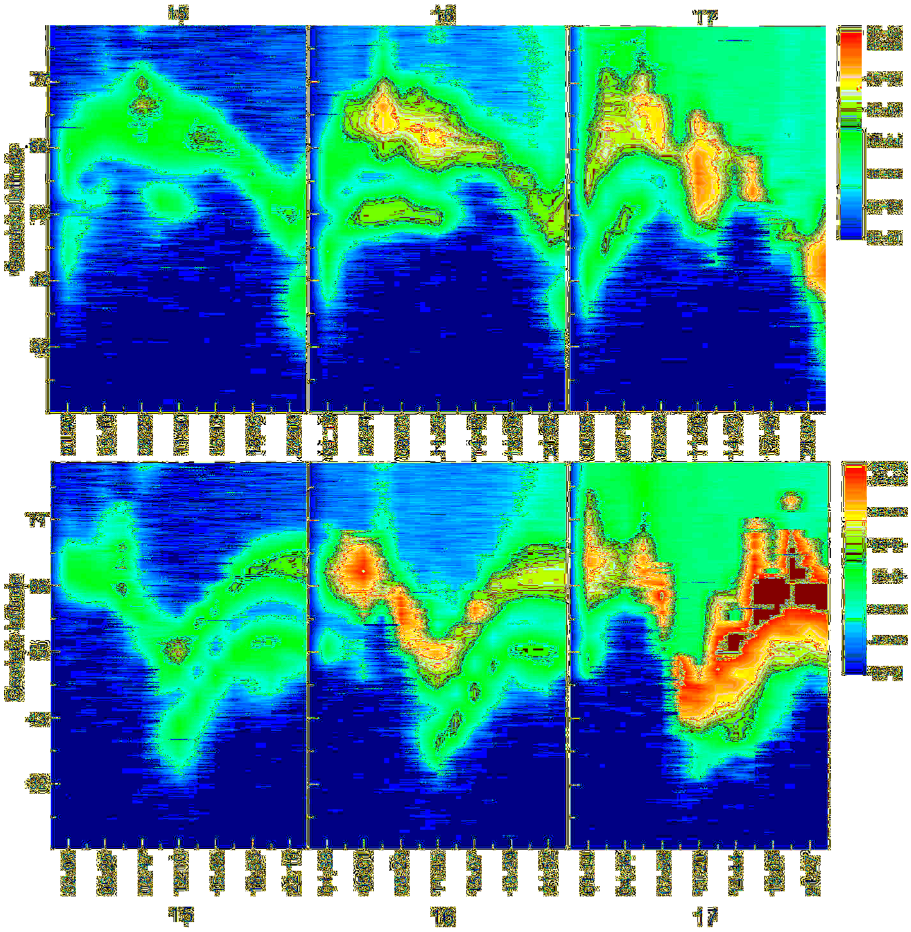

Fig. 5. The same as on Fig. 4, but for electrons that were recorded from «anti-Earth» direction

as the rotation of the «tail» on the map synchronized with the motion of the GNSS satellite are noticeable. In the bottom parts of finger-like structures resting upon the ionosphere, ionization of the residual atmosphere by high-energy electrons is observed. As a result, a large number of secondary electrons are produced that are manifested as an increase of TEC in regions of "heads". As far as the "heads" of structures are presumably formed at ionospheric heights their displacement along geographic coordinates was not noticed when the GNSS satellite moved. The jagged by intensities temporal profiles of high energy electron fluxes with energies of tens of keV, recorded on the NOAA-15/POES spacecraft with a time resolution of 2 seconds can be as the reason for registration of "finger-like" structures in TEC.

Visualization of electron density spatial distribution in the bottom of magnetosphere demonstrated in this paper is like the results of tomographic studies. However, there is one significant difference. In our studies solution of inverse tasks are not carried out and, accordingly, the minimum requirements are applied

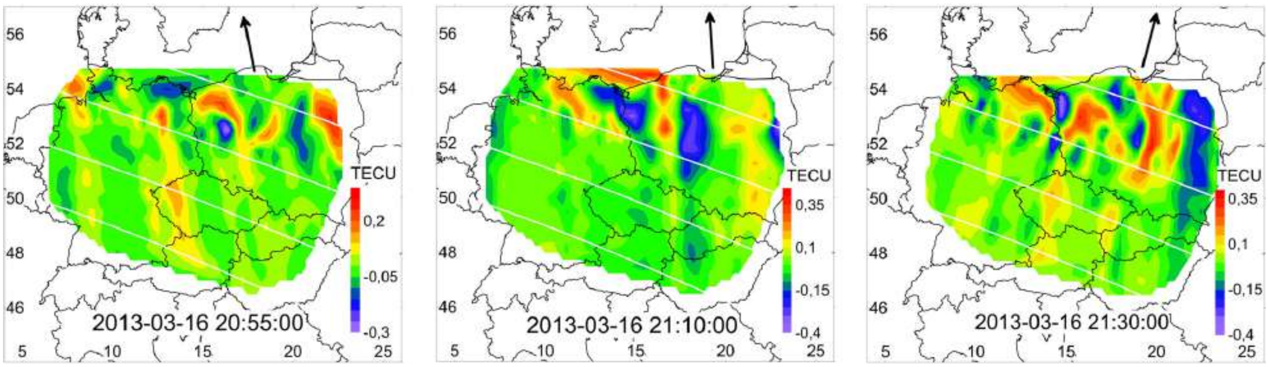

Fig. 6. Maps of TEC variations above Central Europe before SC of the geomagnetic storm on March 17, 2013. Arrows indicate the projections of directions to GNSS satellite. In white color isolines of the geomagnetic field at ionospheric altitude are shown

to models used. These requirements constitute an independence of spatial-temporal distributions of the electron content in the ionosphere along horizontal, and in the magnetosphere along vertical. Requirements, accompanied by the provision of the presence of noticeable spatial variations of TEC, which are relatively stable in time scales of about dozen minutes, are realized in some phases of the geomagnetic storm.

It should also be noticed that the fundamental fact in this study is that the signals of high-orbiting GNSS satellites "shine through" the entire of the lower magnetosphere. Further work on the mapping of TEC disturbances, conducted continuously in monitoring mode, can provide new information on dynamic processes in the ionosphere and the lower magnetosphere.

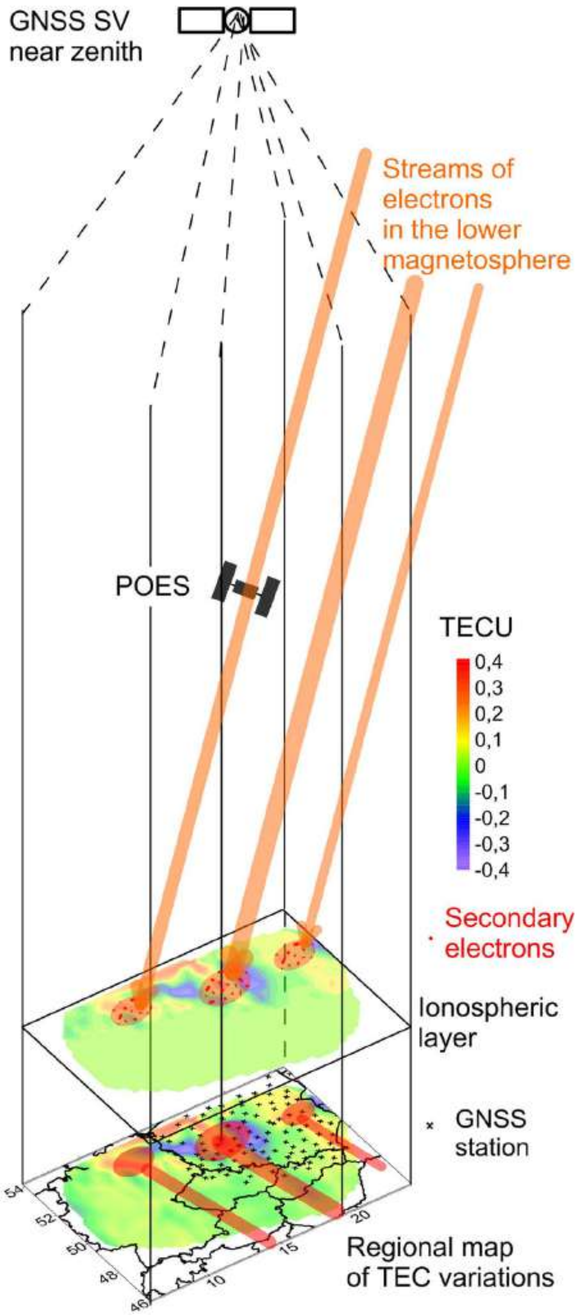

Fig. 7. Model representation of the mapping of energetic electrons forming finger-like structures in the magnetosphere in the form of «tails» and secondary electrons in the form of "heads" on the map of TEC variations

Conclusions

1. The solar flare on March 15, 2013, generated geo-effective coronal mass ejection, and the geomagnetic storm that followed caused significant variations of particle fluxes intensity in the inner layers of the magnetosphere.
2. The motion of the southern boundary of TEC variations in the Northern hemisphere is being confirmed with changes in the location of the southern boundary of the penetration of electrons with energies of few tens of keV onto heights of low-orbiting satellites during the main phase of the geomagnetic storm.
3. Medium-scaled variations of TEC at the middle latitudes can be associated with sporadic microbursts of high energy electrons under Van Allen radiation belts and in the gap between inner and outer belts.
4. Variations of TEC contain significant information on processes in the ionosphere and magnetosphere. Visualization of variations provides one more effective tool for retrieval of this information.

REFERENCES

1. *Zanimovskiy Y., Dudnik O.* Coupling of TEC variations over Central Europe with precipitations of energy particles during geomagnetic storm on March 17, 2013 / Abstracts of the 17th Ukrainian conference on space research, August 21–25, 2017, Odesa, Ukraine. – P. 24.

2. *Zanimonskiy Y.M., Dudnik O.V., Nykiel G., Figurski M.* Investigation of some magnetospheric phenomena of geomagnetic storm on March 17, 2013, based on observations from GNSS and NOAA-15 satellite // Proceedings of the 6th International Radio Electronic Forum (IREF'2017). International Scientific Conference "Radar. Satellite navigation. Radiomonitoring", October 24–26, 2017, Kharkiv, Ukraine. – P. 196–199 (in Russian).

3. *Zanimonskiy Y.M., Nykiel G., Figurski M., Yampolski Y.M.* Modeling of the travelling ionospheric disturbances. Case study of ASG-EUPOS network/ Proceedings of the EGU General Assembly, April 17–22, 2016, Vienna, Austria; Geophysical Research Abstracts, 2016. – V. 18. – EGU2016-17484.

4. *Zanimonskiy Y.M., Nykiel G., Paznukhov A.V., Figurski M.* Modeling of TEC Variations Based on Signals from Near Zenith GNSS Satellite Observed by Dense Regional Network / Proceedings of the 2016 International Technical Meeting of The Institute of Navigation, January 25 – 28, 2016, Monterey, California. – P. 585–590.

5. *Nykiel G., Zanimonskiy Y.M., Yampolski Yu.M., Figurski M.* Efficient Usage of Dense GNSS Networks in Central Europe for the Visualization and Investigation of Ionospheric TEC Variations // Sensors. – 2017. – V. 17. – Iss.10. – P. 2298. DOI: 10.3390/s17102298.

RESULTS OF OBSERVATION OF IONOSPHERIC PROCESSES OVER UKRAINE IN 2016–2018

L. Chernogor, I. Domnin, L. Emelyanov, D. Kotov, M. Lyashenko, S. Panasenko, A. Bogomaz

Institute of Ionosphere of NAS of Ukraine and Ministry of Education and Science of Ukraine
(IION NASU and MESU)

Ionospheric Observatory of the Institute of Iono-sphere is located in 50 kilometers to the south-east from Kharkiv city (49.6° N, 36.3° E; $\Phi = 45.7°$, $\Lambda = 117.8°$). The Ionospheric Observatory facilities include the 158 MHz VHF incoherent scatter (IS) radar equip-ped with the zenith parabolic Cassegrain antenna of 100 m diameter; the 158 MHz VHF IS radar equipped with the fully steerable parabolic antenna of 25 m diameter and ionosonde "Bazis" [1, 2].

Incoherent scatter radar with zenith-directed antenna allows measuring with high accuracy (usually error is 1–10 %) and acceptable altitude resolution (10–100 km) the following ionospheric parameters: electron density N, electron T_e and ion T_i temperatures, vertical component of the plasma drift velocity V_z, and ion composition. The investigated altitude range is usually 100–700 km, but can reach 100–1500 km in high solar activity period [1, 2].

The aim of this paper is a brief overview of the investigation results of ionospheric processes over Ukraine, obtained in 2016–2018. During this period, we conducted monitoring of ionospheric processes in quiet and disturbed conditions, modernization of measuring systems, improving of geophysical data measurement and processing techniques.

Regular processes in the ionosphere over Ukraine

Variations of the main parameters of the ionospheric plasma [3–12]. Observations of diurnal and seasonal variations of the electron density, electron and ion temperatures over a wide range of altitudes (100–750 km) were carried out during the period of 2016–2017. The experimental data were obtained by means of Kharkov IS radar for the specific geophysical periods: vernal and autumn equinoxes and summer and winter solstices in quiet heliogeophysical conditions. Comparative analysis of variations of the main ionospheric parameters on the maximum and decline phases for the 23rd and 24th solar cycles was performed.

Obtained results of observations of diurnal and seasonal variations of environmental parameters are used to verify and correct existing global ionospheric models, as well as to improve the regional ionospheric model CERIM IION, which developed in the Institute of Ionosphere and based on data from the Kharkov IS radar [12].

Variations in the vertical component of the plasma transfer velocity. Fig. 1 shows the time variations of the velocity V_z obtained for specific dates on the descending branch of solar activity in the period 2015–2017. On the upper panel of Fig. 1, *d*, V_z variations in December 2016 at an altitude of 530 km are not shown due to the low level of the IS signal at low solar activity (signal-to-noise ratio less than 0.1). The same figure shows the variations of V_z obtained on the following days on December 22 and 23, 2016. There is a satisfactory repeatability of the results of measurements in these days, as well as their close agreement with the variations on December 22, 2015. Diurnal variations of V_z were characterized by the morning extremum (decrease in the absolute value of the velocity of downward motion of plasma ($V_z < 0$) with changing direction of the plasma motion to upward ($V_z > 0$) at high altitudes of the ionosphere) and the evening extremum (increase in the velocity module of downward plasma motion). Important feature of observations on March 20, 2015 is the fact that they were carried out on the background of the geomagnetic storm relaxation and from 09:09 to 11:21 UT the partial solar eclipse was observed over Kharkov. During this eclipse, the absolute value of the velocity of downward plasma flow increased and reached its maximum at the time when the solar disk was completely covered (see Fig. 1, *a*).

From Fig. 1 it is possible to see a good agreement in the variations of V_z in 2016 and 2017 in the spring (Fig. 1, *a*) and in the summer (Fig. 1, *b*), in 2015 and 2016 in the autumn (Fig. 1, *c*) and in the winter (Fig. 1, *d*), whereas there are significant differences in

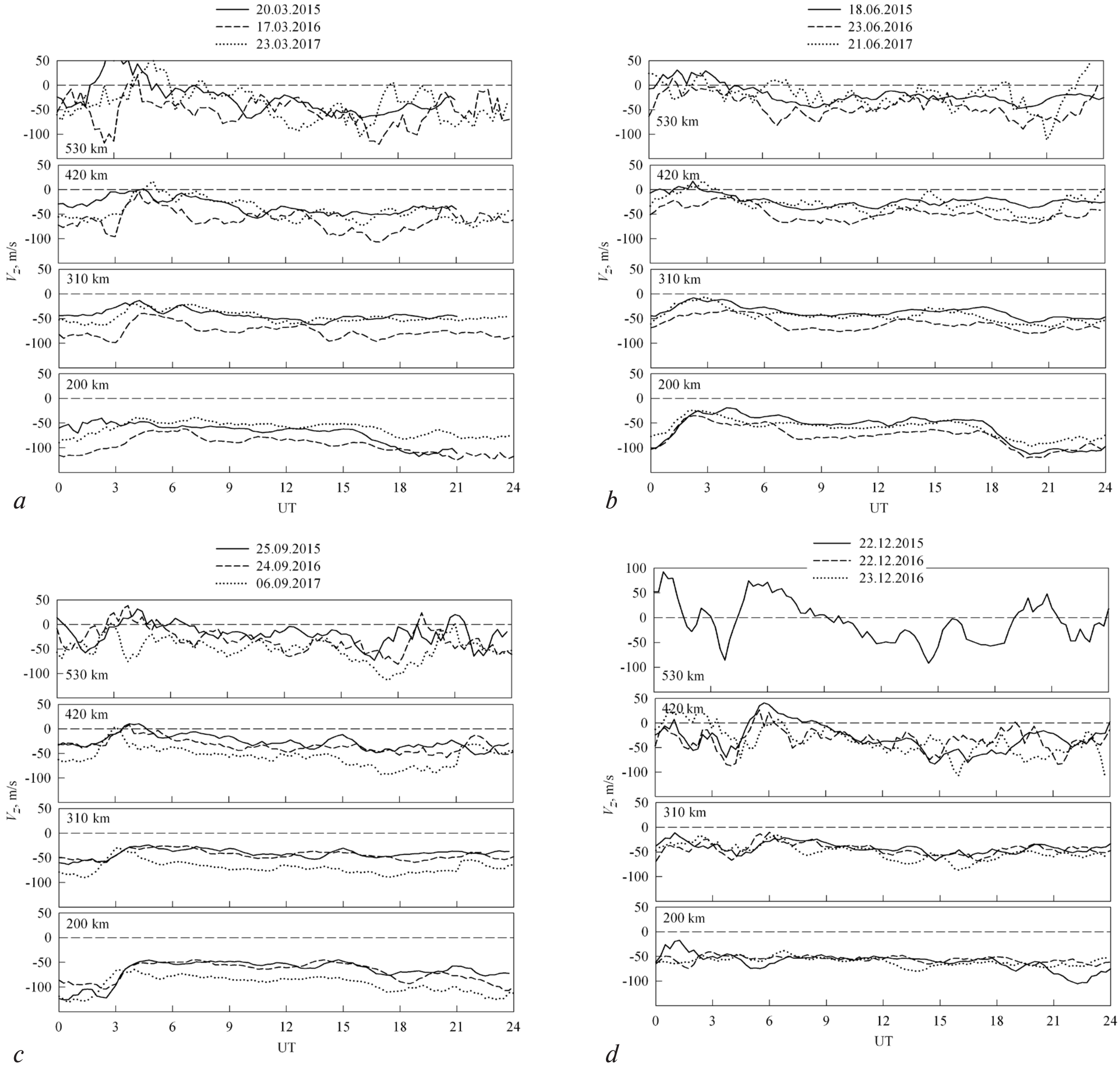

Fig. 1. Variations in the vertical component of the plasma transfer velocity at fixed altitudes near vernal (*a*) and autumn (*b*) equinoxes and summer (*c*) and winter (*d*) solstices

the values of V_z in March and June 2016, September 2017, and also in certain moments of time during the day for individual experiments in different years (for example, at nighttime in March 2015, 2016 and 2017). This indicates the multifactorial effect on the variation of V_z, including the effect of geomagnetic storms and disturbances on the vertical transport of ionospheric plasma.

The effects of seasonal and semiannual anomalies [8]. The analysis of diurnal and seasonal variations of the electron density at the maximum of the F2 region of the ionosphere at different phases of the 23rd and 24th solar cycles (2003–2014) during equinoxes and solstices was performed. It was found that at the maximum of solar activity the winter values of N_m exceeded the summer values by approximately 2 times. During the decline and growth phases of solar activity the noontime values of N_m in winter exceeded the summer values by approximately 1.3–1.4 times. At the minimum of solar activity, the effects of the seasonal anomaly in N_m variations were not appeared. The effect of the semi-annual anomaly was that the values of the electron density N_m during the equinoxes exceeded the values of N_m during the summer and winter solstices. For the observation periods under review, this excess was 1.1 to 2.5 times, depending on the phase of the solar activity cycle. A comparative analysis of the calculations for the IRI-2012 and CERIM IION models with experimental data was performed. It was found that the considered models in most cases correctly calculate the electron density at the maximum of the F2 region of the ionosphere and reproduce the seasonal features in the variations of N_m at different phases of the solar activity cycle.

Variations of the ion composition of the upper ionosphere [3, 7, 9, 10]. The investigations to determine the degree of influence of weak geomagnetic disturbances on the concentration of hydrogen ions H^+ under conditions of moderate solar activity in the period 2015–2016 were performed. The main idea of these investigations is that weak geomagnetic activity can lead to global rearrangement of the thermospheric circulation and the transfer of neutral hydrogen atoms from the exosphere to the heights of the outer ionosphere. This can cause an abnormal increase in the concentration of H^+ ions not only during low, but also during moderate level of solar activity.

The analysis of hydrogen ion concentration variations for September 23–26, 2016 and June 21–24, 2016 was performed. During these periods, quiet geomagnetic conditions (index $K_p = 0–2$) changed to weakly disturbed conditions ($K_p = 3–4$). It was found that the change in the level of geomagnetic activity leads to noticeable change in the concentration of H^+ ions. For example, the concentration of hydrogen ions during nighttime on September 26, 2016 ($K_p = 4$) was two times less than the nighttime concentration of H^+ on September 24 ($K_p = 2$).

Additional theoretical calculations performed by using the physical model of the ionosphere SAMI3 (using the resources of the international geophysical modeling center Community Coordinated Modeling Center) and the empirical model TTS-05 (International Reference Ionosphere – 2012) show that the existing models are imperfect because they predict significantly smaller changes in the concentration of hydrogen ions compared to the experimental results. In this case, proposals regarding possible mechanisms for accounting for the weak geomagnetic disturbances influence on the concentration of H^+ ions were formulated.

Dynamic and thermal processes in the ionosphere. Calculations of the variations of dynamic and thermal process parameters in geospace plasma were performed. The experimental data obtained on the Kharkov IS radar during the periods of equinoxes and solstices in 2016 were used for these calculations. The calculations were based on the experimental data (N, T_e, T_i, V_z) obtained on the Kharkov IS radar during the periods of equinoxes and solstices in 2016. The diurnal and seasonal variations of the vertical component of the plasma transfer velocity due to ambipolar diffusion, the full plasma flux density and its diffusion component Π_p and Π_d, the energy, supplied to the electrons, the heat flux density transferred by electrons from the plasmasphere into the ionosphere were calculated.

Irregular processes in the ionosphere over Ukraine

Irregular processes in the ionosphere are associated with ionospheric storms [6, 13, 14], solar eclipses [15, 16], generation and propagation of wave disturbances [17–22], etc.

Data base of ionospheric storms (ISt) was created in the Institute of ionosphere. We thoroughly investigated features of a number of ionospheric storms of varying intensity. These storms were accompanied by magnetic disturbances and were observed between 1998 and 2017 [1, 2, 6, 13, 14].

Analysis of the effects of a number of ISts made it possible to formulate the basic laws and especially in the development of ISts at mid-latitudes in Central Europe [1, 2] and allowed to classify considered storm in four groups, according to their characteristics and the scheme of development: 1) a strong magnetic storm (MS) accompanied by strong ISt; 2) a weak MS accompanied by strong ISt; 3) strong MS accompanied by a weak ISt; 4) a weak MS is accompanied by moderate ISt.

Ionospheric storm on March 14–17, 2016. [13]. Geomagnetic conditions on March 14–17, 2016 were disturbed as a result of several subsequent substorms. The K_p index reached values of 5–5.3, which is typical for a moderate geomagnetic storm. The D_{st} index reached –55 nT. Magnetic storm effects were manifested in variations of the critical frequency and electron density at the maximum of the F2 region. During the magnetic storm, a change in the phases of ionospheric disturbances from negative to positive was observed. Deviation of the critical frequency δf_oF2 (relative to the data for reference day on March 13, 2016) has changed from –34 % to +30 %. Respectively, N_mF2 density decreased approximately 2.3 times, and then increased to about 1.7 times. Then there was a decrease in the values of the critical frequency in comparison with values of f_oF2 in the absence of perturbations (March 13, 2016). The relative deviation of δf_oF2 reached –22 % and after 07:00 on March 17 it did not exceed this value (by module). Moderate magnetic storm was weakly affected on the variation in the height of maximum of the F2 region in the recovery phase. Deviation of the height of maximum of the F2 region δh_mF2 did not exceed 15–16 %. Moderate magnetic storm has led to a significant change in the dynamic and thermal conditions of ionosphere (Fig. 2). During the main phase of the storm increase in the velocity of downward motion of plasma V_z

with maximum at 02:45 UT and its subsequent decrease were observed. The amplitude of deviation of V_z increased with altitude and was 7–97 m/s at altitudes of 200–530 km. On March 17, 2016, in the time interval from 12:00 to 18:00 UT at altitudes of 200–420 km quasiharmonic oscillations of V_z with a period of 2 h 15 min and amplitude of about 10 m/s were detected, which is obviously associated with a change in geomagnetic activity.

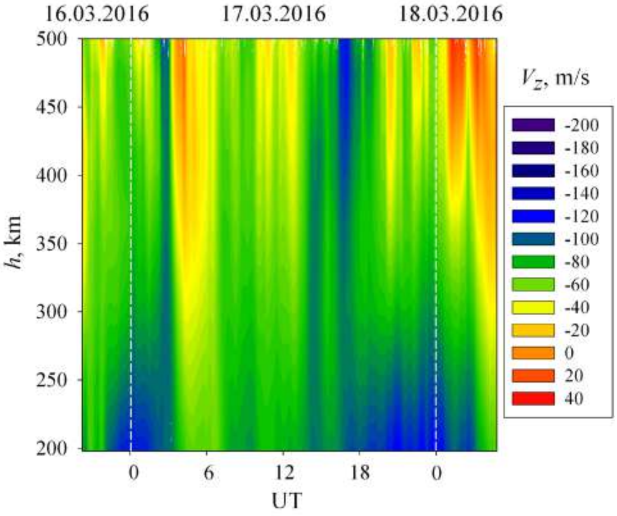

Fig. 2. Spatial-temporal variations of the vertical component of the plasma transfer velocity during ionospheric storm on March 14–17, 2016 [13]

Solar eclipse (SE) on March 20, 2015. [15, 16]. SE started at 09:09 UT, ended at 11:21 UT. Maximum coverage of the solar disk area amounted 44 %, in diameter –54 %. SE proceeded on the background of the recovery phase of strong MS, which took place on March 17–18, 2015 (The maximum value of the geomagnetic activity index $K_{pmax} = 8$). Heliogeophysical situation during the eclipse was disturbed ($D_{st} \approx -50$ nT, $K_p = 5$, $A_p = 24$). The solar radio flux index $F_{10.7} = 113$. The effect of storm did not allow using of observational data on March 19, 2016 for comparison with variations on March 20, 2016. The dates of March 20, 2013 and March 29, 2012 were selected as reference days. Despite the disturbed state of geospace plasma, SE effects were noticeable in the ionosphere parameters variations. At the moment of maximum Sun disk coverage (10:15 UT) height of maximum of F2 region of ionosphere has increased about 40 km (from 240 to 280 km). The SE effects significantly masked by ISt in variations of critical frequency and electron density at peak of F2 region of ionosphere. Critical frequency changes were not more than 12 %. Electron density N decrease in the maximum phase of eclipse was about 18.5 and 16.5 % at altitudes of 190 and 210 km, respectively.

There was no reaction of N to SE at altitudes of 240 km and above. T_e decreasing during maximum coverage of solar disk reached 12.1, 12, 17.7, 17, 19.5, 19, 15.5 and 13.4 % at the heights of 190, 210, 240, 290, 340, 410, 490 and 580 km, respectively. SE effect was weak in T_i variations. The results of experimental studies and theoretical calculations showed that SE has led to a significant change in the dynamic and thermal conditions of ionosphere. During SE at altitudes above 308 km, increase of absolute values of downward motion of ionospheric plasma velocity V_z was observed. Its maximum was near the moment of SE maximum phase and after V_z was recovered. The amount of V_z change increased with increasing height, and the greatest change value (relatively to undisturbed day data and average value of V_z before and after SE) was 19–55 m/s in the height range 363–583 km. The amount of energy supplied to the electrons at the time of maximum coverage of the solar disk decreased and was about 30 % at altitudes of 200–300 km. The amount of heat flux density transferred by electrons decreased and was about 63, 50 and 42 % at altitudes of 300, 350 and 400 km, respectively.

Wave disturbances in the ionosphere [17–22]. By the use of software package developed at the Institute of the ionosphere it was found that in all seasons the traveling ionospheric disturbances (TID) were observed. These disturbances were noticeably manifested in variations of the IS signal power and in electron and ion temperatures. The vertical phase velocity of TIDs was directed downward and increased with increasing altitude. This indicates that sources of disturbances were in the lower atmosphere. It was found that the prevailing periods of disturbances varied in the range of 40–80 minutes and their duration does not exceed 2–5 periods. The relative amplitudes of TIDs were 0.1–0.3 for the IS signal power and 0.03–0.1 for electron and ion temperatures.

The results of joint analysis of TIDs observations over Kharkov (49.6° N, 36.3° E) and Millstone Hill (42.6° N, 288.5° E) showed the following. The prevailing TIDs are observed near solar terminators. In addition, TIDs are detected for both sunrise and sunset terminators. Characteristics of TIDs suggest that they propagate upward from lower altitudes. We do not find any obvious dependence of TID characteristics on global auroral indexes or local auroral electrojet, though moderate storms occurred during both observation days.

The TID periods varied mostly in the range of 40–80 minutes and occasionally in the range of 20–40 minutes (see Fig. 3). Relative amplitudes were usually within 0.03–0.15 for electron density

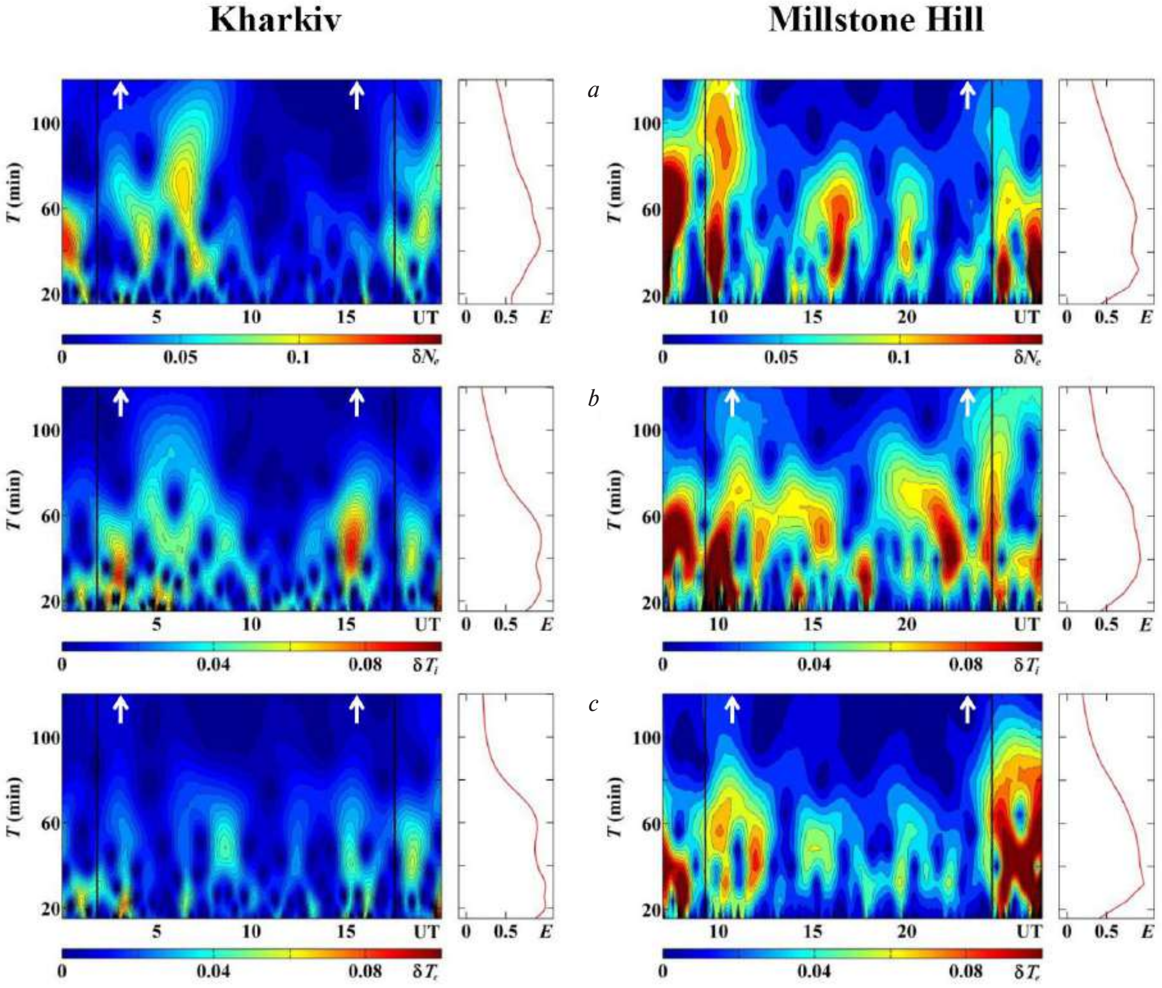

Fig. 3. Results of spectral analysis performed for temporal variations of electron density (*a*), ion temperature (*b*) and electron temperature (*c*) using Kharkov (left column) and Millstone Hill (right column) data at the height of 280 km for March 17, 2016. The solid lines show the times of local sunrise and sunset terminator passage at the analyzed height and white arrows depict the same times at ground level

and 0.03–0.10 of plasma temperature at Kharkiv, and 0.08–0.35 in electron density and 0.03–0.15 in temperatures at Millstone Hill. Larger TID relative amplitudes are observed over Millstone Hill during vernal equinox as compared to summer solstice. The maximum TID amplitudes are observed at the heights of 200–250 km. The absolute amplitudes of TIDs in N over Millstone Hill were lower than over Kharkiv near vernal equinox. In contrast, absolute TID amplitudes for all observed ionospheric parameters were higher over Kharkiv during summer solstice. The durations of TID events over each radar site were usually 2–5 periods.

Ionospheric disturbances caused by effect of powerful decameter radio transmission

For effect on the ionosphere plasma we used heating facility "Sura" (Nizhny Novgorod, Russia) and Tromsø (Norway). Coordinated experiments were carried out in 2009–2015. Diagnostics of environment was conducted by Kharkiv IS radar. In addition, the data of the ionosondes from European network was involved.

A special feature of our research was that quasi-periodic disturbances were observed far beyond antenna pattern [23].

Generation of aperiodic disturbances in the ionosphere [23]. Spatial distribution of aperiodic large-scale disturbances in the ionosphere was studied with the help of the European network ionosondes. These disturbances were accompanied by an effect on plasma by powerful radio transmission of heating facility "Sura" [23].

In the time variations of the critical frequency of the F2 region, aperiodic bursts of 0.1–0.4 MHz were observed. These bursts were accompanied by an action on the ionosphere by powerful radio emission with 15 minute duration. The time delay of disturbances in relation to the moment when the heating facility was turned on was 5–15 min and its duration was 10–15 min. Horizontal size of the perturbed ionospheric region was not less than 2200 km. The magnitude of perturbations has decreased with increasing distance from the heating facility. It worth to note that in a number of cases the "accumulation effect" of disturbances was observed, when aperiodic bursts occurred during operation of the heating facility in the mode [+5 min; –5 min].

The observed bursts of the critical frequency could be masked by wave disturbances of natural and artificial origin. In the latter case, wave disturbances were generated by powerful radio emission, as evidenced by their estimated propagation velocity (about 300–500 m/s) and its dependence on altitude.

Aperiodic bursts of the critical frequency indicate 1–10 % increase in the electron density in the F region of the ionosphere. It is mainly determined by the high-energy electrons precipitation from the Earth's radiation belt, which is in a metastable state. Such a condition could be caused by the weak and moderate geomagnetic storms that occurred during the measurement campaign. The observed regularities require verification and more detailed study involving other methods of diagnostics and measurement of electron fluxes [23].

Modernization of measuring systems, improvement of measurement and processing methods

In 2016–2018, the modernization of measuring systems continued, as well as the further improvement of methods for measuring and processing ionospheric data [24–32]. On key issues, Ukraine patents were obtained [33–35].

Using research results in the educational process

The results of research aimed at the modernization of measuring systems, development and improvement of methods for measuring and processing of measurement data were used in the preparation of bachelors and masters in the specialties "Applied Physics and Nanomaterials" and "Computer Engineering" [36, 37].

Conclusions

1. Experimental and theoretical studies of the ionospheric parameters variations, dynamic and thermal processes in geospace plasma in a wide range of altitudes (100–750 km) over Ukraine (Central Europe) in the period 2016–2018 were carried out.

2. Experimental and theoretical studies of the effects in geospace during geomagnetic storm on March 14–17, 2016 and solar eclipse on March 20, 2015 were performed.

3. The method for detecting travelling ionospheric disturbances (TID) based on the data of the IS radar was proposed and tested. It was found that the prevailing periods of disturbances varied in the range of 40–80 minutes and their duration does not exceed 2–5 periods. The relative amplitudes of TIDs were 0.1–0.3 for the IS signal power and 0.03–0.1 for electron and ion temperatures.

4. Spatial distribution of aperiodic large-scale disturbances in the ionosphere was studied with the help of the European network ionosondes. These disturbances were accompanied by an action on plasma by powerful radio transmission of heating facility "Sura". In the time variations of the critical frequency of the F2 region, aperiodic bursts of 0.1–0.4 MHz were observed. These bursts were accompanied by an impact on the ionosphere by powerful radio emission with 15 minute duration. The time delay of disturbances in relation to the moment when the heating facility was turned on was 5–15 min and its duration was 10–15 min.

5. Modernization and improvement of means of radio sounding of the ionosphere, as well as the further development of measuring methods, analysis and interpretation of geophysical data were carried out during the period of 2016–2018.

REFERENCES

1. *Chernogor L.F., Domnin I.F., Emelyanov L.Ya., Katsko S.V., Kotov D.V., Lyashenko M.V., Panasenko S.V.* Observation results of the ionospheric processes over Ukraine in 2012–2014 // Space research in Ukraine. 2012–2014 / Ed. O. Fedorov. – Kyiv: Akademperiodyka, 2014. – P. 20–27.

2. *Chernogor L., Domnin I., Emelyanov L., Katsko S., Kotov D., Lyashenko M., Panasenko S.* Results of observations of ionospheric processes over Ukraine in 2014–2016 // Space research in Ukraine. 2014–2016 / Ed. O. Fedorov. – Kyiv: Akademperiodyka, 2016. – P. 34–41.

3. *Kotov D.V., Richards P.G., Bogomaz O.V., Chernogor L.F., Truhlik V., Emelyanov L.Ya., Chepurnyy Ya.M., Domnin I.F.* The importance of neutral hydrogen for the maintenance of the midlatitude winter nighttime ionosphere: Evidence from IS observations at Kharkiv, Ukraine, and field line interhemispheric plasma model simulations // J. Geoph. Res.: Space Physics. – 2016. – V. 121. – Iss. 7. – P. 7013–7025.

4. *Siusiuk M.M., Kotov D.V., Chernogor L.F., Bogomaz O.V.* Variations of plasma temperatures in ionosphere over Kharkiv during extreme solar minimum // Radio Physics and Radio Astronomy. – 2016. – Vol. 21. – No. 4. – P. 132–140 (in Russian).

5. *Siusiuk M.M., Kotov D.V., Chernogor L.F., Bogomaz O.V.* Variations of plasma temperatures in ionosphere over Kharkiv in the solar activity growth phase // Radio Physics and Radio Astronomy. – 2016. – Vol. 21. – No. 4. – P. 279–284 (in Russian).

6. *Lyashenko M.V.* Dynamic and Thermal Processes in the Mid-Latitude Ionosphere over Kharkov, Ukraine (49.6° N, 36.3° E), During the 13–15 November 2012 Magnetic Storm: Calculation Results // Acta Geophysica. – 2016. – V. 64.38 – No. 6. – P. 2717–2733. DOI: 10.1515/acgeo-2016-0087.

7. *Shulha M.* Investigation of the ion composition in the topside ionosphere at solar maximum using incoherent scatter technique: master thesis in physics. – Tromsø: UiT The Arctic University of Norway, 2016. – 90 p.

8. *Lyashenko M.V., Lyashenko N.S.* The effects of seasonal and semi-annual anomalies in the variation of the electron density at the maximum of the F2 region of the ionosphere at different phase of the solar activity // Bulletin of National Technical University «Kharkiv Polytechnic Institute». Series: «Radio Physics and ionosphere». – 2016. – No. 34 (1206). – P. 49–57 (in Russian).

9. *Shulha M.A.* Investigation variations of the relative concentration of hydrogen ions in the upper ionosphere during the period of maximum solar activity using incoherent scatter technique // Bulletin of National Technical University «Kharkiv Polytechnic Institute». Series: «Radio Physics and ionosphere». – 2016. – No. 34 (1206). – P. 58–62 (in Russian).

10. *Kotov D., Richards P., Erickson P.J., Goncharenko L., Bogomaz O., Truhlík V., Shulha M., Siusiuk M., Domnin I.* Strong Changes in H^+ Fraction and Upper Transition Height Induced by Minor Geomagnetic Storm of September 23 – 26, 2016 / 32nd URSI General Assembly and Scientific Symposium, Montreal, August 19 – 26, 2017.

11. *Lyashenko M.V., Shnitsar I.R.* The spatial-temporal variations of the electron concentration in ionosphere in minimum and maximum of solar activity // Bulletin of National Technical University «Kharkiv Polytechnic Institute». Series: «Radio Physics and ionosphere». – 2017. – No. 47 (1268). – P. 24–32 (in Russian).

12. *Lyashenko M.V., Sydorenko A.V.* Regional model of ionosphere CERIM IION: calculation of the maximum height of the ionospheric F2 layer // Bulletin of National Technical University «Kharkiv Polytechnic Institute». Series: «Radio Physics and ionosphere». – 2017. – No. 47 (1268). – P. 51–56 (in Russian).

13. *Katsko S.V., Emelyanov L.Ya., Chernogor L.F.* The ionosphere effects observing over Kharkiv during the relaxation phase of geomagnetic storm on March 14 – 17, 2016 // Bulletin of National Technical University «Kharkiv Polytechnic Institute». Series: «Radio Physics and ionosphere». – 2016. – No. 34 (1206). – P. 8–12 (in Russian).

14. *Katsko S.V., Chernogor L.F.* Response of the ionosphere to moderate magnetic storm on December 21, 2016 / Proceedings of XV Conference of Young Scientists «Interaction of fields and radiation with matter», September 11–16, 2017, Irkutsk, Russia. – P. 101–103 (in Russian).

15. *Domnin I.F., Emelyanov L.Ya., Lyashenko M.V., Chernogor L.F.* Reaction of the ionosphere on solar eclipse of March 20, 2015 over Kharkov // Bulletin of National Technical University «Kharkiv Polytechnic Institute». Series: «Radio Physics and ionosphere». – 2016. – No. 34 (1206). – P. 63–72 (in Russian).

16. *Domnin I.F., Emelyanov L.Ya., Lyashenko M.V., Chernogor L.F.* Ionospheric response to a solar of 20 March 2015 above Kharkiv: results of incoherent scatter radar observations and simulations / Book of abstracts. International Conference «Astronomy and Space Physics in Kyiv University», May 24–27, 2016, Kyiv, Ukraine. – P. 98–99.

17. *Aksonova K.D., Panasenko S.V.* Seasonal variations in the parameters of wave processes in the ionosphere according to the method of incoherent scattering // Bulletin of National Technical University «Kharkiv Polytechnic Institute». Series: «Radio Physics and ionosphere». – 2016. – No. 34 (1206). – P. 73–77 (in Russian).

18. *Panasenko S.V., Goncharenko L.P., Erickson P.J., Aksonova K.D., Domnin I.F.* Traveling ionospheric disturbances observed by Kharkiv and Millstone Hill incoherent scatter radars near vernal equinox and summer solstice // J. Atm. Sol.-Terr. Phys. – 2018 (in press).

19. *Chernogor L.F., Barabash V.V.* Wave disturbances in the ionospheric F2 layer electron density: diurnal and seasonal variations during the declining phase of the solar cycle // Radio Physics and Radio Astronomy. – 2017. – Vol. 22. – No. 3. – P. 212–221 (in Russian).

20. *Zhivolup T.G., Panasenko S.V.* Seasonal variations in the parameters of wave processes in the midlatitude and auroral ionosphere according to the data of ionosonde observations // Bulletin of National Technical University «Kharkiv Polytechnic Institute». Series: «Radio Physics and ionosphere». – 2017. – No. 47 (1268). – P. 61–66 (in Russian).

21. *Goncharenko L.P., Panasenko S.V., Erickson P.J., Domnin I.F.* Characteristics of travelling ionospheric disturbances observed by Kharkiv and Millstone Hill radars / JpGU-AGU Joint Meeting, May 20–25, 2017, Makuhari Messe, Chiba, Japan.

22. *Panasenko S., Otsuka Y., Yamamoto M., Domnin I.* Study of travelling ionospheric disturbances in the European and Japanese longitudinal sectors with Kharkiv incoherent scatter and MU radars / 11-th MU Radar / Equator Atmospheric Radar Symposium, September 7–8, 2017, Kyoto, Japan.

23. *Chernogor L.F., Frolov V.L., Barabash V.V.* Effects of powerful radio emission exposure on the ionosphere on the background of moderate geocosmic storms: results of observation using ionosondes // Bulletin of Volga State Technological University of Technology. Series: «Radio Engineering and Infocommunication Systems». – 2016. – No. 2 (30). – P. 6–27 (in Russian).

24. *Emelyanov L.Ya., Bogomaz O.V., Bravichev B.R.* Device for generation of signals for testing the incoherent scatter radar // Bulletin of National Technical University "Kharkiv Polytechnic Institute". Series: "Radio Physics and ionosphere". – 2016. – No. 34 (1206). – P.84–94 (in Russian).

25. *Bogomaz O., Miroshnikov A., Domnin I.* Peculiarities of database for Kharkiv incoherent scatter radar / 2017 International Conference on Information and Telecommunication Technologies and Radio Electronics (UkrMiCo), 2017. DOI: 10.1109/UkrMiCo.2017.8095424.

26. *Bogomaz O., Kotov D., Panasenko S., Emelyanov L.* Advances in software for analysis of Kharkiv incoherent scatter radar data / 2017 International Conference on Information and Telecommunication Technologies and Radio Electronics (UkrMiCo), 2017. DOI: 10.1109/UkrMiCo.2017.8095425.

27. *Emelyanov L.Ya.* Development of principles and equipment for formation the testing and monitoring signals of the incoherent scatter radar // Radio Technology: Ukr. Interdep. Scientific and Engineering Digest. – 2017. – No 188. – P. 41–49 (in Russian).

28. *Domnin I.F., Levon O.O.* Synthesis of the second order fuzzy-regulator for the control system of the filter-compensating device // Bulletin of National Technical

University "Kharkiv Polytechnic Institute". Series: "RadioPhysicsandionosphere". – 2017. – No. 47 (1268). – P. 20–23 (in Russian).

29. *Emelyanov L.Ya., Chepurnyy Ya.M.* Providing a simultaneous ionospheric sounding mode in vertical and inclined directions using incoherent scatter radars // Bulletin of National Technical University "Kharkiv Polytechnic Institute". Series: "Radio Physics and ionosphere". – 2017. – No. 47 (1268). – P. 44–50 (in Russian).

30. *Bogomaz O.V., Iskra D.A., Kononenko A.F.* Synchronization of the incoherent scattering radar data processing system in the mode for sounding the middle ionosphere // Bulletin of National Technical University "Kharkiv Polytechnic Institute". Series: "Radio Physics and ionosphere". – 2017. – No. 47 (1268). – P. 16–19 (in Russian).

31. *Rogozhkin E.V., Pulyayev V.A.* Digital technologies for ionosphere probing by the incoherent radio-scattering technique // Telecommunications and Radio Engineering. – 2017. – V. 76. – Iss. 6. – P. 551–556. DOI: 10.1615/TelecomRadEng.v76.i6.80.

32. *Chepurnyy Ya.M., Emelyanov L.Ya., Iskra D.O., Shulga M.O.* Estimation of clutters from aircrafts during ionospheric measurements using incoherent scatter radar with 100-meter two-mirror antenna / Proceedings of the XI International Conference on Antenna Theory and Techniques (ICATT), 24-27 May, 2017, Kyiv, Ukraine. – P. 401–405. DOI: 10.1109/ICATT.2017.7972675.

33. *Patent of Ukraine No. 112634.* Method of determining the altitude-temporal distribution of electron density of ionospheric plasma / Pulyaev V.O., Bogomaz O.V., Lyashenko M.V., Panasenko S.V.; published 25.11.16. – Bull. No. 22 (in Ukrainian).

34. *Patent of Ukraine No. 112018.* The method of restoration the height profile of the power of the incoherent scattered signal / Pulyaev V.O., Rogozhkin E.V.; published 25.11.16. – Bull. No. 22 (in Ukrainian).

35. *Patent of Ukraine No. 120837.* The method for calculating the autocorrelation function of the incoherently scattered signal using multichannel device / Pulyaev V.O., Rogozhkin E.V., Emelyanov L.Ya.; published 27.11.17. – Bull. No. 22 (in Ukrainian).

36. *Domnin I.F., Levon O.O., Katsko S.V.* Computer simulation and design of Fuzzy-regulators for radioelectronic systems. – Kharkiv: Publisher NTU "KhPI", 2016. – 120 p. (in Ukrainian).

37. *Bogomaz O.V., Kotov D.V., Panasenko S.V.* Software development for incoherent scatter radar data processing in the C programming language. Guidelines on laboratory practice. Courses: "Digital signal processing" for students of 7.04020402, 8.04020402 "Radio physics and electronics" specialization, "Software development for radio physical data processing" for students of 7.05010203, 8.05010203 "Specialized computer systems" specialization. 2nd ed. – Kharkiv: NTU "KhPI", 2016. – 36 p.

RESULTS OF THE INVESTIGATION OF PHYSICAL EFFECTS IN THE GEOSPACE ENVIRONMENT UNDER QUIET AND DISTURBED CONDITIONS

L. Chernogor, V. Rozumenko
Kharkiv V.N. Karazin National University (KhNU MESU)

Introduction

During 2016–2018, Kharkiv V.N. Karazin National University has continued to conduct experimental and theoretical studies of physical processes operating in geospace under quiet and disturbed conditions. The observations were made with the radio instrumentation located at the Radiophysical Observatory (49°38′ N, 36°20′ E) and with the magnetometer located at the Magnetometric Observatory (49°38′ N, 36°56′ E).

The purpose of this paper is to report the results of experimental and theoretical studies, and simulations of physical processes acting in the geospace environment, which were conducted at Kharkiv V.N. Karazin National University during 2016–2018. The study is based on systems science approach to understanding of the Earth–atmo-sphere–ionosphere–magnetosphere sys-tem and the Sun–interplanetary-medium–magnetosphere–ionosphere–atmosphere–Earth system [1–3].

Solar Eclipse Effects

The intercomparisons of the solar eclipse effects observed near Kharkiv City (Ukraine) on August 11, 1999, May 31, 2003, October 3, 2005, March 29, 2006, August 1, 2008, January 4, 2011 and March 20, 2015 have been made (see, e.g., [4–7]).

The solar eclipse over Kharkiv City commenced at 09:09 UT and ended at 11:21 UT on March 20, 2015. The eclipse magnitude of 0.55 was observed at 10:15 UT (12:15 LT), when the eclipse obscuration was equal to 0.45. The solar eclipse occurred shortly after the geomagnetic storm of March 17–18, 2015 (maximum $K_p \approx 8$-, minimum $D_{st} \approx -230$ nT).

The observations of disturbances in the atmosphere, ionosphere, and the geomagnetic field have been taken from the MF radar over 60–100 km altitude region, the Doppler radar at vertical incidence at 3.2 MHz and 4.2 MHz from 100 km altitude to the F2 peak, the digital ionosonde from 100 km altitude to the F2 peak height, a navigation satellite system, the fluxgate magnetometer in the 0.001–1 Hz frequency range, and a standard thermometer system at the Kharkiv V.N. Karazin National University Radio Physical Observatory (near Kharkiv City).

A decrease of approximately 0.5 MHz or 6.4% in the critical F2-layer frequencies (f_oF2) occurred at approximately 10:00 UT with the corresponding decrease of 12% in the electron number density. The critical E-layer frequencies (f_oE) decreased by 11%.

During the course of the eclipse, the Doppler shift of frequency f_D first decreased approximately by 0.15 Hz, then gradually increased to approximately 0 Hz at 10:30 UT, further increased by 0.15 Hz, and subsequently decreased to 0.0 Hz. The quasi-periodic oscillations with periods of 10 min to 60 min were superimposed on the slow variations in f_oF2 and f_D. The relative amplitude of 5–7% was observed in the electron density [6, 7].

On the day of the solar eclipse and on reference days, quasi-periodic variations in the horizontal components of the geomagnetic field occurred with an amplitude of 0.5–1 nT. A response to the solar eclipse was partially masked by fluctuations in the background [7].

On the day of the solar eclipse, the sun could be observed through translucent clouds in the sky. The cloudiness resulted in a maximum decrease in the air temperature by a mere 0.9–1 K at an altitude of 3 m, with the minimum observed at 10:37 UT. The reduction in the air temperature continued over 40 min from 10:33 UT to 11:13 UT [5].

Because of the influence from the relaxing ionospheric storm, the effects of the March 20, 2015 solar eclipse substantially differ from those caused by August 11, 1999, May 31, 2003, October 3, 2005, March 29, 2006, August 1, 2008, and January 4, 2011 solar eclipses near Kharkiv City.

The spatial distribution of wave disturbances near the F2 peak height over Europe during the March 20, 2015 solar eclipse is described in [4].

The basic results are as follows:

(1) The March 20, 2015 solar eclipse is confirmed to be accompanied by the intensification of wave processes at altitudes of the ionospheric F2 layer. The magnitude of the response to the eclipse depends on the ionosonde geographic location.

(2) In approximately half of the cases, the variations intensifies with a delay time, Δt, of approximately 0.2–0.5 h after the solar eclipse onset, and in another half of the cases, they are suppressed with $\Delta t \approx 1.2$–1.3 h. The suppression is evidently explained by the interference of the oscillation generated by the eclipse with the oscillation that existed in the ionosphere before.

(3) At most ionosonde sites, the eclipse results in the intensification of quasiperiodic variations in the ionospheric parameters as compared to the variations on the reference day. At one ionosonde, the variations reduce, because the variation generated by and existed before the solar eclipse interfere in antiphase.

(4) The eclipse results in a substantial change in the amplitudes and the spectral composition of quasiperiodic processes. The relative amplitude of the electron density variations increases by a factor of 2–3 on average as compared to those observed on the reference day.

(5) The magnitudes of the variation period (30–100 min) and the relative amplitude (0.04–0.19) indicate that traveling ionospheric disturbances are caused by the atmospheric gravity waves generated in the Earth's atmosphere by the Moon's shadow.

Effects from Geospace Storms

A geospace storm is comprised of inextricably linked geomagnetic, ionospheric, atmospheric, and electrical storms [1, 8]. Solar storm consequences are felt in all Sun – interplanetary – medium – magnetosphere – ionosphere – atmosphere – Earth system subsystems.

All geospace storms, which occurred during the 2016–2018 interval, have been analyzed.

A comparative study of the strong and moderate storms that occurred during the 23 and 24 solar cycles continued to be carried out. New storm features have been detected and a classification of geomagnetic storms and their manifestations has been put forward [8]. New indices for geospace and ionospheric storms have been suggested [8].

Effects from Large Celestial Body Passages through the Earth's Atmosphere

Theoretical Studies and Simulations [9–21]. The passage and airburst of the Chelyabinsk bolide (a tiny asteroid) with the initial kinetic energy about 440 kt TNT have caused appreciable (or strong) disturbances in all geospheres [9]. The altitude of the Chelyabinsk object explosion is determined to be equal to approximately 23 km. The excess pressure at the ground near the explosion epicenter is equal to a few kPa. This pressure disturbance is large enough to cause destruction of structures over a surface area of 6 000 km^2. The flash of light energy and power are equal to approximately 375 TJ and 313 TW, respectively. The flux is one or two orders of magnitude lower than that needed to set fire to substances and start fires. The shock and acoustic oscillation energy is equal to 560 TJ and 19 TJ, respectively. A Richter magnitude of the earthquake induced by the Chelyabinsk object does not exceed 3–4. Relative electron pressure and density disturbances at ionospheric heights over the explosion epicenter attain hundreds of per cent. The geomagnetic disturbance in the vicinity of the Chelyabinsk object explosion is equal to 0.5–1 nT. Disturbances from the explosion are propagated in the horizontal direction over a distance range of a few thousand kilometers. Space objects similar to the Chelyabinsk bolide (tiny asteroid) enter the Earth's atmosphere one time each 65 years. A comprehensive understanding of all these phenomena requires the systems science approach to the Earth – atmosphere – ionosphere – magnetosphere system studies.

Atmospheric Effects [12, 14]. A physics and mathematical model for the upwelling and descending of the gas-aerosol cloud created by the passage and airburst of the Chelyabinsk meteorite have been developed. The explosion of the celestial body ejected into the atmosphere 10 kilotons of aerosols embedded in the gas heated to 10^4 K that rapidly expanded in the direction perpendicular to the trajectory. The hot cloud of 15 km in length and of 0.5 km radius began rising up in accordance with Archimedes's principle. The initial acceleration was equal to about 470 m·s^{-2}. Subsequently, it moved actually steadily at a speed of 125–210 m/s. As the cloud ascended, it expanded and cooled due to the expansion and eddy mixing. When the density of the cooling matter approached to that of the cold air, the upward force exerted on the cloud significantly decreased and an uplifting of the cloud essentially ceased. For 55 s, the cloud rose at an altitude of approximately 10 km. Subsequently, the ~10^{-4} m-sized aerosols descended at a speed of 10 m/s for 400 s. After the ascent, the aerosols took part in the following three movements: subsidence, eddy mixing, and a horizontal drift with the wind speed. The 10^{-6} m to $3{\cdot}10^{-4}$ m aerosols existed in the stratosphere for 20–1 days, respectively. The light aerosols could travel a few times around the globe.

A comparison of the model with the lidar observations taken at Moscow and Obninsk (Russia) showed a good agreement. The observations showed the vertical movement speeds of 130–170 m/s and an ascent to a maximum altitude of 12 km. The traces of the aerosols were observed 20 days after the Chelyabinsk meteorite event.

Ionospheric Effects [9, 16]. The manifestations of the disturbances in the lower-ionosphere electron density ($z \approx 65$–70 km), which are due to the action of the acoustic wave with a period of 200–230 s and propagation speed of 290–400 m/s, have been detected at a distance of approximately 1 575 km from the explosion. The reflection level shows oscillations with amplitude of 0.1–0.2 km, while the signal phase exhibits oscillations with amplitudes of 4–7 degrees, and the electron density perturbations of 2.7–4.6 %. The ionosonde observations have allowed the manifestations of atmospheric gravity waves (AGWs) with periods of $T \approx 70$–135 min and propagation speeds of 520–700 m/s to be detected over a distance no less than 3 000 km. The electron density disturbances with amplitudes of 10–20 % last for 4–5 h. A significant disturbance in f_oF2 (up to 0.5–1 MHz) that is observed in the 09:00–16:00 UT period at two widely separated ionosondes could also be caused by the meteoroid passage and explosion. Such a disturbance should be classified as long-living. Analysis of the time variations in the total electron content (TEC) data acquired nearby the explosion (at a few hundred kilometers) has revealed the presence of quasi-periodic wave like disturbances exhibiting propagation speeds of 500–550 m/s, durations of 40–60 min, and periods of 10–15 min. The amplitudes of the TEC waves are of the order of 1–10%. The observations are in good agreement with theoretical estimates.

Magnetic Effects [9, 21]. Analysis of the time variations in the geomagnetic field components on the day of the Chelyabinsk event and on reference days has been performed. The Novosibirsk, Almaty, Kharkiv, Kyiv, and Lviv magnetometer sites are chosen for the analysis. The distance range, R, from the explosion to the sites varies from 1 200 km to 2 700 km. The passage and explosion of the Chelyabinsk bolide is mainly associated with variations in the horizontal component of the geomagnetic field. The magnetic field vary quasi-periodically with a ~30–40-min period and a 0.5–2 nT amplitude for distances 2 700 km to 1 200 km, respectively, during 2–3 h. The horizontal speed of the wave perturbations in the geomagnetic field is equal to approximately 260–370 m/s. The following theoretical model of the quasi-periodic perturbations in the geomagnetic field has been proposed. The perturbations are due to the internal gravity waves generated in the atmosphere by the falling bolide that give rise to the traveling ionospheric disturbances modulating the dynamo currents in the E region and consequently giving rise to the perturbations in the geomagnetic field. The estimated amplitudes of the perturbations are equal to 0.6–1.8 nT at distances of 2 700 km to 1 200 km, respectively. The observations are in good agreement with the estimates, while at the same time the geomagnetic perturbations in the 1–100 s-period range are determined to be insignificant (less than 1 nT).

Magnetospheric Effects. The analysis of the geomagnetic variations in the H-component acquired at the Novosibirsk, Alma-Ata, Kiev, and Lvov magnetic observatories reveals quasi-periodic 1.2–1.5 nT amplitude variation of 22–33 min in duration occurring 33–38 min before the explosion. The variations in the horizontal H- and D-components of the geomagnetic field in the 1–1000 s period range acquired at the Kharkiv V.N. Karazin National University Magnetometric Observatory (in the vicinity of Kharkiv City) attain a maximum value of 2–3 nT, continue 27 min and 38 min, have quasi-periods of 13–15 min, and occur 44 min and 47 min in advance, respectively. At the midlatitude Mondy magnetic observatory (51.4° N, 100.5° E), noise-like peaks in the 0.2–5 Hz frequency range of approximately 23 min in duration are observed in the H- and D-components of the geomagnetic field 45–22 min before the meteorite explosion. The geomagnetic disturbances described above could originate only from the magnetosphere.

In the past Chernogor has advanced the following model of the magnetic disturbances observed before the meteoroid impacts the planet Earth. As a celestial body enters the magnetosphere, it acts to create a void in the magnetic field whose front is traveling at the meteorite speed. The disturbed region is a nearly cylinder-shaped area of 10 000 km in length and of (1–8) · 1 000 km radius at McIlwain L-parameters of ~5–10, respectively. The meteorite speed of 18.5 km/s results in a disturbance duration of about 27 min. The disturbance of the magnetic field is equal to approximately 6–1 nT at the same L's within the magnetosphere and 1–2 nT at the ground.

The noiselike character of the geomagnetic field variations acquired at the Mondy magnetic observatory is most likely associated with plasma turbulence in the meteorite tail with a specific power of 10^9–10^{12} J/kg·s, which results in geomagnetic field variations of 0.1–0.2 nT at the ground, with periods of 0.7–10 s.

The calculations show good agreement with the observations.

Acoustic Effects [10, 11, 13, 17, 20]. The infrasound waves, which arose from the Chelyabinsk meteoroid, were detected with sensitive microbarographs after they undergone multiple reflections, refractions, and traveled distances of hundreds and thousands kilometers. The amplitude and spectrum of the infrasound deliver information on the source of the waves and atmospheric parameters. The observation site closest to the site of the meteoroid explosion is situated at Aktubinsk City, Republic of Kazakhstan (at a distance of 520 km from the infrasound source), the farthest sites is situated in Antarctic (at a distance of 15 000 km).

The main results of the investigation of Chelyabinsk meteoroid infrasound effect are as follows.

The passage and explosion of the Chelyabinsk meteoroid is accompanied by the generation of intense infrasound. The time delay of the infrasound signal vs. the distance between the infrasound source and an observation site increases approximately linearly. The corresponding regression fit is constructed. The mean speed of the infrasound wave is determined to be equal to 266 ± 3 m/s.

The harmonic with the 30.09 ± 0.44 s period (33.2 ± 0.7 mHz frequency) prevails in the infrasound spectrum.

The infrasound signal amplitude decrease from 5–7 Pa to 0.2–0.3 Pa as the distance between the sites of infrasound generation and observation increases from 520 km to 5 780 km. The characteristic length scale for infrasound attenuation varies in 2 000–7 000 km interval depending on the propagation path.

The initial meteoroid energy estimated from the infrasound observations is approximately equal to 434.9 ± 18.5 kilotons TNT (estimate error of 4%), which is in good agreement with the energies estimated from the meteoroid radiated power, the shock wave impact, and the seismic effects.

The duration of the infrasound signal has been shown to be determined by the length scale of the infrasound source (about 50–90 km) and by dispersion spreading that depends on the distance over which the wave travels. The total signal duration equals to 6–30 min for the range of approximately 520–5 780 km. The results are in good agreement with the observations.

The period of the principle oscillation is determined by the oscillation of the region heated by the explosion. The estimates yield a period of 33 s, while the observations show periods of 25–34 s.

The main results of the investigation of infrasound effects of the Romanian meteoroid that entered the Earth's atmosphere on January 7, 2015 at the center of Europe (45.4° N, 26.33° E) are as follows [17].

1. The infrasound signal was detected at all six stations with a various degree of reliability. The peak amplitude of 50 Pa was observed at a distance of 53 km from the airburst. The amplitude value attained 3–4 Pa, 3–4 Pa, 0.5–1 Pa, 1–1.5 Pa, and 0.5–0.6 Pa at 313 km distance, 332 km distance, 583 km distance, 1 034 km distance, and 1 423 km distance, respectively.
2. The period of infrasound oscillations varied in the 1–10 s range with the mean of 3.7 s.
3. The trajectory data suggest that the meteorite was stony. Its initial mass was equal to about 2.6×10^6 kg, the volume about 0.7–0.8 m^3, and the diameter 1.1 m.
4. The infrasound signal energy varied from 160–240 GJ in the near-field zone to 180–100 GJ at distances of (0.3–1.5) $\times 10^6$ m, respectively. The ratio of the acoustic wave energy to the initial kinetic energy decreased from 8–14% to 5–6% over this range of distances.
5. The network of spaced stations receiving infrasound signals permitted the true celerity of the infrasonic signal, of about 280 $m \cdot s^{-1}$, and the mean wind speed, of about 20 $m \cdot s^{-1}$, in the troposphere and stratosphere to have estimated.

Seismic Effects [14]. The impact of the shock wave on the Earth's surface excites seismic waves in the lithosphere, which have been recorded at distances of thousands to tens of thousands km from the site of explosion.

The main results of seismic effect studies are as follows.

The earthquake energy estimates yield a Richter magnitude of 3.5–4.1 due to the shock generated by the space body. The seismic observations show a Richter magnitude of 3.6–4.2.

Observations have shown that high-altitude explosion of the meteoroid generates mainly the Raleigh surface wave.

Both the calculations and observations at sites of destruction yield the time delays of 77–295 s between the time of destruction and the instant of shock wave generation at 23–53 km altitude over a range of 23–84 km.

The shock wave impact lasts for approximately 97 s.

The calculations and observations show that the region of destruction has a length of approximately 125–130 km and a width of about 16 km to 60 km when the shock pressure is not less than 0.7 kPa.

The seismogram data show that the seismic waves have a mean speed of 3.08 km·s^{-1} (calculations, 3.07 km·s^{-1}).

The regression fit to the seismic signal vs. distance that the seismic wave propagated has been obtained. The calculations and observations show that the characteristic time of seismic source impact is equal to about 40 s.

The dispersion relation is determined for seismic waves in the period range of $T = 20$–50 s (group velocity of $v_g \sim T^{1/3}$, and wave velocity of $v_{ph} = (4/3)\, v_g$).

Estimates of a characteristic depth for seismic wave attenuation give magnitudes of ~10–20 Mm in the $T = 0.3$–4 s range.

The amplitude of an elastic medium movement due to shock wave is estimated to be equal to 5.7–7.0 μm/s, while the observations show a value of 5.8–7.0 μm/s for $T \approx 1$ s.

A 10^{-5}–10^{-4} fraction of the meteoroid initial kinetic energy is converted into the energy of seismic waves.

The model results and observations are in good agreement.

Global Statistics of Large Celestial Bodies. The global statistics of large celestial bodies entering the Earth's atmosphere has been studied by using the NASA database collected over the 1994–2016 interval. The main results of meteoroid statistics study are as follows [15, 19].

1. The longitudinal distribution of the number of meter-sized celestial bodies entering the atmosphere is almost uniform. The latitudinal distribution of the number of celestial bodies entering the atmosphere decreases with latitude, which is due to the geometrical causes but not due to the astronomical causes.

2. The number of celestial bodies entering the Earth's atmosphere, with the radiated energy of 20–150 GJ, remains practically unchangeable. The fraction of these bodies is equal to approximately 72%. A power-series probability distribution function is preferable when the energy increases from 125 GJ to 3000 GJ.

3. The majority, 70.13%, of the celestial bodies have their velocities in the 12.5 km·s^{-1} to 20 km·s^{-1} range. Speeds in the 45 km·s^{-1} to 49 km·s^{-1} range have been observed twice.

4. In the 20–48 km altitude range, the dependence of the distribution of the number of celestial bodies, entering the atmosphere, on the altitude of peak radiated energy follow a normal distribution. A distinguishable deviation from a normal distribution at altitudes smaller than 20 km and greater than 48 km can be explained by a large difference in the strength of these celestial bodies and stony meteorites.

5. The correlation diagram for the altitude of the peak radiated power, E_r, and the logarithm of the radiated energy indicates some increase in coupling between these parameters over the 26–42 km altitude range and in the $\log_{10} E_r \approx -(1.7$–$0.6)$ interval where E_r is in TJ.

6. A definite statistical correlation exists between the square of the initial celestial body speed and the logarithm of radiated energy.

Affecting the Ionosphere by High-Power HF Radio Transmissions

Model Results. Numerical modeling of nonstationary disturbances in the ionospheric electron density and temperature caused by high-power HF radio transmissions of various frequencies, powers, and polarizations, and associated with heater turn-on and turn-off has been performed. The main results are as follows.

The Sura heater O polarization transmissions are capable of increasing the electron temperature by a factor of 8–10, 2–7 and by tens of percent in the ionospheric D, E, and F regions, respectively. The Sura heater X polarization transmissions are capable of increasing the electron temperature by a factor of 16–17, 5–12, and 1.5–5 in the nighttime ionospheric D, E, and F regions, respectively. During the daytime, disturbances effectively occur only in the ionospheric D region.

The phased array transmitter on the HAARP program, providing 0.4 GW power at 2.8 MHz, during daytime disturbs mainly the ionospheric D region where the electron temperature can increase by a factor of 10 and 20 in O and X polarized radio wave fields, respectively. During the nighttime, the electron temperature can be increased by a factor of 10 and 20, 3–10, and 2–20, as well as 2 in the ionospheric D, E, and F regions, respectively, in O and X polarized radio wave fields, respectively. HAARP transmissions, providing 3.6 GW power at 6 MHz, during the daytime disturb mainly the ionospheric D region where an increase in the electron temperature attains a factor of 15 and 20 in O and X polarized radio wave fields, respectively. During the nighttime, significant disturbance occur in all ionospheric regions where an increase in the electron temperature changes from 20 and 22 times to 2 and 3 times in O and X polarized radio wave fields, respectively.

When the radio wave frequency is equal to the gyro frequency, the disturbance occurs mainly in the ionospheric D region where an increase in the electron temperature attains a factor of 20 and 35 during the daytime for O and X polarization, respectively.

During the nighttime, the X polarized radio wave also disturbs only the ionospheric D region where it is completely absorbed due to the gyroresonance. An exceptionally great increase in the electron temperature occurs here, up to approximately 50 times.

To produce a maximum disturbance in the ionospheric E and F regions by propagated radio waves, an X polarized radio wave should be applied at a frequency of 3–4 MHz.

A disturbance in the electron density due to partially inhibiting recombination is relatively small. An increase in the electron density during the nighttime usually does not exceed a factor of 2, 1.5, and 1.2 in the ionospheric D, E, and F regions, respectively. During the daytime, a perceptible increase in a disturbance of the electron density occurs only in the ionospheric D region.

The effect of amplitude self-action has been numerically modeled for propagated high-power continuous radio waves vs. frequency, power, and polarization, which is due to the disturbance in the temperature, the collision frequency, or the electron density in the ionosphere. The following has been determined.

The effect of amplitude self-action can be neglected near the lower ionospheric boundary, i.e., below about 60 km altitude.

Between 65 and 90 km altitude, the effect of plasma becoming self-transparent is pronounced. The magnitude of the effect increases as the X polarized radio wave frequency approaches the electron gyrofrequency, and the self-action factor for the X polarization significantly exceeds unity at about 75 km and 90 km for the daytime and nighttime, respectively.

At heights above 70–90 km, the effect of plasma becoming self-transparent is gradually replaced by the effect of becoming self-opaque. The factor of self-action for X polarization radio waves vs. the effective radiated power attains minimum values of 0.24–0.33 and 0.28–0.77 for the daytime and nighttime conditions, respectively.

The frequency dependence of the self-action factor for O polarization transmissions is monotonous at all altitudes for the daytime and nighttime conditions: the values of O polarization transmission self-action gradually increase with increasing frequency approaching unity.

The frequency dependence of the self-action factor for X polarization transmissions is not monotonous for the daytime and nighttime conditions: with frequency increasing from 1.4 MHz the self-action factor first decreases attaining a minimum value at the 3.5–4 MHz, and then increases approaching limits of 0.8 and 0.9 during the nighttime or 0.15 and 0.4 during the daytime for the effective radiated power of 3.6 GW and 0.3 GW, respectively.

Experimental Results [22]. Progress has been made in searching for the effects in the ionospheric plasma associated with the action of high-power radio transmissions. The radio facilities used in these experiments were located at distances of 1 000–2 000 km from the observation site near Kharkiv City. The disturbances were created by the ionospheric heating facilities located near Nizhniy Novgorod City in Russia (Sura) and near Tromsø in northern Norway.

The basic results inferred from variations in the geomagnetic pulsation level and spectra in the 1–1 000 s period range that were observed under the action of the Sura heater on the ionosphere in August, 2012 are as follows [22].

Aperiodic bursts in the amplitude of the horizontal components of the geomagnetic field in the period range 300–1 000 s were detected at a distance of about 960 km from the Sura heater. The bursts were delayed with respect to the heater quasi-continuous radiation turn-on by 10–20 min, and they had duration of 10–45 min. The bursts appeared on August 28–30, 2012 when the heater was operated in the [+30 min, –30 min] regime with occurrence rates of 0.64 and 0.45 for the *D*- and *H*-components of the geomagnetic field, respectively. Aperiodic bursts in the geomagnetic pulsations have been explained by bursts in the electron density in the ionosphere at the altitudes of the dynamo region.

A notable increase in the pulsation amplitude was detected in the period ranges 40–80 and 100–140 s with the delay time 8–10 min when the Sura facility was operated in the [+1 min, –1 min] regime. The effect is more pronounced for the *D*-component of the geomagnetic field. The detected enhancement of the pulsations has been explained by the gene-ration of MHD waves with respective periods under the action of the heater high-power radiation.

Quasiperiodic variations in both components of the geomagnetic field were detected in the period range 8–12 min when the heater was operated in the [+5 min, –5 min] and [+10 min, –10 min] regimes having a delay time of 35–45 min, a propagation speed of 320–460 m/s, and the wave packet duration of 40–90 min. When the heater operated in [+15 min, –15 min] regime, variations in the period range 12–18 min were detected with a delay time of 35–45 min, the propagation velocity 355–460 m/s, and the train duration of 55–90 min. The appearance of the geomagnetic pulsations with such periods was associated with the modulation of ionospheric currents at the altitudes of the dynamo region by atmospheric gravity waves under the action of high-power radio waves from the heater. We have verified the possibility of observing such waves at distances of about 960 km many times before.

Further studies of the patterns established are needed.

A network of ionosondes was used to study the spatial distribution of large-scale aperiodic disturbances in the lower ionosphere arising under the action of high-power radio transmissions. The heater transmissions in the [+30 min; –30 min] mode of operation was accompanied by an increase in the minimum frequency observed in the ionograms with periods of 0.5 h and 1 h. The greatest surges in the minimum observable frequency occurred at the Troitsk ionosonde (in the vicinity of Moscow City, Russia), when the minimum observable frequency increased from 1.8 MHz to 3.0–3.2 MHz. An increase in the minimum observable frequency at Kazan City (Russia), Gaidary Village (near Kharkiv City, Ukraine), Pruhonice City (Czech Republic), and Vasilsursk Town (near Nizhniy Novgorod City, Russia) did not exceed 0.3–0.4 MHz on August 29, 2012. An increase in the minimum observable frequency suggested an increase in the electron number density and radio wave absorption, and due to its time scales, could not be associated with an increase in the electron temperature. Estimates have shown that an increase in the lower ionospheric density averaged over the height interval is equal to a factor of 3, 1.4, 1.3, and 1.3–1.4 at Troitsk, Kazan, Gaidary, Pruhonice, and Vasilsursk, respectively. The cause of insignificant variations in the minimum frequency observed at Vasilsursk on August 28 and 30, 2012 remained not understood.

The features of the effects arising under the action of the high-power HF heater on the ionosphere during geomagnetic storms in the background are discussed in [22]. The main results are as follows.

1. Non-periodic bursts in the critical F2-layer frequency of 0.1–0.4 MHz associated with the action of the heater on the ionosphere over 15 min intervals have been detected. The time delay of the disturbances with respect to the heater turn-on lies in the range 10–15 min, and its duration, in the 10–15 min range. The horizontal extent of the disturbed ionospheric area is no less than 2 200 km. The magnitude of the disturbance shows an insignificant decrease as the distance from the heater increases.

2. In some cases, the buildup effect is observed when non-periodic bursts arise from the heater operation in the [+5 min, –5 min] regime.

3. The bursts detected in the critical F2-layer frequency may be disguised by wave-like disturbances of natural and anthropogenic origin. In the latter case, the wave-like disturbances are generated by the high-power radio emissions. This is suggested by the disturbance speed estimated to be equal to approximately 300–500 $\mathrm{m \cdot s^{-1}}$ and by the dependence of speed on height. The source of natural disturbances is usually not known, and their speed cannot be estimated.

4. The non-periodic bursts in the critical frequency suggest that the F region electron density increases by 1–10 %, which is most likely due to the precipitation of energetic electrons from the Van Allen radiation belt that is in a metastable state. Such a state could be prepared by the weak and moderate geospace storms that occurred during the measurement campaign. The detected patterns require confirmation and the more detailed study employing additional techniques for diagnosing and measuring electron fluxes onboard low Earth orbit satellites.

Rocket Engine Burn Effects

A special feature of this study is the search for the effects that rocket burns have at a significant (~1 000–10 000 km) distance from a space vehicle path [23–25]. The database contains disturbances observed in both the geomagnetic field and the ionosphere in association with rocket launches from Baikonur, Plesetsk, China, U.S., and the Guiana Space Center at Kourou launch sites. Of special interest are the magneto-ionospheric effects from launches of rockets from different launch sites and the specific features observed during geomagnetic storms. Approximately 5 000 observations taken over the 1970–2018 time interval during rocket launches have been analyzed and classified. The main results are as follows.

Rocket engine burns are shown to be associated with the generation and/or amplification of wave disturbances in the geomagnetic field and in the ionosphere in a wide period range of 5–10 min to 2–3 h. It has been verified that the ionospheric response to a rocket launch significantly depends on the state of space weather. Perhaps the ionospheric storm effects can couple synergistically with the effects from rocket burns by enhancing each other. As expected, ionospheric storms significantly complicate the detection of the effects from rocket burns. Two types of disturbance with speeds of $2\,\mathrm{km\cdot s^{-1}}$ and $600\,\mathrm{m\cdot s^{-1}}$ have been distinguished. These speeds, which have been observed earlier in numerous studies, could belong to the slow MHD waves and to the atmospheric gravity waves, respectively. The relative amplitude of disturbances in the electron density, δ_N, attains 0.05–0.07 and the magnitude of its quasi-period, is approximately 2–3 hr.

The statistical and spectral analyses of the geomagnetic pulsations associated with 351 rocket launches from launch pads located at distances of 1 500–9 500 km from the observation site have shown that the pulsation features appreciably alter, their level increase (more rarely decrease), and their spectrum content significantly change after a rocket launch.

The features of the geomagnetic effects from rocket launches are as follows.

Three types of possible disturbance have been identified and studied. Their time delays linearly increase with distance from the region of generation to the observation site. These disturbances have average speeds of approximately $2.3–2.5\,\mathrm{km\cdot s^{-1}}$, $1–1.2\,\mathrm{km\cdot s^{-1}}$, and $0.5–0.7\,\mathrm{km\cdot s^{-1}}$. A group of disturbances propagating at speeds over $\sim 10\,\mathrm{km\cdot s^{-1}}$ is observed uncertainly. The second and third type of disturbance could belong to one group of disturbance. The duration of the disturbance, ΔT, usually changes from 20–30 min to 60–70 min with distance, R, from the observatory to a launch site at a distance from 1 500 km to 9 500 km, and an increase in ΔT shows almost a linear dependence on R. The characteristic scale distances, over which the duration of the disturbance increased by two times, are equal to 5 000 km, 15 000 km, and 21 000 km for the three types of disturbance outlined above. The magnitude of the predominant periods in the pulsations also follows a linear law over the range of distances, R, from 1 500 km to 9 500 km; however, these changes are insignificant.

The wave disturbances generated by rocket engine burns act to induce a partial rearrangement of coupling between the subsystems in the Earth – atmosphere – ionosphere – magnetosphere system. The coupling occurs via waves of different physical nature (atmospheric gravity waves (AGWs), MHD waves, magneto-gradient waves, and others) and via energetic particle fluxes.

Effects from Natural and Great Man-Made Disasters in the Atmosphere and Geospace

Chernogor [26–41] has studied the physical effects and ecological consequences of natural and great man-made disasters. The disasters include earthquakes, volcano eruptions, avalanches, tropic cyclones, potentially hazardous asteroids that can impact the Earth, as well as multiple explosions at ammunition depots, gas and oil field accidents, gas pipeline disasters, etc.

The disturbances from natural and man-made disasters are determined to encompass not only the Earth's surface and the atmosphere at the air-earth boundary, but also the upper atmosphere and even the magnetosphere, i.e., the entire Earth – atmosphere – ionosphere – magnetosphere system. The disturbances are transported by atmospheric gravity waves, heat and aerosol fluxes, as well as by variations in geophysical fields, and by other processes. A technique has been developed for calculating physical effects and ecological consequences caused by natural and man-caused disasters in the Earth – atmosphere – ionosphere – magnetosphere system.

Space Science and Education

The results of the scientific studies have been used in education [42, 43], outreach activities on the radio and television, as well as in preparing the popular scientific literature [27–32, 34–41, 44–47].

Conclusions

1. The experimental studies of the physical processes acting in the geospace environment proceeded during the 2016–2018 period of gradually decreasing solar activity during solar cycle 24.

2. The experimental studies were conducted of the disturbances in geospace associated with an impact on the medium from high-energy sources (solar terminator, March, 20, 2015 solar eclipse, geospace storms, celestial bodies entering the atmosphere and exploding, HF high-power emissions, rocket engine burns, great disasters, and others).

3. Theoretical models of physical processes arising from high-energy sources in geospace have been developed and advanced. Measurements are in good agreement with theoretical modeling.

4. The theoretical ideas and physical models of processes launched by natural and man-made

disasters into the Earth – atmosphere – ionosphere – magnetosphere system have been developed.

5. Based on the Chelyabinsk meteoroid event, the physical and mathematical models for processes associated with the celestial body passage and explosion have been developed. The processes include deceleration, heating, ablation, explosion, bolide fragment fallout, the generation of infrasound and atmospheric gravity waves, the disturbances in the atmosphere, the ionosphere, and the geomagnetic field, the occurrence of electric and electromagnetic effects, the heating and relaxation of the meteorite trail, the generation of turbulence in the trail. The magnetospheric effect from the Chelyabinsk meteoroid has been detected and modeled. The effect of the gas-aerosol plume and the acoustic and seismic effects arising from the Chelyabinsk meteoroid have been studied and modeled in detail.

6. The infrasound effect of the Romanian meteoroid that entered the Earth's atmosphere on January 7, 2015 has been investigated experimentally and theoretically. The basic parameters of the infrasound signal have been determined.

7. The NASA database collected over the 1994–2016 interval has been used to obtain the basic statistical characteristics of large celestial bodies entering the Earth's atmosphere.

8. The parameters of non-periodic disturbances in the ionosphere caused by high-power radio emissions from the heater located at 1 000–2 000 km from the observation site have been determined.

9. The basic parameters of wave-like disturbances generated by the March 20, 2015 eclipse have been determined at a network of ionosondes over Europe.

10. It has been verified that the impact of high-energy sources on the Earth – atmosphere – ionosphere – magnetosphere system (Sun – interplanetary-medium – magnetosphere – ionosphere – atmosphere – Earth system) is associated with the generation and/or amplification of wave disturbances. Generally, the wave disturbances in the neutral atmosphere give rise to wave processes in the ionosphere and in the geomagnetic field. Wave disturbances can sometimes be nonlinear. The techniques for estimating their parameters have been developed. The role of wave disturbances is great, as they, to a large extent, provide a means of subsystem coupling in the Earth – atmosphere – ionosphere – magnetosphere system (Sun – interplanetary-medium – magnetosphere – ionosphere – atmosphere – Earth system).

11. The conclusion of the authors that an adequate description of the entire set of physical processes operating in the Earth – atmosphere – ionosphere – magnetosphere system and in the Sun – interplanetary-medium – magnetosphere – ionosphere – atmosphere – Earth system is possible only within a systems science paradigm has been confirmed.

REFERENCES

1. *Chernogor L.F.* Space, the Earth, Mankind: Contemporary Challenges (in Russian). 2-ed. – Kharkiv: Kharkiv V. N. Karazin National University, 2017. – 384 p.

2. *Chernogor L., Rozumenko V.* Results of the investigation of physical effects in the geospace environment under quiet and disturbed conditions // National Academy of Science of Ukraine. State Space Agency of Ukraine. Kyiv, Akademperiodyka, 2016. – P. 23–30.

3. *Chernogor L., Domnin I., Emelyanov L., Katsko S., Kotov D., Lyashenko M., Panasenko S.* Results of observations of ionospheric processes over Ukraine in 2014–2016// National Academy of Science of Ukraine. State Space Agency of Ukraine. Kyiv, Akademperiodyka, 2016. – P. 31–38.

4. *Chernogor L.F.* Wave Processes in the Ionosphere over Europe that Accompanied the Solar Eclipse of March 20, 2015. // Kinematics and Physics of Celestial Bodies. – 2016. – V. 32, No.4. – P. 196–206.

5. *Chernogor L.F.* Atmosphere–Ionosphere response to Solar Eclipse over Kharkiv on March 20, 2015// Geomagnetism and aeronomy. – 2016. – V. 56, No. 5. – P. 592–603.

6. *Domnin I.F., Yemelyanov L.Ya., Lyashenko M.V., Chernogor L.F.* Response of the ionosphere to the March 20, 2015 solar eclipse over Kharkiv City (in Russian) // Bulletin of National Engineering University "KhPI" – 2016. – No. 58 (1167). – P. 63–72.

7. *Chernogor L.F., Garmash K.P.* Magneto-Ionospheric Effects of the Solar Eclipse of March 20, 2015, over Kharkov// Geomagnetism and Aeronomy. – 2017. – Vol. 57. – No. 1. – P. 72–83.

8. *Katsko S.V., Yemelyanov L.Ya., Chernogor L.F.* Observations of ionospheric effects over Kharkiv City during the recovery phase of the March 14 – 17, 2016 geomagnetic storm (in Russian) // Bulletin of National Engineering University "KhPI". Ser.: Radio Physics and Ionosphere. – 2016. – No. 34 (1206). – P. 8–12.

9. *Chernogor L.F.* Physical effects associated with the passage and airburst of the Chelyabinsk meteoroid (in Russian) // Radio Engineering. Pan-Ukranian Interdepartmental Scientific and Engineering Digest. – 2016. – Issue 184. – P. 32–36.

10. *Chernogor L.F., Shevelev N.B.* Parameters of infrasound effects caused by the Chelyabinsk meteoroid on February 15, 2013 (in Russian) // Bulletin of Kharkiv

V.N. Karazin National University, Ser.: Radio Physics and Electronics – 2016. – Issue 25. – P. 70–73.

11. *Chernogor L.F., Liashchuk O.I.* Parameters of Infrasonic Waves Generated by the Chelyabinsk Meteoroid on February 15, 2013 // Kinematics and Physics of Celestial Bodies. – 2017. – Vol. 33. – No. 2. – P. 79–87.

12. *Chernogor L.F.* Atmospheric effects of the gas-dust plume of the Chelyabinsk meteoroid of 2013. – Izvestiya, Atmospheric and Oceanic Physics. – 2017. – Vol. 53. – No. 3. – P. 259–268.

13. *Chernogor L.F.* Acoustic effects of the Chelyabinsk meteoroid (in Russian) // – Radio Physics and Radio Astronomy. – 2017. – Vol. 22. – No. 1. – P. 53–66.

14. *Chernogor L.F.* Atmospheric and seismic effects of the Chelyabinsk meteoroid (in Russian) // – Radio Physics and Radio Astronomy. – 2017. – Vol. 22. – No. 2. – P. 123–137.

15. *Chernogor L.F., Shevelev N.B.* Global statistics of bolides in the Earth's atmosphere (in Russian) // – Radio Physics and Radio Astronomy. – 2017. – Vol. 22. – No. 2. – P. 138–145.

16. *Chernogor L.F.* Disturbance in the Lower Ionosphere That Accompanied the Reentry of the Chelyabinsk Cosmic Body // Cosmic Research. – 2017. – Vol. 55. – No. 5. – P. 323–332.

17. *Chernogor L.F., Liashchuk O.I.* Infrasound observations of the bolide explosion over Romania on January 7, 2015 // Kinematics and Physics of Celestial Bodies. – 2017. – Vol. 33. – No. 6. – P. 276–290.

18. *Milovanov Yu.B., Chernogor L.F.* Regularization algorithms for calculating temporal and height characteristics describing the dynamics of the Chelyabinsk meteoroid entering the atmosphere (in Russian) // Bulletin of Kharkiv V.N. Karazin National University, Ser.: Radio Physics and Electronics. – 2017. – Issue 26. – P. 75–79.

19. *Chernogor .F., Shevelev N.B.* Statistical characteristics of meter-sized meteoroids in the Earth's atmosphere (in Russian) // Bulletin of Kharkiv V.N. Karazin National University, Ser.: Radio Physics and Electronics. – 2017. – Issue 26. – P. 80–83.

20. *Lazorenko O.V., Chernogor L.F.* System Spectral Analysis of Infrasonic Signal Generated by Chelyabinsk Meteoroid // Radioelectronics and Communications Systems. – 2017. – Vol. 60, No. 8. – P. 331–338.

21. *Chernogor L.F.* Magnetic and Ionospheric Effects of a Meteoroid Plume // Geomagnetism and Aeronomy. – 2018. – Vol. 58, No. 1. – P. 119–126.

22. *Chernogor L.F., Frolov V.L., Barabash V.V.* Effects caused by the action of high-power radio wave emissions with geospace storms in the background: Ionosonde observations (in Russian) // Bulletin of Volga State University of Technology. – 2016. – No.2 (30). – P. 6 – 27.

23. *Chernogor L.F., Blaunstein N.,* Radiophysical and Geomagnetic Effects of Rocket Burn and Launch in the Near-the-Earth Environment. – Boca Raton, London, New York: CRC Press. Taylor & Francis Group, 2017. – 542 p.

24. *Chernogor L.F.* On the possibility of affecting the Earth's magnetic field with rocket launches // Rocket's environmental impact (in Russian) / Eds. V.V. Adushkin, S.I. Kozlov, M.V. Silnikov. – Moscow: GEOS. – 2016. – 795 p.

25. *Chernogor L.F., Garmash K.P., Rozumenko V.T., Smirnova K.O.* Geomagnetic variations caused by rocket launches from the Plesetsk and the Baikonur cosmodromes// Bulletin of Kharkiv V. N. Karazin National University, Ser.: Radio Physics and Electronics. – 2017. – Issue 26. – P. 84–87.

26. *Chernogor L.F.* Nonlinear models in sea and ocean ecology (in Russian) // Nonlinear World. – 2016. – No. 3. – P. 57–64.

27. *Chernogor L.F.* Greatest industrial disasters (in Russian) // Science and Engineering. – 2016. – No. 4 (119). – P. 54–60.

28. *Chernogor L.F.* Consequences of regional and global wars (in Russian) // Science and Engineering Science and Engineering. – 2016. – No. 5 (120). – P. 28–32.

29. *Chernogor L.F.* Greatest explosions in ammunition depots. Part 1 (in Russian) // Science and Engineering. – 2016. – No. 7 (122). – P. 10–13.

30. *Chernogor L.F.* Greatest explosions in ammunition depots. Part 2 (in Russian) // Science and Engineering. – 2016. – No. 8 (123). – P. 8–13.

31. *Chernogor L.F.* Greatest natural gas pipeline and tank disasters in (in Russian) // Science and Engineering. – 2016. – No. 10 (125). – P. 14–19.

32. *Chernogor L.F.* Seven greatest natural disasters (in Russian) // Science and Engineering. – 2016. – No. 12 (127). – P. 52–57.

32. *Chernogor L.F., Barabash V.V.* Wave like disturbances in the F2 ionospheric region electron density: Diurnal and seasonal variations during the declining phase of the solar activity cycle (in Russian) // Radio Physics and Radio Astronomy. – 2017. – Vol. 22, No. 3. – P. 212–221.

33. *Chernogor L.F.* Telluric currents have no significant effect on the Earth's core seismicity // Geomagnetism and Aeronomy. – 2017. – Vol. 57. – No. 1. – P. 119–120.

34. *Chernogor L.F.* Seven greatest natural disasters. Part 2. Greatest tropical hurricanes (in Russian) // Science and Engineering. – 2017. – No. 1 (128). – P. 10–12.

35. *Chernogor L.F.* Seven greatest natural disasters. Part 3. Great East Japan earthquake (in Russian) // Science and Engineering. – 2017. – No. 2 (128). – P. 4–7.

36. *Chernogor L.F.* Seven greatest natural disasters. Part 4. Greatest XXI century tsunamis (in Russian) // Science and Engineering. – 2017. – No. 3 (129). – P. 4–7.

37. *Chernogor L.F.* Seven greatest natural disasters. Part 5. Gigantic volcano eruptions (in Russian) // Science and Engineering. – 2017. – No. 4 (130). – P. 6–11.

38. *Chernogor L.F.* Seven greatest natural disasters. Part 6. Greatest 2010 summer wild fires (in Russian) // Science and Engineering. – 2017. – No. 6 (133). – P. 6–7.

39. *Chernogor L.F.* Seven greatest natural disasters. Part 7. Global warming or climate oscillations? (in Russian)// Science and Engineering. – 2017. – No. 7 (134). – P. 4–7.

40. *Chernogor L.F.* Disaster at the greatest ammunition depot (in Russian) // Science and Engineering. – 2017. – No. 5 (132). – P. 4–10.

41. *Chernogor L.F.* Greatest disaster at a military ammunition storage depot in Ukraine (in Ukrainian) // Outlook. – 2017. –No. 6 (68). – P. 68–73.

42. *Chernogor L.F.* Nonlinear Radio Physics: Textbook (in Russian). – Kharkiv, Kharkiv V. N. Karazin National University, 2016. – 208 p.

43. *Chernogor L. F.* Nonlinear Radio Physics: Textbook (in Ukrainian). Kharkiv, Kharkiv V. N. Karazin National University, 2016. – 204 p.

44. *Chernogor L. F.* On the History of Space Radio Physics. How was the new branch of science being conceived? // Science and Engineering. – 2016, No.2 (117). – P. 58–63.

45. *Chernogor L. F.* The XXI century sensation: Gravity waves are found! (in Ukrainian) // Outlook Outlook. – 2016. – No. 3 (59). – P. 44–50.

46. *Chernogor L. F.* Universe's gravity wave pulse (in Russian) // Science and Engineering. – 2016. – No. 4 (119). – P. 10–14.

47. *Chernogor L. F.* Sensation of the universal scale: Gravity waves are discovered (in Russian) // Universitates. – 2016. – No. 2. – P. 4–10.

GROUND BASED INFORMATION SYSTEM OF "IONOSAT–MICRO" SPACE PROJECT

O. Piankova[1], **O. Protas**[2], **G. Lizunov**[1]

[1] Space Research Institute of NAS of Ukraine and SSA of Ukraine (SRI NASU-SSAU)

[2] Ecognize.me OÜ Ltd., Estonia

The launch preparation for the Ukrainian space research/technology satellite Microsat-M hosting the Ionosat-Micro instrument suite reached the final phase. The goal of the Ionosat-Micro mission is to convey a wide array of space assays in the domains of ionospheric physics, space weather and studies of ionosphere effects of anthropogenic and terragenic origin [1, 2]. In order to engage a large range of scientists to the result analysis, the project's priority task is distribution of experimental data via the Internet both during the mission lifetime and after its end. The same goal is further emphasized by the data disclosure policy which stipulates that the mission measurements become available in open access half a year after their acquisition.

Overall over a Terabyte of data is expected to be received, subdivided among around 30 ionospheric parameter registration channels, segmented into records and tied to individual Microsat-M spacecraft orbital revolutions. Several hundred thousand records will be produced overall which require decryption and cross-analysis. Such amount of data processing is unfeasible to conduct manually solely by direct project participants. Therefore, a special center for collection, processing and distribution of Ionosat-Micro experimental data complemented by an automated information system (named PROMIS abbreviated from "PROcessed Measurements of Ionospheric Satellites") is created within Space Research Institute of National Academy of Sciences of Ukraine and State Space Agency of Ukraine.

PROMIS consists of the service for data collection from ground side receiving stations' servers, data decryption, systematization and georeferencing toolkits, the storage for data of various processing levels which will be updated throughout the space experiment, the metadata database for executing storage queries efficiently, and the Web interface for remote end users to access the data with.

Processing order and data representation level classification

Aboard the spacecraft the data is registered into an onboard data handling unit (OBDH) in the form of binary files. The telemetry information (TMI) needed for subsequent analysis is further added from the spacecraft housekeeping systems. Before queueing the data for transmission to the ground, OBDH produces transport packets based on CCSDS recommendations in order to provide for the interference resistance and data recovery. Additionally, the transmission employs data convolutional encoding.

The ground receiving station proceeds to decode and put the resulting bitstream on the FTP server where it is downloaded from automatically by PROMIS. The data experiences several processing cycles afterwards and the result is saved to the storage. Thus, data representation levels are created.

The level 0 stores the binary files recovered from the bitstream in the original representation by the OBDH. The unpacking is done automatically by the software supplied by developers of the OBDH and integrated into PROMIS. The level 0 is internal, inaccessible for the users outside system machinery.

The level 1 contains measurement data as provided by the onboard scientific instruments. Level 1 data is formed by extracting the data from binary formats and dividing them into measurement channels. Additionally, TMI is also extracted. At the same time, georeferencing is performed using either TMI or spacecraft orbit prediction given the ballistic parameters supplied by the flight control center.

The level 2 stores the calibrated measurement data in natural units commonly used by the ionospheric physics community and addressed at a large range of scientist users. PROMIS either does the level 1 to level 2 conversion on its own or allows optionally for the equipment developers to provide such a conversion. In the former case, the equipment

Table 1

User status of Ionosat-Micro mission data

User status	Description
Admin	System administrator and operator monitoring the experiment progress
Experiment participant	Member of the project Consortium of Ionosat–Micro space mission
Data processing participant	Person with an individual authorization by the Consortium to data processing without time limitation
Logged-in external user	Any person who registered on the PROMIS website
Observer (unauthorized external user)	Anyone who uses the website without registration

developers validate their data using PROMIS center services. In the latter case, PROMIS services send level 1 data for conversion to the developers and waits for the calibrated data in response. The full set of level 2 data types is the following:

– MWC magnetic wave complex data – 3 components of the DC magnetic field, 3 components of AC magnetic field, 3 components of AC electric field, 3 components of AC electric flux density;

– RFA spectral analyzer data – 3-component spectrum of HF electric field;

– PDA particle density analyzer data – concentration and temperature of neutral gas, concentration and temperature of ionosphere plasma electron component;

– ID-2 ion driftmeter data – concentration, temperature and 3 components of plasma ion component drift, ion inhomogeneities spectrum.

The level 3 is considered to be the data processed by PROMIS per user request (quick look generation, standard data analysis etc.). Data of this level are not meant to be permanently stored.

Data access policy

The subscribers of the PROMIS web portal consisting of researchers and Ionosat-Micro project data end users are categorized as per Table 1. The data access conditions are detailed in the Table 2.

Design of the system's web-application

General structure for obtaining data through PROMIS web-application is shown in Fig. 1. Web-interface (Frontend) communicates with the server side of the system (Backend) (as well as external services if necessary) using REST API (Representational State Transfer Application Programming Interface). Advanced users may as well use the API for batch queries and downloads bypassing the web interface entirely.

And, of course, the standard way to access the data is using the Web interface of the PROMIS system (Fig. 2) where the user can find handy means for data search and filtering by the measured parameter name and by the condition of the satellite orbit's intersection with spatial-temporal window specified by user.

The Web interface has a header, a footer and the main part of site that contains functional windows.

Except for the site logo and the link to the Ionosat-Micro project site, the header has the user authentication and registration buttons that open the corresponding windows. Web interface appearance changes according to the user status (Tabl. 2): certain additional functional elements become available.

Table 2

Data access rights

User status	Level 0, TMI	Level 1	Level 2	Level 3	
Admin	+	+	+	+	
Experiment participant	–	+	+	+	
Data processing participant	–	As decided by the experiment PIs			
Logged-in external user	–	–	–	+ in 6 months	+ in 6 months
Observer (unauthorized external user)	Reduced set of review information				

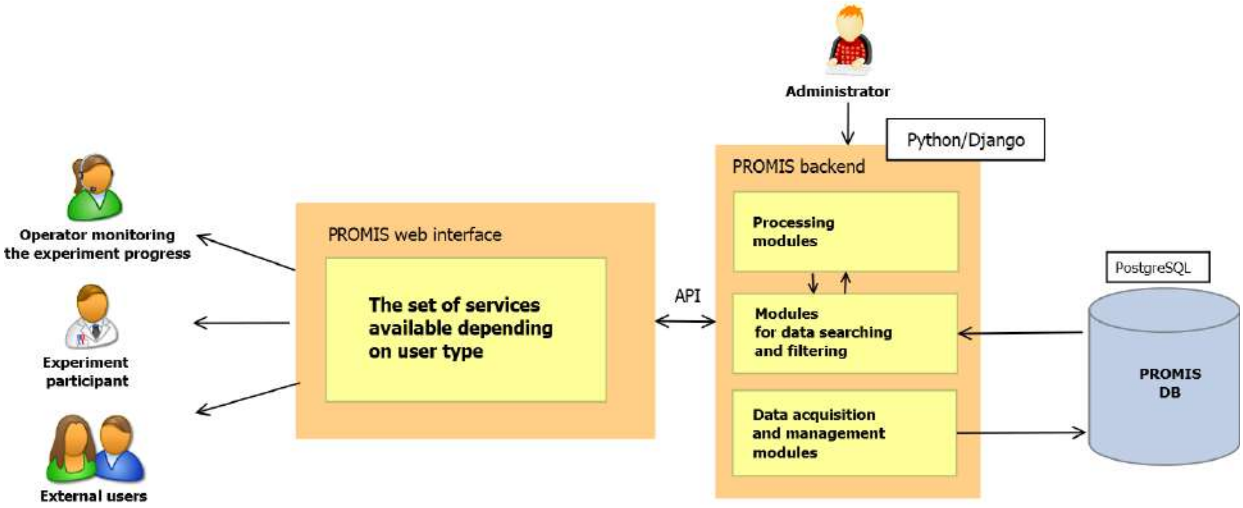

Fig. 1. Scheme of the user interaction with the PROMIS system

There are four windows in the main part of the site. The "Time and position" window contains fields for defining the data search time and spatial ranges. The "Search" window provides measured ionospheric parameters selection (for users with proper access status, a data-level switcher is available in this window too). The "Search Result" window provides details and access to the data found.

But the most interesting one is the "Map" window that provides geographical maps of the Earth that can be expanded to full screen if needed. Search areas and the parts of the satellite orbit matching the search

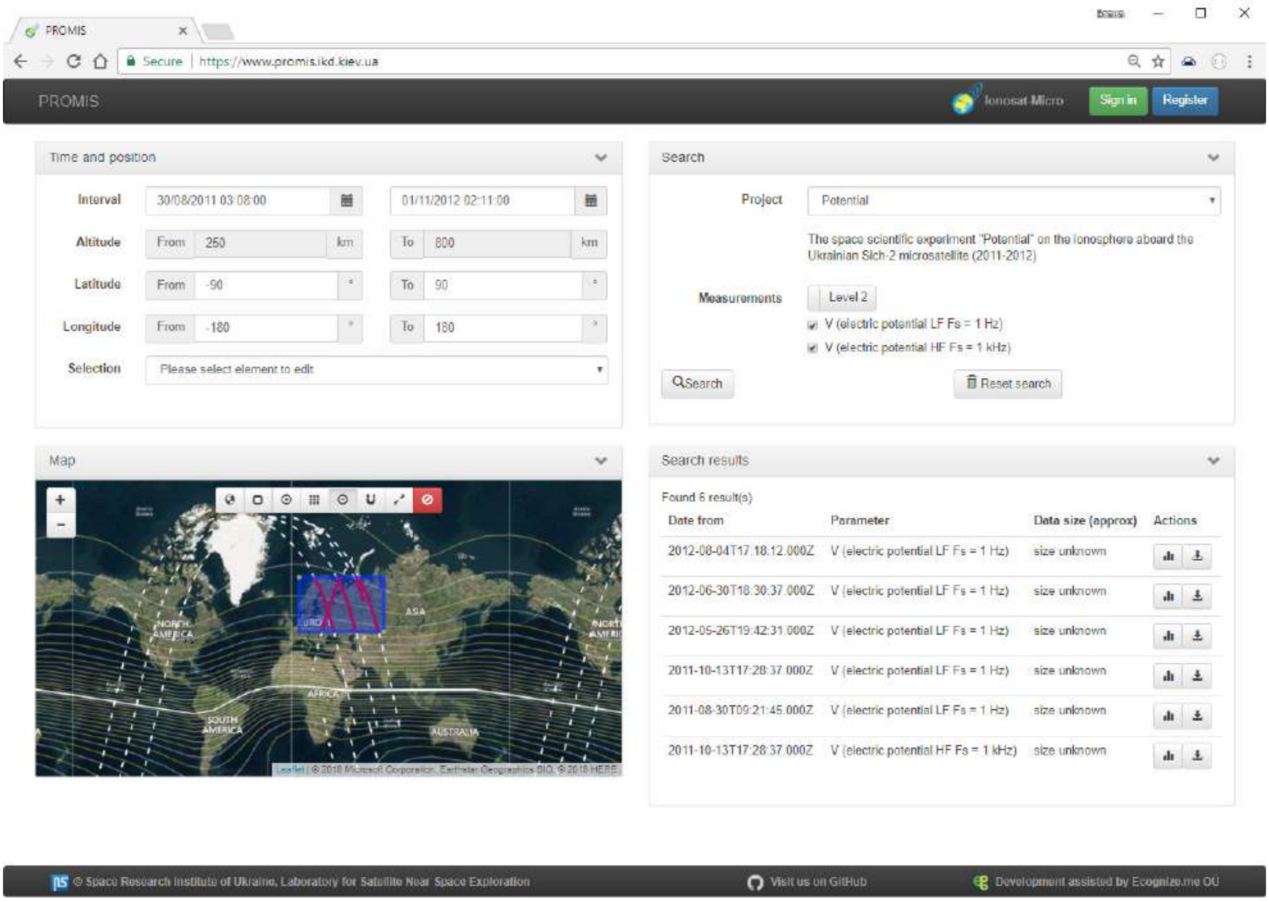

Interval: 30/08/2011 03:08:00 – 01/11/2012 02:11:00
Altitude: From 250 km To 800 km
Latitude: From -90 ° To 90 °
Longitude: From -180 ° To 180 °
Selection: Please select element to edit

Project: Potential
The space scientific experiment "Potential" on the ionosphere aboard the Ukrainian Sich-2 microsatellite (2011-2012)
Measurements: Level 2
☑ V (electric potential LF Fs = 1 Hz)
☑ V (electric potential HF Fs = 1 kHz)

Found 6 result(s)

Date from	Parameter	Data size (approx)	Actions
2012-08-04T17:18:12.000Z	V (electric potential LF Fs = 1 Hz)	size unknown	
2012-06-30T18:30:37.000Z	V (electric potential LF Fs = 1 Hz)	size unknown	
2012-05-26T19:42:31.000Z	V (electric potential LF Fs = 1 Hz)	size unknown	
2011-10-13T17:28:37.000Z	V (electric potential LF Fs = 1 Hz)	size unknown	
2011-08-30T09:21:45.000Z	V (electric potential LF Fs = 1 Hz)	size unknown	
2011-10-13T17:28:37.000Z	V (electric potential HF Fs = 1 kHz)	size unknown	

© Space Research Institute of Ukraine, Laboratory for Satellite Near Space Exploration

Fig. 2. The Web interface of PROMIS system. The map window is in 2D mode

criteria are visualized and superimposed on both 2D and 3D geographical maps (Fig. 2, 3).

The «Map» window has its own toolbar that allows to:

– Switch from 2D to 3D map;

– Enter Full screen mode;

– Clear the map;

– Define the search area selection on the map: rectangular and circular areas in 2D and 3D map; multi line polygon areas for 3D map exclusively (areas selected in 2D map are carried over to 3D map and vice versa);

– Overlay additional geophysical information based on the user needs such as geographic and geomagnetic coordinate grids and magnetic field coordinate inclination and intensity grids. (For illustration, magnetic field inclination contour lines are switched on in Fig. 2 and 3).

A click on the "Search" button activates the data search in system. Notably if the user does not select a search area, the search will be carried out over the entire period of the space experiment's duration and over the entire globe by default.

While the search is being executed the user sees a Progress Bar and the search results are being dynamically added in "Search Result" table with the parts of the matching satellite orbit superimposed over the map.

The "Search Result" table is formed by rows with information which describes continuous sequences of measurements matching the search constraints. Each sequence is characterized by the start and end time of the continuous time measuring period and by measured parameter name. The user can preview the data by clicking on the "Quicklook" button (Fig. 4) or by activating the data file generation for download by clicking the "Download" button. The results table indicates the approximate data file size of to estimate how much time and resources will be needed for downloading process.

At the time of this article's writing, the beta-version of PROMIS system is available by the link http://promis.ikd.kiev.ua with different structured data from previous similar experiments "Variant" onboard Sich-1M and "Potential" onboard Sich-2 [3–6] being loaded into the system for testing. Several stages of the system testing and inter-agency pre-flight trials will be performed up to the time of "Microsat-M" satellite launch. Authors will be sincerely grateful for reporting any errors and

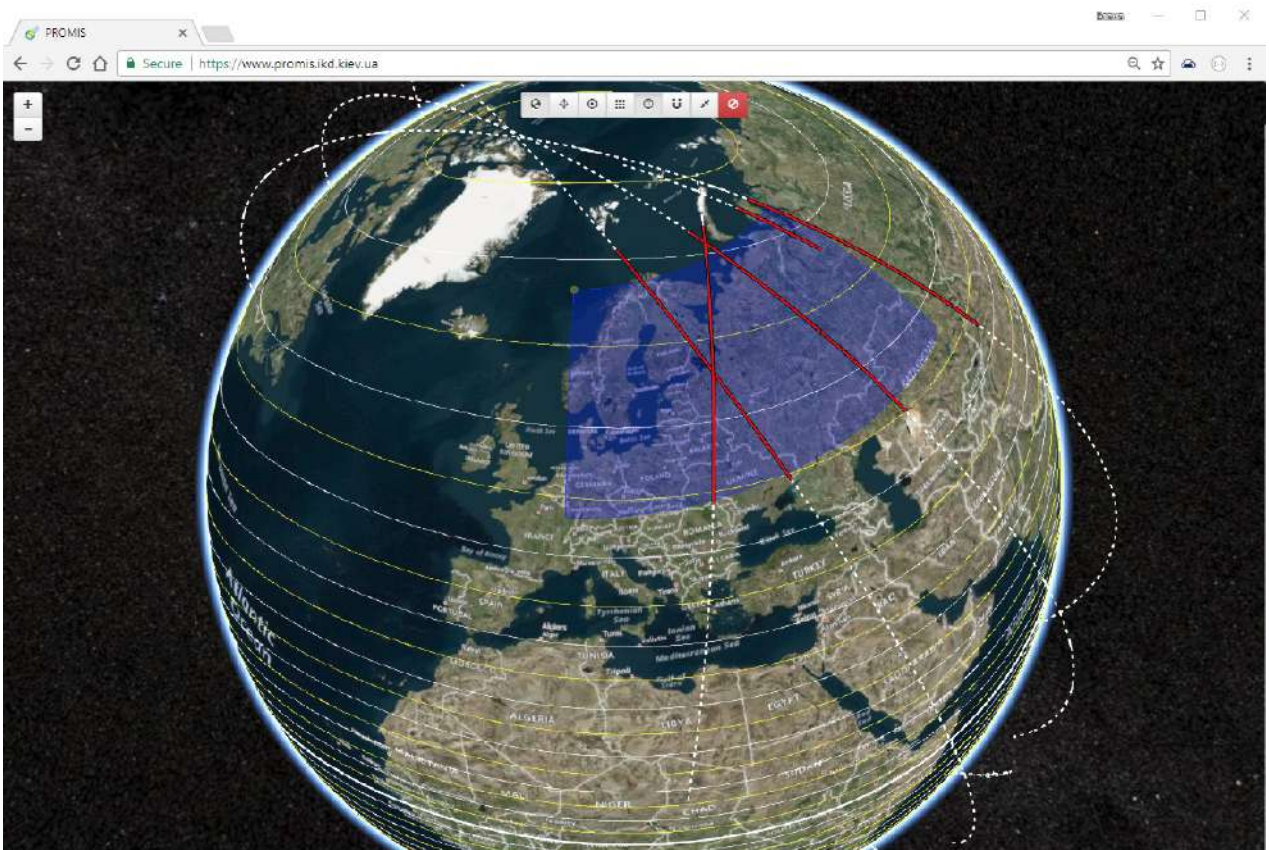

Fig. 3. Map window in the 3D mode

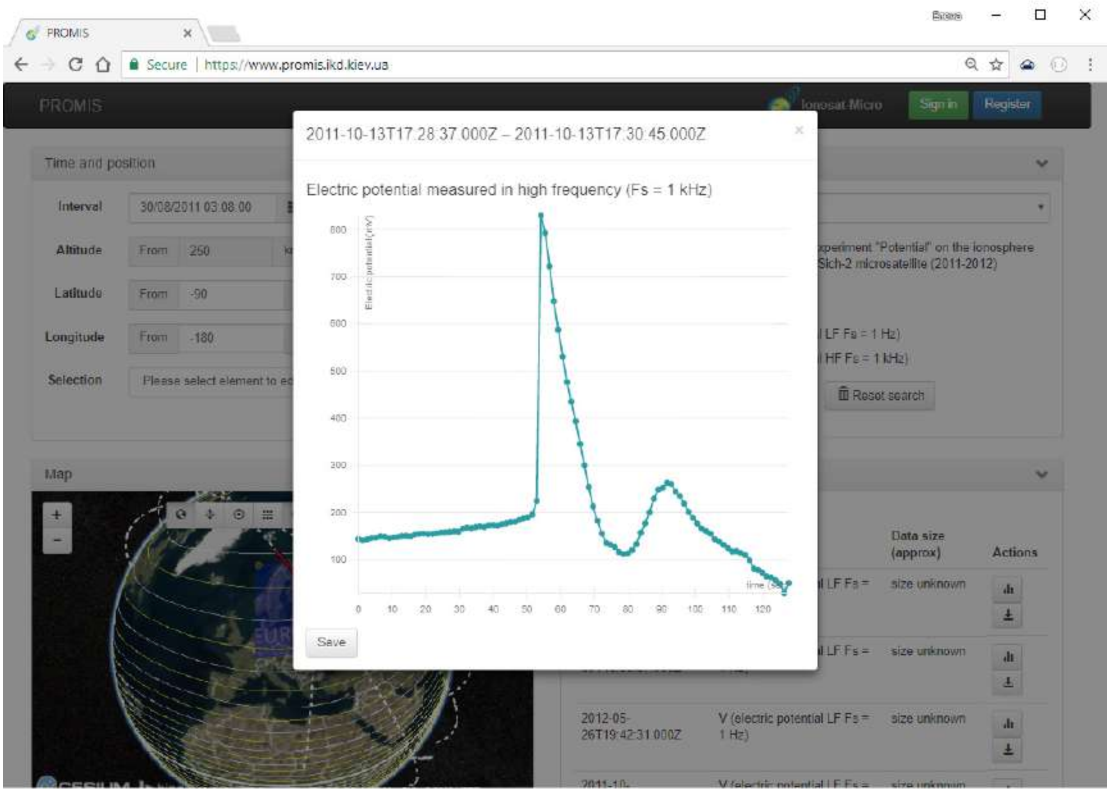

Fig. 4. Quicklook produces a downsampled measurement data plot

providing feedback and suggestions for improving the system.

The work was funded by the State Space Agency of Ukraine under the contract No. 4-23/16.

REFERENCES

1. Space Project "Ionosat-Micro": monograph / Ed. S.A. Zasukha, O.P. Fedorov. – Kyiv: Akademperiodyka, 2013. – 218 p. (in Russian).

2. *Lizunov G., Skorokhod T.* Space Project "Ionosat-Micro" // Space research in Ukraine 2014–2016 / Ed. O. Fedorov. – Kyiv.: Akademperiodyka, 2016. – P. 7–13.

3. *Korepanov V.Ye, Kriuchkov Ye.I., Lizunov G.V., Fedorenko A.K., Dudkin F.L.* Experiment "Variant" onboard Sich-1M – first results // Space science and technology. – 2007. – V. 13. – No. 4. – P. 10–17. (in Ukrainian).

4. *Korepanov V., Lizunov G., Dudkin F., Kriuchkov Y.* Experiment "Variant" aboard satellite "Sich-1M" / Space Research in Ukraine 2004-2006. – Kyiv, 2006. – P. 7–13.

5. *Lizunov G.V., Lukeniuk A.A., Korepanov V.Ye., Shenderuk S.G., Leontiev A.Yu., Priyimak A.I.* Space experiment "Potential" onboard Sich-2 // Space research in Ukraine 2010-2012 / Ed. O. Fedorov. – Kyiv: Akademperiodyka, 2012. — P. 7–11. (in Russian).

6. *Makarov O.L., Lizunov G.V., Lukeniuk A.A., Korepanov V.Ye., Shuvalov V.O., Shovkoplias Yu.A., Moskalev S.I.* Experiment POTENTIAL onboard SICH-2 microsatellite – first results / Proceedings of the 63rd International Astronautical Congress, October 1–5, 2012, Naples, Italy. – IAC-12-B4.2.13571. – 7 p.

TRANSPORT OF MAGNETIZED PARTICLES IN A RANDOM ELECTRIC FIELD

O. Cherniak, V. Zasenko

Bogolyubov Institute for Theoretical Physics of NAS of Ukraine (ITPh NASU)

The state and evolution of laboratory and space plasma are significantly influenced by transport processes. Often plasma is in non-equilibrium state and various instabilities in plasma are developing. The intensities of inducted fields overwhelm the thermal energy and, consequently, transport caused by interaction with collective fields dominates over classical diffusion caused by particles collisions.

The known statistical approaches to transport processes usually deal with random fields with small correlation time compared to other characteristic times in plasma. While less attention were paid to low-frequency fields with long correlations, they can significantly influence on a state of outer space plasma. The statistical approaches to transport processes caused by the fields with long correlations require new methods to close statistical equations, because of particle trapping effects.

There is an interesting problem to develop an analytical approach to transport processes in two-dimensional random fields, where particle trapping effects are most clear – magnetized particles move for a long time along streamlines. The infinite correlation time is the most complicated problem from the analytical approaches perspective since the random walk approximation is invalid. Moreover, the drift motion is purely diffusive, so unperturbed motion is absent. This means no zero-approximation and no iterative expansion for a statistical evolution of particles ensemble. For the energetic particles of space plasma it is also important to account for their finite Larmor radius. There are expected non-trivial transport coefficients dependence on magnetic field and correlation time of random electric field.

Numerical simulation equations

The exact and drift motion of ensemble of particles in random electric field superposed by uniform magnetic field is considered. The random field is isotropic and defined as weighted sum of $N = 1440$ harmonic waves. There is a unique realization of random electric field for each particle that is determined by set of random phases of waves.

We consider a drift motion of particles with the set of constant random phases to study transport in a random field with infinite correlation time. So, the random field is static and random potential is constant along the particle's drift trajectory. This leads to a particle trapping.

When finite Larmor radius r_L cannot be neglected, i.e. for particles transport with significant initial velocities, we consider exact motion equation. This enables particles to change streamline along their trajectories. So depending on the value of initial velocity, they can travel on distances greater than trapped particles can.

For a numerical simulation of particle's drift motion in fields with a finite correlation time the set of jumping in time random phases is considered.

Numerical calculation of particles trajectories is done using Runge-Kutta method of 5-th order. There are $N_r = 10^4$ realizations of random field in the ensemble, if there isn't other mentioned. Obtained particles trajectories are used to calculate mean square displacement, diffusion coefficient and correlation function of drift velocity components along particles trajectories. The correlation function of drift velocity components in fixed points of reference frame is obtained using explicit form of random field that used further in analytical approximation.

Analytical approach

We use Taylor relation for analytical approximation of magnetized particles transport in a random electric field. This gives the diffusion coefficient $D(t)$ that depends on time and mean square displacement $\Delta(t)$ in terms of correlation function of drift velocity components along particles trajectories. Such correlation $C^L_{vv}(t) = \langle v(r(t+t_0))v(r(t_0))\rangle$ function is unknown and named Lagrangian. It's determination is a key problem in this approach. In contrast, the correlation function in fixed points of reference

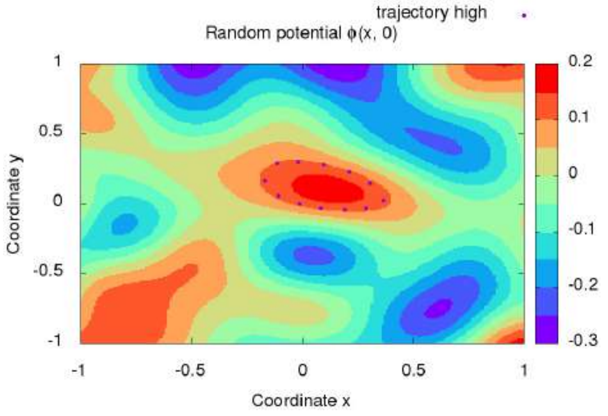

Fig. 1. A typical trajectory of trapped particle in a random field

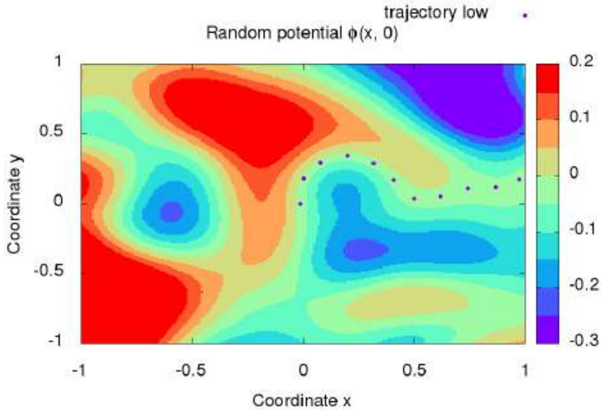

Fig. 2. A typical trajectory of untrapped particle in a random field

frame $C^E_{vv}(r,t)=\langle v(r+r_0,t+t_0))v(r_0,t_0))\rangle$ is known and called Eulerian. It is used to construct the approximated Lagrangian correlation function. There is no mathematically strict method to calculate Lagrangian correlation function using Eulerian one in general, thus various approximations are used – closures of statistical equations.

There are a few known methods to obtain approximated Lagrangian correlation function using Eulerian one. Among them Corrsin approximation that is valid for a small Kubo numbers $K<<1$ (where $K=V\cdot t_c/\lambda_c$ is a dimensionless correlation time, V is an initial value of mean drift velocity, t_c and λ_c are correlation time and correlation length respectively) leads to asymptotic diffusion coefficient $D\equiv D(t)_{t\to\infty}\sim K^2$. For a large Kubo numbers $K>>1$ there is so-called Bohm scaling law $D\sim K$. But it contradicts to the results of numerical simulation that is done by us and other authors, where asymptotic diffusion coefficient is found to be $D\sim K^\gamma$, $\gamma<1$.

We proposed the moment approximation for the infinite correlation time $K\to\infty$ of isotropic random field [1, 2]. It uses mean square displacement for a statistical closure to obtain Lagrangian correlation function of drift velocity components $C^{L,D}_{v_d v_d}(t)$. There is approximation presented in [3] that accounts for dynamics of various groups of trapped particles, which can be characterized by initial values of random potential.

The gyroaveraging procedure of random potential is applied to moment approximation in [4, 5] to consider finite Larmor radius r_L effects on particles transport. For the obtained effective potential the Eulerian correlation function of drift velocity components is presented. So, combining it with proposed statistical closure of moment approximation the Lagreangian correlation function $C^{L,R}_{v_d v_d}(t)$ is obtained.

At last, correlation function with explicit exponential decay in time $C^{L,T}_{v_d v_d}(t)$ is used for a moment approximation to consider finite correlation time problem.

Substitution of mentioned approximated Lagrangian correlation functions of drift velocity components $C^{L,D}_{v_d v_d}(t)$, $C^{L,R}_{v_d v_d}(t)$, $C^{L,T}_{v_d v_d}(t)$ in Taylor relation gives us the final equation for mean square displacement $\Delta(t)$, that is solved numerically.

Results

For infinite correlation time of random field the drift motion of particles is along the streamlines, so almost all of the particles, except the particles at zero potential level probably, are trapped in random field. The typical motion of trapped particles along closed trajectories is presented in Fig. 1. These particles can travel for a relatively small distances compared to untrapped ones, which schematic trajectories are presented in Fig. 2. Motion of trapped particles is strongly correlated and thus can't be considered as random walk.

Such motion of particles in ensemble of realizations leads to an infinitely long negative tail of Lagrangian correlation function of drift velocity components. That can be seen in Fig. 3 for direct numerical simulation and moment approximation [1, 2]. The negative tail of correlation function causes asymptotically zero diffusion coefficient and subdiffusive evolution of mean square displacement.

Detailed comparison between various approximations for an infinite correlation time is presented in [2]. The comparison of mean square displacement presented in Fig. 4 demonstrates agreement between moment approximation and direct numerical simulation.

The moment approximation with account for different dynamics of particles grouped by initial

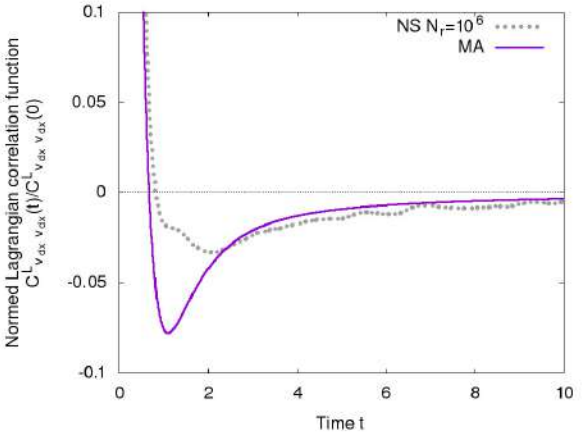

Fig. 3. Lagrangian correlation function obtained by numerical simulation (NS) and moment approximation (MA) for infinite correlation time

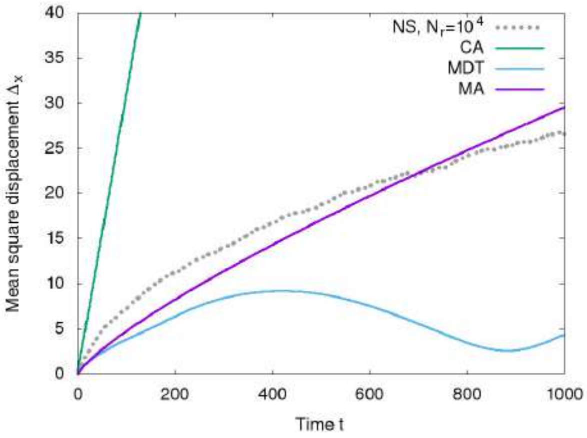

Fig. 4. Mean square displacement obtained by numerical simulation (NS), Corrsin approximation (CA), decorrelation trajectory method (MDT) and moment approximation (MA) for infinite correlation time

values of random potential is presented in [3]. Such approach provides a better agreement between moment approximation and direct numerical simulation.

The exact motion of particles leads to a decorreation of trajectories – particles with non-zero Larmor radius can jump between streamlines and thus travel for longer distances. The various methods of gyroaveraging and calculated Eulerian correlation function of drift velocity components for moment approximation was studied in detail [4, 5]. Comparison between direct numerical simulation and moment approximation demonstrates, that the most accurate results gives the gyroaveraging of random potential with further calculation of Eulerian correlation function [4]. The evolution of diffusion coefficient for different initial values of Larmor radius is shown in the Fig. 5. It should be pointed, that at small times for small values of initial Larmor radius the greater diffusion coefficient is obtained, but with a time it decays faster and becomes smaller than a diffusion coefficient for a greater initial Larmor radius. It is also important to note, that the same behavior is obtained for a mean square displacement [5] presented in Fig. 6.

Recently the particles transport in fields with a finite correlation times was studied. The particle trapping is limited in time in this situation. Consequently, the area of negative values of correlation function of drift velocity components decays with a decay of correlation time. In a limit of ultra high-frequency random field we can suppose, that particles moves under random force, which corresponds to a Brownian motion. For a small correlation times, the Corrsin approximation is valid and gives for a asymptotic diffusion coefficient $D \sim K^2$.

Lagrangian correlation function for a moment approximation with exponential decay of correlation in time is presented in Fig. 7. For a small correlation times moment approximation gives correlation

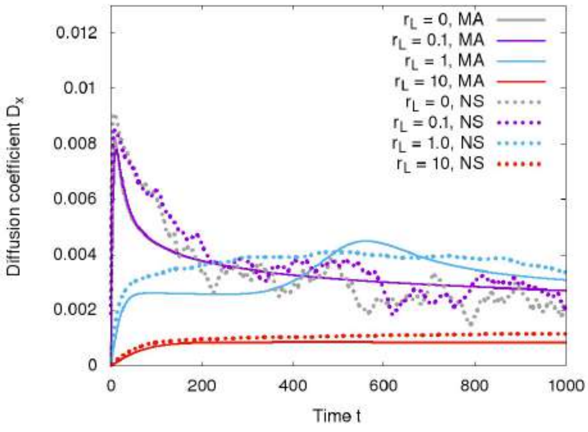

Fig. 5. Diffusion coefficient obtained by numerical simulation (NS) and moment approximation (MA) for a given initial Larmor radius r_L

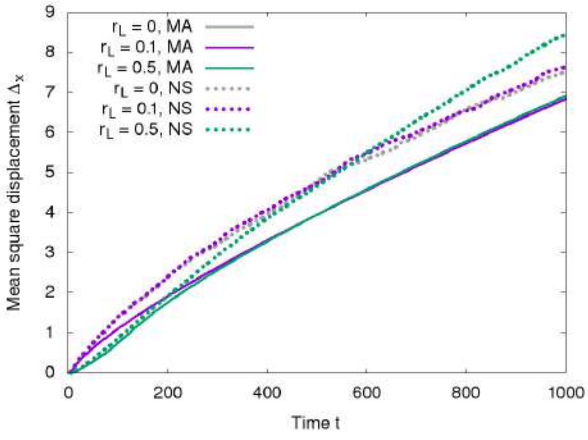

Fig. 6. Mean square displacement obtained by numerical simulation (NS) and moment approximation (MA) for a given initial Larmor radius r_L

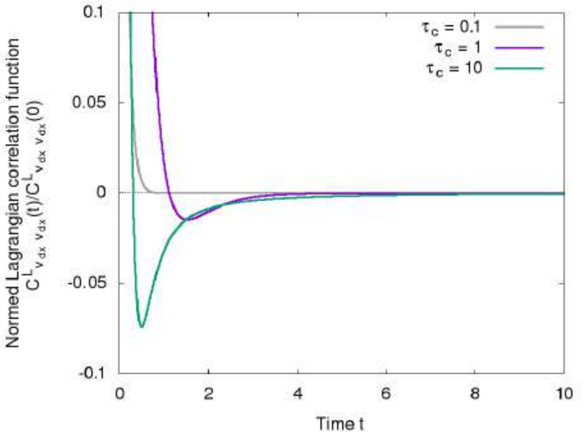

Fig. 7. Lagrangian correlation function by moment approximation (MA) for a given finite correlation times t_c

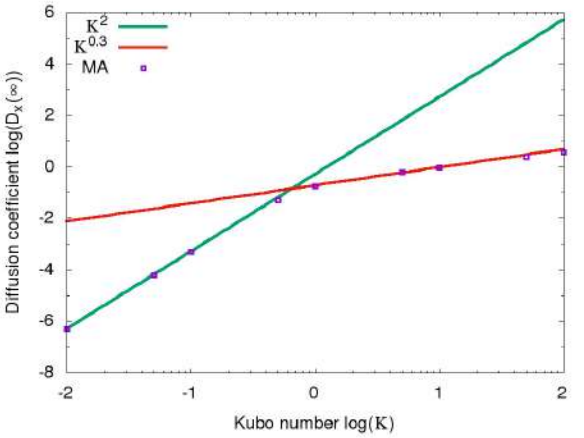

Fig. 8. Asymptotic diffusion coefficient by moment approximation (MA) for a given Kubo numbers $K = V\cdot t_c/\lambda_c$

function of drift velocity components without negative values, while for a large correlation times they appear. The area of negative values of correlation function grows with a growth of correlation time. It limits the value, when asymptotic diffusion coefficient turns zero.

The dependence of asymptotic diffusion coefficient on Kubo number is presented in Fig. 8. Moment approximation for correlation function with explicit exponential decay in time recovers known result of Corrsin approximation $D \sim K^2$ for a small Kubo numbers $K << 1$ and for the large ones $K >> 1$, we have $D \sim K^\gamma$, $\gamma \approx 0.3$, that corresponds to a subdiffusive regime.

Conclusions

We proposed a new method to close statistical equations, which describes a diffusion of magnetized particles in a random electric field. It is shown that closure by mean square displacement [1] recovers the results of direct numerical simulation [2] in zero Larmor radius approximation. Analytic approach to account for particles grouped by different values of initial random potential [3] gives more accurate agreement with a direct numerical simulation.

The effects of finite Larmor radius on particles transport are accounted for the wide range of values [4]. It is demonstrated for infinite correlation time that for a small times running diffusion coefficient decays with a growth of initial Larmor radius but with a time this dependence changes vice versa [5].

The dependence of diffusion coefficient on correlation time of random field is obtained. It recovers the limits of quasilinear scaling relation $D \sim K^2$, for small correlation times and anomalous $D \sim K^\gamma$, $\gamma < 1$ for large ones.

The work is partly supported by project № 7-02/17 «Research of wave and turbulent processes in outer space plasma».

REFERENCES

1. *Zasenko V.I., Zagorodny A.G., Chernyak O.M.* Diffusion in a Frozen Random Velocity Field // Ukrainian Journal of Physics. – 2001. – V. 56. – No. 10. – P. 1007–1010.

2. *Cherniak O.M.* Particle's Diffusion in a Two-Dimensional Random Velocity Field // Ukrainian Journal of Physics. – 2015. – V. 60. – No. 12. – P. 1196–1210.

3. *Zasenko V.I., Cherniak O.M., Zagorodny A.G.* Subensemble concept in 2d magnetized particle transport model // Problems of atomic science and technology. – 2016. – V. 106. – No. 6. – P. 77–80.

4. *Cherniak O.M., Zasenko V.I,, Zagorodny A.G.* Finite Larmor radius effects on turbulent transport of test-particles // Problems of atomic science and technology. – 2016. – V. 106. – No. 6. – P. 96–99.

5. *Cherniak O.M., Zasenko V.I.* Finite Larmor Radius Effects on a Test-Particle Diffusion // Ukrainian Journal of Physics. – 2017. – V. 62. – No. 6. – P. 495–501.

SPACE BIOLOGY: RESULTS AND PROSPECTS

E. Kordyum
M.G. Kholodny Institute of Botany of NAS of Ukraine (IB NASU)

During 2016–2018 years, the investigations in the field of space biology continued in the areas of plant biology at the cellular and molecular levels in simulated microgravity and astrobiology. The search for new approaches to testing the properties of substrates adequate to the requirements of space planting were conducted. An original biological experiment was proposed for nanosatellites.

Gravi-dependent modification of reproductive development of mosses

Gravireactions widen phenotypical plasticity of bryophytes and are of adaptive significance in vital species strategy. The obtained results extend our knowledge about the role of gravity in development biology of bryophytes.

The peculiarities of the generative and vegetative reproduction of the some mosses species, depending on environmental factors were determined. It was established that gravireactions and initiation place of the brood bodies in *Bryum pseudotriquetrum* two ekomorphs formed in different regions depending on climatic conditions (Fig. 1).

It was showed that the gravity polarizing effect can be active osmotic regulatory factor for renewal and acceleration of *Bryum argenteum* vegetative reprodiction during seasonal water shortage in natural environment. In the conditions of hypoxia and altered gravity vector alcohol dehydrogenase (ADH) activity is a precondition for rapid maturation of the male gametangia than female, which provides a higher probability of fertilization (Fig. 2).

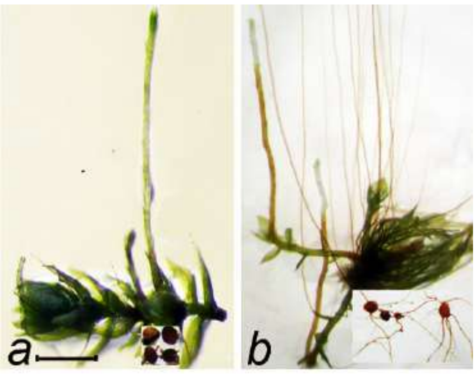

Fig. 1. Two ekomorphs of *Bryum pseudotriquetrum* with different gravisensitivity of gametophyte organs: *a* – antarctic population with gravisensitive shoots, which formed brood tubers at the base; *b* – lviv (Ukraine) population with gravisensitive protonemata and tubers on protonemata stolons. Bar: *a*, *b* = 1.5 cm; bar on the inserts = 400 µm

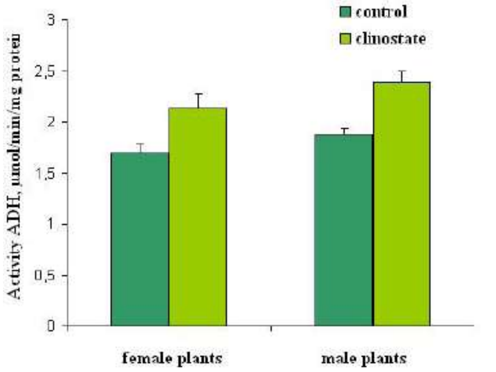

Fig. 2. Alcohol dehydrogenase activity of heterosexual plants *Bryum argenteum* Hedw. depending on the gravity vector changing

Photosynthesis of *B. argenteum* female plants was less sensitive to changes of gravity vector than male plants (Fig. 3).

It was established that in natural environment male plants was also smaller and under an unfavorable conditions they were absent (Stark et al., 2000). Thus, the formation of fertile plants and reproductive organs, predominantly male, was sensitive to the environmental factors – changes of gravity

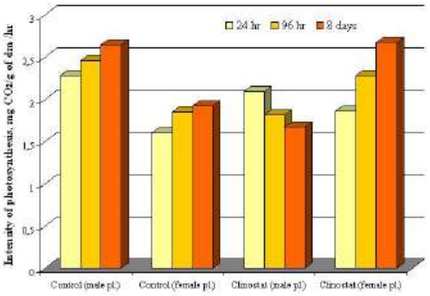

Fig. 3. Influence of clinorotation on the photosynthesis intensity (mg CO_2/g of dry weight /hour) in *Bryum argenteum* fertile plants

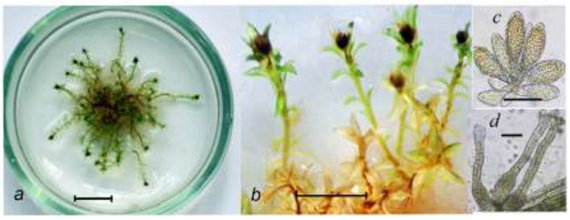

Fig. 4. Monoicous turf of Physcomitrella patens (Hedw.) B.S.G. with the roundish capsules immersed into the perichaetial leaves: *a* – control; *b* – after clinorotation; *c* – antheridium; *d* – archegonium. Bar = 2 mm (*a*, *b*); *c*, *d* = 0.2 mm

Fig. 5. a – the formation of sporogonium *Bryum argenteum* Hedw. bending under the conditions of 1 g; the places of maximum starch accumulation in statocytes of seta and capsule neck are marked with arrows; *b*, *c* – turf of *Grimmia anomala* Hampe with inclined capsules

and environmental stress and required of significant energy resources.

Gravitation influence on space orientation and morphogenesis of mosses sporophyte has been investigated. It has been established that sporogonia are formed as bipolar structure with apical and basal growth centres, the direction of which is changed relative to the gravitation vector. The result of such growth is inclined form of capsule (Fig. 4).

Space orientation of capsules is gravidependent for some moss species, the formation of specific capsules is gravidependent for others. Besides that the form and capcule space orientation is taxonomic feature, the formation of inclined capsule is graviadaptive growth reaction (Fig. 5). Spores are sown near paternal turfs in moss species which are the first to be settled on destroyed substrates from inclined capsules, and thanks to turf local attaching and spending out this promotes quick population of larger territory.

Thus, generative and vegetative reproduction of mosses is the gravidependent process. It was established that formation of sexual organs, especially male are sensitive to the influence of altered gravity and requires the significant energetic resources. Gravireactions expand phenotypic plasticity of bryophytes and have the adaptive importance in the species vital strategy. The obtained results expand our knowledge on a role of gravity in development biology of bryophytes. (*Institute of Ecology of Carpathians, National Academy of Sciences of Ukraine, O. Lobachevska, Ya. Chorkavtsiv*)

Clinorotation increases the heat shock response and thermotolerance in Arabidopsis thaliana seedlings

Clinorotation used to simulate microgravity effects in ground-based experiments is considered as a mild stress factor for plants. We have assumed that it might influence the plant tolerance to other stressful factors. To test this, *Arabidopsis thaliana* seedlings were grown on a horizontal clinostat (2 rpm) or under stationary conditions (control) and then subjected to heat treatment. The kinetics of gene expression of cytosolic HSP70s and HSP90s during exposure to 37 °C for 0,5–2 h was examined by RT-qPCR to estimate level of the heat shock reaction. It was shown that clinorotation caused the minor increase in transcript abundance of five AtHSP70s and AtHSP90-1 under normal temperature as well as a faster onset and enhancement of their induction during heat shock. Data on inducible HSP70-4, HSP70-5 and HSP90-1 are presented on (Fig. 6). The heat tolerance was evaluated as a function

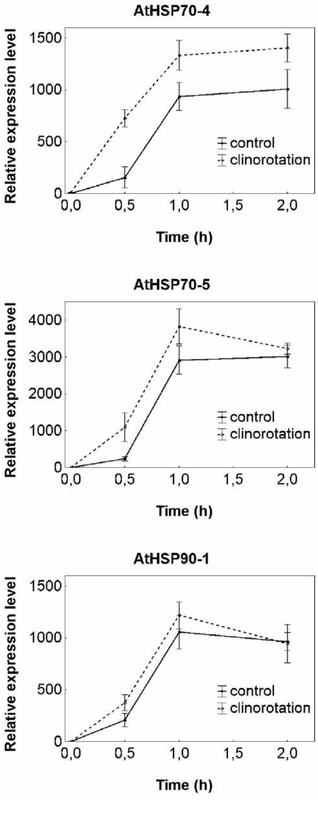

Fig. 6. Effects of clinorotation and high temperature on the expression of inducible heat shock genes in *Arabidopsis thaliana* (Col) seedlings. Time course (0–2 h) of the expression of HSP70-4, HSP70-5 and HSP90-1 genes during the exposition at 37 °C after clinostat rotation or stationary conditions (control) at 22 °C. mRNA levels were analyzed by RT-qPCR, and the changes were calculated as a fold change to the stationary control (= 0 h of the high temperature exposition). Data are means ± SD

of seedling survival after exposure to 45 °C for 45 min. Seedlings grown under clinorotation were determined to withstand heat treatment better than seedlings grown under stationary conditions. These results support the assumption that clinorotation may provide cross-protection of plants against fluctuations in environmental conditions.

(*M.G. Kholodnt Institute of Botany, Natiomal Academy of Sciences of Ukraine, Kozeko L.*)

Lipid rafts in plant cells are sensitive to simulated microgravity

The cytoplasmic membrane (CM) is considered as one of the most dynamic supramolecular structures in a cell, which is the intermediate link between the cytoplasm and extracellular environment and involved in numerous processes such as transport of metabolites and ions, endocytosis, cell proliferation and differentiation, defence from pathogens (Edidin, 2003; Engelman, 2005; Sprener, Gensen, 2010). It has been experimentally shown that the CM is gravisensitive as well as an impact of gravity on ion channels and fluidity (microviscosity) of artificial and cellular membranes (Goldmann, Hanke, 2001; Sieber et al., 2004), that may explain certain biological effects of gravity.

Currently it has been shown the presence of functional microdomains with the specific localization and content of lipids and proteins in the CM of plant cells, that became known as "lipid rafts" (Fig. 7).

It is supposed that rafts enriched on cholesterol and sphingolipids take part in many vitally important cell processes (Brown, London, 1998, Cacas et al., 2012). The investigations of lipid rafts help to explain the biochemical processes which occur in cell membrane in the normal conditions and in responses on stress and can’t be explained by using the other models. We studied the composition and content of fatty acids and srterols in lipid rafts isolated from the root CM of *Pisum sativum* seedlings grown during 6 days under slow horizontal clinorotation. The fractions of CM and rafts were obtained with an ultracentrifuge "Optima L-90K". The raft fraction was controlled by the electron-microscopic method with a transmission electron microscope JEM 1230 (Jeol, Japan). Fatty acids and sterols were determined by the method of gas chromatography with a chromatograph HRGC 5300 (Carlo Erba Instruments, Italy).

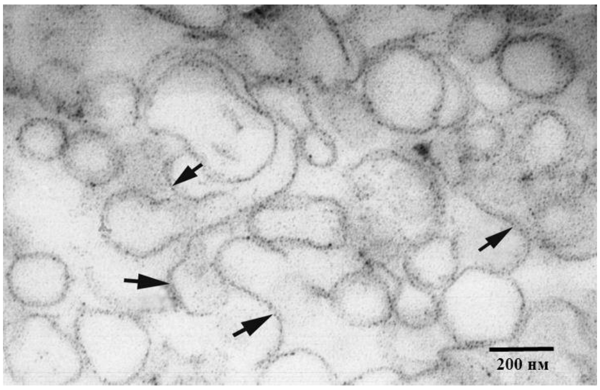

Fig. 8. Rafts obtained from roots of pea 6-day old seedlings (electron transmission microscopy). Arrows indicate rafts

It was shown that lipid rafts from the root plasmalemma of pea seedlings grown in the stationary conditions and under clinorotation have the appearance of thin tapes of 80–100 nm in length (Fig. 8), they were similar to those in other plant species on the structure and size, and also were enriched on cholesterol and saturated fatty acids.

Under clinorotation, the content of arachidonob acid significantly increased in rafts while the content of linole decreased, the percentage of cholesterol in lipid rafts increased 7 times in comparison with control, It is of interest that a significant increase in content of cholesterol and some saturated fatty acids under clinorotation was determined in the CM microdomains, while the CM fluidity reached the control level (Fig. 9).

A character of changes in the lipid content of rafts clearly indicate an increase in their density. Based on these firstly obtained data, it is proposed to increase attention to study the impact of microgravity on the behavior of rafts as they contain the protein complexes responsible for perception and transmission of external signals, activity of membrane-gound enzymes, in particular

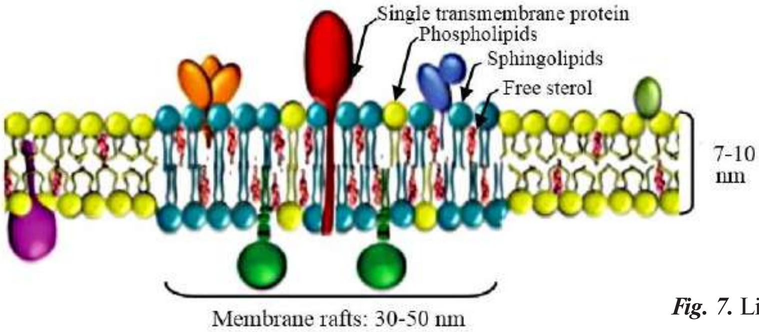

Fig. 7. Lipid rafts (Mongrand et al., 2010)

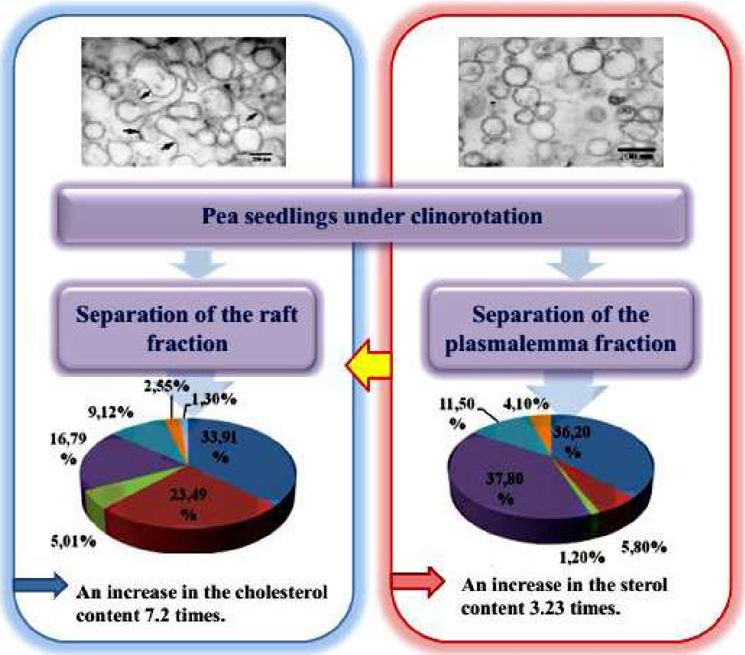

Fig. 9. The main fatty acids with the content more than 1 % in the fractions of rafts and CM from roots of pea seedlings grown under clinorotation are presented. Saturated fatty acids in the raft fraction: 33.91 % – palmitic, 23.49 % – stearic, 5.01 % -arachidic; unsaturated fatty acids: 16.79 % – arachidonic, 9.12 % –linoleic, 2.55 % – oleic, 1.3 % –linoelaidic. Saturated fatty acids in the CM fraction: 32.6 % – palmitic, 5.8 % –stearic, 1.2 % – myristic; unsaturated fatty acids: 37.80 % – linoleic, 11.50 % – oleic, 4.10 % – linoelaidic

phospholipase C and H+ATPase, vesicular transport, protection from stress. Further understanding the gravisensitivity of basic cell processes and mechanisms of plant adaptation to microgravity is necessary for working out the technologies of the autotrophic chain in the Bioregenerative Life Support Systems and its reliability. (*M.G. Kholodny Institute of Botany of the National Academy of Sciences of Ukraine, E. Kordyum, I. Bulavin*)

Expression of the myb3r3 transcriptional factor root cells of *Arabidopsis thaliana* under clinorotation

Future long-term space expeditions require a huge amount of metabolic resources – water, food, oxygen, requiring special conditions and equipment, and they are too heavy for existing missiles. In addition, such life support systems can not exist without a high level of circulation. A comparison of the results of protein study and gene's transcription in plants showed a positive, some limited interaction between the regulation of protein synthesis and gene expression in general plant reactions under space flight conditions (Kordyum, Chapman, 2017). The coordinated regulation of the interaction of plant cells is carried out by the synthesis of special hormones (cytokinin and auxin) which cause the signaling cascade in the cells (Herranz, Medina, 2014). In the event that the signal leads to changes in the level of gene's expression, the transcript factor (TF) is often the end point of the cascade. TF - is one of the groups of proteins that provides for the reading and interpretation of genetic information. They bind DNA and promote the initiation of a program to increase or decrease transcription of the gene. Thus, they are need for the normal functioning of the body at all levels. One of the most numerous types of TF plants is MYB-proteins (MYB-myeloblastosis). This family of TF contains proteins that controling such processes as root development, patterning of the leaf, formation of trichomes, cell cycle, circadian rhythms, transmission of a photochromic signal, etc. We analyzed the expression of TF MYB3R3 in *Arabidopsis thaliana* root cells in a stationary meristem of four-day seedlings and in the rudiments of the lateral roots (Fig. 10).

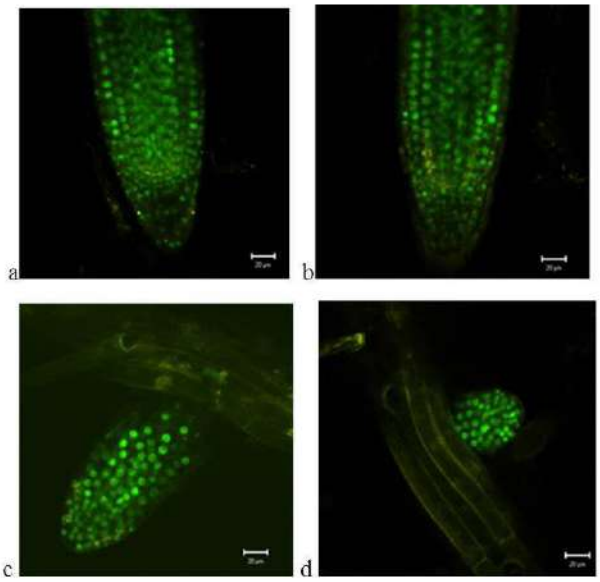

Fig. 10. Expression of MYB3R3 in the roots of 4 daily seedlings and in the *Arabidopsis thaliana* lateral roots rudiments (*a*, *c* – control, *b*, *d* – clinorotation)

In conditions of clinorotation observed a loss of TF expression in comparison with control, which may be due to a decrease in the activity of the cell cycle and growth of the root. At the same time, in the rudiments of the lateral roots, when there is a peak of proliferative activity in the places of the formation of lateral roots, the expression of TF is also at a high level in both control and clinorotation. The difference in the size of the lateral roots of control and experiment is due to a later onset of growth of the lateral roots in the clinorotation conditions, which is confirmed by the earlier known data on the reduction of growth parameters in the conditions of the changed gravity (Artemenko, 2015).

The obtained data on the influence of clinorotation on the process and duration of the cell cycle phases, as well as subsequent changes in the growth and development of plants in these conditions, and are key in the development of onboard greenhouses and bioregenerative life support systems. Investigating the control of cell cycle events and the interaction between the molecular and cellular mechanisms of these processes is important for understanding undesirable changes in plant growth and development, since the quality and quantity of products that cosmonauts will use depend on it. (*M.G. Kholodnt Institute of Botany, National Academy of Sciences of Ukraine, O. Artemenko*)

Regulation of cortical microtubule organization by associated proteins in plant cells under clinorotation

We consider investigation of the cytoskeleton under simulated microgravity to be important for understanding plant growth regulation keeping in mind that removing of constant 1g might reveal the mechanisms of cytoskeletal structure arrangements. 2D clinorotation, where plant is not gravistimulated, but disorientated in relation to gravity vector and thus, does not sense direct impact of gravity vector is applied widely in this type of research (Kordyum, 1997).

Cortical MTs are known to be stabilized by numerous MT associated proteins which perform their function by influencing either polymerization of tubulin or stabilizing MT arrays as well as taking part in MT rearrangements. It is not excluded that such proteins' functioning is different in simulated microgravity due to affection by mechanical stress. *MAP65s* and CLASPs protein families are known to participate in induction of MT polimerization and assembly of cortical MTs. Basing on *MAP65-1* activity in bindling of antiparallel cortical MTs, activity of *MAP65-1* is suggested to be affected by simulated microgravity. Therefore, we find it necessary to check *MAP65-1* expression profile in *A. thaliana* seedlings exposed to slow clinorotation (2 rpm).

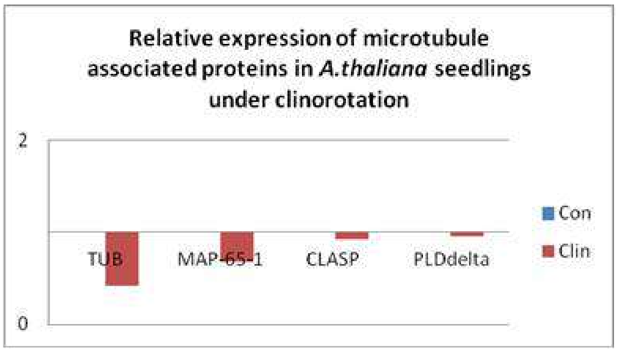

Fig. 11. Expression of *TUB*, *MAP65-1*, *CLASP* and *Phospholipase D delta* in *A. thaliana* seedlings under clinorotation (qPCR results)

Therefore, to add to the understanding of cMTs organization and regulation we investigated expression of *MAP65-1*, *CLASP* and *PLD*-delta in *A. thaliana* roots under clinorotation since above proteins stabilize cMTs and promote their interaction with plasma membrane, taking part in plant cell morphogenesis and growth. In order to decipher nature of cMT rearrangements, we have performed pharmacological studies with MT depolymerizing drug oryzalin which helps us to see how disruption of cMT affects root growth in simulated microgravity.

Our experiments have shown that expression of *TUB* was down-regulated under clinorotation (Fig. 11).

The same tendency for *TUB* was observed after oryzalin treatment in the control (Fig. 12) and under clinorotation (Fig. 13). This might indicate that decrease of *TUB* expression in simulated microgravity resulted in cMT distortion (as a consequence of partial remove of gravity force). Clinorotation might cause either chaotic reorganization of MT bundles or depolimerization of separate microtubules affecting proper cMT arrangement .

In our experiments, expression of *MAP65-1* was decreased under clinorotation (Fig. 11). In the control, depolimerization of MT activity by oryzalin, also caused decrease of *MAP65-1* expression (Fig. 12). *CLASP* and *PLD-delta* expression was shown almost not to be

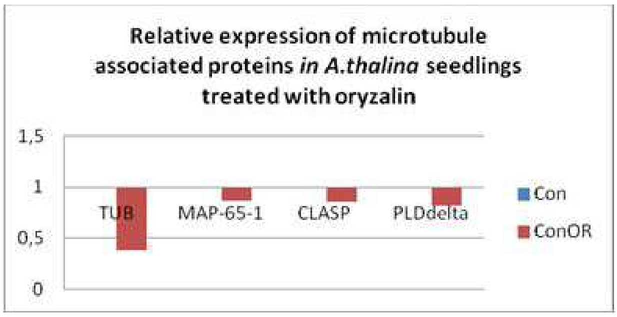

Fig. 12. Expression of *TUB*, *MAP65-1*, *CLASP* and *Phospholipase D delta* in *A. thaliana* seedlings treated with oryzalin (qPCR results)

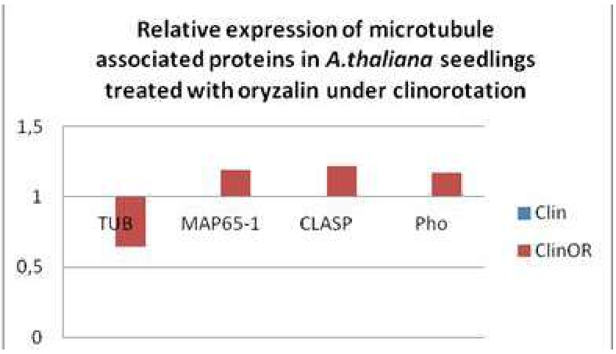

Fig. 13. Expression of *TUB*, *MAP65-1*, *CLASP* and *Phospholipase D delta* in *A. thaliana* seedlings treated with oryzalin under clinorotation (qPCR results)

affected by clinorotation (Fig. 11). In the control, disruption of MTs by oryzalin caused decreased expression of *CLASP* and *PLD-delta* as in the case of *TUB* and *MAP65-1* (Fig. 12). Contrary to *TUB*, under clinorotation, application of oryzalin resulted in increased expression of *MAP65-1*, *CLASP* and *PLD-delta* (Fig. 13).

To our mind, down regulation of *MAP65-1* expression under clinorotation happens probably due to cMT distortion and this shows dependence of *MAP65-1* activity upon cMTs state. Clinorotation does not impact *CLASP* and *PLD-delta* activity directly, but disruption of tubulin resulted in enhancement of *CLASP* and *PLDdelta* expression, thus, also showing its dependence upon MT state. In general, under clinorotation, all proteins: *MAP65-1*, *CLASP* and *PLD-delta* are suggested to stabilize distorted MT. It worth to note that *CLASP* and *PLD-delta* are activated only by clinorotation. Activities of *CLASP* and *MAP65-1* are known to be interconnected and both proteins stabilize MTs applying using different mechanisms in the control and under clinorotation.

Referring to its functions *MAP65-1* could keep MT bundling and antiparallel MT order preserving in this way proper arrangement of cortical MTs. Since *CLASP* stabilizes microtubule plus ends it might promote MT stabililty and functioning under clinorotation. *PLD-delta* activity also was shown to depend upon the state of MTs and is enhanced by clinorotation. Since *PLD-delta* is involved in MT attachment to plasma membrane it might preserve organization of cortical MTs and promote plasma membrane –cytoskeleton continuum under clinorotation.

To sum up, our experiments have shown dependence of MT associated proteins *MAP65-1*, *CLASP* and *PLD-delta* upon the state of microtubules. Application of oryzalin under clinorotation has revealed that this dependence for *CLASP* and *PLD-delta* is activated only in simulated microgravity. Under clinorotation, activity of all proteins is aimed at prevention of tubulin depolimerization and promotion of MT stabilization. But, the mechanisms of this process is different for each separate protein. Decreased expression of *TUB* also might explain retardation of plant root growth observed under clinorotation. Thus, analysis of *MAP65-1*, *CLASP* and *PLD-delta* functioning under clinorotation is likely to make a valuable contribution to understanding the fundamental principles of cMTs organization and regulation and their integration in cell elongation and plant growth. (*M.G. Kholodny Institute of Botany, National Academy of Sciences of Ukraine, G. Shevchenko*)

Microcosm is a perspective model for biological experiments at the nanosatellites

Nowadays the space biological experiments with plants may be only performed on the International Space Station, that very restricts their number necessary for understanding adaptive potential, reproduction and productivity of different plants, as well as the optimization and test of new larger space green houses.

We firstly propose the utilization of nanosatellites to perform biological investigations in space, get the actual proof of their efficiency for obtaining the new scientific knowledge (Brykov, 2017). The space experiment (SE) "Microcosm–M" a task of which is to elucidate the long-term influence of spaceflight factors on the ecological interaction of plants by both the visual observations of plant growth and development and using the sensors of photosynthesis and respiration parameters. It is planned to make the chamber for plant cultivation (hermoblock) and its testing on the nanosatellite PolyITAN-5-BioSat in space flight. Nanosatellites of the sees PolyITAN on the primary standards CubeSat have been worked out and made in the National Technical University of Ukraine "Igor Sikorsky Kyiv Polytechnic Institute". A PolyITAN-2-SAU is used in the Atmospheric International Research Mission on the project QB50 (Rassamakin et al., 2017). Perennial plants, including orchids, will be the main objects in the proposed SE. It was known that orchids well tolerate to microgravity (Cherevchenko et al., 1986) and they are able to grow in the hermetic conditions during long time (Fig. 14). Since a biosatellite does not return on Earth, all information on the SE state will be only obtained by telemetry.

Nowadays the proposed SE has no analogs and it will be the first attempt to use nanosatellites for carrying out a SE based on the technology of "microcosm". In future, nanosatellites may become the powerful tool for the realization

Fig. 14. Microcosms with orchids which grow in these conditions during 1.5 (*a*) and 13 (*b*) years in the M.M. Grishko National Botanical Garden

Fig. 15. The size of solid particles is 0.15–0.2 mm

Fig. 16. The size of solid particles is 1.5–2.0 mm

of programs on biology of plants in space. Microcosm is the closed artificial system capable to self-regulate the biosphere. Exposure of the "microcosm experiments" in space flight may be favorable for the development of new technologies of space plant cultivation, namely designing the stable exosystem to support plant communities on the extraterrestrial vehicles in the autonomous unmanned conditions. (*M.G. Cholodny Institute of Botany, National Academy of Sciences of Ukraine, National Technical University of Ukraine "Igor Sikorsky Kyiv Polytechnic Institute", H National Botanical Garden, National Academy of Sciences of Ukraine; V. Brykov, YE. Kovalenko, B. Ivanyzka*)

Formation of spiral constructions of solid fractions in the conditions of simulated microgrogrivity

The role of the root system of plants in the distribution of anions and cations in the volume of soil substitute in the presence of stochastic processes was analyzed. The role of simulated microgravity in the root system architectonics was determined, and the kinetics of fluid motion in fibrous substrates of different colors and different agrophysical parameters was investigated. Unfortunately, the problem of the orientation of the mass forces vector in time and space, which arise in weightlessness remain unclear, as well as the uncertainty of conditions on the boundary between the solid phase and the liquid. The presence of the effect of vibration on the free distribution of phases in a porous medium is well known; therefore, we investigated the features of distribution of solid particles of different sizes during rotation in horizontal and vertical projections in clinostat to find out the kinetics of convective fluid motion in model experiments.

For the first time, based on the dynamic and kinetic analysis, an analytical-geometric approach was demonstrated to determine the trajectory of the motion of particles in a limited volume of 0.5 dm^3 in simulated weightlessness. It is shown that the parameters of the spatial curve are related to the magnitude of the angle between the absolute speed of solid particles and the tangential speed of the clinostat rotation.

With a slow rotation of the clinostat (8 rpm), the solid particles move in a spiral trajectory counter clock-wise. According to the change in the step of a spiral twisting in space, and observation of the solid particles migration towards the center, it has been proved that the action of centrifugal forces weakens with time, and the effect of centripetal forces, which always have an advantage over the centrifugal, remains unchanged. In addition, the obtained dependence was traced to particles of 0.15–0.2 mm and 1.5–2.0 mm in diameter (Fig. 15, Fig. 16). The most acceptable explanation for the motion of particles in a limited volume is Hopf's theory, the scientist found a way to fill the entire space with circles. According to his theory, when applying the well-known geography and geometry of the stereographic projection, when the motion of particles is displayed, it is possible to keep the angles between the straight lines (conformal transformation), and the circles to move into other circles or straight lines (circles of an infinite radius); therefore, according to our results, the entire space is filled with nested one in one tori. As well as the set of points fill entire circle of latitude, and the set of such rings, meshed one after another, completely covers the surface of the corresponding Torus (Fig. 17).

The obtained results concerning the features of the trajectory of solid particles in the conditions of clinostat rotation are of great importance for the study of the kinetics of the solution motion in a porous inert medium and for the determination of physical phenomena occurring on the boundary between free distribution of solid, liquid and gas phases. (*M.M. Gryshko National Botanical Garden, National Academy of Sciences of Ukraine, N. Zaimenko*)

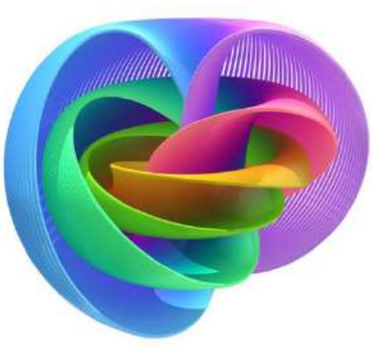

Fig. 17. Hopf Fibration by Niles Johnson (2012)

Aftereffect of long-term space flight on physiological and biochemical processes and resistance. To pathogens of *lycopersicon esculentum* Mill plants

Tomatoes (Lycopersicon esculentum Mill.) are one of the most popular vegetables in Ukraine, they are avaluable to product therapeutic and dietetic foods, as they contain a significant amount of nutrients and essential to the human body minerals and vitamins. In addition, tomatoes are the powerful antioxidants due to the content of carotenoids – lycopene and β-carotene in fruits. Therefore, tomato plants may be successfully used as a food for astronauts oin long-term space flights.

We studied of aftereffect of long-term space flight on seeds of the tomato variety "Mir-1", which were on board the orbital station "Mir" during 6 years. After long-term storage on earth, seeds were sown in laboratory in 2011 year and obtained seedlings grew in the field conditions of the Kyiv and Poltava regions. We have previously shown in 2011–2012 years that plants from "space" seeds increased the resistance to PVY and PVM viruses against a natural infectious background. We continued the investigation in 2013–2017 years, because plants grew constantly in the field, there was a high probability of their injury with pathogens of different nature, including viruses. It was known the concentration of carotene and lycopene decreased in tomatoes affected by viruses (Raithak, 2012). In addition, symptoms of viral infection were observed on control plants were observed: in 2011, leaf twisting and even mosaics in 2012. These results were confirmed in 2013, no symptoms were observed on the plants from "space" seeds, while potato virus Y (method RT-PCR) and symptoms of leaf twisting and mosaic were displayed on control plants.

To determine the photosynthetic pigments, leaf samples were collected from bearing plants. It should be emphasized that fruits ripened earlier in 8 days and and mass flowering – on 5 days in "space" plants in comparison with control ones. In "space" plants, the content of photosynthetic pigments exceeded that in control plants: chlorophyll *a* –1.3 times, chlorophyll *b* – 1.5 times, the amount of carotenoids was higher 1.2 times. A ratio of chlorophyll/carotenoids was higher in "space" plants 5.8, it was 5.1 in control plants. A ratio of chlorophyll *a* and *b* did not change. The content of dry substances in the fruits of "space" plants exceeded that in control plants 0.6 %, the total quantity of sugar 0.67 % and phenolic compounds 14 mg % ($p \leq 0.01$). The lycopene content also increased in "space" plants on 162 mg / 100 g, the β-carotene – on 45 mg / 100 g.

The resistance to diseases, including late blight (on a SEV scale) according the data of the Ustymivsky Research Station in Poltava region. In 2014 and 2015 was evaluated 9 points of control plants and 5 and 7 in "space" 2015 year was favorable for growth and development of vegetables, especially tomatoes, which showed a high yield. Severe symptoms of viral infections in plants in 2017 was not observed.

In 2017, we observed, as in previous years, the earlier attainment of fruits in the "space" plants (Fig. 18, *a*, *b*) compared to the control ones. Light leaf twisting and mosaic were observed on control plants (Fig. 18, *c*).

The obtained data testify the absence of the harmful influence of long-term orbital flight on *L. esculentum* seeds and the possibility of obtaining a quality crop of tomatoes grown from "space" seeds on Earth (*Taras Shevchenko Kyiv National University, L. Mischenko*).

Fig. 18. Tomato plants of the Mir-1 variety: *a* – plants of the fifth reproduction of seeds exposed in space flight; *b* – plants of the first reproduction of seeds exposed in space flight; *c* – plants from steady control seeds. 2017, Poltava region

NEUROTOXICITY ASSESSMENT OF INORGANIC ANALOGUE OF MARTIAN DUST ENRICHED WITH THE NOVEL CARBON NANOPARTICLES

N. Pozdnyakova, T. Borisova

O.V. Palladin Institute of Biochemistry of NAS of Ukraine (IBCH NASU)

A comprehensive assessment of risks is of great importance in the planning long-term manned space missions, in particular the missions to Mars, that include access to open space. Microgravity provokes structural changes in the brain during long duration spaceflight [1]. One of the possible causes of brain impairment under these conditions may be toxicity of planetary and interstellar dust, the composition and properties of which, as well as the impact on human health, in particular, neurotoxicity, are not sufficiently investigated. It is known that particles of lunar dust are sorted into spacesuits and fall into space stations, resulting in irritation of the eyes, respiratory tract and skin of astronauts during several missions of Apollo [2–6].

Meteorites and interstellar dust contain from 2 to 10 % carbon in various physical forms, including polycyclic aromatic hydrocarbons [7]. The analysis of carbon from the Tissint Martian meteorite provided evidence of the existence of organic matter encapsulated in the interior gaps of the meteorite. [8]. Hence, meteorites and interstellar dust may contain nano-sized particles of carbon with different structure and surface charge.

The neurotoxic action of nanoparticles is realized due to their ability to pass through the epithelium of the respiratory and the gastrointestinal tracts, and then through the blood-brain barrier to the brain [9, 10].

Glutamate and γ-aminobutyric acid (GABA) are the main excitatory and inhibitory neurotransmitters involved in the most aspects of mammalian brain functioning. The neurotransmission is initiated by the presynaptic plasma membrane depolarization and leads to the neurotransmitter release into the synaptic cleft, their interaction with the postsynaptic membrane receptors and the activation of the signaling pathways. Impairment of glutamate and GABA transport, an increase of the extracellular level of both neurotransmitters causes misbalance of excitatory/inhibitory signals, which is a characteristic feature of the pathogenesis of almost neurological diseases [11–13]. In this context, nanoscale particles as dust components can reach the central nervous system and influence the key characteristics of the neurotransmission that in turn can result in brain dysfunctions.

Carbon nanoparticles (CNP) represent a recently discovered class of nanosized compounds ranging in size from 1 to 6 nm [14–16]. It has been found that they can be absorbed by cells, probably by endocytosis [17].

Thus, the purpose of the study was to analyze the influence of the inorganic analogue of Martian dust enriched with the novel carbon nanoparticles (CNP-MD) on the key characteristics of glutamatergical and GABA-ergic neurotransmission, namely: 1) the potential of the plasma membrane of isolated rat brain nerve terminals (synaptosomes); 2) the extracellular level of L-[^{14}C]glutamate and [^{3}H]GABA.

In this study, was used an inorganic Martian dust analogue (MD) derived from volcanic ash (JSC, Mars-1A, Orbitec Orbital Technologies Corporation, Madison, Wisconsin, USA) and carbon nanoparticles (CNP) produced by combustion of carbohydrates, namely cysteine, using microwave heating [18] and provided by Prof. O.P. Demchenko and M. Dekalyuk. Two preparations with different concentrations were received: 1) 2.0 mg/ml and a weight ratio of 1 : 1 of the carboxylic and inorganic component (1 : 1 CNP-MD); 2) 0.2 mg/ml and a weight ratio of 1 : 10 carbon and inorganic component (CNP-MD 1 : 10).

Effect of Martian dust analogue on the membrane potential of rat brain nerve terminals

The potential of the plasma membrane of nerve terminals is one of the key parameter that determines the normal transporter mediated uptake, extracellular level and release of neurotransmitters. The membrane potential of synaptosomes was measured using a potentials-sensitive fluorescence dye rhodamine 6G (Rh 6G).

No significant changes were found in the emission spectrum of rhodamine 6G in response to the addition maximal concentrations of MD (2.0 mg/ml), CNP (2.0 mg/ml) and CNP-MD (1 : 1). However, a slight fluorescence signal quenching was observed (Fig. 1, *a*).

The addition of synaptosomes to the medium containing the dye rhodamine 6G was accompanied by a partial decrease in fluorescence due to its binding to the plasma membrane. (Fig. 1, *b*). The addition of the CNP-MD in the ratio of 1 : 10 did not affect the intensity of the fluorescence signal, but an increase in CNP content (1 : 1 ratio) resulted in an increase in the signal, indicating the depolarization of the plasma membrane (Fig. 1, *b*).

The addition of MD in a concentration of 2.0 mg/ml and CNP at a concentration of 0.2 mg/ml did not significantly affect the intensity of the fluorescence signal (Fig. 2, *c*) that indicated absence of depolarizing effect on the plasma membrane. Changes in the membrane potential have been reported only with an increase in the concentration of CNP up to 2.0 mg/ml. Nevertheless, no CNP-MD (1 : 1) nor CNP (2.0 mg/ml) did not affect the ability of synaptosomes to be depolarized in respond to the addition of high-KCl (Fig. 1, *b*, *c*).

Effects of CNP-MD on the ambient level of L-[^{14}C]glutamate and [^{3}H]GABA in the preparations of nerve terminals

The extracellular level of neurotransmitters is established as a balance between their transporter-mediated accumulation and tonic unstimulated release [11, 12]. Maintaining the proper balance of the intracellular/extracellular concentration of glutamate and GABA and their extracellular homeostasis in the central nervous system is important for the normal functioning of the brain. Disbalance leads to many neurological diseases.

In the next stage of the work, it was determined the effects of CNP-MD on the extracellular level of neurotransmitters after loading of synaptosomes with L-[^{14}C]glutamate or [^{3}H]GABA and their preliminary incubation for 5 min at 37 °C in a standard salt solution containing: 1) MD; 2) CNP; 3) CNP-MD.

As shown in Fig. 2, CNP-MD (1 : 1) caused a significant increase (more than twice) in the extracellular level of L-[^{14}C]glutamate in synaptosomal suspension. The extracellular level of L-[^{14}C]glutamate consisted of 0.193 ± 0.030 nmol × mg^{-1} of protein in the control and 0.587 ± 0.063 nmol × mg^{-1} of protein in the presence of CNP-MD (1 : 1) ($P < 0.001$, Student's t-test, $n = 6$). CNP added to synaptosomes at a concentration of 2.0 mg/ml also induced a significant increase in the extracellular level of L-[^{14}C]glutamate, which was equal to 0.555 ± 0.049 nmol × mg^{-1} of protein ($P < 0.001$). The MD itself did not affected this parameter, which was equal to 0.228 ± 0.040 nmol × mg^{-1} of protein. However, CNP-MD (1 : 10) or CNP at a concentration of 0.2 mg/ml did not significantly change the extracellular level of L-[^{14}C]glutamate, which

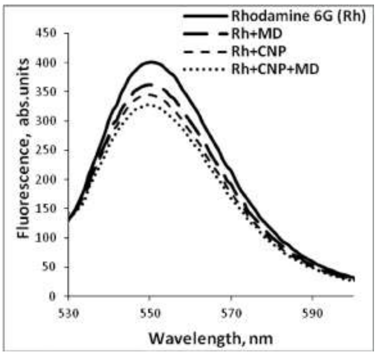

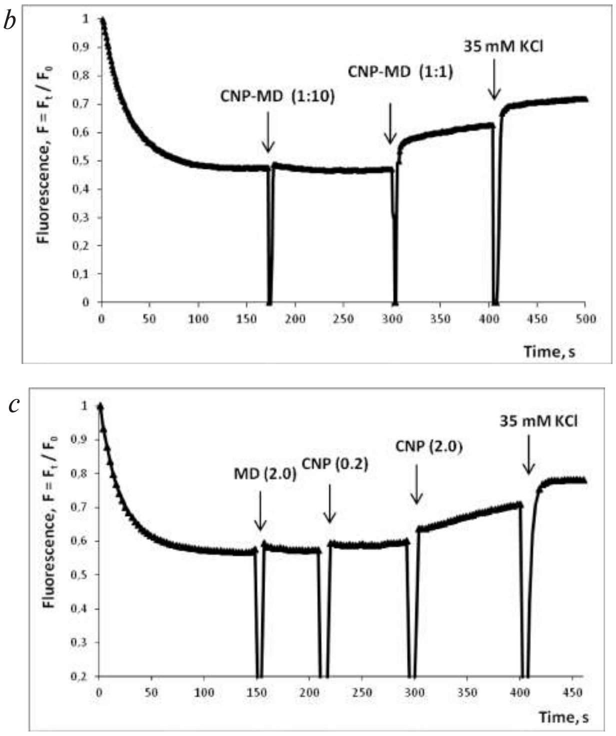

Fig. 1. Fluorescence emission spectra of rhodamine 6G (0.5 μM) in the standard salt solution before and after application of MD (2.0 mg/ml), CNP (2.0 mg/ml), CNP-MD (1 : 1) (*a*); *b* – the effects of CNP-MD (1 : 10) and CNP-MD (1 : 1) on the membrane potential of synaptosomes: the suspension of synaptosomes was equilibrated with potential-sensitive dye rhodamine 6G (0.5 μM), when the steady level of the dye fluorescence had been reached, the CNP-MD (1 : 10) and CNP-MD (1 : 1) were added to synaptosomes (marked by arrows); *c* – dose-dependent effect of CNP on the membrane potential of synaptosomes. When the steady level of the dye fluorescence had been reached, the MD (2.0 mg/ml), CNP (0.2 mg/ml) and CNP (2.0 mg/ml) were added to synaptosomes (marked by arrows). Trace represents four experiments performed with different synaptosome preparations

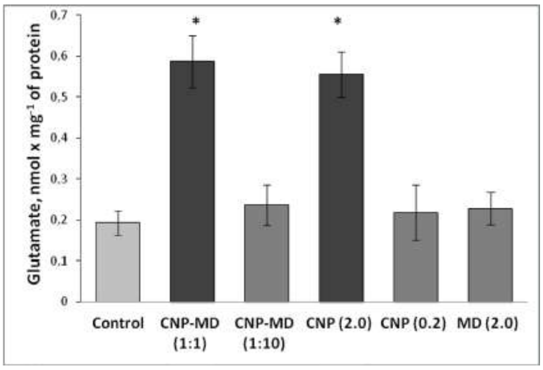

Fig. 2. Extracellular level of L-[^{14}C]glutamate in synaptosomal suspension after preliminary incubation with analogue of Martian dust enriched by carbon nanoparticles (CNP-MD) in ratio 1:1 or 1:10; carbon nanoparticles (CNP) at a concentration of 2.0 mg/ml or 0.2 mg/ml; and an analogue of Martian dust (MD) at a concentration of 2.0 mg/ml; * – $P < 0.001$ compared to control

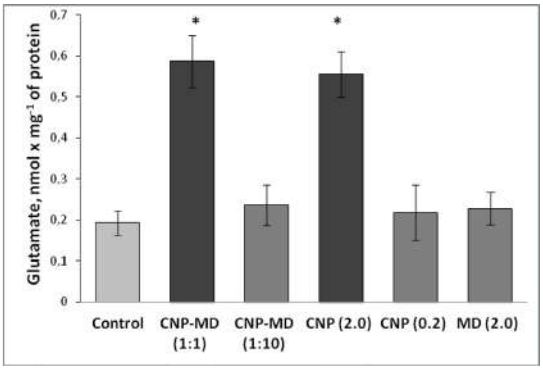

Fig. 3. Extracellular level of [^{3}H]GABA in synaptosomal suspension after preliminary incubation with analogue of Martian dust enriched by carbon nanoparticles (CNP-MD) in ratio 1:1 or 1:10; carbon nanoparticles (CNP) at a concentration of 2.0 mg/ml or 0.2 mg/ml; and an analogue of Martian dust (MD) at a concentration of 2.0 mg/ml; * – $P < 0.05$ compared to control

consisted of 0.236 ± 0.049 nmol×mg^{-1} protein and 0.218 ± 0.067 nmol×mg^{-1} of the protein, respectively.

Further studies have shown that (similarly with the experiments with L-[^{14}C]glutamate) CNP-MD (1:1) and CNP (2.0 mg/ml) significantly increased (by 70%) the extracellular level of [^{3}H]GABA in synaptosomal suspension, which was equal to 133.67 ± 8.53 pmol×mg^{-1} of protein in the control, 229.34 ± 18.14 pmol×mg^{-1} of protein ($P < 0.05$, Student's t-test, $n = 6$) in the presence of CNP-MD (1:1) and 232.48 ± 17.84 pmol×mg^{-1} of protein ($P < 0.05$) in the presence of CNP (2.0 mg/ml). However, CNP-MD (1:10) and CNP (0.2 mg/ml) were not effective and did not alter the extracellular level of [^{3}H]GABA in synaptosomal suspension, which consisted of 152.26 ± 9.68 pmol×mg^{-1} of protein and 153.94 ± 16.38 pmol×mg^{-1} of protein, respectively. MD (2.0 mg/ml) did not affect the extracellular level of [^{3}H]GABA in synaptosomal suspension, which was equal to 145.17 ± 14.13 pmol×mg^{-1} of protein (Fig. 3).

So, the extracellular levels of L-[^{14}C]glutamate and [^{3}H]GABA were significantly increased after CNP-MD administration at a 1:1 ratio that was associated presumably with CNP influence at a concentration of 2.0 mg/ml.

Thus, the neurotoxicity assessment of inorganic analogue of Martian dust with different content of carbon nanoparticles was performed. An increase in the content of the carbon component in the CNP-MD was accompanied by the depolarization of the plasma membrane and an increase in extracellular level of the neurotransmitters L-[^{14}C]glutamate and [^{3}H]GABA in the nerve terminals. Therefore, the neurotoxic effect of CNP-MD is developed exclusively due to CNP activity but not due to action of its inorganic component. A decrease in the CNP content in CNP-MD reduces its neurotoxicity.

Continuation of comprehensive and detailed studies of the Martian dust analogue and its component effects allows developing strategies and discovering new means of elimination or reduction of neurotoxic risks under conditions of long-term space missions.

REFERENCES

1. *Danbolt N.C.* Glutamate uptake // Prog. Neurobiol. – 2001. – V. 1. – P. 1–105.

2. *Borisova T., Krisanova N., Sivko R., Borysov A.* Cholesterol depletion attenuates tonic release but increases the ambient level of glutamate in rat brain synaptosomes // Neurochem. Int. – 2010. – V. 3. – P. 466–478.

3. *Borisova T., Nazarova A., Dekaliuk M. et al.* Neuromodulatory properties of fluorescent carbon dots: effect on exocytotic release, uptake and ambient level of glutamate and gaba in brain nerve terminals // Int. J. Biochem. Cell Biol. – 2015. – V. 59. – P. 203–215.

4. *Dorcéna C.J., Olesik K.M., Wetta O.G., Winter J.O.* Characterization and toxicity of carbon dot-poly(lactic-co-glycolic acid) nanocomposites for biomedical imaging // Nano Life. –2013. – V. 1. – P. 1340002.

5. *Esteves da Silva J.C.G., Gonçalves H.M.R.* Analytical and bioanalytical applications of carbon dots // TrAC Trends Anal. Chem. – 2011. – V. 8. – P. 1327–1336.

6. *Li H., Kang Z., Liu Y. et al.* Carbon nanodots: synthesis, properties and applications // J. Mater. Chem. – 2012. – V. 46. – P. 24230.

7. *Wang X., Qu K., Xu B. et al.* Microwave assisted one-step green synthesis of cell-permeable multicolor photoluminescent carbon dots without surface passivation reagents // J. Mater. Chem. – 2011. – V. 8. – P. 2445.

8. *Demchenko A.P., Dekaliuk M.O.* Novel fluorescent carbonic nanomaterials for sensing and imaging // Methods Appl. Fluoresc. – 2013. – V. 4: https://doi.org/10.1088/2050-6120/1/4/042001.

INVESTIGATION OF PLANT CELL AND TISSUE ADAPTIVE MECHANISMS TO MODIFIED MICROGRAVITY

**O. Kravets, A. Yemets, I. Horyunova, S. Plokhovska, V. Olenieva,
D. Lytvyn, S. Spivak, Ya. Blume**

Institute of Food Biotechnology and Genomics of NAS of Ukraine (IFBG NASU)

It is shown that under microgravity conditions due to the liberation from limiting gravity plants exhibit so-called automorphogenesis, one of the manifestations of that is stimulation of growth and elongation of the stem. The basis of automorphogenesis consists of rearrangements of apical meristem structural-functional organization, in particular the changes in biogenesis of the cell wall components. The structural changes taking place in the meristems reflect the events at the regulatory level: via signaling, restructuring of a cytoskeleton, proliferation and differentiation of cells, trophic supply of meristems [1–6]. However, under prolonged clinorotation the development of adaptive process can be traced, namely: modification of the metabolism of phytohormones and lipids, the alterations in synthesis of cell wall components and gene expression, encoding cytoskeleton proteins, development of autophagy and regulation of cell division [1–3, 6–9]. As shown, the microtubules as a component of the cytoskeleton are involved in the induction of autophagy [3, 6, 9–12].

There are methodological problems in study of microgravity such as the reproducibility of the results, the effect of seasonality, etc., indicating the influence of other factors and/or changes in the regulatory relationships relevant for adaptation. Microgravity like other stressors changes structure and orientation of microtubules and microfilaments, and thus affects cell and tissue architecture, on different types of cellular mobility, developing of programmed cell death (PCD) and cell-to-cell interactions [1–3, 6, 9, 12]. It is shown an important role of signaling with the participation of secondary messengers that transmits sensory information through these subcellular structures and it triggers various adaptive processes in the cells in response to changes in gravity by inducing the response at the genetic level [3, 5, 7–8]. In particular, we have established changes in the expression levels of different genes of α-tubulin and protein genes of *atg* family involved in autophagy development due to the effects of various stress conditions of plant cultivation (including UV-B) [3, 6, 9–11]. Since various stressors cause changes in level expression of these genes and in certain conditions may lead to PCD, it is assumed that the mechanisms of adaptation of plants to microgravity are also realized through the development of stress-induced autophagy. That is why we believe that further studies are needed to address regulatory issues of plant morphogenesis and cellular and systemic polarity, which are coordinated by the signaling and signaling systems involved to the formation of the response to gravistimuli. To answer these questions it is necessary to study systematically plant morphogenesis at microgravity conditions of, as well as meristem gravity sensitivity in particular the passage of their cells throught the cell cycle and the role of the cytoskeleton in these processes as well as autophagy mechanisms.

For studies of plant morphogenesis under long-term clinorotation we have been investigation on bean plants (*Phaseolus vulgaris*) under horizontal clinorotation (4 rpm). These series of experiments allowed us to obtain a number of original results regarding the influence of microgravity on apical plant meristem at different stages of vegetative development.

Root system. The root system of the control plants in the process of vegetative development retains their shape: several major roots dominate simultaneously with formation of a significant number of active lateral roots (Fig. 1).

The conditions of prolonged clinorotation modify the development of the root system, with the type of development of the root system is often changed (Fig. 1). Under clinorotation for 10–14 days the development of the main root and biomass accumulation are inhibited. In the root system is predominantly formed adventitious roots, and lateral roots lose gravitropism. Over time the number of lateral roots decreases and the root system becomes more elongated (Fig. 1, *b–d*). After 3–5 weeks of clinorotating the root system extends due to the competitive growth of several apical branches of the main root.

Root apex. Root apex beans, by length 1–1.5 mm, has a typical vertical zoning (Fig. 2). The volumes of root meristem usually range from 5 to 15 thousand cells. The root meristem is characterized by significant heterogeneity and consists of numerous subpopulations of cells that differ in form, size, duration of cell cycle. The structural organization of the meristem and the order of the transition of cells to elongation under clinorotation are generally maintained. However much of the lateral roots remain short and mitotic inactive. Within the same root system the sizes of the meristem and the number of amiloplast in columella varies. With age of plants the number of amiloplasts in columella cells decreases (Fig. 2, *a–e*), then in three-week plants increases again which is possibly due to the transition of seedlings to autotrophic nutrition. In 7-day-old experimental plants deformations of columella cells, prolongation of cells along the axis, formation of cell clusters with amyloplasts placed in cells without a certain order, are observed.

Therefore the effects induced by clinorotation can be noted as the following:

- In experimental plants dominates the development of adventitious roots which wound the stem base and sometimes show disorientation, while the formation of lateral roots is mostly inhibited (Fig. 1, *a*).
- Although the growth of the primary root and the formation of lateral roots are inhibited, they generally retain a normal orientation relative to the stem (Fig. 1, *b*).
- With prolonged experiments the development of the root system varies but over time can be renewed. In most cases, the root system is more elongated compared to control, with the domination of one or more roots. Much of the lateral roots are short (Fig. 1, *b*, *c*).
- Under prolonged clinostating apical meristem of the root in many cases exceed the meristem of control plants in terms of size and mitotic activity, while the meristem of lateral roots is inferior to the same indicators.
- The size of the root cap is often increased and the shape of the columella cells is stretched along the axis of the root compared to control (Fig. 2, *d*, *e*).
- Amyloplasts of columella cells have a heterogeneous structure and size as well unorganized

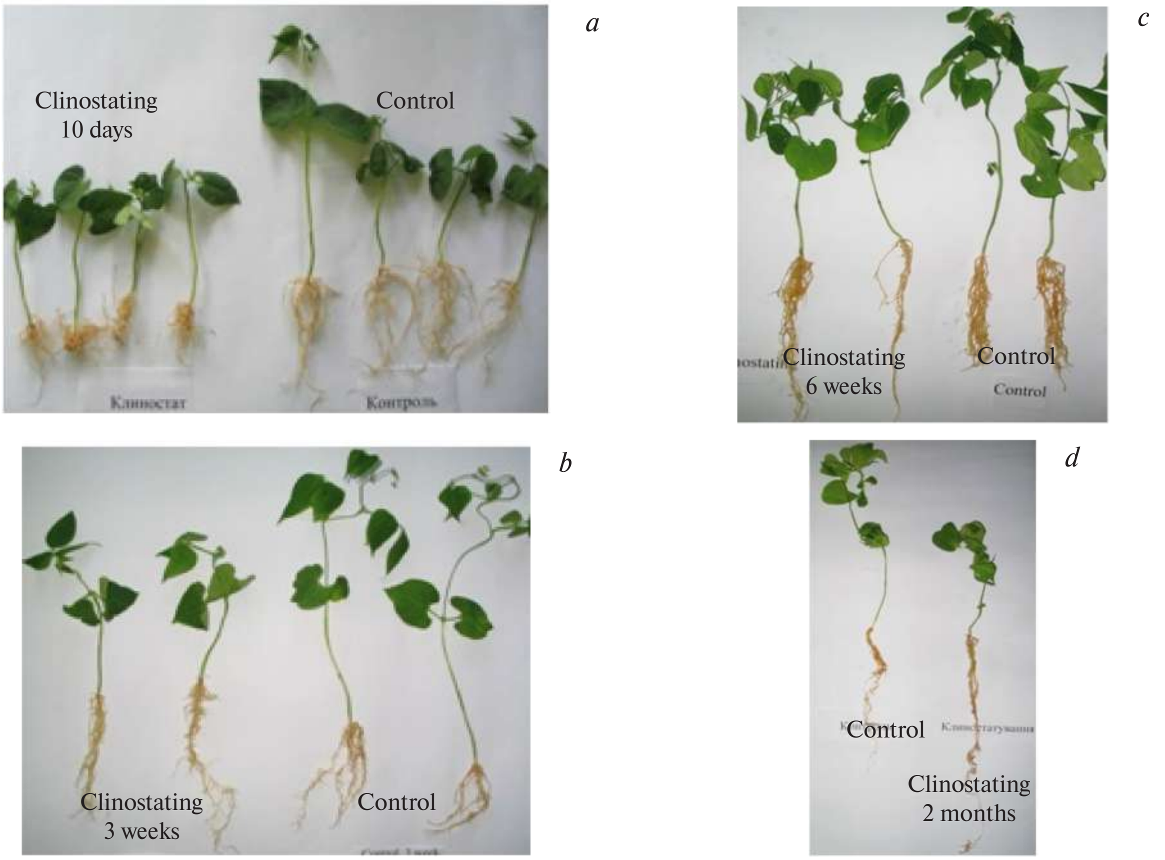

Fig. 1. Development of the seedling under clinostating: *a* – inhibition of plant growth and development, development of adventitious roots at the 10-day clinostating; *b* – renewal of root development in 3-week of clinostating; *c, d* – inhibition of the main and lateral root growth in experimental plants with long-term clinostating

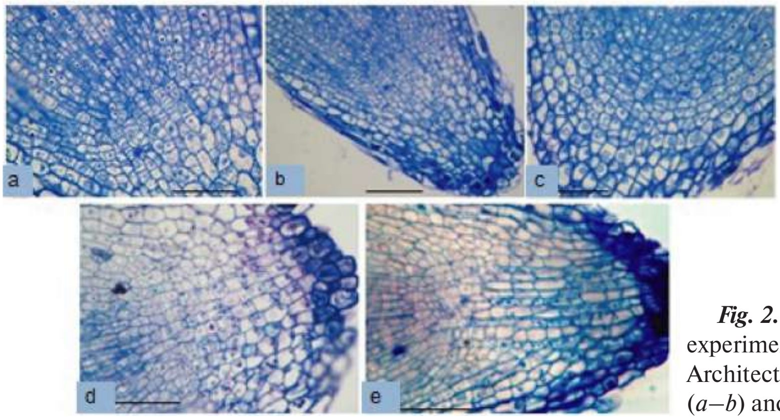

Fig. 2. Meristem of control (*a, g* – 7, *b* – 14 days) and experimental bean plants (*b* – 14, *d* – 7 days clinorotation). Architectonica of distal meristem and center of rest (CR) (*a–b*) and root cap (*d–e*). Bars represent 150 μm

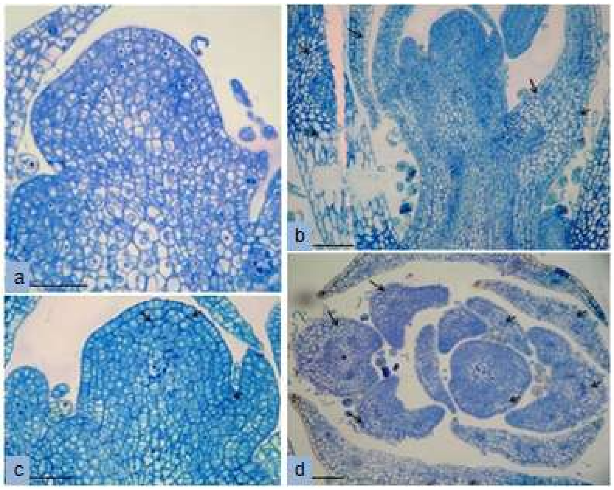

Fig. 3. Stem apex of beans on the 7th day of clinostating: *a* – control, *b–d* – experiment, early parenchymalization of cells (arrows), restructuring of intercellular area and cell walls (arrows) in experimental plants. Bars represent 150 μm

location, namely, around the nucleus or polar above the nucleus, whiles the nucleus of the columella cells is compressed to the shell and deformed.

Stem apex. The stem apex of the bean is characterized by a complex and dynamic structure, the shape and size of which depend on the stage of ontogenesis and the intensity of leaf initial formation (Fig. 3–5). The apex structure and the development of the main zones of stem meristem in control and experimental plants did not differ significantly (Fig. 3–5). The stem buds of the three-day seedlings, both in control and in experiment, consist of meristem and several pairs of leaf primordia and scales around it (Fig. 4). In the 7th day seedlings the first leaf and the initials of the second folded leaves and 4th leaf primordia are differentiated (Fig. 3, 4, *c*, *e*).

For two-three weeks a multi-tier structure with numerous leaves, axillary buds and consistently

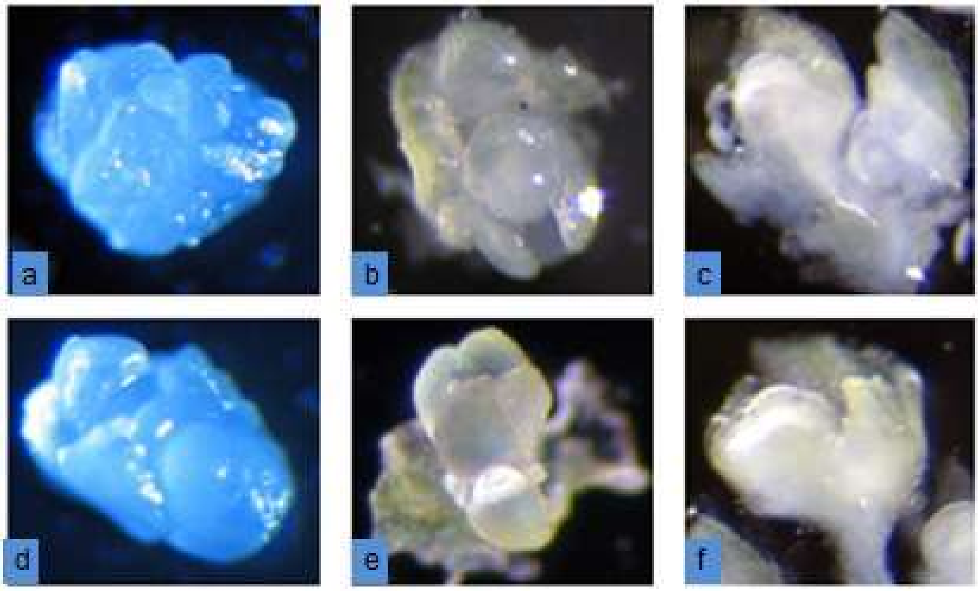

Fig. 4. Genesis of the apical stem buds in control (*a–c*) and experiment (*d–f*): *a*, *d* – apex of a three-day seedlings, *b*, *e* – apex of 7-day plants, *c*, *f* – apex of 21-day plant beans

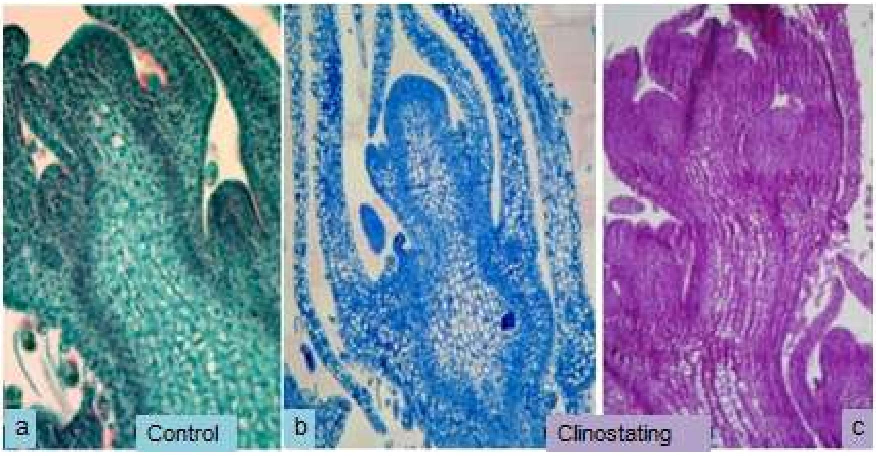

Fig. 5. Stem apex of beans on 14th (*a, b*) and 21 (*c*) days of clinostating: *a* – control, *b, c* – experiment, earlier differentiation and parenchymatization of the leaf and scale initial cells

growing interstitials (Fig. 4, 5) is reproduced at the stem apex. At 21st day stem buds undergo intense changes: the apex consist of a meristem with three primordia, under which lay three folded leaves. At the base of the first leaf, the axillary buds are formed (Fig. 4, *c*, *f*; Fig. 5). Under clinostating early cell parenchymalization especially lateral meristem in stem apex which gives rise to the primary crust, the prokambium, and the initials of the leaves and lateral organs is observed (Fig. 5, *a*–*c*). The consequence of such parenchymalization is to reduce the branching of the stem and leaf plate mass indicating certain problems in trophic nutrition of plants. Thus, in the structure of the stem apex under clinorotation can note the following features:

- Violation of the orientation of the growth of the stem apex, especially the lateral bads and shoots.
- Reducing the branching of the stem and mass of the leaf plate.
- Curves and changes in the cell walls and intercellular spaces in certain areas of stem meristem and leaf initials (Fig. 5, *a*, *c*).
- Earlier differentiation and parenchymatization of the leaf and scale initial cells (Fig. 5, *b*, *c*), indicating premature of cell differentiation and possibly aging of tissues.
- Changes in the orientation of trichom growth and the location of their amyloplasts.
- Reduction of dry biomass weight of plants compared to control.

Increasing of the plant biomass. In the most cases prolonged clinorotation inhibited the growth, development, increasing of biomass and the rate of ontogenesis of plants to a small extent. Usually the growth activity of the roots after some time is restored (Table). Inhibition of the growth activity of the roots is accompanied by a decrease in the zones of division and elongation as well the reduce of volume of root apexes of juvenile plants in general, indicating some problems in the competitive provision of assimilates. However over time changes in correlation relations and increasing of root growth activity are observed, indicating the formation of a regulatory connection and compensatory changes.

Effect of different duration clinorotation on the growth indexes of root apexes and plant beans

	Indexes of growth	Duration of experiment					
		7 days		14 days		21 days	
		Control	Clinost.	Control	Clinost.	Control	Clinost.
1	Mass of above-ground part of plant, g	0.15	0.155	0.115	0.096	0.11	0.105
2	Mass of root, g	0.025	0.031	0.044	0.032	0.034	0.029
3	Mass of whole plant, g	0.175	0.186	0.159	0.128	0.144	0.134
4	Length of division zone, mm	-	-	1.4	1.1	1.2	1.0
5	Length of elongation zone, mm	-	-	4.3	3.8	3.6	3.5
6	Volume of root meristem, mm^3	-	-	0.71	0.48	0.15	0.10

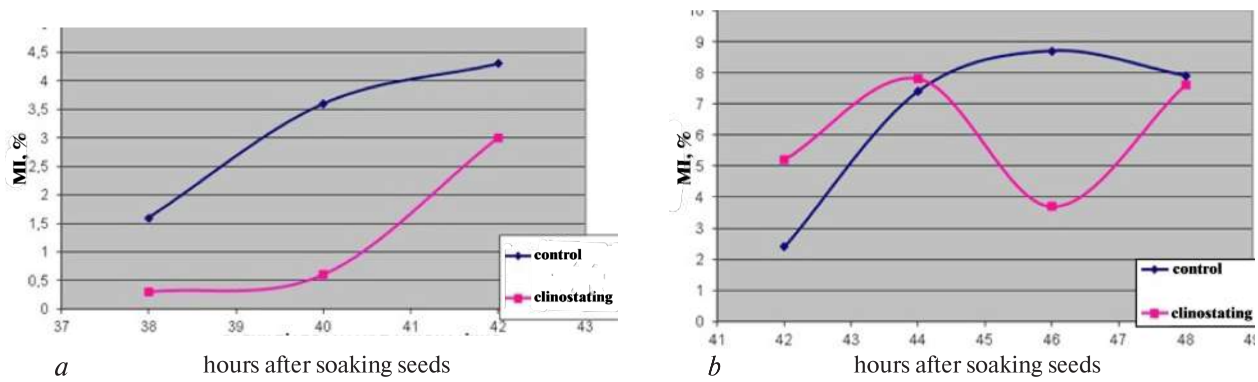

Fig. 6. Effect of clinorotation on kinetics of the first cell division of bean plant meristem (*a* – 38–42, *b* – 42–48 hours after soaking of seeds)

The conditions of clinorotation also influenced the development and size of the leaves. The mass of leaves (the weight of dry biomass) decreased by an average of 13 %. However, the asymmetry indexes of the leaf plate of beans do not increase.

Variations in proliferative pool and in size of the root apical meristem. Growth of the plant can be determined as a function of meristem cell proliferation. The proliferative pool, or growth fraction, is defined as the percentage of cells currently present in the mitotic cycle. Beans meristem is characterized by relatively low indicators of proliferative activity (Fig. 6). Under clinotating the passage of cells in the cycle and entry into mitosis were delayed. Into the first mitosis simultaneously entered about 8 % of meristem cells (Fig. 6, *a*). Mitotic index (MI) of further cellular cycles was close to the control level but was observed by fluctuations (Fig. 6, *b*). In the meristem of beans which consists of 6–7 subpopulations the duration of the cell cycle of the largest subpopulation corresponded to 20 h.

The linear sizes of the meristem and the total number of cells that make up it are also considered as a cell proliferation function. However in the root system of plants differentiate varies types of apexes, which shoud be taken into account in its overall assessment.

The volume of root apexes for 7–14 days usually decreases (Table). At 3–5 weeks the root system is lengthened due to the competitive growth of several apical branches of the root. The apexes of these roots are long and thin. At the same time the short and thickened roots which are characterized by functional load, but low proliferative activity are differentiated. Mitotic index of the cell meristem decreases to 0.5 %. The ratio of active and inactive meristems obviously determines the general growth activity of the root system.

The relationship between the level of attragation and the cytological parameters of root apexes. Paradoxically, the fraction of active roots in control 3-week plants was inferior to the experimental variant. Under clinostating the average size of meristem exceeded such an index in control more than twice. Thus the number of cells in the meristem was about 4000, compared with 1500–2000 cells in control [1]. In comparison with the control the attracting ability of 3-week-old plant roots in the conditions decreases by 1.6 times, and the percentage of radioactive tags decreases by 2.2 times. In the correlation relations the ratio of the root system mass to the overland part of the experimental plants exceeds the value of the control (0.22 vs. 0.15). On average, the mitotic activity of the root meristem under clinostating is 2.6 % compared with 2.35 % in control. Formation of larger by sizes and activity of root meristems can be regarded as a reaction to the decrease of the influx of assimilates and the formation of a regulatory connection in the system of «source-runoff», which reflects the mechanisms of adaptation to the conditions of microgravity.

Investigation of clinostating induced- oxidative stress and NO tread effect. Among potential modifiers and adapters of plant morphogenesis to microgravity conditions, particular attention is paid to nitrogen oxide (NO) – a universal signaling molecule involved in intracellular signaling with the participation of phytohormones and reactive oxygen species. We consider the effect of microgravity on the development of oxidative stress and its mediation with the participation of NO in plant cells [13]. Experiments have been performed using wild type *Arabidopsis thaliana* (Columbia 0) and an inactive mutant of MyO-inositol-1-phosphatase synthase (AtIPS1) transformed by the gene encoding the glutaradoxine chimeric gene and roGFP2 to determine dynamic oxidative-reduction changes by means of confocal laser microscopy. For this, *Arabidopsis* plants were pre-treated with NO nitrogen fertilizer (SNP) at a concentration of 10–100 μM, which should help to detect a reduced level of oxidative stress. In mutant plants, this protective effect of SNP is usually more expressed and manifested in tolerance to microgravity that we hope to confirm in tests for growth parameters [7]. Thus, preliminary treatment of wild-type plants with 10 μM of SNP before clinorotation can not significantly influenced by changes in the length of roots and hypocotyls. It is expected that the negative effects of microgravity exposure should be less pronounced for root and hypocotyls of mutants under the same conditions. Consequently, these data should indicate the relationship between NO signaling and the metabolism of myo-inositol when mediated by oxidative stress in plant cells caused by microgravity.

Role of cytoskeleton in response of cells to microgravity conditions. The cytoskeleton is one of the integral gravissensor cells whose components are involved in signaling, compartmentalization of metabolism, induction of autophagy, etc. The actin cytoskeleton is involved in the regulation of the lateral distribution of auxin, the gradient of which is formed due to the protein carriers of the PIN family. Microgravity alters not only the structure of microfilaments, but also the structure and the orientation of the microtubules and thus affects the cell and tissues architecture. Under microgravity conditions the level of expression of the α-, β- and γ-tubulin genes which are responsible for coding proteins forming the microtubules. The regulation of the level of expression of these genes is at the heart of the adaptive reorientation of microtubules during the stress factor. In particular, we have established alterations in the levels of expression of the various genes of α-tubulin and genes of the proteins of autophagy of the *atg* family under effects of various stressful conditions of plant cultivation. Whereas various stress factors cause nonspecific changes in the expression of these genes, we can assume that the mechanisms of adaptation of plants to microgravity also involve these mechanisms, for example, the development of stress-induced autophagy. Therefore, further in-depth study of autophagy in microgravity conditions is relevant because can identify new patterns in the interaction of the gene isotypes of α-tubulin and proteins *atg* (in particular, prote8s, atg8b, atg8g and atg8h) mediating the development and implementation of this adaptation process [2, 8–9]. Thus the cytoskeleton plays an important role in the transmission of signals under microgravity, but the molecular genetic mechanisms of this process remain weakly elucidated and require further research.

Microgravity-induced autophagy: transcriptome and biochemical analyses. The data obtained by us in the future clearly indicate that the conditions of microgravity, as well as some other stress factors, affect the induction and development of autophagy [6, 11]. In order to investigate the involvement of α-tubulin acetylation in the realization of microgravity-induced autophagy we used the *A. thaliana* line expressing autophagy-related protein 8h (atg8h)-GFP. To investigate the interrelation between microtubule functioning and autophagy, the profiles of different gene expression of α-tubulin and *atg8* is considered [12]. The result the dependence of expression of certain genes of *atg8* and α-tubulin during autophagy development under clinostating is revealed. Obviously, the processing of *atg8*, implying lipidation with phosphatidylethanolamine, effectively occurs in the conditions of microgravity. Respectively, increasing of α-tubulin acetylation level involved in the regulation of the interaction of microtubule process with proteins of the autophagy apparatus, can be detected the role of mentioned modification in the development of autophagy in plants for similar to regulatory mechanisms discovered in animals. Obtained results can allow predict the peculiarities of the mechanisms of autophagy functioning as a one of key elements of the development of adaptation of plants.

Conclusions. The conditions of prolonged clinorotation negatively affect the growth, development and accumulation of plant biomass, alter the proliferative and functional activity of meristems and primary tissues. Under these conditions the root system is most affected. Under clinorotation plants repeatedly changing the type of root system which was originally dominated by the formation of adventitious and lateral roots, and later – one or more dominant long roots. Indicated the slight inhibition of growth and branching of the stem, premature parenchymalization of its primary tissues and leaves. Over time in clinorotation the changes in correlationships between stems and roots occur, and at the cytological level - in increasing the size and proliferative activity of the root apical meristem which enhances its attracting ability compensating for the shortage of assimilate inflow. Thus, under prolonged clinostating the development of the adaptive process through the formation of regulatory relationships can be traced, resulting in renewal of growth activity of the roots and improving the nutrition of its tissues. Clinostating affects the organization components of the cytoskeleton – the microtubules and the actin microfiber – and their involvement in the transmission of intracellular signals important for maintaining structural polarity, compartmentalization and subcellular mobility of organelles, as well as in initiating autophagy induced by microgravity conditions.

The research was partially supported by the grant of the State Space Agency of Ukraine "Conducting scientific space research in the framework of the implementation of international programs. Development of scientific programs on promising biological space researches. Study of vegetable food at the conditions of space flight» № 0116U007975 (2016).

REFERENCES

1. *Kravets O.A., Berezhna V.V., Sakada V.I., Ovsyannikova L.G., Rashydov N.M., Yemets A.I., Blume Ya.B., Grodzinsky D.M.* Influence clinostating on structure, growth activity and attracting of apical meristem of bean plants / Abstracts of the 16th Ukrainan Conference on Space Research, August 22–27, 2016, Odesa, Ukraine. – P. 66 (in Ukrainian).

2. *Kravets O.A., Horyunova I.I., Plokhovskaya S.G., Olenieva V.D., Spivak S.I., Blume Ya.B., Yemets A.I.* Development of adaptive processes to conditions of modified gravitation at tissue and cellular levels in plants / Abstracts of the 17th Ukrainan Conference on Space Research, August 21–25, 2017, Odesa, Ukraine. – P. 57 (in Ukrainian).

3. *Blume Ya.B., Krasylenko Yu.A., Yemets A.I.* The role of plant cytoskeleton on phytohormone signaling under abiotic and biotic stresses. In book: Mechanism of Plant Hormone Signaling Under Stress: A Functional Genomic Frontier, Vol. 2, Ed. G. Pandey. – Wiley-Blackwell, 2017. – P. 127–185.

4. *Blume Ya.B., Kordyum Ye.L, Yemets A.I.* Achievements and prospects of plant space biology in Ukraine in the context of the priorities of European Research Programs / Abstracts of the 17th Ukrainan Conference on Space Research, August 21–25, 2017, Odesa, Ukraine. – P. 60. – ISSN 2309-2130 (in Ukrainian).

5. *Krasylenko Yu.A., Yemets A.I., Blume Ya.B.* Cell mechanisms of nitric oxide signaling in plants under abiotic stress conditions / In book: Mechanism of Plant Hormone Signaling Under Stress: A Functional Genomic Frontier, Vol. 1, Ed. G. Pandey. – Wiley-Blackwell, 2017. – P. 371–398. DOI: 10.1002/9781118889022.ch15.

6. *Lytvyn D.I., Blume Ya.B.* Microtubular cytoskeleton in autophagy and programmed cell death development in plants. In book: Programmed Cell Death in Plants and Animals, Ed. J. Rice, Nova Science Publishers: New York, 2016. – P. 1–26.

7. *Lytvyn D., Kravets E., Yemets A., Blume Ya.* Clinorotation induced oxidative stress and protective effects of NO under myo-inositol-deficient background in Arabidopsis / Abstracts of the 16th Ukrainan Conference on Space Research, August 22–27, 2016, Odesa, Ukraine. – P. 52. – ISSN 2309-2130.

8. *Lytvyn D., Fedyna V., Yemets A., Blume Ya.* Investigation of microgravity-induced autophagy process as a key element of plant development and growth in space conditions: transcriptome and biochemical analyses. / Abstracts of the 16th Ukrainan Conference on Space Research, August 22–27, 2016, Odesa, Ukraine. – P. 51. – ISSN 2309-2130.

9. *Olenieva V., Lytvyn D., Yemets A., Bergounioux C., Blume Ya.* Tubulin acetylation accompanies autophagy development induced by different abiotic stimuli in Arabidopsis thaliana // Cell Biology International. – 2017. DOI: 10.1002/cbin.10842.

10. *Olenieva V.D., Lytvyn D.I., Yemets A.I., Blume Ya.B.* Effect of fasting, osmotic and salt stress on the gene transcriptional profiles of major proteins involved in the development of autophagy with the participation of microtubules // Bulletin of Ukrainian Society Geneticists and Breeders. – 2018. – V. 16 (2). – P. 174–180 (in Ukrainian).

11. *Olenieva V.D., Lytvyn D.I., Yemets A.I., Blume Ya.B.* Effect of UV-B on the transcriptional profiles of genes of major proteins involved in the development of autophagy with the participation of microtubules // NASU Reports. – 2018. – No. 1. – P. 100–108. Available at: https://doi.org/10.15407/dopovidi2018.01.100. (in Ukrainian).

12. *Fedyna V.I., Lytyin D.I., Yemets A.I., Blume Ya.B.* Implementation of stress-induced autophagy in plants involving microtubules // Molecular and Applied Genetics. – 2017. – V. 22. – P. 52–61. (in Russian).

13. *Lytvyn D.I., Raynaud C., Yemets A.I., Bergounioux C., Blume Ya.B.* Involvement of inositol biosynthesis and nitric oxide in the mediation of UV-B induced oxidative stress // Frontiers in Plant Science. – 2016. – V. 7. DOI: 10.3389/fpls.2016.00430.

DEEP LEARNING APPROACH FOR CROP MAPPING ON BIG DATA

N. Kussul[1,2], A. Shelestov[2,1], M. Lavreniuk[1,2], B. Yailymov[1], A. Kolotii[1,2], H. Yailymova[1,3],
S. Skakun[4], L. Shumilo[1,2]

[1] Space Research Institute of NAS of Ukraine and SSA of Ukraine (SRI NASU-SSAU)

[2] National Technical University of Ukraine «Kyiv Polytechnic Institute» (NTUU «KPI»)

[3] Taras Shevchenko National University of Kyiv (KNU)

[4] University of Maryland, College Park, MD, USA

The last several years and onwards could be called the years of Big Free Data in domain of Remote Sensing. During the 2013–2016 period, several optical and synthetic aperture radar (SAR) remote sensing satellites were launched with high spatial resolution (10–30 m), in particular Sentinel-1A/B and Sentinel-2A within the European Copernicus program [1]. These datasets are freely available on operational basis. This opens unprecedented opportunities for a wide range of pre-operational and operational applications in the environment and agricultural domains taking advantage of high temporal and spatial resolution datasets and advances in the multi-sources data fusion techniques [2–4]. Due to clouds and shadows, the amount of available optical data over the region of interest is limited. SAR Sentinel-1 (both A and B) data are weather independent and new opportunities for crop classification have opened.

Crop mapping based on high resolution satellite data is a very important component for solving various applied problems, in particular crop area estimation [4], yield forecasting [5] and drought risk quantification [6–9]. Earlier, SAR data were quite expensive, infrequent and most of the studies on crop state assessment and crop type mapping were performed with optical data only. High spatial (10 m) and temporal (6 days revisit) resolution of the Sentinel-1 mission brings new opportunities in the agriculture domain and challenges of «Big data» problems in Remote Sensing that should be addressed.

In this paper, we propose a multi-layer Deep Learning (DL) architecture that is targeted for classification of multi-source multi-temporal remote sensing images, both optical and SAR, at a pixel level [10, 11, 12]. The core of the architecture is an ensemble of convolutional neural networks (CNNs) [13, 14]. The proposed architecture is applied for crop classification using Sentinel-1A time-series and provides accuracy high enough to be considered for operational context at the national level.

Data description

We address the problem of land cover and crop classification for Kyiv region of Ukraine using multi-temporal multi-source images acquired by Sentinel-2 and Sentinel-1A satellites [15]. The study area is classified into eleven classes including major agricultural crops (water, forest, grassland, bare land, winter wheat, winter rapeseed, spring cereals, soybeans, maize, sunflowers and sugar beet). It is rather large area (28.000 square km) with big diversity of different land cover types and agricultural crops. The territory is big enough to be considered as a representative one for the extension of the technology to the entire country. For the 2016 vegetation season (since October 2015 till September 2016) five cloud-free Sentinel-2 and twenty Sentinel-1 images were used for the study area. Sentinel-1A images were preprocessed via following steps: calibration, multi-looking (with 2 × 2 window), speckle filtering (3 × 3 window with Refined Lee algorithm), and terrain correction using SRTM DEM. A time-series of four 10 meter spectral bands from each Sentinel-2 scene and two bands with VV and VH polarizations from each Sentinel-1 scene are used as an input to the classification model.

For crop classification for the territory of Ukraine time series of only SAR Sentinel-1 data [16, 17, 18] were used. For the territory of Ukraine 9 paths of Sentinel-1 were used. Each of these paths consist of several images (Table 1, Fig. 1) and is constructed by merging them for one date in single stripe.

Table 1

The data size needed to crop mapping for the territory of Ukraine

Ukraine			
Path	Number of images for each path	Number of path 2016	Size of one Path, GB
7	4	19	7.19
21	3	21	2.32
36	6	20	11.31
65	6	19	12.08
80	4	19	7.14
94	5	20	8.26
109	3	22	6.69
138	5	22	11.89
167	5	23	10.67
Total	41	185	1576.08

More than 800 images were used for covering the territory of Ukraine with Sentinel-1A data during the vegetation season. The data amount used for land cover classification for 2016 is over 1.5 Tb in total.

Crop type and cropland mapping datasets were collected during 2-stage along the road surveys separately for winter crops (in the spring of 2016) and summer crops (in the summer of 2016) – 5526 samples for calibration and 2154 samples for validation purposes for major cropland and non-cropland classes – Fig. 2.

Non-cropland classes were added using both in-situ surveys and photo-interpretation from high-resolution imagery from Google Earth. Data collection was performed according to climatic zonation of Ukraine and with respect to JECAM guidelines – within 4 main climatic stratas of Ukraine (Woodlands, Forest and Steppe, Steppe and Mountains) – Fig. 3.

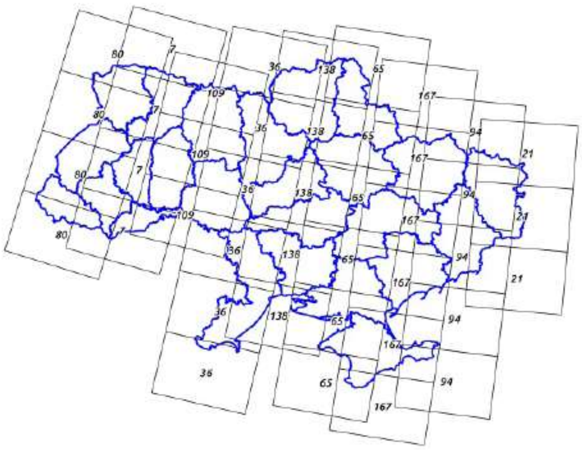

Fig. 1. Coverage of the territory of Ukraine by Sentinel-1A data with relative orbit number

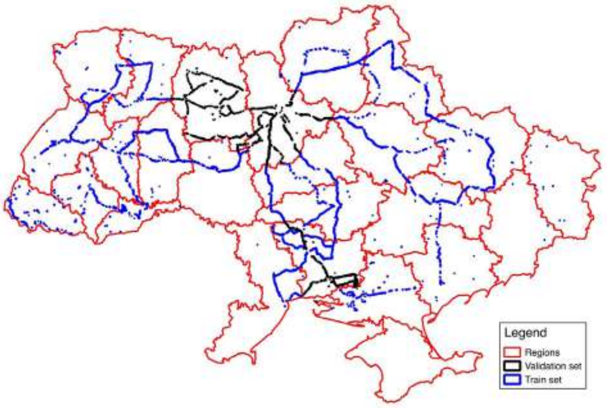

Fig. 2. In-situ data distribution over the territory of Ukraine

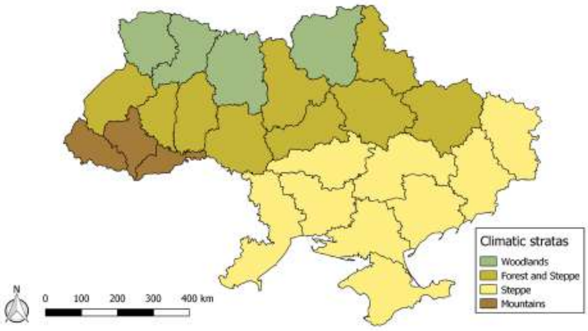

Fig. 3. Main climatic stratas of Ukraine

Methodology and products

When providing large scale crop mapping using multi-temporal satellite imagery, the following challenges should be addressed while using DL. First, pixels of a satellite image contain physical values. In particular, each pixel of the optical imagery contains spectral reflectance values in multiple spectral bands, and can be contaminated with clouds and shadows; while each pixel of the space-borne SAR imagery is characterized by backscatter intensity and phase in multiple polarizations. Both of the data sources have multi-temporal nature and different spatial resolutions. That is why, DL implementation for land cover and crops classification based on data fusion of multi-temporal multi-sensor satellite data is a challenge.

A four-level architecture is proposed for classification of crop types from multi-temporal satellite imagery. These levels are pre-processing, supervised classification, post-processing and geospatial analysis (Fig. 4).

Since optical satellite imagery can be contaminated with clouds and shadows, one have to deal with missing values in the imagery. Most classifiers accept only valid pixel values as an input, and therefore a pre-processing step should be performed to

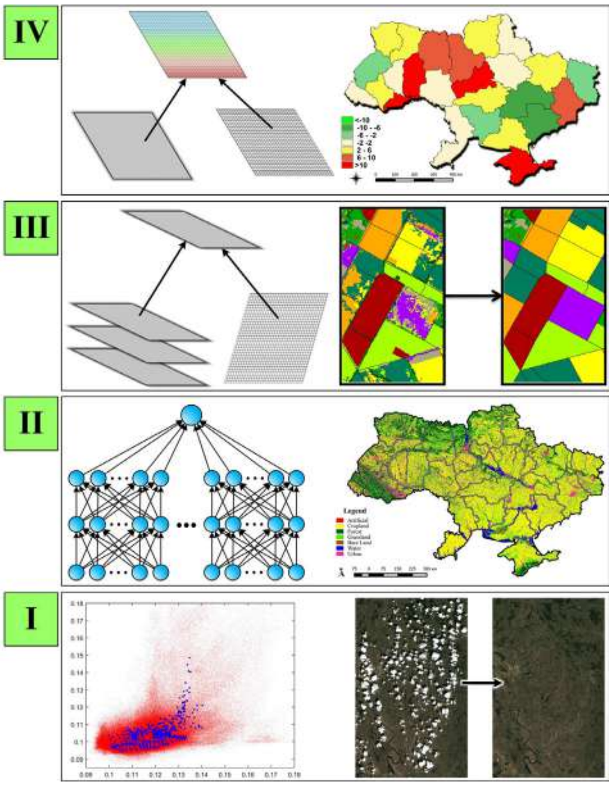

Fig. 4. A four-level hierarchical deep learning model for satellite data classification and land cover/land use changes analysis (I – pre-processing for dealing with missing data on optical images due to clouds /shadows, II – supervised classification, III – post-processing using additional geospatial data to improve classification maps, IV – geospatial analysis for a high-level product, e.g. crop area estimation)

impute (or fill gaps) missing values. This procedure is performed within level I of the architecture. The next step is supervised classification (level II) which is the core of this study. We propose CNNs architectures, namely 2-d, to explore spectral and spatial features, respectively. Levels III and IV are aimed at improving the resulting classification map with available geospatial layers and building high-level products.

For pre-processing, we utilize self-organizing Kohonen maps (SOMs) for optical images segmentation and subsequent restoration of missing data in a time-series of satellite imagery [15]. SOMs are trained for each spectral band separately using non-missing values. Missing values are restored through a special procedure that substitutes input sample's missing components with neuron's weight coefficients. Pixels that have been restored are masked, the number of cloud-free scenes available for each pixel from optical imagery is calculated, and these two layers are used for further post-processing procedure (at level III) to improve the resulting classification map [19]. The detailed description of the restoration algorithm is given in [2, 15].

The core element of the model is the supervised classification, which is performed at the second stage (level II). The CNN, in turn, builds a hierarchal set of features through local convolution and down-sampling. The two bands from each of the twenty Sentinel-1A scenes and the four bands from each of the four Sentinel-2 scenes form a CNN input feature vector with dimension size 60 ($20\times2+5\times4$). Traditional CNNs (2-d) take into account a spatial context of an image and provide higher accuracy comparing to a per pixel-based approach. However in this case, CNN smooths not only some misclassified pixels but also small objects like roads, and forest «stripes» and clear cuts within the forest (with linear dimensions of several pixels) are missed. Each CNN in the corresponding ensemble consists of two convolutional layers, each of them followed by max-pooling and two fully connected layers in the end (Fig. 5). We used a rectified linear unit (ReLU) function that is one of the most popular and efficient activation functions for deep neural networks. There are advantages of using ReLU such as biological plausibility, efficient computation and gradient propagation. Therefore, ReLU function is faster and more effective for training CNNs comparing to a sigmoid function. Each of the CNNs has the same convolution and max-pooling structure but differs in the trained filters and number of neurons in the hidden layer (NNH) being 60, 70, 80, 90 and 100 for five CNNs, respectively.

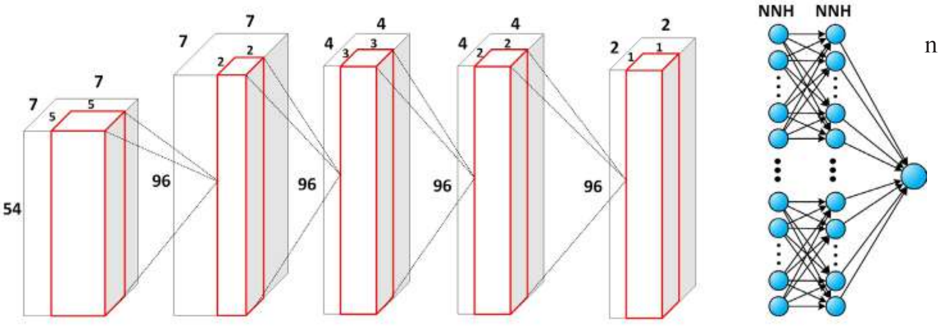

Fig. 5. Deep convolutional neural network architecture

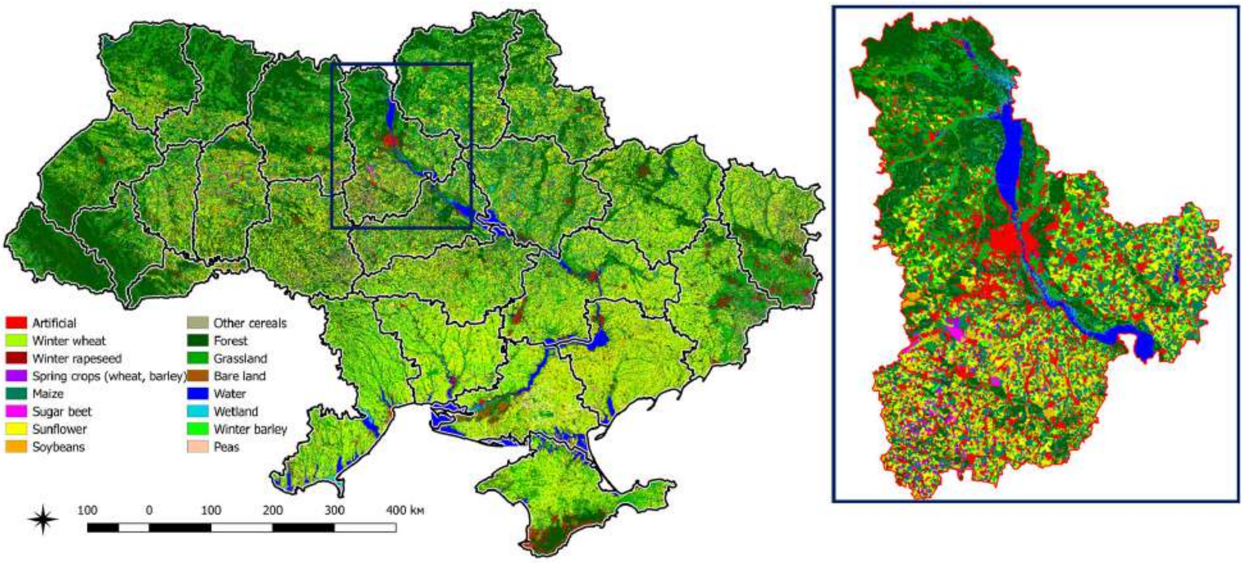

Fig. 6. Crop type map for Ukraine,2016 (SRI product)

To improve the quality of the resulting map, we developed several filtering algorithms, based on the available information on quality of input data and fields boundaries [19]. Those filters take a pixel-based classification map and specifically designed rules to account for several plots (fields) within the parcel. In the result, we obtained a clear parcel-based classification map. The final level of data processing provides data fusion with multi sourced heterogeneous information, in particular, statistical data, vector geospatial data, socio-economic information and so on. It allows interpreting the classification results, solving applied problems for different domains, and providing the support information for decision makers. For example, classification map coupled with area frame sampling approach can be used to estimate crop areas [6].

Results analysis

With use of the proposed four-level architecture were in Space Research Institute (SRI) obtained crop classification map for Kiev region and for territory of Ukraine. These maps were validated on independent in-situ data from ground survey. The overall accuracy of classification map for Kiev region is over 93 % and over 90 % for Ukraine in 2016. Land cover maps in the end of vegetation period for territory of Ukraine is shown on Fig. 6. For main crops the F1-score has been calculated based on independent test set: winter wheat – 90,

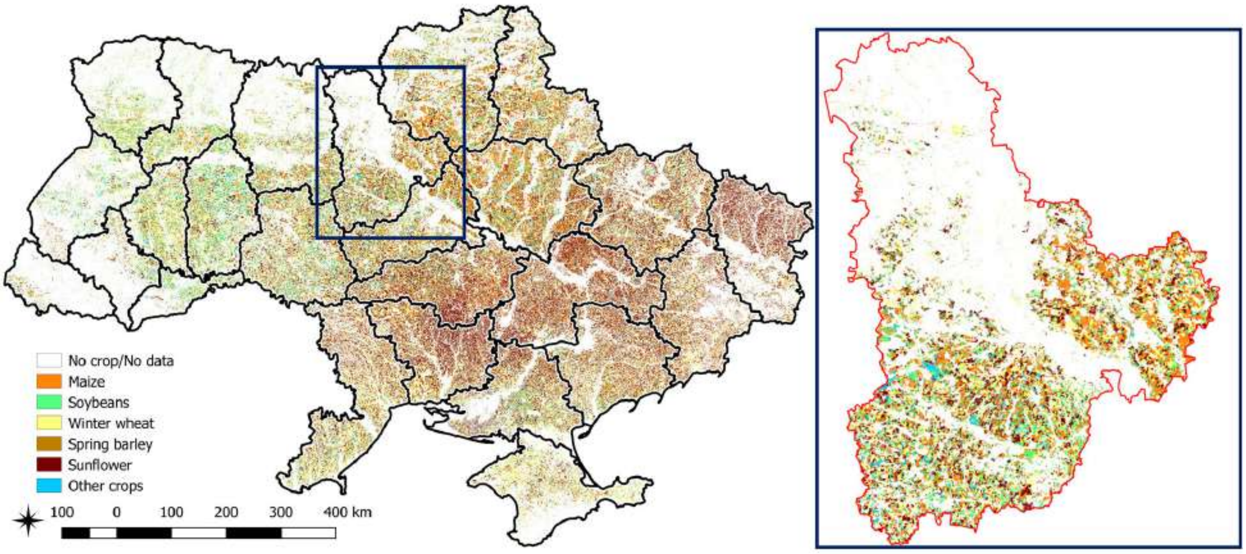

Fig. 7. Crop type map for Ukraine, 2016 (Sen2-Agri product)

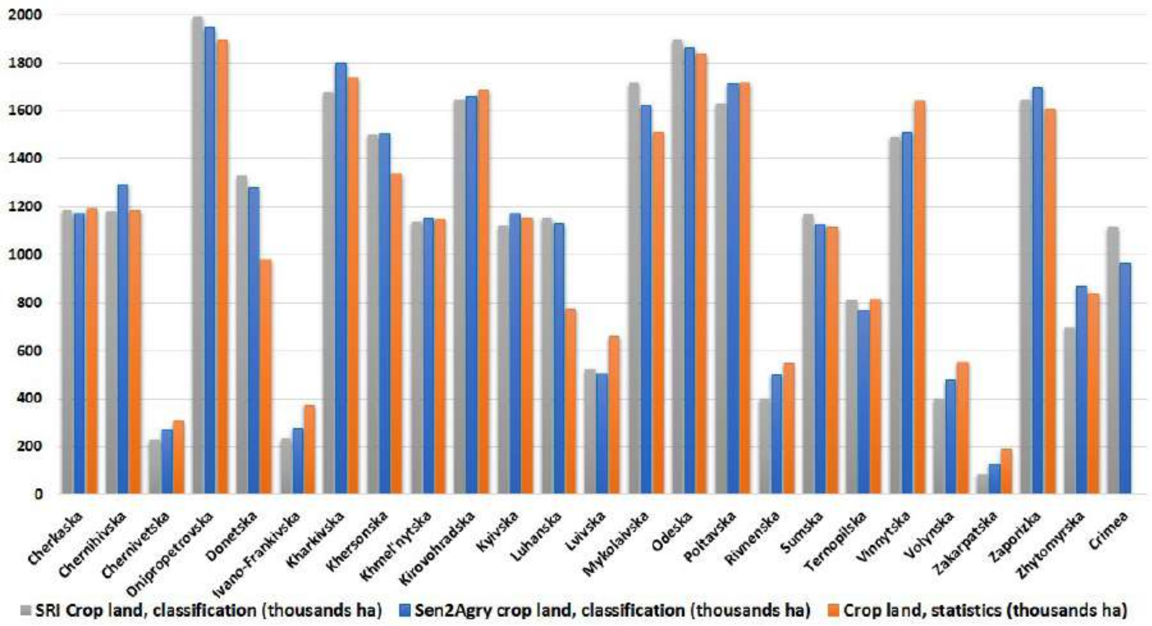

Fig. 8. Crop area comparison to official statistics

winter rapeseed – 83.6, maize – 93, sugar beet – 93.6, sunflower – 94.3, soybeans – 82.5, peas – 70.9.

In this section SRI crop type map for Ukraine will be compared to statistical information from State Statistical Service of Ukraine. Cross-comparison of SRI crop type map developed with use of deep learning and alternative Sen2-Agri crop type map (Fig. 7) will be performed as well (Fig. 8).

According to official data the biggest difference in cropland area correspond to the conflict area in the Eastern part of Ukraine (Donetska and Luhanska regions – Fig. 8) and caused by several reasons: (1) non-fully coverage of the area be statistical observations; (2) significant decrease of agricultural activity over this areas [13].

Discrepancies in the Western part of Ukraine is common for this region and caused by the specifics of agriculture and statistical data collection for these regions.

Table 2

Cross-comparison of crop type maps with official statistics over pilot areas for major crops

Crop type	Areas in thousands of hectares		
	SRI	Sen2-Agri	Statistics
	Kiev region		
Maize	314.9	312.6	268
Winter wheat	204.5	262.4	197.2
	Mykolaiv region		
Maize	99.7	166.4	132.8
Winter wheat	480.6	481.0	331.8

For main crops (maize and winter wheat) for two regions we performed cross-comparison of SRI and Sen2-Agri crop type maps with official statistics – Table 2. In Kiev region results are highly agreed for maize, in Mykolaiv region – for winter wheat.

Conclusions

In this paper, we proposed a multi-level Deep Learning approach for land cover and crop types classification using multi-temporal multi-source satellite imagery. The architecture uses both unsupervised and supervised neural networks for segmentation and subsequent classification of satellite imagery, respectively. In this study, we used Sentinel-2 and Sentinel-1A images for Kiev region and all Ukraine. In general, the use of CNN allowed us to reach the target accuracy over 90 % for all territory of Ukraine in 2016 (by 9 % more than the results of Sen2-Agri national demonstration). In the future it is planned to implement the developed architecture in the cloud [20] for the operational updating of land cover maps for Ukraine.

REFERENCES

1. *Kussul N., Kolotii A., Shelestov A., Lavreniuk M., Bellemans N., Bontemps S., Defourny P., Koetz B.* Sentinel-2 for agriculture national demonstration in Ukraine: Results and further steps // IEEE International Geoscience and Remote Sensing Symposium (IGARSS). – 2017. – P. 5842–5845. DOI: 10.1109/IGARSS.2017.8128337.

2. *Kussul N., Skakun S., Shelestov A., Lavreniuk M., Yailymov B., Kussul O.* Regional scale crop mapping using multi-temporal satellite imagery // International Archives of the Photogrammetry, Remote Sensing & Spatial Information Sciences. – 2015. – P. 45–52.

3. *Lavreniuk M.S., Skakun S.V., Shelestov A.Ju., Yalimov B.Ya., Yanchevskii S.L., Yaschuk D.Ju. and Kosteckiy A.M.* Large-Scale Classification of Land Cover Using Retrospective Satellite Data // Cybernetics and Systems Analysis. – 2016. – V. 52. – No. 1. – P. 127–138. DOI: 10.1007/s10559-016-9807-4.

4. *Francois W., Kussul N., Guerric le Maire, Dupuy S.* Towards a set of agrosystem-specific cropland mapping methods to address the global cropland diversity // International Journal of Remote Sensing. – July 2016. – V. 3714, No. 14. – P. 3196–3231. DOI: 10.1080/01431161.2016.1194545.

5. *Kogan F., Kussul N., Adamenko T., Skakun S., Kravchenko O., Kryvobok O., Shelestov A., Kolotii A., Kussul O., Lavrenyuk A.* Winter wheat yield forecasting: A comparative analysis of results of regression and biophysical models // Journal of Automation and Information Sciences. – 2013. – V. 45. – No. 6. – P. 68–81.

6. *Gallego J., Kussul N., Skakun S., Kravchenko O., Shelestov A., Kussul O.* Efficiency assessment of using satellite data for crop area estimation in Ukraine // International Journal of Applied Earth Observation and Geoinformation. – 2014. – V. 29. – P. 22–30.

7. *Kussul N., Skakun S., Shelestov A., Kussul O., Yailymov B.* Resilience Aspects in the Sensor Web Infrastructure for Natural Disaster Monitoring and Risk Assessment Based on Earth Observation Data // IEEE Journal of Selected Topics in Applied Earth Observations and Remote Sensing. – 2014. – V. 7. – No. 9. – P. 3826–3832.

8. *Kussul N., Shelestov A., Skakun S.* Flood Monitoring from SAR Data // NATO Science for Peace and Security Series C: Environmental Security. – 2011. – P. 19–29. DOI: 10.1007/978-90-481-9618-0_3.

9. *Kravchenko A., Kussul N., Lupian E., Savorsky vV., Hluchy L., Shelestov A.* Water resource quality monitoring using heterogeneous data and high-performance computations // Cybernetics and Systems Analysis. – 2008. – V. 44. – No. 4. – P. 616–624. DOI:10.1007/s10559-008-9032-x.

10. *Kussul N., Shelestov A., Skakun S., Kravchenko O.* High-performance intelligent computations for environmental and disaster monitoring // Int. J. Information Technologies & Knowledge. – 2009. – V. 3. – P. 135–156.

11. *Kussul N., Shelestov A., Basarab R., Skakun S., Kussul O., Lavreniuk M.* Geospatial intelligence and data fusion techniques for sustainable development problems // 11th International Conference on ICT in Education, Research and Industrial Applications: Integration, Harmonization and Knowledge Transfer (ICTERI 2015), May 14–16, 2015, Lviv, Ukraine. – 2015. – V. 1356. – P. 196–203.

12. *Lavreniuk M., Kussul N., Skakun S., Shelestov A., Yailymov B.* Regional Retrospective High Resolution Land Cover For Ukraine: Methodology And Results // International Geoscience and Remote Sensing Symposium 2015 (IGARSS 2015), № 15599383. – P. 3965–3968. DOI: 10.1109/IGARSS.2015.7326693.

13. *Kussul N., Lavreniuk N., Shelestov A., Yailymov B., Butko I.* Land Cover Changes Analysis Based on Deep Machine Learning Technique // Journal of Automation and Information Sciences. – 2016. – V. 48. No. 5. – P. 42–54. DOI: 10.1615/JAutomatInfScien.v48.i5.40.

14. *Kussul N., Lavreniuk M., Skakun S., Shelestov A.* Deep Learning Classification of Land Cover and Crop Types Using Remote Sensing Data // IEEE Geoscience and Remote Sensing Letters. – 2017. – V. 12. – No. 5. – P. 778–782. DOI: 10.1109/LGRS.2017.2681128.

15. *Skakun S.V., Basarab R.M.* Reconstruction of Missing Data in Time-Series of Optical Satellite Images Using Self-Organizing Kohonen Maps // Journal of Automation and Information Sciences. – 2014. – V. 46. – No. 12. – P. 19–26.

16. *Kussul N., Skakun S., Shelestov A., Kussul O.* The use of satellite SAR imagery to crop classification in Ukraine within JECAM project // IEEE International Geoscience and Remote Sensing Symposium (IGARSS). – 2014. – P. 1497–1500.

17. *Skakun S., Kussul N., Shelestov A.Y., Lavreniuk M. and Kussul O.* Efficiency Assessment of Multitemporal C-Band Radarsat-2 Intensity and Landsat-8 Surface Reflectance Satellite Imagery for Crop Classification in Ukraine // IEEE Journal of Selected Topics in Applied Earth Observations and Remote Sensing. – 2016. – V. 9. – No. 8. – P. 3712-3719. DOI:10.1109/JSTARS.2015.2454297.

18. *Abramov S., Rubel O., Lukin V., Kozhemiakin R., Kussul N., Shelestov A., Lavreniuk M.* Speckle reducing for Sentinel-1 SAR data // IEEE International Geoscience and Remote Sensing Symposium (IGARSS). – 2017. – P. 2353–2356. DOI: 10.1109/IGARSS.2017.8127463.

19. *Kussul N., Lemoine G., Gallego J., Skakun S., Lavreniuk M.* Parcel based classification for agricultural mapping and monitoring using multi-temporal satellite image sequences // The International Geoscience and Remote Sensing Symposium (IGARSS), 2015 IEEE International. – 2015. – P. 165-168. DOI: 10.1109/IGARSS.2015.7325725.

20. *Kussul N., Shelestov A., Skakun S.* Grid technologies for satellite data processing and management within international disaster monitoring projects // Grid and Cloud Database Management. – 2011. – P. 279–305.

RESEARCH OF THE HEALTH OF WINTER WHEAT SEEDING DURING SPRING-SUMMER VEGETATIVE PERIOD IN 2016 USING SENTINEL-2 VEGETATION INDICES

**V. Lyalko, O. Sakhatsky, H. Zholobak, O. Sybirtseva, S. Duhin,
M. Vakolyuk, Yu. Zakharchuk**

State Institution «Scientific Centre for Aerospace Research of the Earth
of Institute of Geological Sciences of NAS of Ukraine» (CASRE IGS NASU)

In the framework of the Copernicus Program for the space monitoring of the Earth of the European Space Agency the new-generation Sentinel-2A satellite was launched in April 2015. It is equipped with the Multi-Spectral Camera, which is acquired data in 13 spectral bands at the spatial resolution of 10, 20 and 60 m; 290 km field of view. In light of the emergence of the new high-quality images from this satellite the specialists of the CASRE IGS NAS of Ukraine have estimated the capabilities for the spectral vegetation indices obtained by Multi-Spectral Camera data (Sentinel-2) to respond to the variations of the agrophytocenoses during the vegetation period [1] and compared their values with the vegetation indices (VIs) estimated from the spectrometric measurements, which were carried out by ASD FieldSpec®3FR over the identical geographical areas of the earth's surface [2].

Our object was the study of the production seeding of winter wheat (WW) for two cultivars Bohdana and Skagen, which are grown on the farmlands belonging to the Grain Alliance Ukraine. The production crop fields are located near Berezan town of the Baryshivka Raion, Kyiv Oblast and studied in2016 by the remote and field methods following by the statistic (mathematical) processing of data. Fig. 1 shows the location for these fields.

The field study showed that the testing Field 2 (Bohdan cultivar) has been characterized by the more heterogeneity than Field 1. In the booting stage in May 10, 2016 the study revealed the infestation of this field by plant pathogenic fungi (mildew, fusariosis, septoriosis). We observed the blackening of the ears and the decrease in the biomass of vegetation and as a result the WW grain production loss for the Bohdan cultivar in comparison with the Skagen one.

We have analyzed the behavior of three normalized difference VIs such as NDVI (842, 665), NDVI (740, 665) and Green NDVI estimated on a basis of Sentinel-2 data within the two production WW crop fields of the Grain Alliance Ukraine during the winter dormancy and spring – summer vegetative stages in 2016 (Fig. 2).

It is determined that the similarity among these indices is a result of the analogical courses for the lines of their dynamics according to conditions

Fig. 1. Location scheme of the winter wheat fields under the study, Baryshivka Raion, Kyiv Oblast, 2016. Field 1 – WW, Scagen cultivar; Field 2 – WW, Bohdana cultivar

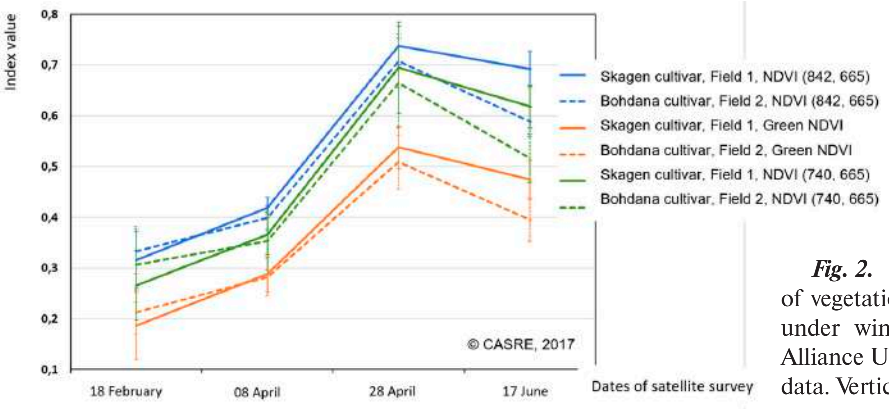

Fig. 2. Dynamics of averaged values of vegetation indices for the investigated fields under winter wheat belonging to the Grain Alliance Ukraine, 2016, based on the Sentinel-2 data. Vertical bars are the standard deviations

of two crops, and the difference lies in absolute value of indices (the highest and lowest figures are characteristic for NDVI (842, 665) and Green NDVI, respectively).The values of investigated normalized difference indices estimated by remote sensing data indicate that the inversion for the state of crops occurred immediately after the spring growth recovery of WW plants. Fixation time for the inversion of crop state varies depending on wavelength, which is selected to estimate the index: NDVI (842, 665) captures the inversion earlier than other indices. So NDVI (740, 665) and Green NDVI testify to it 2–3 weeks later.

Thus, VIs values estimated by Sentinel-2A data reveal the inversion of crop state in our investigation earlier (28 April, 2016) that it provides the visual field monitoring (10 May, 2016). This fact can be used in the models for the forecasting cereal crop production.

Addition to these three Sentinel-2A VIs for the geographically identical areas of WW production crop of two cultivars of Bohdana and Skagen ten different VIs have been estimated and compared with the proper VIs obtained from the ground spectrometry measurements. The discrepancies among the VIs estimated by Sentinel-2A and ASD FieldSpec®3FR data show the vegetative stage dependence for winter wheat, so during the vegetation development the correlation coefficients among them increase for the both cultivars. The values for the most Sentinel VIs are similar to those obtained in the narrow bands of ASD FieldSpec®3FR except DRICI (Double Ratio Index for Chlorophyll Index) and CIgreen (Ratio Green Chlorophyll Index).

The analyzed indices demonstrate the different behavior in dependence on the state of vegetation cover that allows recommending their application to the further study of WW crop productivity. Furthermore, Sentinel-2A data show the high potential for monitoring of state of seedlings health for the agricultural crops.

REFERENCES

1. *Zholobak G.M., Sybirtseva O.M., Vakolyuk M.V., Zakharchuk Yu.V.* Remote monitoring of health of winter wheat seedlings during spring-summer vegetative period in 2016 using Sentinel-2 vegetation indices (a case study of Forest-Steep Zone, Ukraine) // Ukrainian Journal of Remote Sensing. — 2017. — Iss. 15. — P. 23-30. Available at: http://ujrs.org.ua/ujrs/issue/viewIssue/15/pdf_19 (in Ukrainian).

2. *Lyalko V.I., Sakhatsky O.I., Zholobak G.M., Sybirtseva O.M., Dugin S.S., Vakolyuk M.V.* Analysis and comparison of vegetation indices of winter wheat crop areas, calculated on the basis of Sentinel-2 and FieldSpec spectroradiometer data // Ukrainian Journal of Remote Sensing. — 2017. — Iss. 12. — P. 37–46. Available at: http://ujrs.org.ua/ujrs/article/view/94/110 (in Ukrainian).

APPLICATION OF SATELLITE MONITORING SYSTEMS FOR IDENTIFICATION AND ASSESSMENT OF ECOLOGICAL AND ECONOMICAL CHANGES WITHIN THE ANTI-TERRORIST OPERATION ZONE IN UKRAINE

V. Lyalko, L. Yelistratova, O. Apostolov

State Institution «Scientific Centre for Aerospace Research of the Earth
of Institute of Geological Sciences of NAS of Ukraine» (CASRE IGS NASU)

An accurate assessment of economic situation in a country or region is the difficult issue even in the peacetime, when there are reliable statistic data. As a result of an armed conflict in the Eastern Ukraine the analysis of the economic losses, in particular, in the territories beyond the Ukraine's control is carried out by the indirect methods of evaluation. One of the ways of indirect assessing of economic activity is based on the analysis of varying illumination over the investigated area at night using the satellite images.

Here we use remote sensing data received from Suomi NPP satellite, which was launched in 2011. Thematic processing uses the DNB imagery product developed on a basis of VIIRS nighttime sensor images, i.e. monthly composite of night illumination of territory (a unit of light measurement is nanoWatt/cm^2/sr).

The analysis of DNB product for the area of Ukraine was realized by means of ERDAS Imagine, which provides the processing of the satellite imaging data. The monthly component of nighttime illumination for March 2014, 2015 and 2016 as well as the demarcation boundary for ATO (the anti-terrorist operation) zone to the status as per 2016. The official start date of ATO is 14 April 2014, when the decision of the National Security and Defense Council of Ukraine went into operation.

We proposed the illumination value scale to compare the satellite images on different dates. It gives the opportunities to study the changes that have occurred for the period of military operations. Fig. 1 shows the examples of satellite images over Debaltseve and Mar'inka cities for March 2014, 2015 and 2016.

For two years (from 2014 to 2016) the area and intensity of night illumination for the territory disappeared completely in the towns, where the severe fights (Debaltseve) and heavy firing (Avdiivka and Mar'inka) were waged, the considerable reduction of illumination is observed (Fig. 1). The settlements

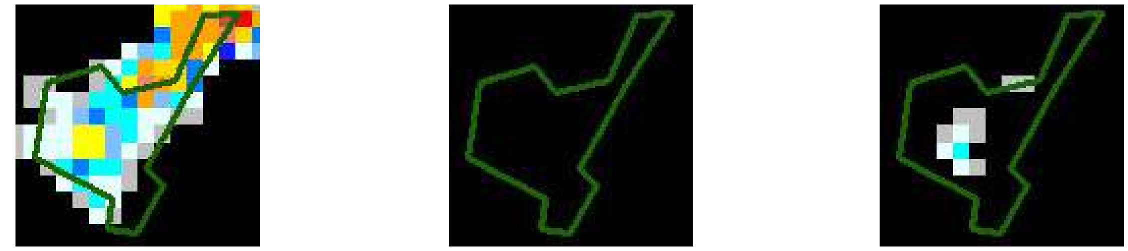

DEBALTSEVE march 2014 march 2015 march 2016

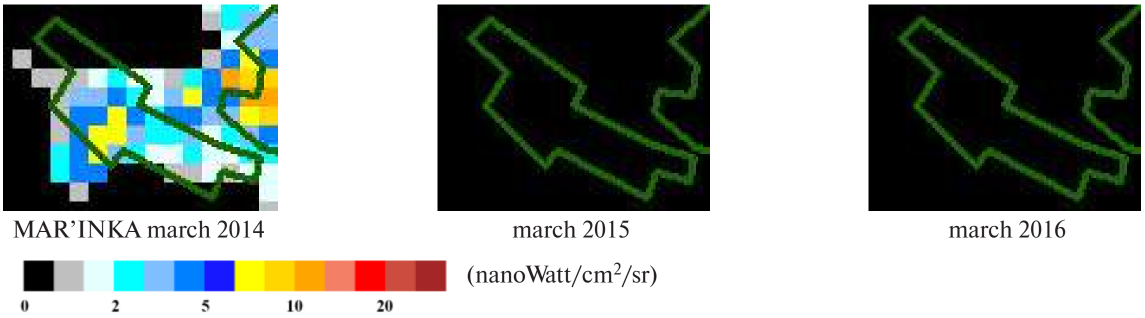

MAR'INKA march 2014 march 2015 march 2016

Fig. 1. Nighttime satellite images over the cities for March 2014, 2015 and 2016

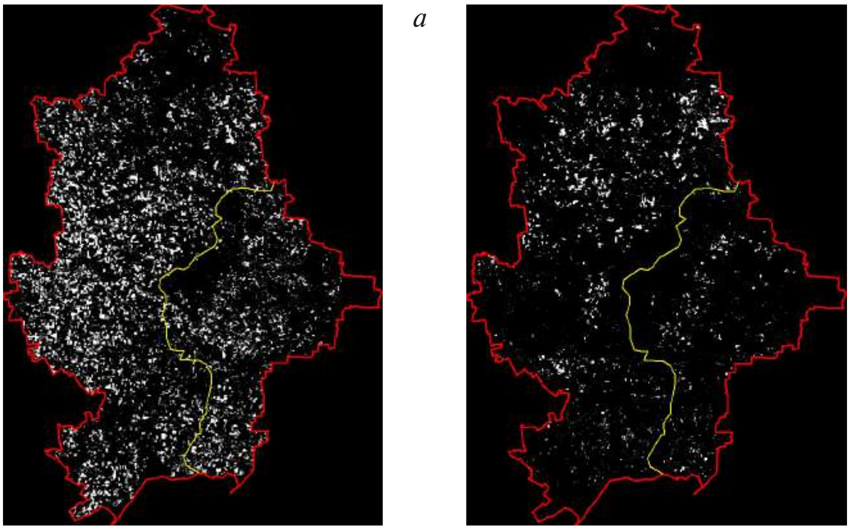

Fig. 2. Indication of winter plantings in the Donetsk Oblast by means of Landsat-5 images for 2011 (*a*) and Landsat-8 images for 2016 (*b*)

located at the confrontation line have minimum illumination, which doesn't exceed 10–20 % of the level for March 2014. The towns placed far away from the combat zone both in the territory of Ukraine temporarily beyond its control and remaining part of country have 50–70 % illumination of the level for March 2014. It was determined that mean variation of night illumination for the occupied territory of Donetsk and Luhansk Oblasts in the spring 2015 and 2016 was 54 % of the level for March 2014 (before the fighting). Accordingly, economic activity in the east of Ukraine has probably decreased almost twofold. These indicators can provide a picture of damage on economy in the region due to the military conflict, since the information from the State Statistics Service of Ukraine about this territory is absent.

In addition to the economic conditions of agroecosystems are very difficult to assess during the conduct of combat operations. The purpose of the study was to identify the sown area under winter crops using Landsat data in the conflict zone (Donetsk Oblast) and assess economic losses.

In order to compare the winter crop areas we have analyzed the imagery archive of the Landsat satellites for the east of Ukraine. The images were analyzed by tows (176 paths, 26 and 27 rows) for April 24, 2011, which covered about 100 % of Donetsk Oblast; Landsat-5 images for August 30, 2011; and Landsat-8 images for April 5 and August 11, 2016.

We have used the method of assessment for winter crop areas. The principle of method is the comparison of the Normalized Difference Vegetation Index (NDVI) and Water Index (WI) for the period of withdrawal from winter to the winter crop mowing in the fields [1, 2].

Fig. 2 shows the diminishing the areas under winter crops in 2016. An attempt was made to assess the economic losses in the Donetsk Oblast due to combat conflict in the east of Ukraine as a result of analysis of winter crop areas for 2011 and 2016 using satellite survey data.

The conducted computations have shown that winter crop areas were five times less in 2016 against 2011. We try to evaluate the indicative economic effects such as the losses from the decline in yields in the monetary equivalent.

According to the calculation results the approximate value of winter crop yield from the Donetsk Oblast was UAH 3737 million ($467 million) and UAH 601 million ($23 million) in 2011 and 2016, respectively.

The study of the findings has shown that the profit from selling winter crops decreased 6 times in the UAH equivalent and 20 times in the USD equivalent. This is due to the decrease of crop areas five times, lowering cost of the main winter crops in 2016 against 2011, and dollar rate increase more than 3 times. These findings can provide insights into the economic losses owing to the declining harvests of winter crops within the region under the study as a result of combat conflict, because the information for this territory from the State Statistics Service is not entirely comprehensive or doesn't exist at all.

REFERENCES

1. *Lyalko V.I., Yelistratova L.O., Apostolov O.A.* The estimation of cultivated area under winter crops by Landsat survey data over the Donetsk region // Reports of NAS of Ukraine. – 2017. – Iss. 6. – P. 51–57 (in Ukrainian).

2. *Lyalko V.I., Yelistratova L.O., Apostolov O.A., Sakhatsky O.I.* Application of products from NPP/VIIRS satellite images at night for assessment of the economic crisis in the East of Ukraine (the Donetsk and Luhansk regions) // Visnyk of NAS of Ukraine. – 2017. – Iss. 2. – P. 48–53 (in Ukrainian).

EROSION HAZARD ESTIMATION FOR THE TERRITORY OF UKRAINE USING REMOTE SENSING DATA, CLIMATIC FACTORS AND VEGETATION

V. Lyalko, L. Yelistratova, A. Khodorovsky, O. Apostolov
State Institution «Scientific Centre for Aerospace Research of the Earth
of Institute of Geological Sciences of NAS of Ukraine» (CASRE IGS NASU)

It is considered that a third of croplands in Ukraine are characterized by the different manifestations of erodability. However, these data are coarse and largely outdated, because the regular updating of information relative to soil conditions, in particular, the monitoring of their erodability that defined according the Ukraine legislation haven't been carried out over a long period of time. This monitoring within Ukraine area is possible only with the application of remote sensing data (RSD).

Our goal was to quantify the erosional ruggedness of relief in Ukraine using the known morphometrical factors such as vertical and horizon ruggedness. The Fig. 1 shows the distribution of values for erosion rugged relief index (ER) obtained by our technique [1–3]. The value of obtained ER index allows distinguishing the potential hazardous areas of erosion processes.

The erosion ruggedness of relief dependences on such factors as precipitation and vegetation cover development. Their impacts were estimated and these estimations were calculated in terms of averaged precipitation rate (R) for 117 years using hydrometeorological data and vegetation index (NDVI).

The modified ER index taking into account of precipitation rate (R) and vegetation index (NDVI) is compared with ER index (Fig. 2).

The conducted computation shows that total consideration of ruggedness of relief (ER), climatic factors (precipitation rate, R), vegetation character, NDVI as a case study on Carpathians provides the ranking of erosion hazardous areas and distinguishing the plots with the significant impact of vegetation (near 76.6 %).

The proposed technique is effective for rapid assessment of erosion hazardous plots of soil in Ukraine using remote sensing data (ER index) taking into account the climatic factors and vegetation and it is useful both mountainous and flat parts of Ukraine that can provide opportunities to trace the special distribution of erosion processes of soils and locate the areas with the highest potential hazard of erosion. Satellite observations allow the identification

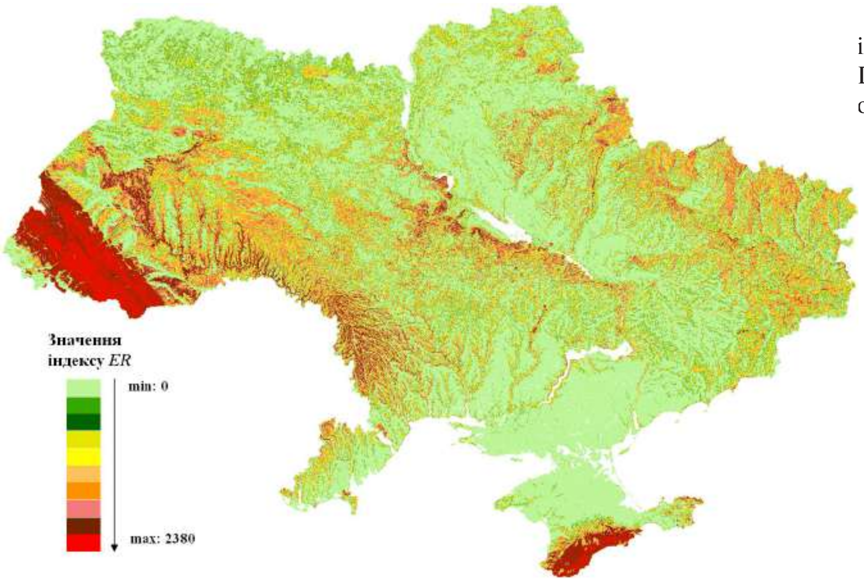

Fig. 1. Value of erosion rugged relief index for whole Ukraine terrain using DEM obtained by the space vehicle of Shuttle

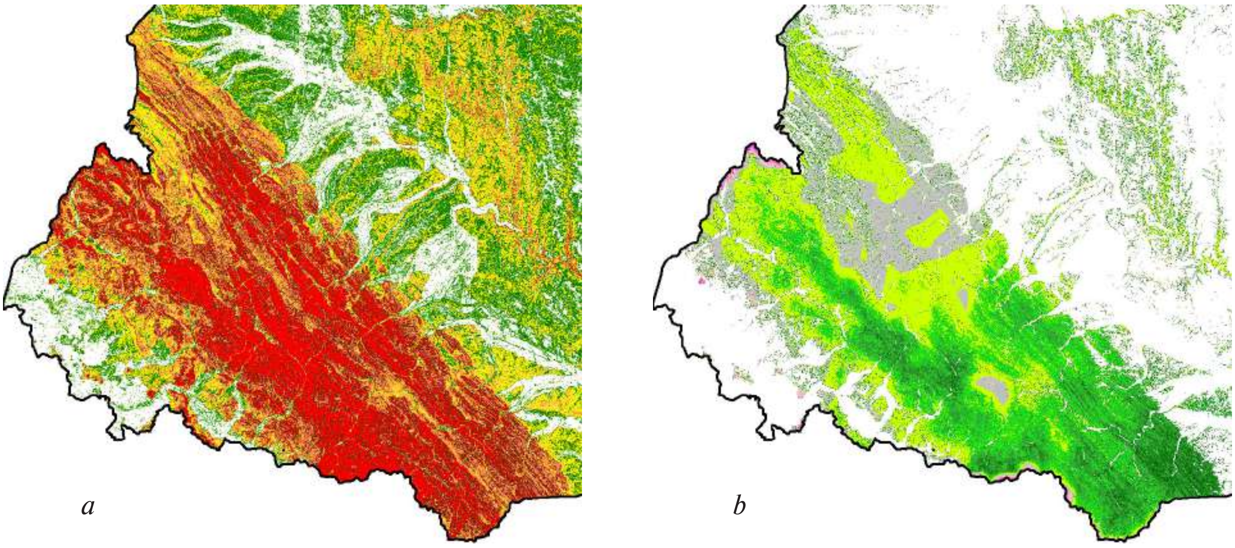

Fig. 2. Carpathians according to ER index, precipitation rate (R) and NDVI (normalization) (*a*); a difference between the modified ER index with account of precipitation rate (R) and vegetation (NDVI) and ER index (*b*)

of negative processes and phenomena, which take place in soil cover, especially in the places uncontrolled by common way that might be a signal to proper services and authorities to take the urgent agrothechnical measures for the stopping and elimination of erosion processes.

REFERENCES

1. *Lyalko V.I., Yelistratova L.O., Apostolov O.A., Chekhniy V.M.* Analysis of soil erosion processes in Ukraine on a basis of remote sensing of the Earth // Visnyk of NAS of Ukraine. – 2017. – Iss. 10. – P. 34–41 (in Ukrainian).

2. *Lyalko V.I., Apostolov O.A., Yelistratova L.O.* Influence of natural and anthropogenic factors on the formation of dangerous situation: landslides, floods (case study of Upper Dniester) // Ukrainian Journal of Remote Sensing. – 2017. – Iss. 15. – P. 31–39. Available at: http://ujrs.org.ua/ujrs/issue/viewIssue/15/pdf_19.

3. *Lyalko V.I., Yelistratova L.O., Apostolov O.A., Khodorovsky A.Ya., Chekhniy V.M.* Rapid assessment of erosion hazardous areas of soil cover on the territory of Ukraine using remote sensing data, climatic factors and vegetation // Reports of NAS of Ukraine (in press).

SPACE MONITORING OF THE DANGEROUS STATE OF AIR BASIN OVER THE INDUSTRIAL HUBS

O. Azimov[1], **A. Bunina**[2]

[1] State Institution «Scientific Centre for Aerospace Research of the Earth of Institute of Geological Sciences of NAS of Ukraine» (CASRE IGS NASU)

[2] Taras Shevchenko National University (KNU)

The contemporaneous urban ecosystem as a rule is characterized by the high level of pollution that is connected with the intensive development of industry. The urban areas differ in the diversity of the main ecological factors as well as the specific technogenic impact on them. The metallurgical industry is a leading source of pollution for the south-eastern ranges of Ukraine and as a result a number of ecological problems are arisen that requires the urgent solution. In particular, the ecological situation in the cities of the Donetsk Oblast is characterized by the multicomponent chemical pollution of the natural environment.

So, the key problem of Mariupol is the severe air pollution by the emissions from the industrial enterprises of the city (Fig. 1). As far as the air basin pollution, Mariupol belongs to the most troubled cities of the Donetsk Oblast and entire Ukraine. The situation is complicated by the unsuccessful distribution of iron and steel enterprises in the territory of city relative to the main housing estates.

The long-term data reveal that before 1990 the metallurgical enterprises under full load were polluting atmospheric air by dust and gaseous impurities exceeding the maximum allowable concentration established by Ukrainian legislation by 3–5 and more times. Mariupol city of the Donetsk Oblast leads in air pollution index in Ukraine and according of the State Statistic Committee rating it ranks second behind Kryvyi Rih in the severity of ecological conditions of the environment [1].

In Mariupol there are more 50 large enterprises that indeed affect the natural environment. The most intensive sources of pollution, which influence on the urban environment are the enterprises of ferrous industry such as the Joint Stock Company "Illich Iron and Steel Works" (IISW), working from 1897 and the Joint Stock Company "Azovstal Iron and Steel Works" ("Azovstal"), established in 1933.

The anthropogenic flows including into the natural migration cycles induce the rapid expansion of the pollutants into the natural components of urban landscape and cover the areas both sited adjacent to the industrial enterprises and settlement zones where the urban population of Mariupol live. If one considers the city as a special type of ecosystem, its soils are a certain ecologically connecting link among the geosystems in the process of secondary redistribution of various pollutants.

To assess the scales of regions undergoing the negative impact of polluted air from the industrial facilities of Mariupol on a basis of our method using satellite survey [2, 3] we have determined the spatial distribution of smokes from the chimneys of coke

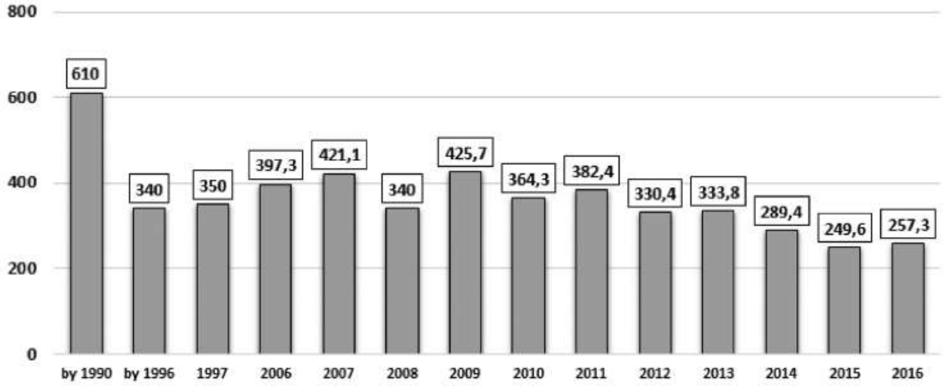

Fig. 1. Dynamics of atmospheric emissions from steel plants in Mariupol, th. t / yr

The list of used satellite images to monitor the atmosphere air conditions within

N	Years	Types of satellite remote sensing	Channels	Research period	Number of satellite images
1	2005	Landsat-7	432	February–April	4
2	2006	–	–	–	–
3	2007	Landsat-5	321	February–April	1
4	2008	Landsat-7	432	January–April	3
5	2009	Landsat-5	321	February–April	1
6	2010	Landsat-5	321	February–April	4
7	2011	Landsat-5	321	February–April	3
8	2012	Landsat-7	432	February–April	5
9	2013	Landsat-8	432	February–April	3
10	2014	Landsat-8	432	February–April	9
11	2015	Landsat-8	432	February–April	8
12	2016	Landsat-8	432	January–April	7

and by-product, agglomeration and blast-furnace processes, steel work of "Azovstal" and agglomerating plant, blastfurnace department, the units of steel-making and rolling of "Illich Iron and Steel Works" as well as the related industrial enterprises in the city [4–7]. The areas of smoke spread is determined by means of thematic interpretation of the satellite images mostly acquired from the space vehicles of Landsat-5, -7, -8 over 2005–2016 (see Table and Fig. 2). The Landsat images for the every year are interpreted for period from February to April (in some years this is January–May).

This period is selected taking into consideration of the character of air mass movement over a year.

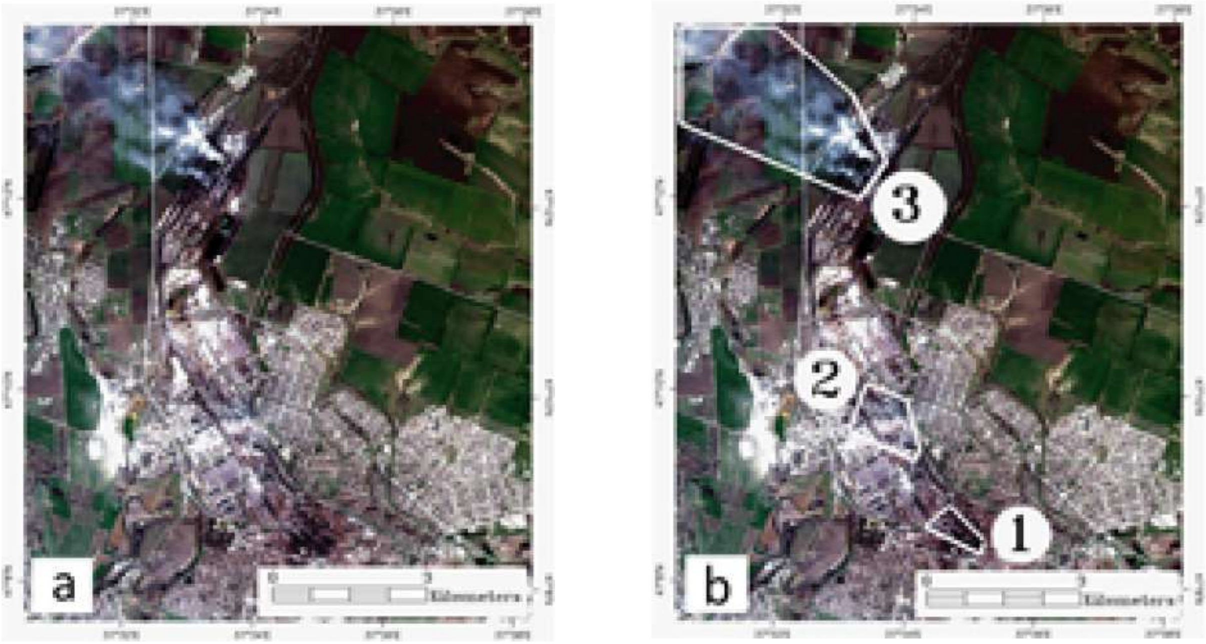

Fig. 2. An image acquired over the northern Mariupol from Landsat-8 on 24.03.2014 (B4_B3_B2 channels synthesis) (*a*); the areas of the spatial distribution of smokes from the following chimneys are distinguished on the image (*b*): 1 – blast-furnace shop of the Joint Stock Company "Illich Iron and Steel Works", 2 – converter shop of the Joint Stock Company "Illich Iron and Steel Works", 3 – mining and refining facility of the Joint Stock Company "Illich Iron and Steel Works"

The processed data of hydrometeorological surveys over eleven years have shown that February–April period is characterized the following pattern of wind rose: east (≈ 36 %), south, south-west and west (18 %, 11 % and 9 %, respectively) directions. The same pattern of wind rose is typical for this area of interest during the entire year for all the years of observations.

In the process of research at the first stage we have developed [7] the conceptual (or basic) technological framework for transformation, interpretation, and subject classification of remote sensing data using geoinformation technologies aiming at the monitoring of air basin pollution within the industrial hubs (Fig. 3).This scheme is based on the modern high-efficient specialized program products such as ENVI as well as the geographical information systems and powerful computer equipment. It is conceptual because its individual components (modules) are self-sufficient and can be used independently. Or, on the contrary, the technological scheme can be complemented by the new modules depending on the hierarchical level of studies of exploratory entities (regional, zonal and local scale levels), their multiplicity and completeness as well as the volume of available remote sensing and ground (validated) data.

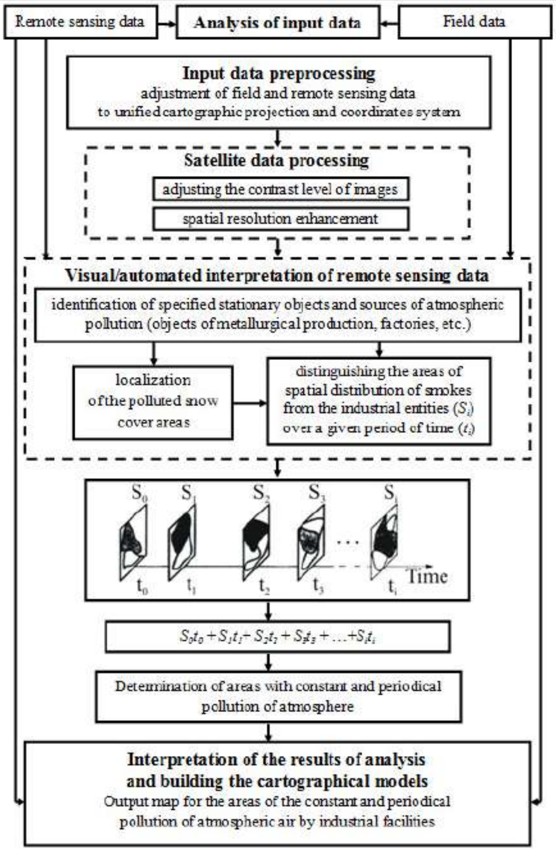

Fig. 3. The conceptual technological scheme for the transformation and thematic interpretation of remote sensing data using geoinformation technologies aiming at the monitoring of air basin conditions over the industrial hubs

At the second stage according to the Landsat image interpretation [4–7] the areas of the continuous air pollution from the industrial facilities of Mariupol are identified and mapped (Fig. 4). The areas spatially confined to the "Illich Iron and Steel Works" and "Azovstal" are distinguished. They are localized in the city districts such as Zhovtnevyi (Tsentralnyi) and Illichivskyi (Metalurgiynyi) in Mariupol (Fig. 5). Obviously, over time the pollutants from the polluted areas of atmosphere deposit in soils of the proper sites of the land surface.

REFERENCES

1. *Zhukov M.N., Kuraeva I.V., Voytyuk Yu. Yu., Stakhiv I.R., Bunina A.Ya., Matvienko A.V.* Comprehensive estimation of contamination of the Mariypol city soil by the method of main components // Geoinformatika. – 2015. – No. 3 (55). – P. 60–67. Available at: http://www.geology.com.ua/en/4394-2/ (in Ukrainian).

2. *Azimov O.T.* Monitoring of the urban agglomeration environment by aerospace survey data / Proceedings of the 12th International Scientific and Technological Conference "Ecology and Human Health. Protection of Water and Air Basins. Waste Utilization", June 7-11, 2004, Berdyansk, Ukraine. – V. 1. – P. 47–50 (in Ukrainian).

3. *Azimov O.T., Bunina A.Ya.* Development of a regional monitoring system for evaluating soil contamination by heavy metals using the complex of terrestrial and remote sensing data / Abstracts of the 10th Ukrainian Scientific and Practical Conference of Young Scientists and Students "State Environmental Safety", April 21, 2016, Kyiv, Ukraine. – P. 123 (in Ukrainian).

4. *Azimov O.T., Bunina A.Ya.* Monitoring of pollution of atmospheric basin over Mariupol using the remote sensing technologies / Proceedings of the 15th International Scientific and Practical Conference "Modern Information Technologies of the Ecological Management, Natural Resource Use and Emergency Measures", October 03–06, 2016, Kyiv, Ukraine. – P. 57–58 (in Ukrainian).

5. *Azimov O.T., Bunina A.Ya.* Estimation of pollution areas of atmospheric air using the satellite data (the Mariupol hub as an example) / Proceedings of the 5th Ukrainian Conference "Aerospace Technologies for Sustainable Development and Security (GEO-Ukraine)", October 10–14, 2016, Kyiv, Ukraine. – P. 38–40. Available at:
https://drive.google.com/file/d/0B3_rN9Ji08-VU3htSGhl
ZkRYWUU/view) (in Ukrainian).

6. *Bunina A.* Assessment of industrial air pollution using remote sensing data: Mariupol industrial area case study // The International Emergency Management Society Newsletter, Special Ed. – April 2017. – Iss. 5. – P. 14–16. Available at: http://www.tiems.info/images/pdfs/
TIEMS2017NewsletterScientificAprilrev1.pdf.

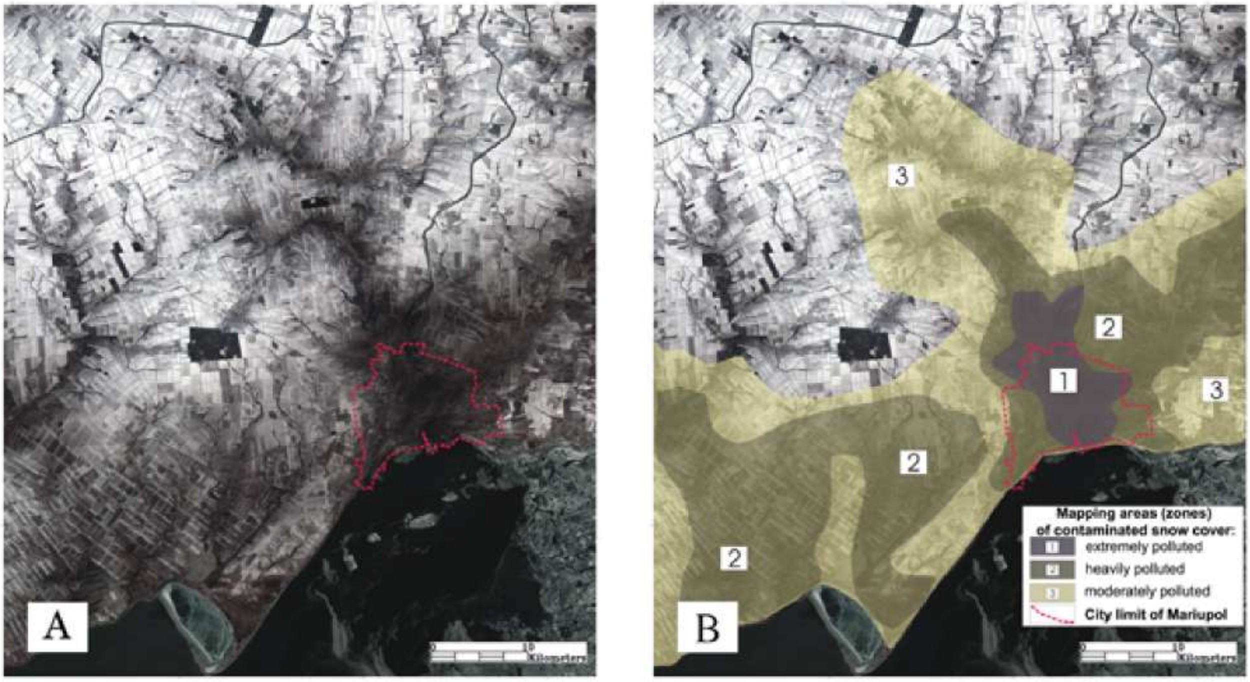

Fig. 4. Mapping areas (zones) of contaminated snow cover from smoke emissions from industrial facilities of Mariupol according to Sentinel-2 on 04.01.2017 (image synthesis *B4_B3_B2*): *A* – initial image, *B* – interpreted image

7. B*unina A.Ya., Azimov O.T., Dorofey Ye.M.* Use of the satellite images to develop the geoinformation system for monitoring air basin state of the Mariupol industrial hub / Abstracts of the 16th EAGE International Conference "Geoinformatics: Theoretical and Applied. Aspects", May 15–17, 2017, Kyiv, Ukraine. Available at: http://www.earthdoc.org/publication/publicationdetails/?publication=89544. DOI: 10.3997/2214-4609.201701874.

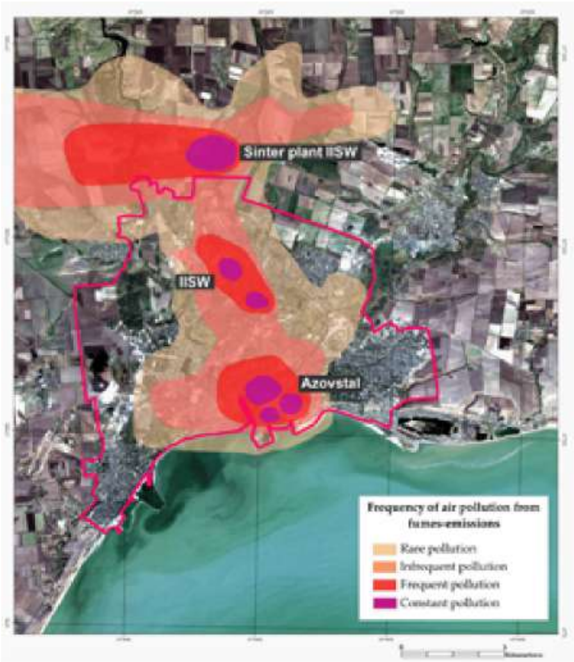

Fig. 5. Schematic map of regions of periodic pollution of atmospheric air from fume emissions of industrial facilities within the Mariupol industrial area compiled by the satellite image interpretation for 2005–2016

LEAF AREA INDEX MAPPING BY SENTINEL-1 DUAL-POLARIZATION RADAR IMAGERY WITHIN ROUGH TERRAIN

S. Stankevich, A. Kozlova, M. Lubskyi, M. Svideniuk, I. Piestova, O. Zakusylo

State Institution «Scientific Centre for Aerospace Research of the Earth of Institute
of Geological Sciences of NAS of Ukraine» (CASRE IGS NASU)

The leaf area index (LAI) is an important feature of the canopy structure, which influences and is influenced by biophysical processes of forest plant communities such as photosynthesis, respiration, transpiration, carbon and nutrient cycle, and rainfall interception. This index is widely applied in ecological and climate modeling, above-ground biomass assessment and forest monitoring. The LAI is a quantity of photosynthetically active part of forest canopies and indicates their rapid response to stress factors. In temperate deciduous and mixed forests LAI varies seasonally and lately more often is used to describe their phenology and climate-dependent changes. For solving such and similar tasks the information at relatively frequent intervals is required. However, LAI is also one of the most difficult to quantify properly, owing to large spatial and temporal variability. Many direct and indirect methods have been developed to quantify LAI.

Remote sensing is generally recognized to be the only reasonable option for LAI estimation at vast areas and difficult terrains. Commonly, LAI retrieving with remote sensing methods is based on optical data. Since LAI has been strongly related to spectral measurements, a variety of studies correlated numerous spectral vegetation indices from different satellite data to ground based measurements. Nevertheless, these methods are limited by the requirement of cloud-free daylight condition. For temperate forests it is not always possible to supply needed amount of cloud-free optical images throughout a growing season. Due to the fact that active microwave energy penetrates clouds, radar data provides an alternative approach to LAI retrieving.

While the dependence of backscattering on LAI of various crops is studied intensively, for estimating LAI of forests, radar data application is still rare. Most studies are devoted to LAI retrieving from C-band SAR in boreal forests. The main data sources in such cases were previous-generation SARs of ERS and Envisat satellites.

A method for LAI estimation of temperate deciduous and mixed forests within rough terrain

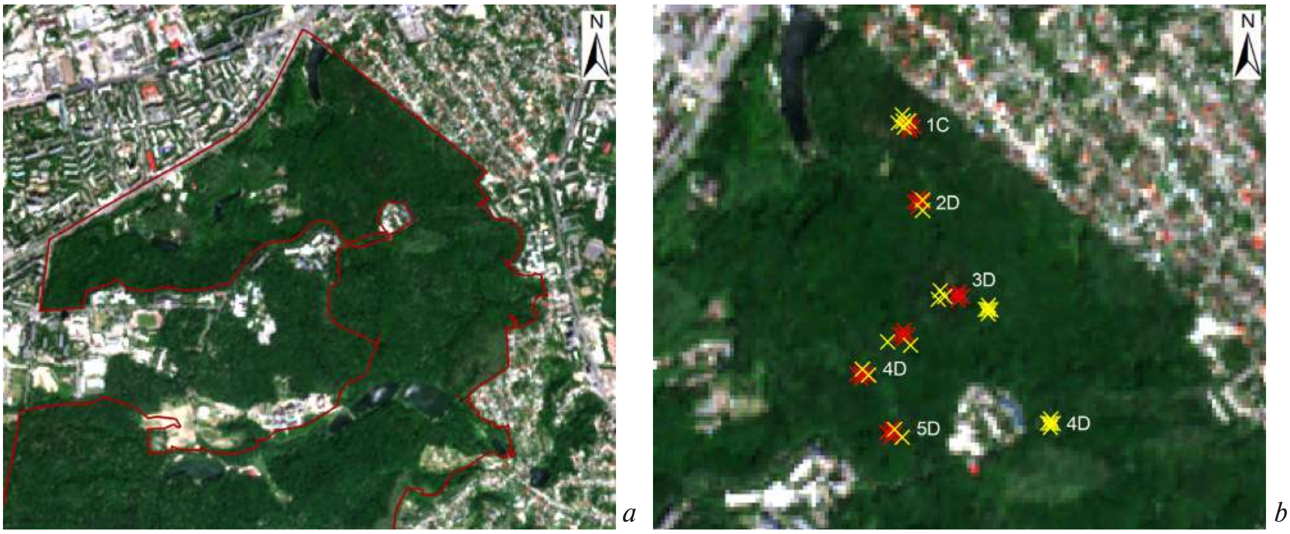

Fig. 1. Sentinel-2 MSI 10 m resolution image of the area of interest containing the scheme of the sample plots (red crosses shows the plots installed in 2016, yellow – 2017). The code describes type of measured plant communities. Data of image acquisition is June 5, 2017. Satellite-2 image bands combination: 665 nm, 560 nm, 490 nm

Forest plant communities of the study site

Code	Description
1C	A middle-aged pine (*Pinus sylvaticus*) stand with developed deciduous understory and grass cover that is severely affected by tourists in the spring-summer period
2D	Well closed maturing hornbeam (*Carpinus betulus*) stand with maple (*Acer L.*) and hazel (*Corylus*) in understory and dense grass cover
3D	Open maturing hornbeam (*Carpinus betulus*) stand. It has dense understory formed primarily witch hazel (*Corylus*)
4D	Well closed maturing oak (*Quercus robur*) stand with typical understory and underdeveloped grass cover
5D	Pure stands of beech (*Fagus sylvatica*), without understory and almost no grass cover, with a dense litter of fallen leaves

using novel Sentinel-1 C-band dual-polarization SAR is presented here. This method based on regression approach, which is de facto standard for various types of radar data analysis. The ground-based LAI measurements were collected for five forest types in Holosiivskyi National Nature Park (NNP) during 2016 and 2017 field seasons.

Study site

The study site (N 50°23.41, E 30°31.01) is situated at the northern part of Holosiivskyi NNP in Kiev, Ukraine (Fig. 1, *a*). It has a rather rugged local terrain with considerable ground height variation and steep slopes. A total of 25 sample plots were installed within the site during the fieldwork in 2016 and 18 ones in 2017 (Fig. 1, *b*).

Forest types selected for the study within the study site are described in the Table.

Data and Methodology

Sentinel-1 Data

The novel European Sentinel-1 SAR satellite system was selected as primary provider for data acquisition over the study site. Sentinel-1 is a radar mission providing continuous all-weather, day-and-night imagery at C-band in dual polarization within 12 days of repeat cycle. The Sentinel-1 Synthetic Aperture Radar (SAR) instrument may acquire data in four exclusive modes as Stripmap (SM), Interferometric Wide Swath (IW), Extra Wide Swath (EW) and Wave (WV) with different processing levels. IW is Sentinel-1's primary operational mode over land. Sentinel imagery is freely available via COPERNICUS Sentinels scientific data hub (https://scihub.copernicus.eu).

For the aim of the study, two Level-1 Ground Range Detected (GRD), dual-polarization (VV+VH) Interferometric Wide swath mode (IW) images were acquired on July 17, 2016 and June 30, 2017 along descending orbit over the area of interest. The false-color composite images of the study area is shown in Fig. 2 using VV, VH and ratio of two polarizations (VH/VV) data.

The SAR images are pre-processed using Sentinel Application Platform (SNAP) open-source software provided by European Space Agency (ESA).

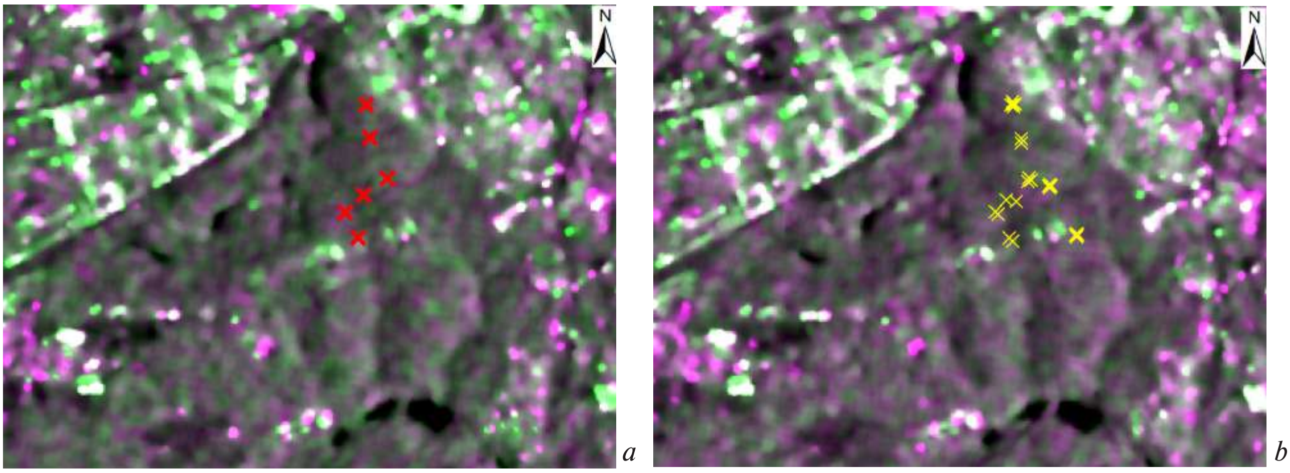

Fig. 2. False-color composite images of Sentinel-1 SAR with band combinations: σ^0_{VV}, σ^0_{VH}, $\sigma^0_{VH}/\sigma^0_{VV}$, containing the schemes of the corresponding sampling plots (red crosses are 2016, yellow ones are 2017): *a*) image acquired in July 17, 2016; *b*) image acquired in June 30, 2017

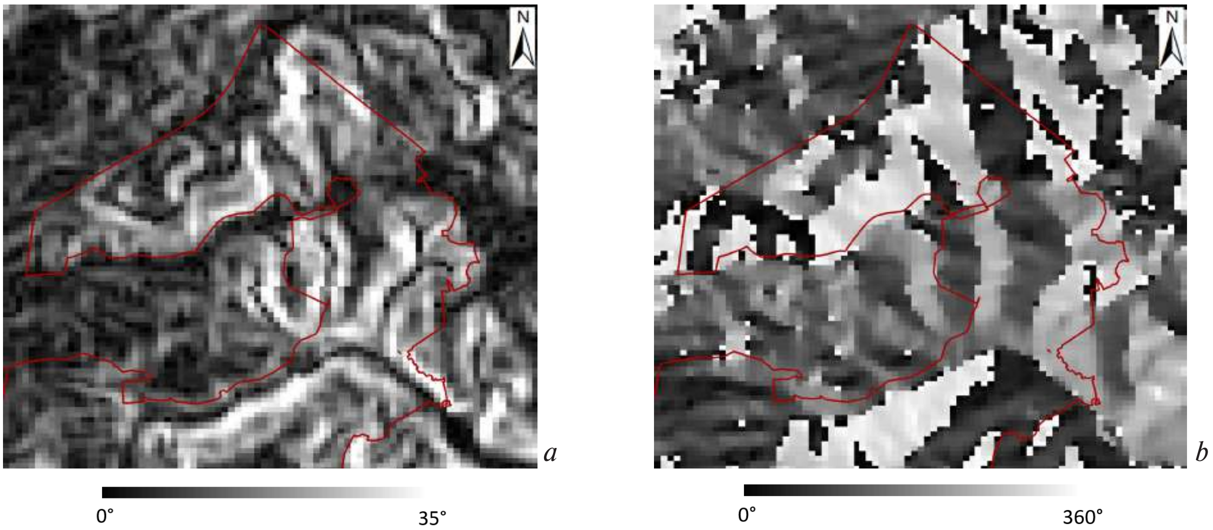

Fig. 3. Slope (*a*) and aspect (*b*) images of the study site. The area of interest is countered by red line

The Level-1 products of Sentinel-1 GRD data were calibrated to σ^0 values, removed of speckle noise using Lee Sigma filtering and terrain-rectified before analysis. For geocoding the SAR images from single 2D raster radar geometry the Range Doppler orthorectification method was used. It is implemented through the Range Doppler Terrain Correction Operator of SNAP.

The STRM v4 (3″ tiles) from the Joint Research Center FTP (ftp://xftp.jrc.it) was downloaded automatically in tiles for the area covered by the image to be orthorectified.

Topographic Data

In order to take into consideration terrain complexity of the study site and improve statistical likelihood of the calculated variables during LAI estimation topographic data was included. Topographic Modeling Operator on the Shuttle Radar Topography Mission (SRTM) SRTM 1 Arc-Second Global terrain elevation data of 1 arc-second (30 meters) resolution was used to compute surface relief, and to extract slope and aspect over the study site.

Slope, the steepness or the degree of incline of a surface, was measured in degrees. The slope degree is the convention of 0° for a horizontal plane. Aspect is the orientation of slope and measured with the convention of 0° to the north (up) and angles increasing clockwise. Slope and aspect images calculated for the area of interest are shown in Fig. 3.

LAI Field Measurements

Sampling strategy and organization of field work in the registration LAI is as important as the choice of technical solutions for measurement. Directly linked to reflectance characteristics of vegetation, LAI estimations depend on species composition, development stage, stand conditions and seasonality. Such parameters as canopy height, density and vertical complexity, plot size, terrain are essential for measurement and affect the reliability of results.

LAI field measurements were taken nearly simultaneously with the acquisition of satellite data from the 15th of July (2016) and 22nd of June (2017). Initially measurements were collected for remote estimation of the leaf area index of forest plant communities in seasonal development using Sentinel-2 MSI data [2–3].

As the test sites were selected homogeneous representative plant communities samples of 30 × 30 m size. Plot size was determined according to the Sentinel-2 MSI spatial resolution. Within the test sites LAI was measured at five points located on the scheme shown in Fig. 4. A gap fraction analysis was used for field LAI estimations.

LAI Calculation Using a Dual-Polarization Radar Image

At the moment, the problem of LAI calculation using radar imaging is discussed intensely. Many authors recommend engaging a color-synthesized composite of multi-polarization radar bands for vegetation classification and biophysical parameters estimation. In this regard the main efforts are focused on the agricultural crops assessment. Radar signal

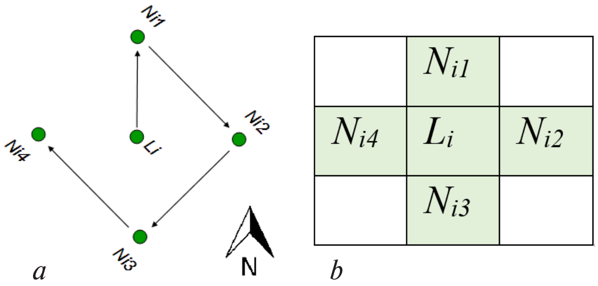

Fig. 4. Scheme of the test site *a* – within a plant community and *b* – in the projection of the image

parameters such as reflectance and scattering in different polarization bans are analyzed for crop types' separation and LAI/biomass estimation. However, it is quite obvious that the radar signal parameters are depended heavily on imaging conditions, mutual orientation of viewing direction and land surface. This circumstance causes serious problems with the accuracy of LAI's radar measurements. So, the differential reflectivity $z_{DR} = \sigma^0_{VV}/\sigma^0_{HH}$ calibration was offered using specific differential phase KDP for rainfall intensity estimation from dual-polarization radar measurements. A special calibration of dual-polarization radar measurements taking into account the local incidence angle and volumetric surface soil moisture is used for LAI calculation of maize and winter wheat. The polarization discrimination ratio $PDR = (\sigma^0_{VV} - \sigma^0_{HH})/(\sigma^0_{VV} + \sigma^0_{HH})$ was also used to estimate LAI/biomass of rice by multi-temporal radar measurements. The coefficient of determination $R^2 = 0.88$ value was achieved for LAI. It also was reported about 0.81 correlation value between the dual-polarization radar measurements and LAI for broad-leaved crops. As for the evaluation of LAI of forest vegetation, this is a more challenging problem, and its accuracy is significantly worse. To address this problem, the multi-temporal measurements are commonly performed, as well as radar and optical data fusion is practiced.

In our case, a more convenient the relative difference polarization index RDPI was used to calculate LAI using backscattering coefficients σ^0_{VH}, σ^0_{VV} registered in different polarization bands and the degree of polarization τ.

The statistical relationship of raw RDPI with LAI is so weak, the coefficient of determination is about 0.45. To improve the statistical likelihood the RDPI index was adjusted by the function

$$f(\alpha, \gamma, \theta, \psi) = cos\gamma sin\theta cos(\psi - \alpha) + sin\gamma cos\theta,$$

which describes the mutual orientation of radar viewing direction and normal line of land surface (α is radar heading angle, γ is radar incidence angle, θ is terrain element slope, and ψ is terrain element aspect). The θ and ψ values are varied for different elements of land surface, and ones distribution can be restored using digital terrain elevation data (DTED). After the RDPI adjustment, the coefficient of determination value over the test sample is increased up to $R^2 = 0.64$, which is acceptable for practical applications. The LAI and RDPI$\cdot f(\alpha, \gamma, \theta, \psi)$ hyperbolic regressional relationship for a test sample of 25 ground-based LAI measurements (2016) and 18 ground-based LAI measurements (2017) is shown in Fig. 5.

Further improvement of regression accuracy can be obtained by means of the degree of polarization τ by solving an optimization problem. The first approximation of degree of polarization value was determined as average $<\sigma^0_{VH}/\sigma^0_{VV}>$ over the ground control sample. Then the τ value was refined by the parameter variation method using the iterative search algorithm. Final setting of the τ value provides a significant boost of the coefficient of determination for the current scene of radar imaging.

Results and Conclusion

The obtained regression relationship between LAI and adjusted RDPI is used to estimate the leaf area index over the area of interest. Its spatial distribution coupling with RDPI index is shown in Fig. 6. The LAI estimation mean errors, absolute and percentage, are calculated for the all sampling plots

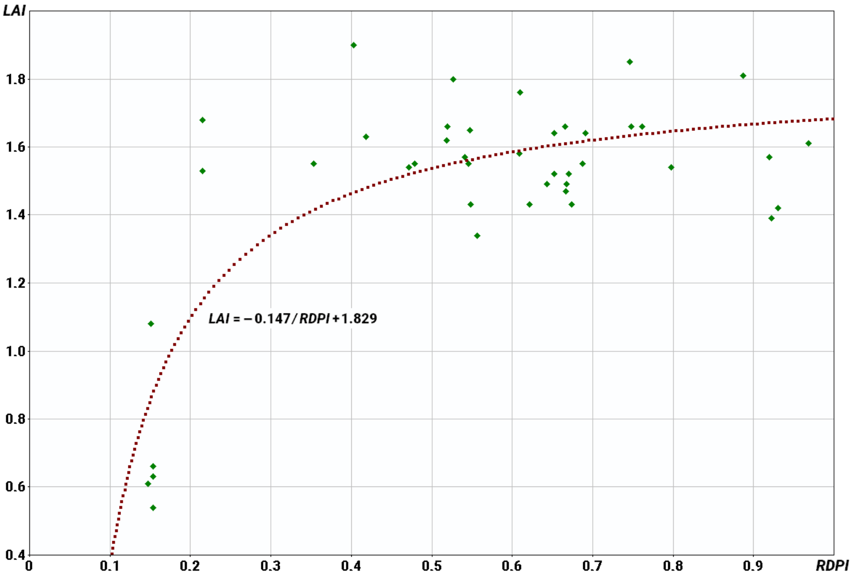

Fig. 5. The plot of regression relationship between LAI and adjusted RDPI

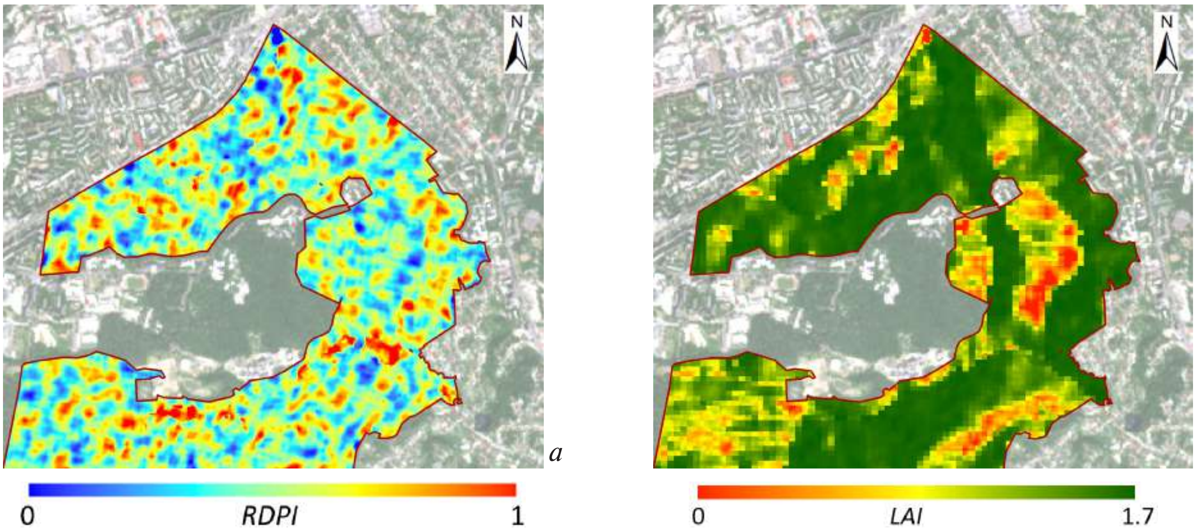

Fig. 6. RDPI (*a*) and LAI (*b*) spatial distribution over the area of interest. Indices are estimated by pre-processed Sentinel-1 dual-polarization radar image acquired in June 30, 2017

$|\Delta LAI| = 0.349$, $|\Delta LAI|/LAI = 32\%$. Generally LAI estimation demonstrate good accuracy for the all test sites (MAE = 0.110). Some weak results possibly may come from sizeable gaps in open canopy of 3D stand and rough patchy canopy surfaces of the maturing oak stand (4D). That can largely affect the VH/VV backscattering ratio.

In this study, the potential of using only SAR imagery to LAI estimations of temperate deciduous and mixed forests was under investigation. Experimental results indicated strong correlations between the LAI of different forest types and proposed RDPI index. The results also emphasize the critical importance of applying topographical adjustments for the areas with complex terrain as well as canopy structure. The study has promising results for multi-temporal monitoring for seasonal and long term analysis. It is concluded, that SAR dual-polarization data provides a good alternative to optical one that is not restricted by the requirements of clear sky conditions.

It is worth to direct future research at increasing the amount of field measurements and on improving the models of the use of RDPI by incorporating the additional adjusting co-drivers that affect the estimates of LAI, such as trees canopy structure, soil moisture, weather conditions, etc.

REFERENCES

1. *Stankevich S.A., Kozlova A.A., Piestova I.O., Lubskyi M.S.* Leaf area index estimation of forest using Sentinel-1 C-band SAR data / Proceedings of 5th Microwaves, Radar and Remote Sensing Symposium (MRRS-2017), August 29–31, 2017, Kyiv, Ukraine. – P. 253–257.

2. *Kozlova A.A., Piestova I.O., Lubskyi M.S.* Estimation of the seasonal leaf area index in forest plant communities using satellite-based vegetation indices / Abstracts of the 16th Ukrainian Conference on Space Research, August 22–27, 2016, Odesa, Ukraine. – P. 177.

3. *Kozlova A.A., Piestova I.O., Lubskyi M.S.* Remote estimation of the leaf area index of forest plant communities in seasonal development / State Environmental Safety: abstracts of IX Ukrainian Scientific and Practical Conference of Young Scientists and Students, April 21, 2016, Kyiv, Ukraine. – P. 197–198.

4. *Piestova I.* Quantitative vegetation mapping of urban area using high-resolution multispectral satellite imagery // Science-Based Technologies. – 2015. – V. 2. – No. 26. – P. 153–158.

SPECIFIC FORMATION OF THE INFORMATIVE SIGNS FOR SEARCHING OF THE HYDROCARBON DEPOSITS IN THE MARINE SHELF USING SATELLITE IMAGES

A. Khyzhniak, A. Porushkevych, O. Fedorovskyi

State Institution «Scientific Centre for Aerospace Research of the Earth of Institute
of Geological Sciences of NAS of Ukraine» (CASRE IGS NASU)

The hydrophysical processes which occur in the near-surface layer of the water and form its hydrothermodynamic regime are quite complicated. First of all, this is due to the flow into the water of the solar radiation and the self-radiation of the atmosphere through the atmosphere – water interface. In its turn, the aquatic environment forms its own flux of long-wave radiation. In addition, the surface layer is influenced by the convective flows occurring therein, turbulence, internal and surface waves, hydrology, wind impact, evaporation, precipitation, cloudiness, flow and surface-active substances. Experimentally it was established that in a near-surface layer a specific boundary layer is formed in a few millimeters and a gradient of temperature is several degrees. This hydrophysical formation was called the skin layer. Moreover, in most cases, the surface temperature is less than the temperature below the lying water layers – a cold skin layer. The temperature field in it is formed under the influence of various hydrophysical and other factors. It was found that the cold film is stored at a wind speed of 10 m/s, and the time of recovery of the skin layer depends on many external factors. After its destruction by the waves and other factors, the recovery time of the film can be tens of seconds. Therefore, one can assume that the existence of a cold skin-layer is a fairly stable phenomenon [1].

The anomalies of the natural origin are created due to the presence of hydrocarbon deposits. By fluid wire fault structures of the lithosphere of the shelf zone, gases from the deposits can be discharged into the water environment, forming bubbles. The mechanism of passing of the migration stream of hydrocarbon fluids through the water layer and its interaction with the water surface is caused by the number of factors, including the type of hydrology, which depends on the season and the water area. Fig. 1 shows the different states of the marine environment: on deep horizons in a stratified environment, in thermocline and in conditions of turbulence. The structure of the water environment is different at different depths, including the thermocline, and depends on the hydrological conditions, changes in temperature, salinity, underwater currents. On the Black Sea, the thermocline is during summer-autumn period is usually at a depth of 15–20 m. The disturbances

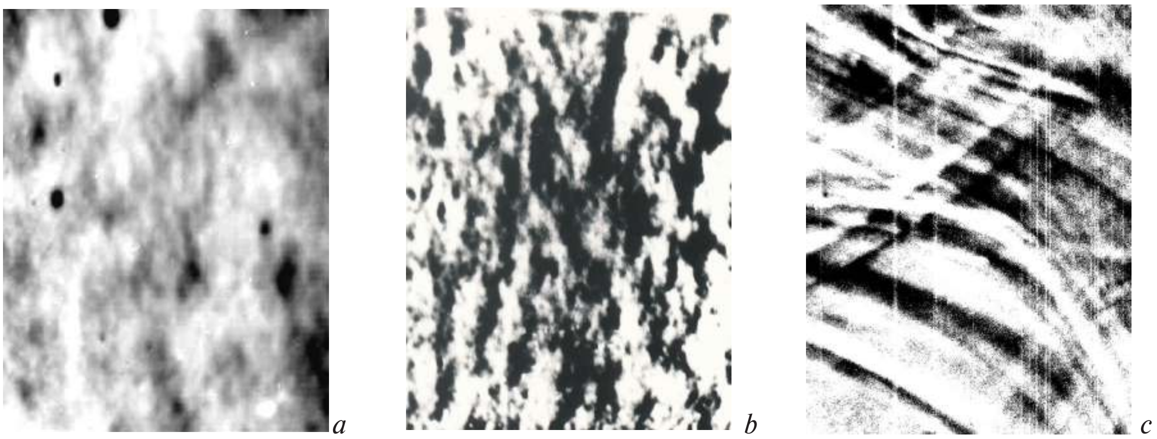

Fig. 1. Examples of a variety of marine environments: on deep horizons in a stratified environment (*a*), in thermocline (*b*), under the turbulence condition (*c*)

that occurs in it generates fluctuations in density and temperature, which propagate from the perturbation region in the form of waves.

With the hydrology close to the isotherm and with the intense flow of fluids, this can be an erlift process – lifting of cold deep water to the sea surface by the fluid flows. With the presence of the column of gradients of density in the stratified water, migrating fluids cause the formation of internal waves, which propagate to the water surface and interact with it. The resulting internal waves, reaching the water surface, cause changes in the hydrophysical characteristics of the near-surface water layer, which appear on the sea surface as anomalies of the surface temperature, and in the near-surface layer as the change in the temperature gradient which is reflected on the free water surface as the temperature anomalies that are recorded on the satellite images using the infrared (IR) spectral range [2].

Previous studies have shown that in the upper layers of the water turbulent heat transfer processes are weakened. This leads to the emergence to the surface layer of significant gradients of temperature, the value of which is determined by the intensity of heat-exchange water-air. Under normal circumstances, the surface temperature of the water is less than at the depth. Fig. 2 and 3 represent the temperature profile of the surface of the water-atmosphere and the near-surface liquid layer, measured using a thermocouple. From the graphs it can be seen that up to 2–3 mm the temperature changes fast with the depth, with the nonlinear distribution, and then begins to fall monotonically to its constant value. Fig. 3 shows the image of the shadow of the vertical section of the near-surface layer of the liquid, which shows that the phenomenon has a rather complicated structure. The upper edge of the image corresponds to the boundary of the air – water section. The magnitude of the density gradient caused by the change in the temperature is proportional to the brightness of the image [3].

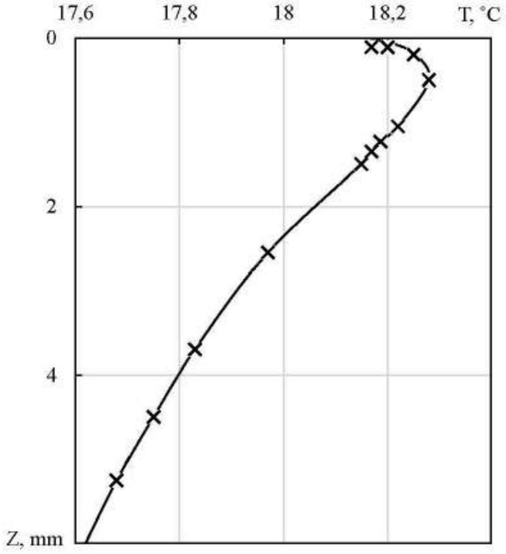

Fig. 2. Characteristic temperature profile in the near-surface of the liquid layer

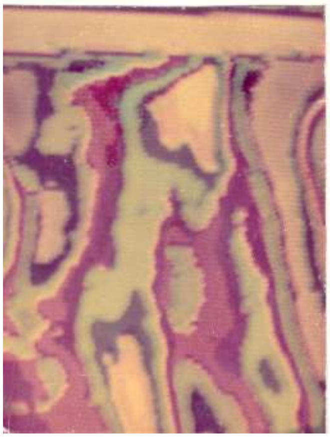

Fig. 3. Vertical section of the surface layer of a liquid

Fig. 4 shows the results of laboratory studies of near-surface layer, obtained with the help of the shadow-tepler-device IAB-451. The development of microconvection in the near-surface layer for 300 seconds is visible on the given images of shadow of the vertical section of a layer. In this case, the colder surface layers, and, consequently, more severe, collapse (in the form of dark bands) down. On the received images it is possible to observe the temperature inversion in the upper layer of the studied fluid volume.

The reason for this phenomenon, with the rare exception, is that the water surface gives the heat back to the atmosphere through the radiant and turbulent heat transfer. To fulfill the condition of the heat balance, a flow that compensates these

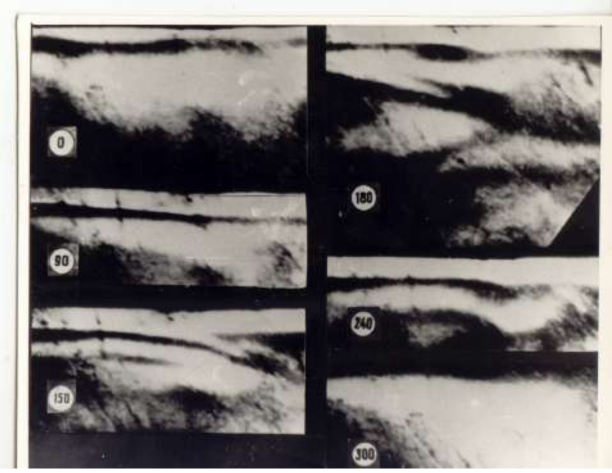

Fig. 4. Shadow patterns of the microconvection in the near-surface layer of 0.5 cm, obtained with the help of the shadow-tepler-device IAB-451

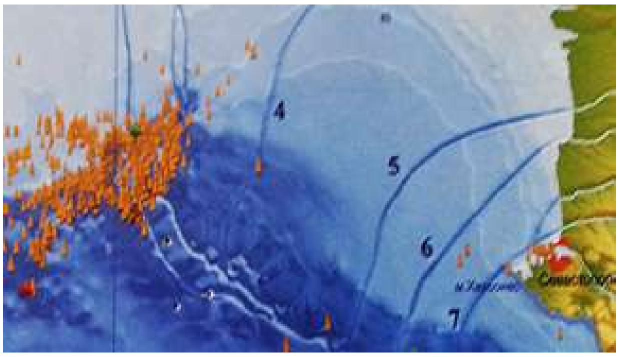

Fig. 5. The map of the bottom of the Black Sea Northwest Shelf with flares

losses to the surface from the lower layers of water must be present. An unstable stratification occurs in the surface layer, which can lead to convective movements. As a result, the upper layers of water flood into the liquid, creating cold fumes. The process of formation of such terms is periodic.

Experimental study of the hydrophysical processes in the near-surface layer of the water is associated with considerable difficulties due to its small size and impossibility to apply contact methods of measurements. This is due to the final dimensions of the recording devices, the effect of the surface tension when the sensor is moved through the water-atmosphere interface and the inertia of the measuring system. Therefore, as a rule, in the study of processes which occur in the vertical plane, non-contact photos and shadow-tepler systems are used, and on the free water surface – remote methods are used such as thermal and radiometric [3].

Fig. 6. The temperature anomaly over the «Golitsyn» deposit

Fig. 5 shows the map of the bottom of the Black Sea Northwest Shelf with flares of the hydrocarbon deposits at the depths of 500 m (yellow spots).

Fig. 6 shows the fragment of the space image (NOAA, Channel 4 (10.3–11.3 μm) of the natural temperature anomaly of BSNWs obtained over the "Golitsyn" hydrocarbon deposit (O. Kotlyar).

Fig. 6 shows the cold (black spots) and warm (bright spots) anomalies on the sea surface, that is, there are both processes of formation of anomaly: bubbles and internal waves.

In order to improve the process of analysis of the temperature anomalies on the infrared images it's proposed to use structural and texture characteristics of anomalies as an informative feature (calculate the Haralick texture features).

The physical nature of the proposed method, is to use structural and textural characteristics of the temperature anomalies, such as the size and shape of the contours of the surface image anomalies, orientation and relative positions of their constituents. The increase of the probability of forecasting and search performance of the hydrocarbon deposits caused by the fact that structural and texture features are more stable sign of informative feature on the sea surface than the temperature. Texture characteristics, despite the seasonal weather variation, preserve qualitative and quantitative assessment throughout the search time. In the works for analysis of the aerospace images [4] it was shown the importance of structure and texture of the images, as well as methods for their identification, including Haralick features.

Table 1 shows the values of Haralick features for the background and the temperature anomalies which differ most from each other.

Table 1

Values of the Haralick features for anomalies and temperature background (Fig. 6)

Haralick features	Anomaly	Background
1. Contrast	4.88	0.01
2. Sum of Squares: Variance	288	0.37
3. Sum Entropy	4.24	0.41
4. Entropy	5.18	0.42
5. Difference Entropy	1.93	0.08

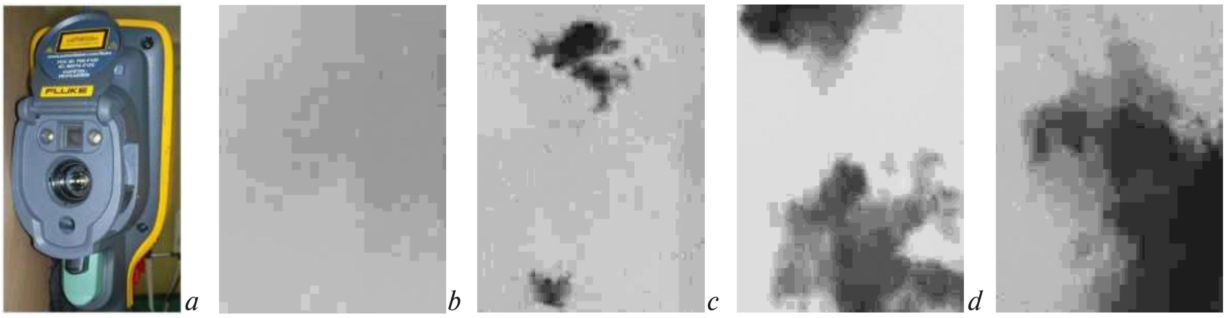

Fig. 7. Thermal imager (*a*), infrared images of the temperature background (*b*), temperature anomalies of different times of existence on the water surface of the hydrodynamic channel (*c, d, e*)

As it's seen from the Table the Haralick features for all parameters of the anomaly have the maximum value in relation to the temperature background.

For the in-depth study and modeling of these processes, the results of studies that were performed in the hydrodynamic channel of the Institute of Hydromechanics of the National Academy of Sciences of Ukraine with a self-propelled model (Fig. 7) were used. The model created hydrodynamic disturbances (HDD) that were recorded remotely by the thermal imager: the spectral range 7.5–14 microns, field of view 22.5°–31° (S. Dugin, I. Pestova).

During the movement of the underwater model in the stratified aquatic the zone of HDD is formed in the form of a turbulent flow environment on the horizon of motion, which is determined by the diffusion processes of the transfer from the object of the momentum, as well as heat and mass. The second zone is wide and develop on the different horizons up to the free water surface, which occurs due to the hydrodynamic pressure of the object's body and wave motions (ship internal waves (SIW). This zone can form the so-called blue-foot trace on the surface in the form of the temperature anomalies.

Table 2

Values of the Haralick features for anomalies of the different lifetimes and temperature background (Fig. 7)

Haralick features	Background	Anomalies		
	b	c	d	e
Correlation	0.97	0.97	0.99	1.0
Sum of Squares: Variance	219	219	2923	3060
Sum Variance	869	869	11669	12222
Entropy	9.1	9.1	10	11
Difference Entropy	2.8	2.8	3.2	3.3

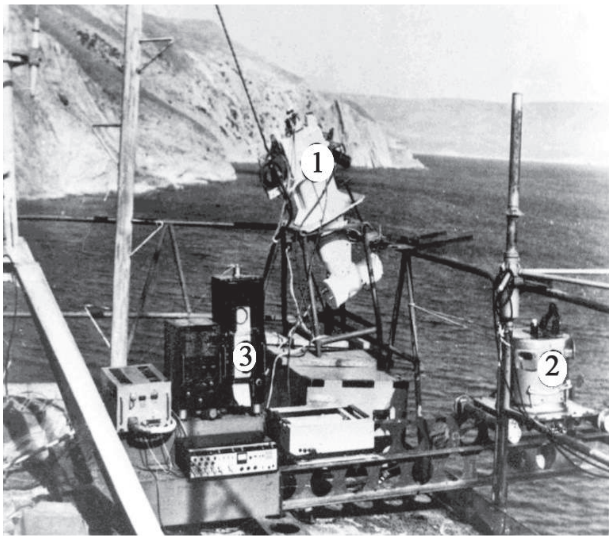

Fig. 8. The naval platform with the equipment: *1* – IR radiometer, *2* – Scanning thermal imager, *3* – Recorder

Table 2 shows the values of Haralick features for the background and the temperature anomalies which differ most from each other.

It's clear from the Table that the anomaly has the maximum value for different lifetimes, in relation to the temperature background for all Haralick features. In order to study the process of formation of the temperature anomalies on the water surface caused by the present hydrocarbon deposits, the previously obtained experimental data (O. Fedorovsky, V. Filimonov) on the formation of temperature anomalies on the free sea surface of the Black Sea in the summer from the sea platform (Fig. 8) with a self-propelled underwater model which generated hydrodynamic disturbances (HDD). The infrared radiometer (Fig. 8, *1*), the high-sensing scanning thermal imager (*2*) with spectral range of 3.5–5.2 microns and spatial resolution on a water surface of 1 m, system of recording on electrochemical paper (*3*) were used for the recordings.

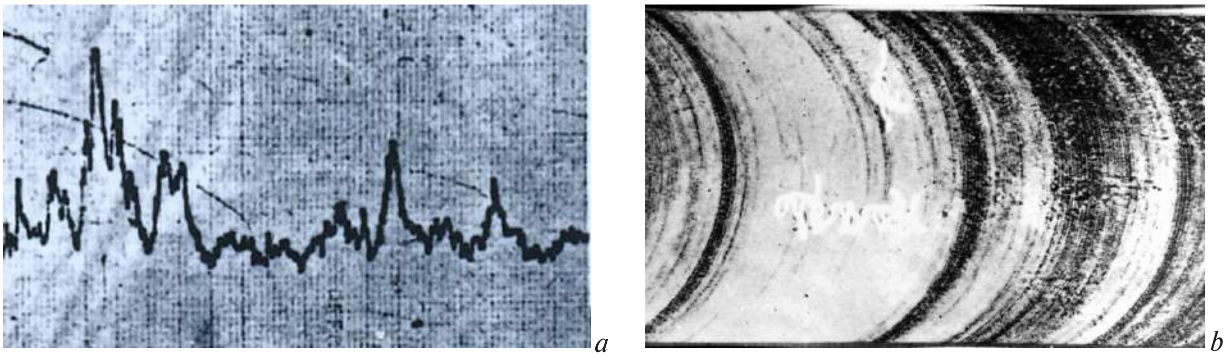
a *b*

Fig. 9. The recorded signal of the temperature anomaly on the surface of the sea: *a* – oscillogram of the radiometer, *b* – the two-dimensional record of the measurements from the scanning thermal imager on the electrochemical paper

The self-propelled model was moving under the platform up to 5 meters depths.

Fig. 9 shows the results of the experiment: *a* – oscillogram of the radiometer, *b* – two-dimensional record of the measurements from the scanning thermal imager on the electrochemical paper. The arched view of the temperature anomalies is related to the relationship between the scanning speed and the speed of the model and the drawing of the paper.

Table 3

The values of the Haralick texture features for temperature anomalies and for the background (Fig. 9, b)

Haralick texture features	Anomalies	Background
1. Contrast	1185	2348
2. Correlation	0.91	0.71
3. Sum of Squares: Variance	7264	4081
4. Inverse Difference Moment	0.18	0.06
5. Sum Variance	2787	1397
6. Entropy	12	14
7. Measure of Correlation 1	0.18	0.08
8. Measure of Correlation 2	0.95	0.82

Calculations of the parameters of the Haralick texture features of the temperature anomalies using infrared image were performed.

From the Table 3 it’s clear that for the Haralick texture features 2, 3, 4, 5, 7, 8 the temperature anomaly has a maximum value, and for the features 1 and 6 – minimum value in relation to the temperature background.

The obtained results of the experiment serve as the basis for the formation of informative for searching the temperature anomalies above the hydrocarbon deposits.

Conclusions

The data on the formation of the thermal anomalies and their structural and textural informative features which are received from satellite images (Tabl. 1), from hydrodynamic channel (Tabl. 2) and from the model of HDD on the free sea surface (Tabl. 3) used as the basis of application of modern methods of classification of thermal fields by their origin. The wide opportunities offered by the aerospace systems for monitoring the Black Sea shelf are not limited to the conducted studies. Along with the continuation of the study of the physical nature of the surface and near-surface (temperature gradient) anomalies aerospace geomonitoring is planned to be used in combination with other measuring devices that will significantly expand the research capabilities in the detection of temperature anomalies of the hydrocarbon deposits on the sea surface.

REFERENCES

1. *Kuftarkov Yu.M., Nelepo B.A., Fedorovsky A.D.* On the temperature skin layer of the ocean // Reports of the Academy of Sciences of USSR. – 1978. – № 2. – P. 296–299 (in Russian).
2. *Nikiforovich Ye.I., Fedorovsky O.D.* Hydrothermodynamics of the near-surface layer of a liquid // Bulletin of the Academy of Sciences of the USSR. – 1984. – No. 11. – P. 15–20 (in Ukrainian).
3. *Fedorovsky A.D., Nikiforovich Ye.I., Prikhod'ko N.A.* Transport processes in gas-liquid systems. – Kyiv: Naukova Dumka, 1988. – 255 p. (in Russian).
4. *Fedorovsky A.D., Yakimchuk V.G., Ryabokonenko S.A., Pakhomov I.P., Sukhanov K.Yu.* Decoding of space images of landscape complexes on the basis of structural and texture analysis // Space Science and Technology. – 2002. – V. 8. – No. 2/3. – P. 76–83 (in Russian).

SPACE BASED GEOMONITORING OF THE KILIYA DELTA OF THE DANUBE

O. Fedorovskyi[1], A. Khyzhniak[1], O. Tomchenko[1], T. Diachenko[2], A. Porushkevych[1]

[1] State Institution «Scientific Centre for Aerospace Research of the Earth of Institute
of Geological Sciences of NAS of Ukraine» (CASRE IGS NASU)

[2] Institute of hydrobiology of the National Academy of Sciences of Ukraine (IHB NASU)

During the analysis of the satellite images the maximum probability of morphological features detection must be ensured. The set of these features allows to recognize the components of the landscape and its type. Experience shows that the satellite image with higher resolution isn't always more informative. For example, small scale images reflect common generalized geological structure features, medium scale ones – relief dismemberment and large scale images – relief components, kind of vegetation, water objects parameters, etc.

The delta of the most affluent Kiliya sleeve is the extremely dynamic formation. There is a change in individual components of the hydrographic network (growth and erosion of spits, sleeves silting) and in conditions of hydrobiots existence associated with it even within one vegetation season.

The aquatic-landscape systems (ALS), formed in the Kiliya part of the Danube Delta, close to the border of Ukraine and buffered by the coastal line of the sea at 5 km from its state in 1985 with a total area of 60 075 hectares was selected as the testing ground.

Medium scale satellite images from Landsat-5, 8 for the end of June – the beginning of September 1985 and 2015 years were used for retrospective analysis of Kiliya delta ALS types structure and areas. Image classifier was built using artificial neural network algorithms.

We were able to determine 6 ALS types using satellite images analysis (Fig. 1, 2, Tabl.).

Since the mouth regions of the rivers represent a self-similar hierarchical (fractal) structure which consist of repeating components of the natural

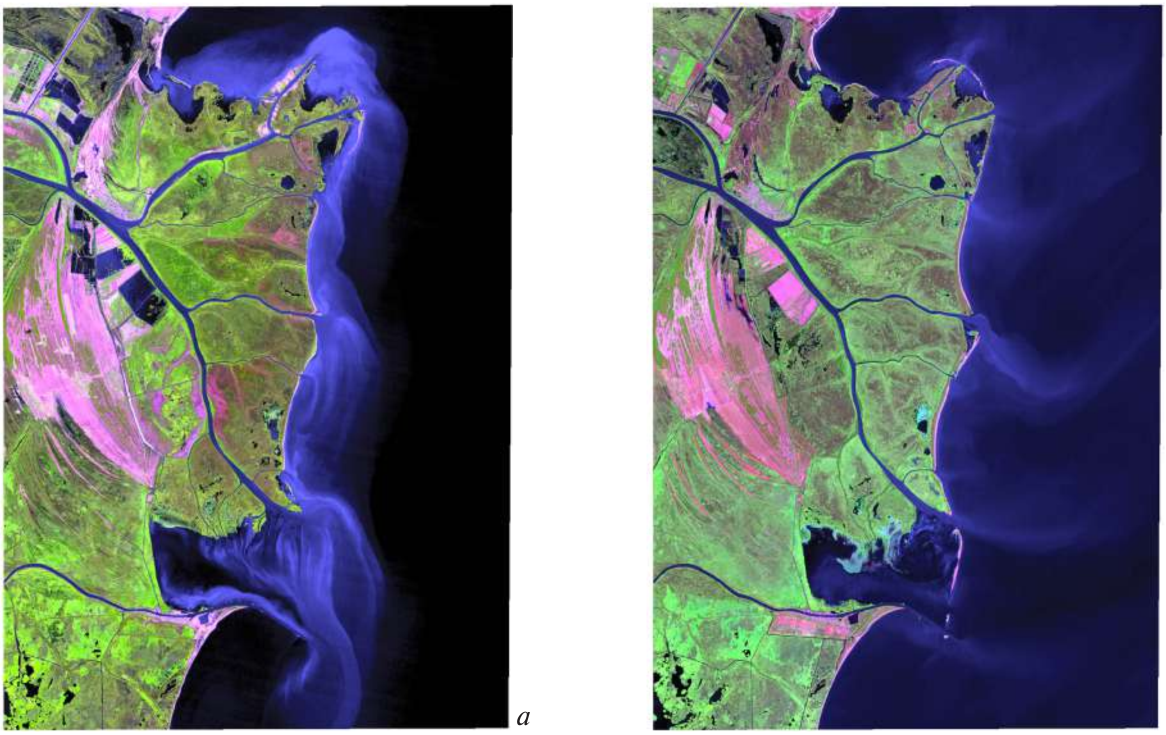

Fig. 1. Kiliya part of Danube delta satellite images from Landsat-5, 8 which were used for determination of ALS: *a* – for 1985.07.30, *b* – for 2015.07.20

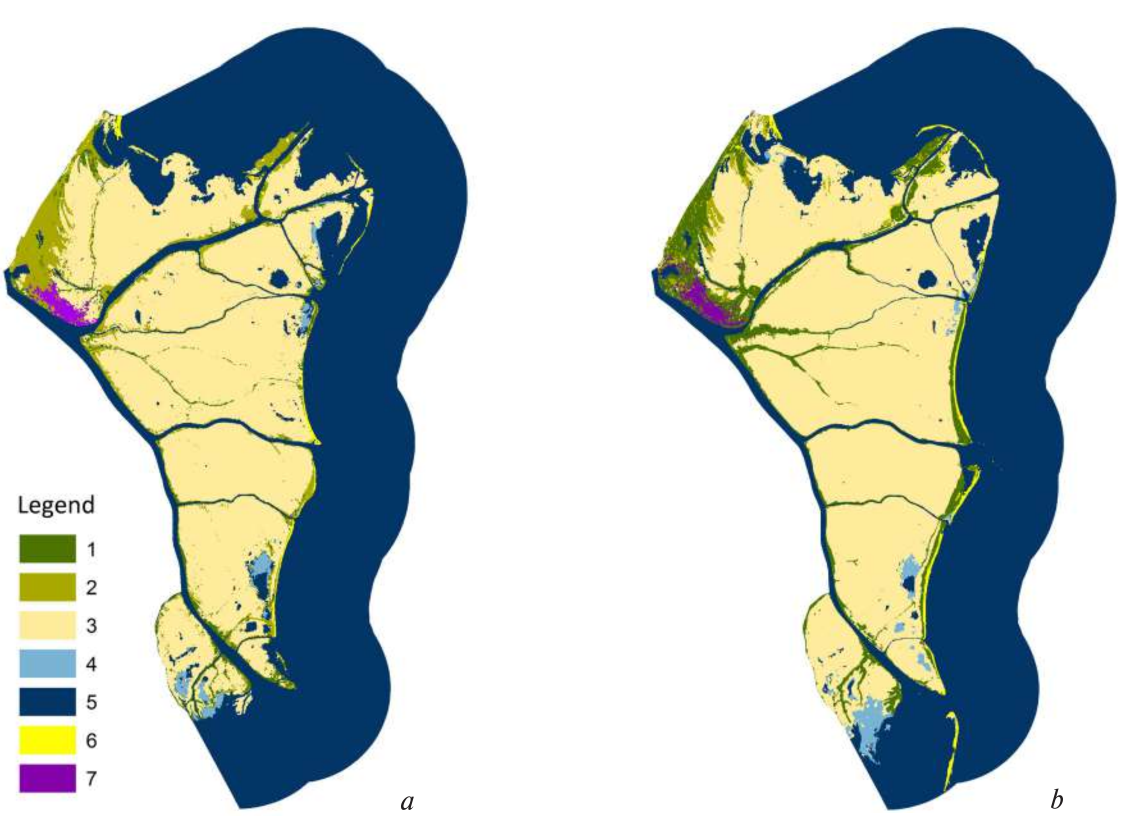

Fig. 2. Results of pixel-oriented classification of remotely sensed data of the medium resolution done by artificial neural network for determination of overfitocenotic level ALS (*a* – for 1985.07.30, *b* – for 2015.07.20)

Legend: 1 – woody-shrub vegetation, 2 – herbal vegetation, 3 – flood-marsh vegetation, 4 – pleistophyte groups, 5 – sand, 6 – water, 7 – anthropogenically created delta objects

Kiliya part of Danube delta ALS areas (ha)

Types ALS	1985	2015
Woody-shrub vegetation	1309.4	3325.3
Herbal vegetation	2258.6	534.7
Flood-marsh vegetation	22030.3	23437.5
Pleistophyte groups	419.4	632.0
Sand	239.4	488.3
Water	33535.8	31342.1

landscape at the various structural levels, the application of multifractal analysis to study the variability of the components of the delta territory is reasonable [2].

To determine the variability of the various components and assess the degree of deviation from the uniform distribution by type, the generalized multifractal dimensions are used $D_q = \tau(q)/(1-q)$ $q \neq 1$, where q – degree of moment (statistical amount), $\tau(q)$ – cacheing exponent.

The function D_q shows how heterogeneous is the distribution of ALS by types and how this distribution differs from the uniform one. The function D_q, is called the spectrum of the generalized dimensions of the Reny multifractal. For $q \to +\infty$, the main contribution to the sum is made by the dominant types of ALS, which are characterized by the largest values of p_l, and for $q \to -\infty$, the main contribution is made up of components with small values p_l which are rare types of the landscape components of the ALS. There is the consideration not to use more than ten values of integers q, and this limitation is used in this paper.

If the distribution of components by types is not the same, then the fractal is heterogeneous (multifractal), and the spectrum of the generalized fractal dimensions D_q is used for this description. The value of $D(q)$ is invariant to the size of the sample (area, scale).

The existence of the multifractal structure of the mouth regions of the rivers is established by verifying the fulfillment of the two necessary conditions of distribution by type:

1) the degree of dependence of the growth of components of the multifractal measure on the sample size;

2) non-increasing form of the function of the spectrum of generalized dimensions $D(q)$.

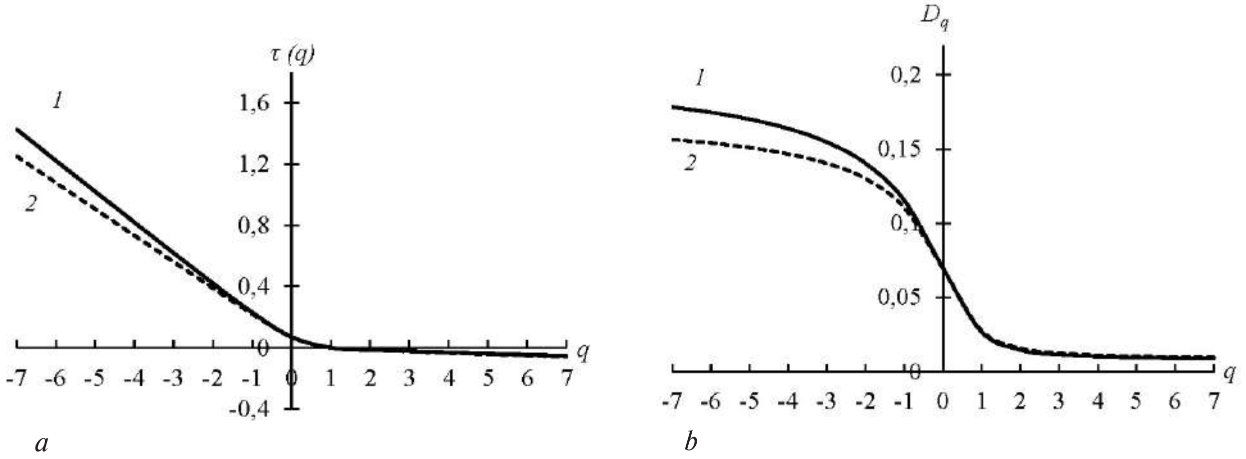

Fig. 3. Estimation of the variability using remotely sensed data (1 — 2015, 2 — 1985):
a — graphs of the dependence of the exponent τ on *q*, *b* — graphs of functions D_q, $q \in [-7, 7]$

Results and discussion

The evaluation of the ALS variability based on the remotely sensed data of the remote sensing data for 1985 and 2015 was performed using the indices of the variability (generalized dimensions of Reny) as the integral estimates. In his aspect, such indices allow to estimate the dynamics of the variability of the ALS.

Fig. 3, *a* shows the nonlinear nature of the dependences τ(*q*) obtained during the study of ALS distribution by type on the example of the Kiliya Delta of the Danube. The nonlinear nature of the dependences τ(*q*) and their deviation from the linear shows a significant variation in the distribution of components by type.

The Fig. 3, *b* shows the results of calculating the dynamics of integral estimations of the ALS variability for the period 1985–2015. From the Fig. 3, it can be concluded that the maximum variability for the analyzed time period is manifested with negative values of *q* of the indices D_q. The most sensitive to environmental processes are the few types of constituents, such as the pseudophytosis and sand spit detected using remotely sensing data.

The spatial-frequency spectrum (SFF), which is characterized by the sum of spatial components (harmonics) with amplitudes and phase shifts between these constituents corresponds to the image of the water object of the certain structure.

In order to determine the direction of the linear elements of the image, the dependence of the normalized azimuthal spectral density (ASD) of the energy spectrum ($S(\Theta)$) on the angular direction Θ is used.

If there are extended structures of different directions in the original image of the delta regions of the rivers, then there will be an expansion of the SFS in the perpendicular directions to their greatest extent. In this case, the azimuthal spectral density by directions is determined for the amplitude spectrum transformed into the polar coordinates. Angles corresponding to directions with local maximum values of the amplitude component, indicate the dominant directions of the extended elements. This shows the possibility of detecting the direction of development and the power of linear elements on the space images of the mouth regions of the rivers with the aid of two-dimensional Fourier transformations.

The proposed approach was used in the analysis of dominant lines of the Danube mouthflows.

The Danube Delta is the example of the one of the world's largest flood-littoral landscapes, and it has a coherent set of ecological-coenotic features that characterize it as a transitional natural entity – the ecoton, the river-sea type [3]. Its known that such functional objects play one of the most important roles in the biosphere, such as the zones of the contact of the energy mass interchange and the increased concentration of all manifestations of life, including increased biodiversity, increased activity of ecological-physiological, bio-production and all other processes of the functioning of the ecosystems. At the same time, the Delta of the Danube, as well as a number of other similar objects, is currently under intensified anthropogenic influence at the local, regional, and global levels. Such combination of the biosphere role of this unique natural complex and its current position in the natural-ecosystem-economic structure of the region makes it imperative to accelerate the study of this object at the general ecological level with the identification of the maximum possible number of ecological-coenotic interconnections and

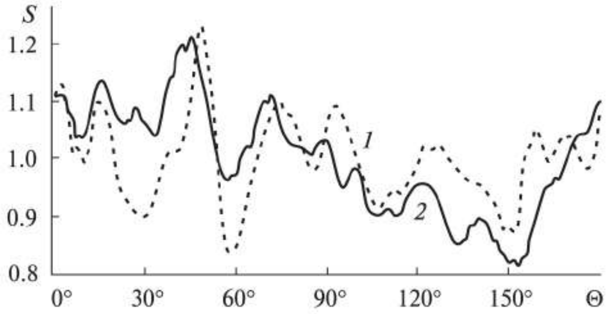

Fig. 4. The analysis of the dominant areas of the Danube mouthflows. Azimuth spectra of the Kiliya Delta of the Danube for (1 – 1985, 2 – 2015)

patterns, with the release to develop a system practical measures to support ecosystem sustainability.

Fig. 4 shows the chart of the azimuthal distribution of the SFS $S(\Theta)$.

Comparing the Fig. 4 with the image of the Kiliya Delta of the Danube, it can be noted that the peaks of the SFS at the angles of 30°, 65° and 130°–170° correspond to the main fluxes, and are more saturated, indicating the predominance of the lower frequencies. The peak of the SFS in the area of 90°–100°, obviously, corresponds to the coastal line located vertically on the satellite image.

The detected changes in the Kiliya Delta of the Danube can be explained by the fact that due to the reduction of the Danube hard drain over the last 10 years because of the construction of dams on the river and its tributaries, with the redistribution of water drainage and sediment from the Kiliya arm to Tulchinsky arm, the intensity of its movement towards the sea became almost 10 times slower (compared with the beginning of the twentieth century). Also the increase of the water level in the Black Sea played its role Sea. The formation of new sleeves in the delta has ceased, on the contrary, there is process of dying of many lateral watercourses. As a rule, from two adjacent sleeves, activates one which is shorter and more aquiferous.

As a result of the redistribution of the drain between the sleeves, the dying out of one and the activation of others, there is a transverse displacement of the channel of the main sleeve in each node of the branch, since, as the side sleeve dies, the angle of its branch rapidly increases, and the angle of continuation of the main channel decreases. The channel of the main sleeve below the branch node shifts toward the shore, from which the dying sleeve starts, and the higher node of the branching – in the opposite direction. The curvature of the channels leads to the downward movement of the side swaddling, which are in the leaks of small sleeves.

The comparison of the dynamics of the dominant directions of the mouths of the Danube and

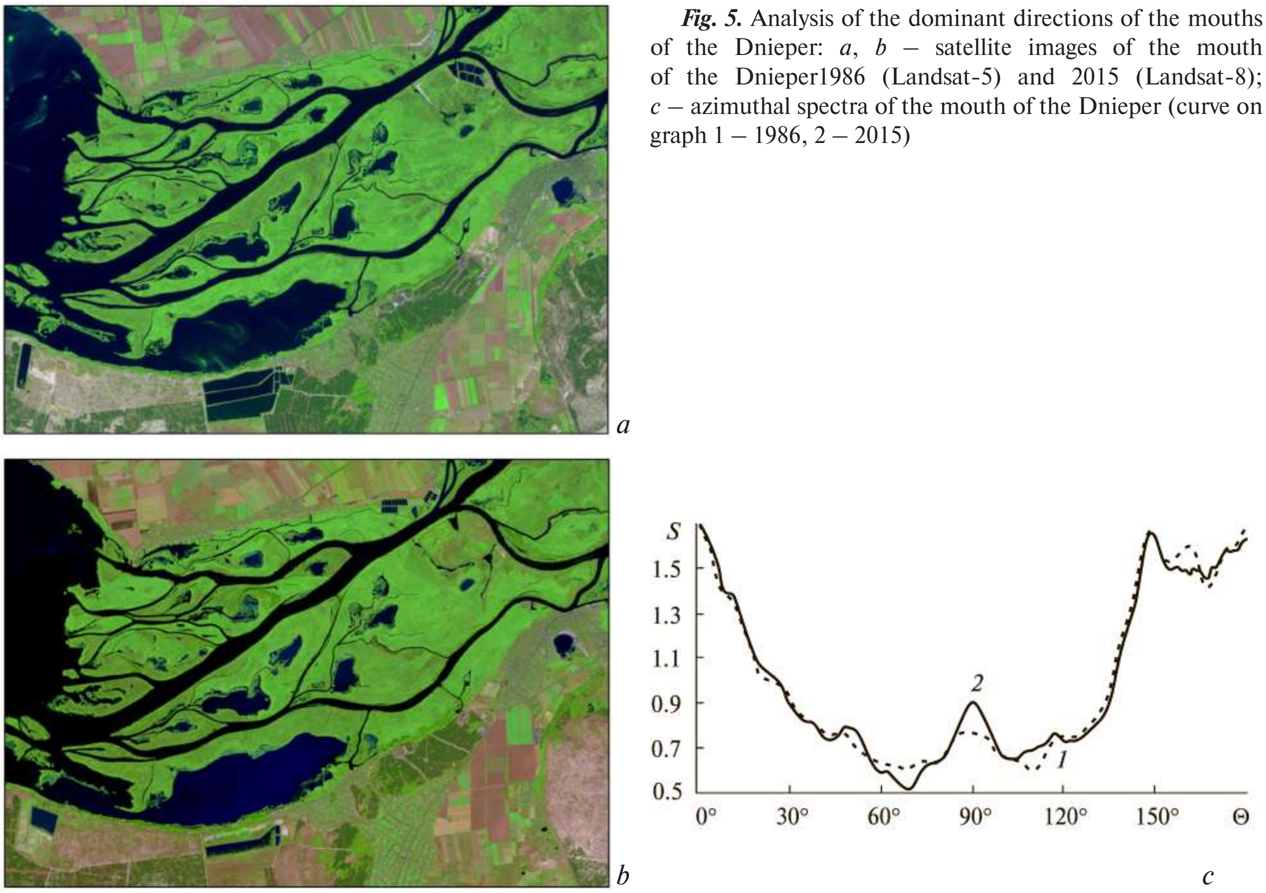

Fig. 5. Analysis of the dominant directions of the mouths of the Dnieper: *a*, *b* – satellite images of the mouth of the Dnieper1986 (Landsat-5) and 2015 (Landsat-8); *c* – azimuthal spectra of the mouth of the Dnieper (curve on graph 1 – 1986, 2 – 2015)

the Dnieper is the object of interest. Fig. 5, *a*, *b* show the satellite images of the mouth of the Dnieper for 1986 and 2015 respectively. Fig. 5, *c* shows the plot of the azimuthal distribution of the SFS from the water streams.

Fig. 5, *c* shows that the spectra of images of the mouth of the Dnieper in 1986 and 2015 remained practically unchanged neither in intensity nor in the azimuthal location of the SFS. In accordance with Fig. 5, *c*, maximum in the range of 150°–175° characterize the main streams of the mouth of the Dnieper.

The extended analysis of the dynamics of the water flows of the Kiliya Delta of the Danube in 2015 was carried out in months: May, June, July, August, September, October, and November in addition the analysis of the Danube flows in 1985 and 2015. Fig. 5 shows the results of research on ASD for each of the above months in 2015.

The fact that the Dnieper estuary is a kind of continuation of the cascade of the Dnieper reservoirs, its lowest step, but created by natural factors (rise of sea level and flooding) under conditions analogous to the building of the Dnieper valley by the hydroelectric dams, may be the explanation of the obtained result. The observed uplift of the spectrum at the regions of 0° and 180° shows the influence of the shoreline and coastal zone on the azimuthal spectra.

It follows from the Fig. 6 that despite constant location of the watercourses, the intensity of the water flow substantially changed depending on months. The most affluent months were October and May, and the shallowest months were November and July, which is typical for the seasons.

REFERENCES

1. *Tomchenko O.V., Khyzhniak A.V., Dyachenko T.M., Fedorovsky O.D.* Assessment of the variability of landscape components of river's mouth areas (by example of the Anankin lake) // Reports of NAS of Ukraine. – 2018. – No. 2. – P. 85–92 (in Ukrainian).

2. *Khyzhniak A.V., Tomchenko O.V., Dyachenko T.M., Fedorovsky O.D.* Multifractal analysis of the components flood-littoral landscape of the Danube's Kiliya delta based on space and ground information // Environmental safety and natural resources. – 2017. – No. 3–4 (24). – P. 124–132 (in Ukrainian).

3. *Fedorovsky O.D., Khyzhniak A.V., Diachenko T.N., Yakimchuk V.G., Pidhorniak D.L., Sukhanov K.Yu., Tomchenko O.V.* Space monitoring of water stream in estuarial areas (by the example of the Dnieper and the Danube) // Space Science and Technology. – 2017. – No. 23(2). – P. 11–16 (in Ukrainian).

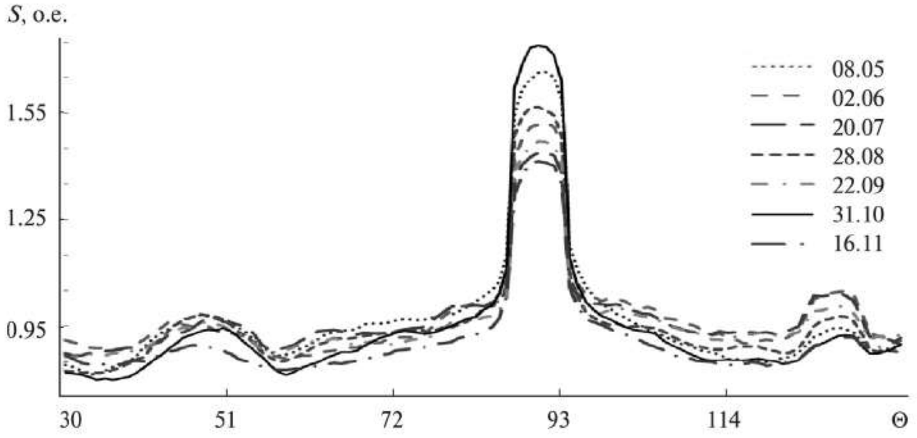

Fig. 6. Azimuthal spectra of the water streams of the Kiliya Delta of the Danube for seven dates from May to November 2015

TECHNOLOGY DETECTION OF LOCAL AREAS OF ILLEGAL AMBER MINING WITH THE USE OF LANDSAT MULTISPECTRAL SATELLITE IMAGERY DATA

V. Filipovich, R. Shevhuck

State Institution «Scientific Centre for Aerospace Research of the Earth of Institute
of Geological Sciences of NAS of Ukraine» (CASRE IGS NASU)

Illegal amber mining in Ukraine has reached catastrophic dimensions which leads to numerous negative consequences. They are: ecological problems, economical and financial losses of the state and deterioration of criminal situation in mining regions. A lot of actions need to be done to confront this and one of them is development of disturbed land monitoring. The solution of this problem is possible by using multispectral satellite data which has a number of advantages compared to traditional methods like field measurements and aerial survey [1]. These advantages are possibility to embrace large areas, cheapness of method, high efficiency and researcher`s safety.

To date, the main achievements in this direction are highlighted in the studies of specialists of CASRE IGS NASU, Institute of Telecommunications and Global Information Space, National University of Water and Environmental Engineering. In these works possibilities of satellite multispectral images application for detection of illegal amber mining areas based on texture, spectral and temperature differences of sand dumps from surrounding environmental objects were investigated. The dynamics of the formation of such deposits was determined by calculating areas of disturbed lands for a long period of time using different time space images [2, 3, 4]. An assessment of losses of the state caused by illegal amber mining was made. But despite the existence of such studies, the problem of remote sensing data application for satellite monitoring of illegal amber mining areas is not yet sufficiently investigated.

Illegal amber mining has number of specific features which are intensity, local and criminal character. It means that new pits of small size often guarded by armed people of unknown subordination regularly appear on the territories covered by the «amber rush». It`s very difficult to identify such pits using existing technologies in absence of high resolution images. The point is these techniques based on supervised classification and visual interpretation has to be done before. It is impossible to exclude a person from this process due to the imperfection of pattern recognition algorithms; therefore the accuracy of the result depends on the experience of the researcher, his knowledge base and the peculiarities of image information perception. The main task of the researcher is to accurately determine the reference areas ("region of interest") that would have the signature of the search object with the maximum contrast to other parts environment. Very often similar in spectral features, but different in origin objects can be included into one class after classification is performed. This is especially often in the case of distinction sand dumps formed by illegal mining and open sands formed by deforestation and other economic activities. In addition, the size of such areas can embrace only one pixel in the Landsat images (usually near-lying several sample pits made to search for new deposits), which makes it impossible to detect them at the stage of visual decoding and to assign to ROI. There is also another technology exist based on temperature differences between the surface objects, but the accuracy of its results is even lower.

Effective solution to this problem could be the use of high resolution satellite images (0.5–2.0 m), but such data are commercial and its price per km^2 varies between $ 15–30, while the total area of the territory covered by illegal amber extraction is about 14 thousand km^2 [1]. At high intensity of illegal extraction, monitoring should be performed on average once a month (in summer months more frequently, and in winter mining activity is practically non-existent). As a result, the cost of purchasing images may even exceed the state`s losses from illegal extraction.

Therefore, we are offering a new technique based on the use of spectral libraries to detect local amber mining sites.

The ***research methodology*** is based on the spectral differences of samples of surface sand deposits from surrounding landscapes and deforestation-disturbed soils. The source materials are satellite images of the Landsat system. The methodology consists of several stages. In the first stage, images are selected to the criteria of the absence of cloud cover and defective pixels on the study area, after which an atmospheric correction of the selected data is performed. The next stage includes visual interpretation of images and further classification and postclassification processing in order to detect large areas of disturbed by amber extraction lands. The third stage includes field spectrometric studies or laboratory studies of selected sand samples and their subsequent processing. We note that Fieldspec-3 spectro-radiometer was used for spectral analysis, and digital data processing with the further development of spectral libraries was carried out in the software products WievSpecPro and ENVI. Spectral characteristics are unique for each type of surfaces, and their difference among sand dumps caused by nature of deposits due to the depth of the land disturbance, depending on the type of activity (Fig. 1). At the final stage, the classification based on spectral libraries with the detection of local areas and, if necessary, the verification of the obtained results is performed. It should be noted that the spectral characteristics of sand dumps from the same territory may vary at different times; depending on the humidity and change in the depth of the pits therefore it is expedient to periodically repeat the field spectrometry or sampling.

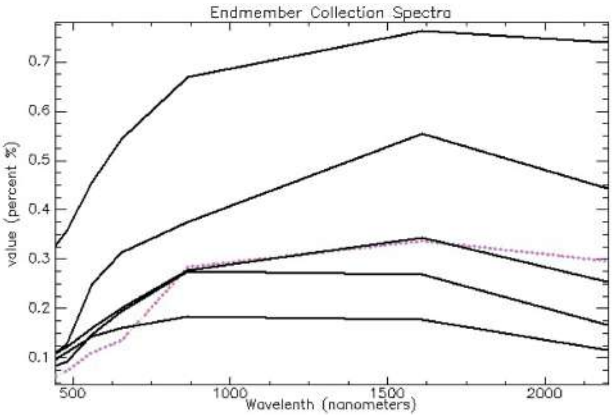

Fig. 1. Spectral characteristics of sand surface deposits. Solid lines – in the areas of amber extraction, hatched in places of deforestation

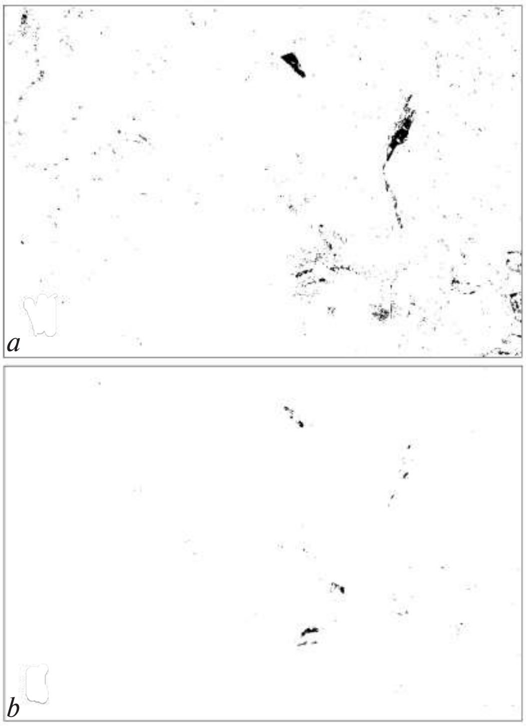

Fig. 2. The area of open sand sediments (*a*) and the area of disturbed by illegal amber mining soil and vegetation layer (*b*) in relation to the total square of the study surface as of October 18, 2017

The results of the study. As a research area, we selected the territory of the Syrnitsa occurrence of the Klesivsko-Perzhanska amber-bearing zone between the villages of Syrnitsa, Kozuli and Slovechno of Ovruch district of Zhytomyr region with a total square of 488.7 km^2. Space images taken by Landsat 8 satellite OLI / TIRS sensor were used for the study. In the initial stages, the open-surface sand areas among other landscapes were distinguished by the method of visual interpretation and using supervised classification named "Maximum Likelihood" (Fig. 2).

The next step was field sampling of surface sediments for spectrometry in laboratory conditions. After digital processing of primary data and building of spectral libraries, we managed to distinguish the lands disturbed by the illegal mining of amber. As a result of the study, several large and more than two dozen local small plots were discovered. The largest of them is situated to the west of village Antonovichy. Large groups of local areas were found in the valley of the Slovechna River near the villages of Kozuli and Begun to the northwest of the Dubi village, which are indicating the beginning of illegal mining in these places (Fig. 3). Smaller areas found near other villages and within the forests are clusters of pit samples made with the aim to find new deposits (Fig. 4).

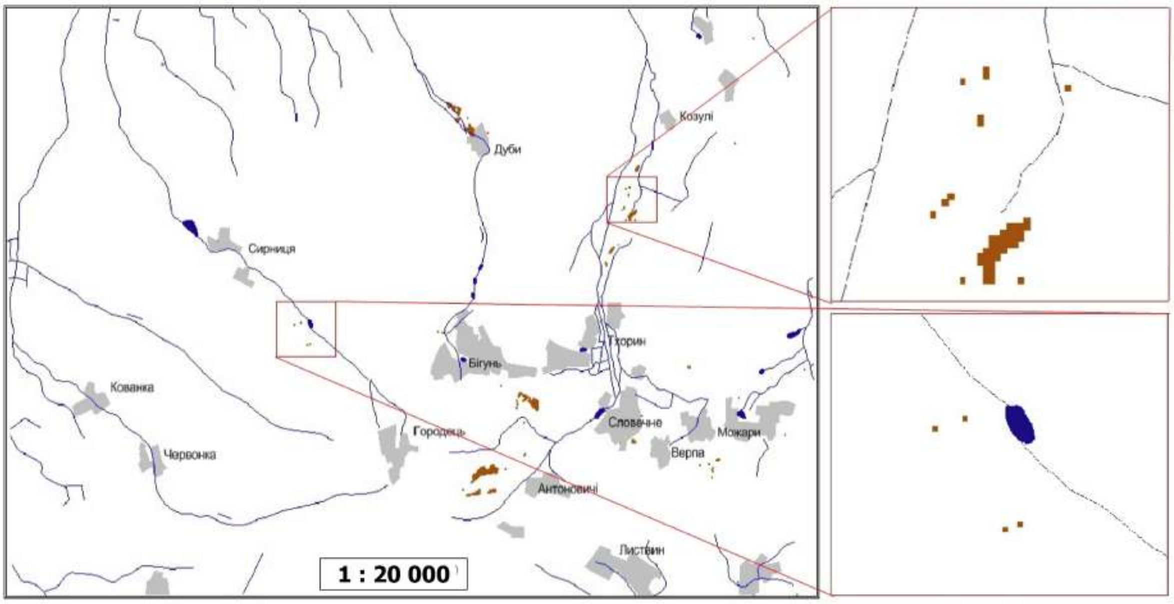

Fig. 3. Map of disturbed by illegal amber mining lands within the area of Syrnitsa occurrence

Fig. 4. The accumulation of near-laying pit-samples affects the spectral curve of the satellite image pixel obtained by the satellite Landsat and can be detected after based on spectral libraries classification

Conclusions

Research shows that with minimal financial costs, having only spectral libraries and free satellite images of the Landsat system, it is possible to perform operational control over the illegal amber mining and to identify with high accuracy the new, small square areas, in order to prevent the conduct of illegal activities.

REFERENCES

1. *Filipovich V., Shevchuk R.* The methodology and technology assessment of damage caused by Ukrainian government as a result of illegal extraction of amber // Ukrainian Journal of Remote Sensing. – 2016. – No. 11. – C. 15–21 (in Ukrainian).

2. *Filipovich V., Krilova G., Lubskiy M.* Search and localization technology of illegal amber mining areas with the use of multispectral satellite data // Modern information technologies for environmental safety and natural resource management, actions in emergency situations: abstracts of 14th. International scientific and practical conference October 5–9, 2015, Kyiv. – P. 181–198 (in Ukrainian).

3. *Filipovich V.* Operational control over illegal amber mining expansion and assessment of damage caused to the state with the use of multispectral satellite data // Environmental safety and natural resources. – 2015. – No. 4. – P. 91–97 (in Ukrainian).

4. *Filipovich V.* Satellite monitoring for the areas of illegal extraction of amber // Ukrainian Journal of Remote Sensing. – 2015. – No. 6. – P. 4–7 (in Ukrainian).

NANOSATELLITE POLYITAN-2-SAU: DYNAMIC AND STRENGTH ANALYSIS DURING REMOVAL

A. Tsybenko, B. Rassamakin, A. Rybalka
National Technical University of Ukraine «Igor Sikorsky Kyiv Polytechnic Institute» (NTUU «KPI»)

Nanosatellite (NS) PolyITAN-2-SAU was developed at NTUU «KPI» in the framework of the international space project QB50 under the overall coordination of the Institute of Hydrodynamics von Karman (Belgium). The main task of the QB50 project is to study the Earth's climate change. At present the PolyITAN-2-SAU launched into the near-Earth orbit is part of the scientific space network intended for studying the thermosphere. The NS carries a payload on board – an experimental sensor for analyzing the oncoming gas flow FIPEX, capable of distinguishing and measuring the characteristics of atomic and molecular oxygen, which is the main element at altitudes of 90–420 km from the earth's surface. This is important for the assessment of thermosphere models.

PolyITAN-2-SAU is made according to the non-hermetic scheme in the CubeSat satellite bus. The Cubesat program was launched at Stanford University in early 1999. The appearance of the CubeSat standard is associated with the need to solve one of the most important problems of training specialists in the space industry: practical work on the creation and operation of real, even the simplest, spacecraft in a short time (1–2 years) and with small budgets.

The existing system for designing new NS includes a number of stages, such as the choice of concept, the layout of the satellite, the creation of design and technological documentation, the calculation-theoretical, experimental, etc.

One of the most important stages in the design and ground testing is the task of ensuring the strength of the NS at various stages of its life cycle, including a comprehensive calculation and experimental analysis of the dynamics and strength of the NS.

The main and most responsible from the point of view of the mechanical loads acting on the NN is the stage of launching into orbit. At this stage, the NS experiences maximum quasistatic overloads [1], harmonic and random vibrations [2–4], impulse and acoustic effects.

The purpose of the study is a computational analysis of the dynamics and strength of the HC POLYITAN-2-SAU at the stage of excretion.

Formulation of the problem

POLYITAN-2-SAU 3D model (Fig. 1, *a*) contains a supporting frame in the form of a spatial frame on which are placed: a scientific module, the module of the orientation and stabilization system (OSS), skin panels, electronic platform (EP), antenna unit. The OSS module consists of a massive flywheel with an electric drive, a control board and two brackets, through which the attachment to the supporting frame is carried out. The EP contains five electronic boards, three rechargeable batteries and four composing racks for articulating and fixing to the supporting frame. The overall dimensions of the 3D model are 100 × 100 × 227 mm, the calculated weight is 1.8 kg.

Table 1

Mechanical characteristics of isotropic structural materials

Material	E, MPa	ν	ρ, кг/м^3	σ_Y, MPa	σ_U, MPa
АМг6	71000	0.3	2640	145	305
Д16	72000	0.3	2770	260	382
Л63	116000	0.35	8440	-	290

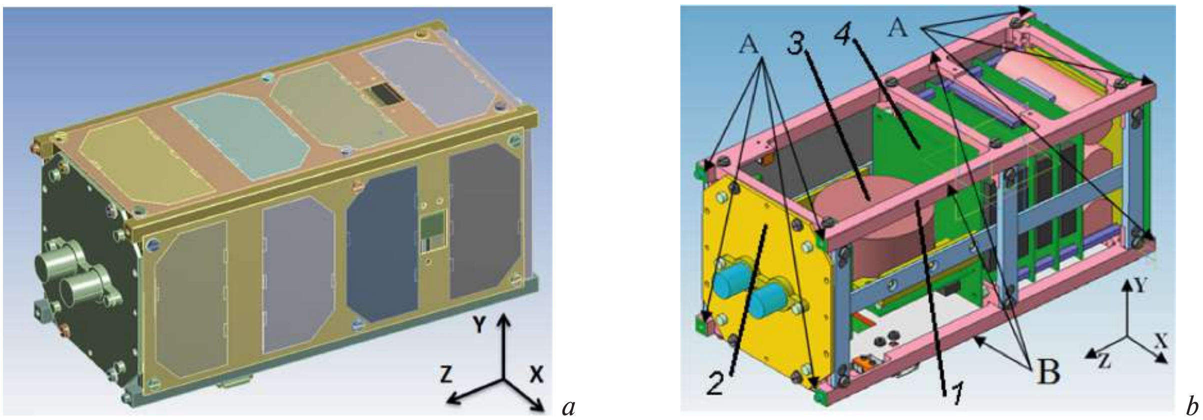

Fig. 1. The appearance of the NS POLYITAN-2-SAU (*a*) and its structural elements (*b*): *1* – frame, *2* – scientific module, *3* – OSS module, *4* – electronic platform, supporting surfaces of the frame; A – face surfaces, B – lateral ribs

The material of the frame and OSS brackets – aluminum alloy D16, antenna module and elements of the EP made from aluminum alloy AMg6, set-up columns EP made made from brass L63, electronic boards fiberglass – KAST-B. Some physical and mechanical characteristics of NS construction materials are given in Table 1, where: E is the Young's modulus, ν – Poisson's ratio, ρ – density of the material, σ_Y – yield strength limit, σ_U – ultimate strength limit.

For CAST-B: $E = 2100$ MPa, $\nu = 0.11$, $\rho = 1800$ kg/m^3, tensile and compressive strength limits, respectively $\sigma_{TU} = 85$ MPa, $\sigma_{CU} = 130$ MPa.

At the launch stage, NS is located in the launch container P-POD (Fig. 2). The NS lower end faces are supported by a spring pusher, the upper ones on the cover of the launch container. The frame lateral edges (Fig. 1, *b*) are supported by the guide rails inside the P-POD.

The dynamic and strength cycle of work implies:

- Static analysis;
- Modal analysis;
- Harmonic and random vibration analysis.

According to the requirements of QB50 and ECSS-E-HB-32-26A, for nanosatellite there is no need to check the strength of acoustic and impulse actions due to small overall dimensions of the NS and the conditions for placing the P-POD on the carrier rocket adapter.

In accordance with the requirements of the QB50 System Requirements and Recommendations, the values of the quasi-static overloads (accelerations) of the NS are assumed to be equal $a_x = a_y = a_z = 13.0g$. The minimum permissible natural oscillation frequency of the NS should not be less than 90 Hz. Harmonic and random vibrations (Table 2, Table 3) are transferred to the NS from the transport container P-POD through the support surfaces (Fig. 1, *b*).

For the modal analysis, as well as the stress-strain state of the NS under the action of quasi-static overloads, harmonic and random vibrations, the finite element method implemented in the ANSYS software

Table 2

The parameters of harmonic vibrations

Frequency, Hz	Vibration acceleration $a_x^{Harm}, a_y^{Harm}, a_z^{Harm}$, g
5–100	2.5
100–125	1.3

Table 3

Characteristics of stationary random vibrations

Frequency, Hz	Spectral densities of accelerations $S_{xx}^a = S_{yy}^a = S_{zz}^a$, g^2/Hz
20	0.01125
130	0.05625
800	0.05625
2000	0.01500

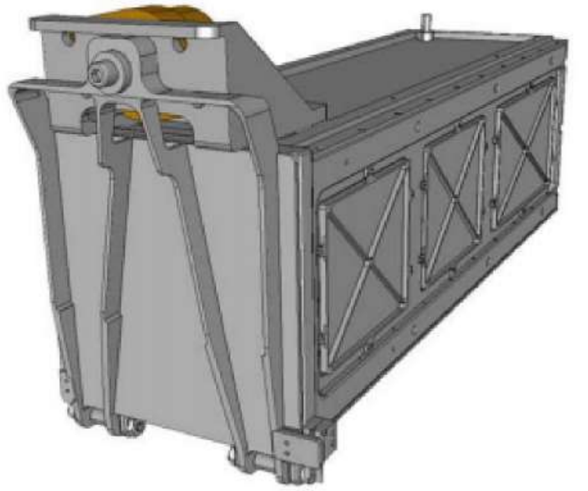

Fig. 2. General view of the P-POD excision system

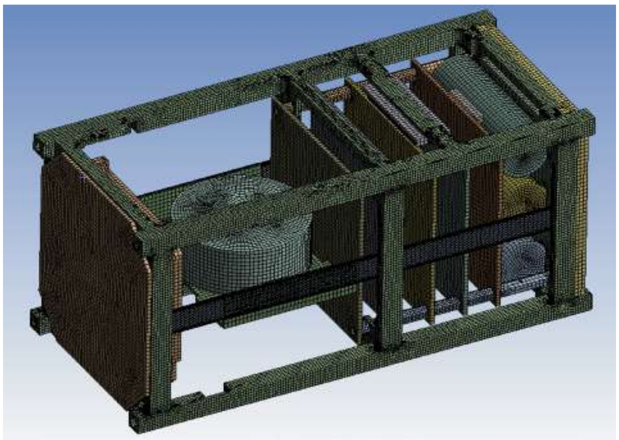

Fig. 3. NS POLYITAN-2-SAU Finite Element Model

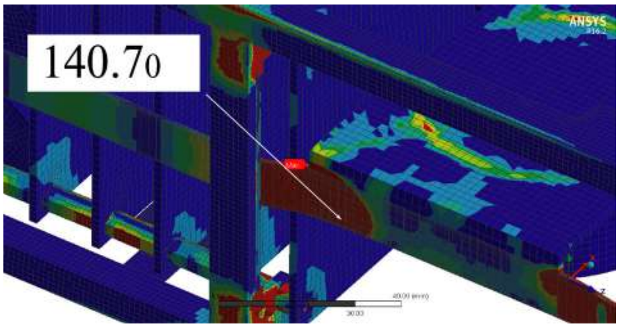

Fig. 4. Distribution of stresses in the bridge of the support frame in the section of fastening of the SOS bracket for the X-axis overload option

package [1–4] was used. An analysis of the dynamics of the NS with the action of harmonic vibrations was carried out on the basis of the modal coordinate method. For the analysis of stationary random vibrations, a combination of modal coordinate methods and spectral expansions was used [3, 4].

The simulation 3D model POLYITAN-2-SAU (Fig. 1, *a*) was simplified – elements excluded from consideration were those whose contribution to the strength and rigidity of the design of the NS can be neglected: skin, sun sensors, magnetometer, and fasteners. The masses of these structural elements were taken into account in the imitating model of the NS by uniformly "smearing" them over the corresponding contact surfaces, and the fasteners were taken into account by "additives" to the density of the material of the supporting frame.

The finite-element model (FEM) of the NS generated in the ANSYS [1] and shown in Fig. 3. For approximation of the framework, scientific module (FIPEX), stacking racks of the EP, batteries and antenna module we used 20 hexagonal finite elements (FE) SOLID186. To approximate the SOS brackets and electronic circuit boards we used FE SHELL181 with 4 layers in thickness. The articulation of plate and volumetric FE was carried out by means of massless absolutely rigid bonds based on two-node beam elements BEAM188. Conjugating fragments of FEM with different partition densities, contact elements of CONTA174 were used with the same type of FE.

The obtained rational FEM NS, consisting of 326 300 elements with 1 221 504 nodes (Fig. 3), was used for static, modal, harmonic and random vibration analysis.

Results of the study

In quasistatic analysis, the conditions for placing the NS in the shipping container were taken into account by setting zero displacements ($u_x = u_y = u_z$) of the frame supporting surfaces, with the exception of longitudinal ($u_z \neq 0$) for the side ribs (Fig. 1, *b*). It was found that the largest Mises stresses occur in the frame bridge (material – D16) near the attachment points to the SOS brackets (Fig. 4, Tabl. 4). In turn, in the stacking rack of the EP (material – L63), the stress is realized during overload in the vicinity of the contacts with the central board. Among the electronic circuit boards of the EP, the lower one

Table 4

The values of maximum equivalent stresses in NS structural elements under the action of quasi-static overloads

Direction overloading / Element constructions	X	Y	Z
Frame bridge	140.7 MPa	27.57 MPa	7.06 MPa
Battery holder	7.74 MPa	7.68 MPa	15.57 MPa
Typesetting rack EP	9.34 MPa	9.54 MPa	2.34 MPa
Fee EP	0.48 MPa	0.58 MPa	1.34 MPa

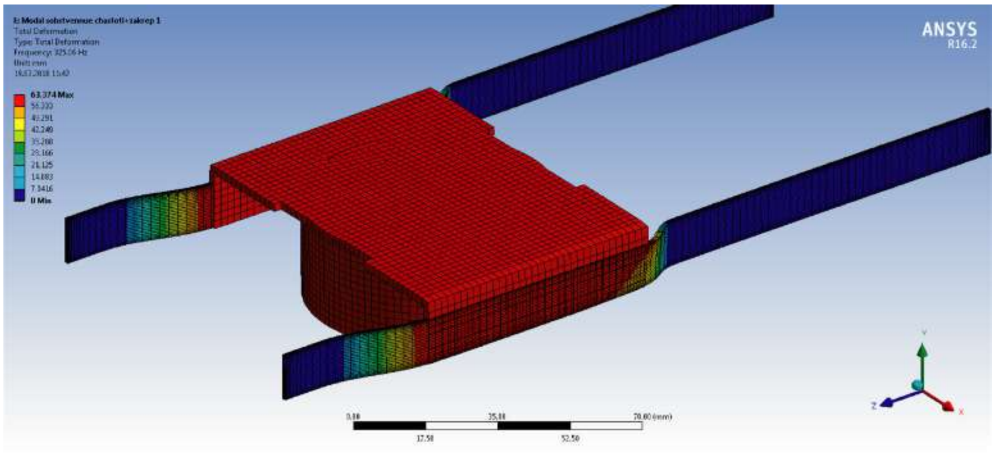

Fig. 5. 1st eigenmode of the NS ($f = 325.06$ Hz)

is the most loaded, for which in case of an overload at the points of contact with the stacking racks (Tabl. 4).

When carrying out the modal analysis, the kinematic constraints corresponding to the placement of the NS in the transport container were assumed to be identical to those of the quasistatic loading.

The results of the modal analysis are given in Tabl. 5. The lowest NS natural frequency is 325 Hz. It corresponds to the vibration shape of the electric motor in the transverse direction X (Fig. 5). Regulated QB50 System Requirements and Recommendations the lower limit of the natural frequency is 90 Hz, in this connection the condition of frequency compatibility (325 Hz > 90 Hz) is fulfilled.

When analyzing harmonic vibrations, it was taken into account that the vibration acceleration (Table 2) is in-phase transferred to the NS from the transport container through the support surfaces of the power frame (Fig. 1, *b*). When carrying out the calculations, the Rayleigh damping model [3, 4] with a constant damping coefficient of 0.02 was adopted.

Table 5

PolyItan-2-SAU Natural frequencies

Frequency number	Frequency, Hz	Frequency number	Frequency, Hz
1	325.06	6	690.51
2	673.92	7	905.11
3	678.15	8	912.16
4	678.59	9	948.01
5	682.07	10	948.35

It was established that the zone of the largest stresses equivalent in Mises (29.78 MPa) is located at the attachment point of the bracket of the SOS module to the bridge of the bearing frame, at the amplitude of vibration acceleration $a_x^{Harm} = 2.5g$ and the frequency of 100 Hz (Fig. 6). For other cases of loading (a_y^{Harm}, a_z^{Harm}), the values of the stresses equivalent to Mises are much less. The relatively low level of stress in the structural elements of the NS

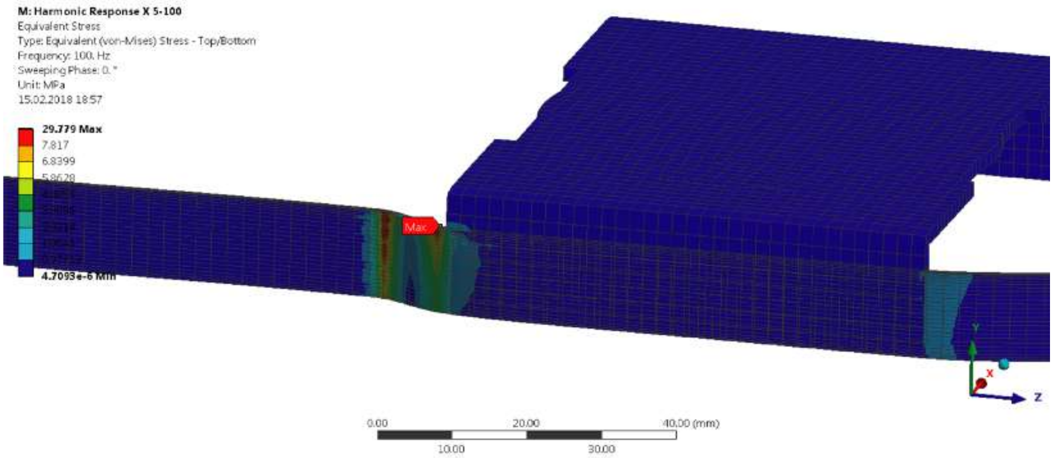

Fig. 6. The distribution of equivalent stresses from the action of harmonic (0–100 Hz) vibrations along the X axis (29.78 MPa)

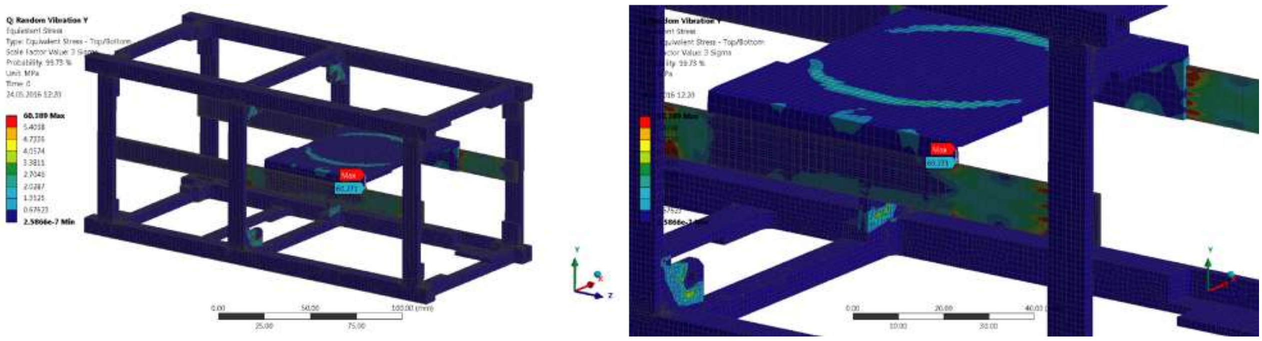

a *b*

Fig. 7. Distribution of RMS stress level 3σ under the influence of random vibrations relative to the Y axis in the supporting frame (*a*), maximum RMS of stresses in the supporting frame (*b*)

is explained by the fact that in the frequency band of the active vibrations (5–125 Hz) there are no values of the resonance frequencies (Tabl. 5).

The loading of the NS with stationary random vibrations (Tabl. 3) from the side of the transport container was carried out through the bearing surfaces of the supporting frame (Fig. 1, *b*). When carrying out the calculations, the Rayleigh damping model [3, 4] with a constant damping coefficient of 0.02 was adopted.

The maximum RMS values of the Mises stresses of level 3σ in NS structural elements for three loading variants S_{xx}^{a}, S_{yy}^{a}, S_{zz}^{a} are given in Table 6.

It is established that the zone of the greatest RMS stress is located near attachment point of the bracket of the SOS module to the bridge of the bearing frame (Fig. 7) in case of vibration loading in Y axis. The maximum RMS stress in the EP boards is achieved near the places of attachment of the middle board to the stacking EP racks for vibration loading (Fig. 8).

The generally design philosophy of a spacecraft, given in ECSS-E-HB-32-26A, involves the consideration of safety factor in strength analysis. Safety factors are introduced to compensate for inaccuracies in determining the loads, operating conditions, inaccuracy of calculation methods, and the like. The safety factors are calculated according to ECSS-E-ST-32-10C for limit and ultimate loads (Tabl. 7).

It should be noted that when analyzing the strength of electronic EP boards, the overload factor $k = 1.25$ was additionally taken into account.

Simultaneous action of loads at the stage of excretion in the strength analysis of structural elements of the NS is taken into account by linear combination of their contributions to the stressed state. The maximum values of the Mises stresses in the NS structural elements are determined as $\sigma_{VM}^{Sum} = \sigma_{VM}^{Stat} + \sigma_{VM}^{Harm} + \sigma_{VM}^{RV}$, where σ_{VM}^{Stat}, σ_{VM}^{Harm}, σ_{VM}^{RV} – respectively, for quasi-static overloads, harmonic and random vibrations.

The strength of NS is determined from the following conditions:

1) the absence of plastic deformation under the action of limit loads;

2) the absence of destruction in the structural elements of the NS under the action of design loads.

Factor of safety for limit η_L and ultimate loads η_U were determined.

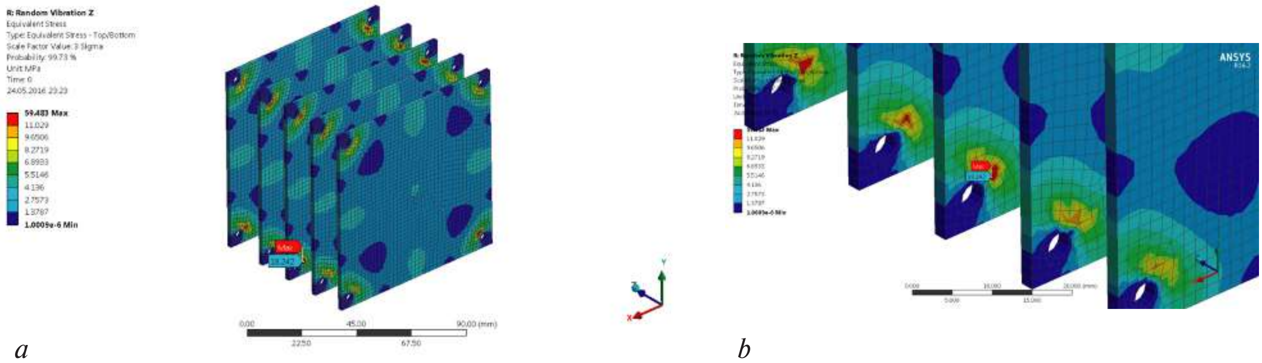

a *b*

Fig. 8. Distribution of RMS stress level 3σ under the influence of random vibrations about the Z axis in EP boards (*a*), maximum RMS voltage in EP boards (*b*)

Table 6

The maximum RMS stress 3σ level of in the elements of the NS

Element constructions \ Direction overloading	X	Y	Z
Frame bridge	8.58 MPa	60.39 MPa	59.48 MPa
Battery holder	0.04 MPa	0.19 MPa	2.62 MPa
Typesetting rack EP	7.89 MPa	14.66 MPa	24.36 MPa
Fee EP	0.66 MPa	0.82 MPa	18.24 MPa

Table 7

Safety factors for limit and ultimate loads

Load types	Limit load, f^L	Ultimate load, f^U
Quasi-static overloads	1.2	1.56
Harmonic vibrations	1.65	1.88
Random Vibration	1.65	1.88

As a result, it was established that the maximum total von Mises stresses (179.06 MPa) occur in the frame bridge near the mounting locations of the SOS brackets when the NS is loaded in the direction of the X axis. In this case, the factor of safety for the limit $\eta_L = 1.12$ and ultimate loads $\eta_U = 1.30$.

The carried out strength and dynamic analysis allows us to state that the strength of the NS at the stage of elimination is ensured.

Conclusions

1. For the developed design of the NA PolyItan-2-SAU, a rational combined ECM is constructed, containing volumetric, shell, beam and contact EC.
2. Calculated way, amplitude-frequency characteristics and parameters of VAT in PolyItan-2-SAU structural elements are determined on the basis of a single CEM under the action of quasistatic overloads, harmonic and random vibrations corresponding to the elimination stage.
3. It is established that, in accordance with the requirements, the considered PolyItan-2-SAU design is rational in terms of strength.

REFERENCES

1. *Tsybenko A.S., Rassamakin B.M., Rybalka A.A.* Stress-Strain State Investigation of Polyitan-2 Nano-Satellite under the Ascent-Stage Quasi-Static Overload Conditions// Strength of Materials. – 2017. – No. 9. – P. 381–387.

2. *Tsybenko A.S., Konyukhov A.S., Rybalka A.A.* A Study of the Dynamic Characteristics of the Cyclone-4 Launch Vehicle on the Basis of a Continuum Rod Model // Strength of Materials. – 2015. – No. 47. – P. 532–535.

3. *Tsybenko A.S., Rassamakin B.M., Rybalka A.A.* Strength of nanosatellite POLITAN-2 in action of random loads at stage of transfer to orbit // Mechanics and Advanced Technologies. – 2017. – No. 81. – P. 28–33 (in Russian).

4. *Burlak K.P., Rybalka A.A., Tsybenko A.S.* Investigation of random vibration of the nanoparticle POLYITAN-2/ Proceedings of the All-Ukrainian scientific and technical conference of young scientists and students "Innovations of youth for mechanical engineering», section "Dynamics and strength of machines» – Kyiv: NTUU "KPI", 2016. – P. 34–35 (in Ukrainian).

THIN-WALLED WELDED TRANSFORMABLE-VOLUME STRUCTURES FOR SPACE APPLICATION

L. Lobanov, V. Volkov

E.O. Paton Electric Welding Institute of NAS of Ukraine (E.O. Paton EWI NASU)

Deployable shell structures are the actively developing field of space technologies, which allow simplifying the delivery of useful load to the near-earth orbit. They are divided into three main classes: soft load-carrying, manufactured on the base of transformable framework, and rigid ones. Modern materials with new properties allow manufacturing the space deployable structures [1], [2], which are capable to increase the own volume by 10 times and more, however, the task of combination of these parameters with a sufficient strength, tightness and long-term life of the shells remains unsolved. It is evident, that the technologically accepted characteristics at simultaneous tightness are achievable only in rigid load-carrying shells, the surface transformation of which for the more compact shape requires the non-ordinary solutions in the field of technologies of a cold volumetric deforming.

At the E.O. Paton Electric Welding Institute the feasibility of volume transformation of closed all-welded metal shells, named the transformable-volume structures (TVS), was theoretically grounded. and technical solutions for its realization were found empirically [3]. The application of evident improvements at the present moment required the selection of type of the load-carrying TVS, accepted for use in the space engineering, testing of new design-technological solutions of load-carrying TVS and design of an universal calculation model, allowing determination geometric and technological parameters in designing and manufacturing of a wide range of TVS with applying different structural materials for extreme service conditions in the open space. Thus, the general aim of these works consisted in the development of scientific bases of theory for construction of deployable space-purpose shell structures. Their practical implementation is an applied development and further investigation of all-welded thin-walled load-carrying TVS, which are optimized for application in the open space conditions and can be used in the realization of existing and challenging projects of the aerospace industry.

The fulfilment of put task required the determination of:

– type of transformable surface, optimum for designing and manufacture of metal long-length space-purpose TVS, as well design diagram of TVS, which requires the development of calculation procedure, determining the relation between its geometric and technological parameters and environment factors (SEF), under the action of which the structure is operated;

– universal algorithm of transformation of surface of the selected type up to the compact shape, which will allow deploying the structure without the loss of its functional properties, and technology of volume deforming, in which the mentioned algorithm should be realized for the shell real materials.

The most interest in manufacture of transformable shells is the class of surfaces, theoretically capable to deploy into a plane, which are linear surfaces of a zero Gauss curvature: cylindrical, conical and torsion surfaces. Two first classes can be a base for design of shell structures and are widely used in the engineering. However, the isometric transformation of a cylinder by the method of a mirror reflection cannot be realized due to flatness of any its horizontal crossing, and transformation by movement is reduced in all cases to fracture of the cylindrical surface for a great number of adjacent plane polygons similarly to the known schemes of "origami folding" transformation. Movement up to plane of the cylindrical shell of real sheet materials in this case represents bending with non-zero radii along the lines of their joining, which leads to the formation of stress raisers, mostly expressed in junctions of forming stiffeners, and significant reduction in compactness of the transformable shell. In particular, the simplest principle of transformation of cylindrical-type TVS with use of the so-called hyperboloid corrugation (Fig. 1, *a*, *b*) allows reaching the transformation ratio K_T, i.e. ratio of structure

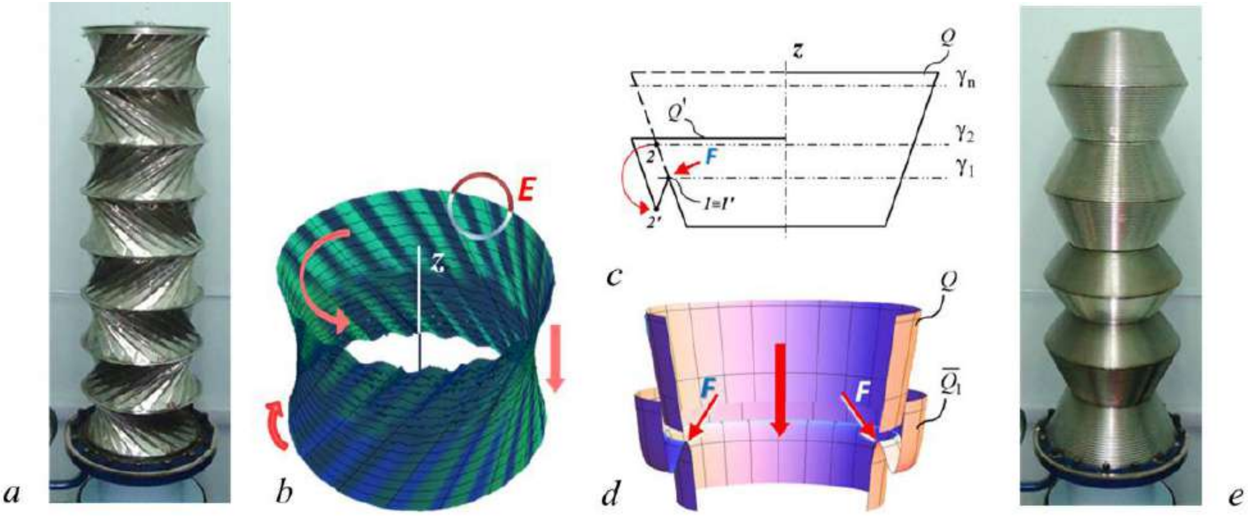

Fig. 1. Cylindrical TVS (*a*) and topological model of transformation of neutral surface of cylindrical shell into hyperboloid corrugation (*b*); transformation of neutral surface of conical shell into circular corrugation: theoretical model of isometric transformation (*c*) and graphical interpretation of mathematical model of movement during formation of fold F with non-zero radii of bending (*d*); conical TVS (*e*)

lengths in a deployable and compact state, which does not exceed the values $K_T = 4 \dots 4.5$.

The use of thin-sheet metals as a shell material and applying the mentioned methods of their transformation limit the ratio of their height and diameters of basements, which, finely, requires sectioning of the long-length shell structure. Thus, the profiles of basements of sections of the cylindrical TVS (Fig. 1, *a*) are not plane curves in any moment of deforming, therefore, the adjacent sections cannot be joined between each other without rigid fixation on the plane circular contour. Influence of edge effect near the boundary of shell rigid contour leads to typical distortion of rectilinear corrugations of the shell along the generating lines (Fig. 1, *b*, *e*), which is the main cause of a low compactness of the cylindrical–type shell transformation.

The TVS of conical type (Fig. 1, *e*) is characterized by a high deformability, however, it is capable to compensate the higher values of load without loss of stability. In addition to high values of coefficient of linear transformation, which can reach the value $K_T = 150$, the conical shell is the only one from the linear surfaces, the compact transformation of which can be realized almost without tensions and compressions (Fig. 1, *d*), and, thus., with practical approaching the theoretical model of the isometric transformation of surfaces $Q \rightarrow Q_1$ by successive mirror reflection of relatively sectional planes $\gamma_1 \dots \gamma_n$ (Fig. 1, *c*). The combination of mentioned advantages allows proving the rationality of application of the conical-type TVS in the solution of task for the manufacture of long-length TVS [4].

The considered task of manufacture of the long-length load-carrying transformable structure was oriented to the solution of the urgent problem of transfer of the useful load of (UL)-scientific equipment of 40 κN weight beyond the own ambient atmosphere of ISS, the negative effect of which on the serviceability of UL equipment is pronounced at the distance of up to 5 m from the space station external surface. Some of basic geometric parameters of TVS depend on the characteristics of a transport compartment of the rocket-carrier (maximum diameter of structure shell, its size in a transportation form and inner volume after deployment). In addition, TVS of the mentioned length under conditions of action of specified inertial and temperature loads should have a double safety factor and provide absence of deviations of a free end from UL for more than 150 mm.

For construction of calculation model of a multi-sectional conical shell the relations of main geometric parameters of the long-length multi-conical TVS were determined. Thus, according to the purposes of structure application, its total length $L = 5$ m and maximum diameter $D = 400$ mm were specified, which allowed presetting the radius of the larger basement of the conical section. Compactness of the multi-sectional structure was specified by values of its height in a compact state (h_{PACK}) and inner volume in the deployment state (V_{TVS}). Angles α of shall conicity were determined, at which it is possible to bend it with keeping the allowable values of relative circular deformations in the structural material. The values of relative deformations should not exceed the values $\varepsilon_{\kappa\partial} \leq 2 \div 2.5\,\%$ for the metallic

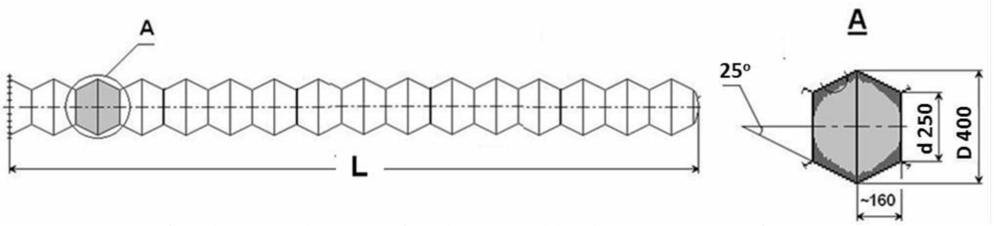

Fig. 2. Schematic diagram of multi-conical load-carrying TVS of space purpose

materials widely applied in the aerospace industry with a plasticity factor within $\sigma_T/\sigma_B = 0.3...0.8$, admissible for realization of problems of the volume deforming of test shells. At scheme of deformation of the thin metal shell, according to Fig. 1, *d*, the values of relative circular deformations were obtained which correspond to values of angle conicity $\alpha = 25°...27°$.

As a whole, the optimization of geometric characteristics of conical TVS (Fig. 2) during designing is reduced to the search for the most promising combination of shell stability and its compactness, or coefficient of transformation K_T, at minimum possible weight. Decrease in conicity angle α and structure section approach to the configuration of cylinder, the most profitable from the point of view of stability against action of non-axisymmetric loads, leads to decrease in the coefficient of TVS transformation. The opposite approach (increase in α) decreases greatly the space rigidity of the structure, but allows increasing K_T and simplifying the compact folding.

It is evident that welding is almost the only method of manufacture of metal pressurized shell structures. One of the main problems in manufacture of TVS shells is the reaching of combination of high physical and mechanical characteristics at the simultaneous vacuum density of straight-linear welds, which are subjected to a complex of effects of mechanical loads and specific aggressive environmental factors (SEF) [5]. Scheme of isometric transformation of shell requires the isotropy of structural material, i.e., the weld should have physical and mechanical properties practically equivalent to those of the structure base metal. In selection of method for welding of butt joints of stainless steel of $\delta = 0.1 \div 0.2$ mm the advantage was given to the microplasma welding. This method allows greatly simplifying the preparation of edges of conical blank for welding, thus increasing the efficiency of TVS manufacture and decreasing the thermal deformations of the weld in applying the preliminary flanging of edges being welded. In welding the stainless steel blanks the flanging of edges for the value equal to two thicknesses of material being welded was used. In addition, the microplasma method could provide the almost complete repeatability of fixed results of welding.

Determination of nature of transformation of the middle surface of the truncated conical shell allowed defining the criterion of approximation to isometricity in the process of its movement and, respectively, providing the lack of a local buckling in the deployment state. However, values of stresses and displacements of a deformed shell are subjected to the precise evaluation. Plotting of fields of the mentioned values can make conclusion about the feasibility of realization of calculation parameters of the isometric transformation process without a local buckling of the TVS shell and confirm the validity of the selected calculation scheme. During the work fulfilment the numerical calculations of stress-strain state of TVS with a rigid fixation around the basement contour, similar to Fig. 2, at the effect of typical factors of the space environment and their combination, were carried out.

Finite-element model of the multi-sectional structure was made in three-dimensional statement by using the shell finite elements of a general statement. As calculation values, the values of loads were taken, under the action of which the structure can be considered in a deployable position, in exposition at outside surface of the basic space vehicle (ISS). Typical effects at the stage of transportation to the orbit (vibrations, pressure drops, and acoustic effects) were excluded from the considerations, as the structure in the transportation position is characterized by a significant safety factor and equipped with a device for fixation of displacements [6].

For the accepted design scheme of TVS, temperature loads for ranges, given in Table, were modelled. Static problem of radiant heat exchange with the Sun was considered, at which maximum and minimum temperature of the proper range are reached at the opposite generating lines of structure shell simultaneously. In all the considered variants the shape-changing TVS was characterized by deviation of the free edge to the side of the least values of the applied temperature. Dependence of values of maximum displacements in this direction of the structure free edge on the range of temperatures ΔT is given in Tabl. Regions with the highest values of stresses are located at the surface, greatly

Dependence of maximum displacements of free edge of TVS on ΔT

Range of temperature, °C	Displacement of free edge, cm
ΔT_1: from +100 °C to –125 °C	6.2
ΔT_2: from +150 °C to –125 °C	7.6
ΔT_3: from +200 °C to –125 °C	9.0

limited in area, their values are abruptly decreased with a distance from the fixation zone. The results of modelling allow making conclusion about the correspondence of maximum displacements, allowable to values of the free edge deviation, which are accepted for the given type of the structure (up to 150 mm). Schematic representation of TVS with UL, rigidly fixed at the universal work station (UWS) on the outside surface of a service module (SM) of ISS, is given in Fig. 3.

At the total calculations of effect of accelerations at the presence of UL, a block of scientific equipment of 40 kN weight, rigidly fixed at a free edge of TVS by six degrees of freedom, and also thermo cycling, the following values of efficient accelerations were taken depending on a natural frequency (ω) of structure. According to the results, frequency of natural oscillations of the structure was ω = 22.43 Hz. Accounting for averaged load from UL mass, which subjected to the action of linear and angular accelerations and fixed at the TVS edge, leads to decrease in frequency of natural oscillations of the structure to ω = 20.45 Hz. For values ω ≥ 20 Hz: $a_x = \pm 4.5$ m/s^2; $a_y = a_z = \pm 6.0$ m/s^2 ; $\varepsilon_x = \pm 0.2$ rad/s^2; $\varepsilon_y = \varepsilon_z = \pm 0.7$ rad/s^2; the directions of accelerations are preset in the right system of coordinates OXYZ, where axis Z is coinciding with longitudinal axis (symmetry axis) of TVS, axes Y and X are normal to it. Respectively, a_x is the acceleration in the direction of axis X, a_y and a_z are the accelerations in any transverse plane, parallel to plane OYZ, ε_x is the angular acceleration around axis X, and ε_y and ε_z are the angular accelerations around any transverse axis, which is lying in a plane, parallel to plane OYZ and passing through the axis X.

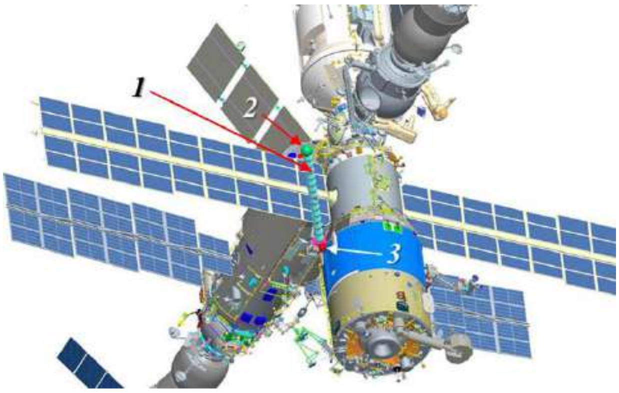

Fig. 3. Scheme of arrangement of TVS (*1*) with UL (*2*) at UWS (*3*) of service module (SM) of ISS

Figure 4 illustrates the dependence of minimum (T_{min}) and maximum (T_{max}) calculation values of temperatures at the surface of TVS of a conical type on relation $A_{S/\varepsilon}$, where $A_{S/\varepsilon}$ is the coefficient of absorption of a solar radiation, ε is the coefficient of radiation of an optic surface TVS in structure service at the optional working spot of the external surface of ISS. The optional zone T_{opt} limits the above-mentioned optimum range of temperatures (–43 °C...+63 °C), which allows realizing the required operations at the outside spacecraft activity and corresponds to the range of relations $A_{S/\varepsilon} = 0.26 \div 0.54$. The object of investigations was the correction of relation $A_{S/\varepsilon}$ of the shell definite material by deposition on its surface of different combinations of materials and their compounds which fulfil the functions of selectively-radiated coatings. It should be noted that the coatings of similar purpose, known in the space engineering, do not meet the conditions of extreme deforming of the test structure either because of absence of elasticity (enamels) or sufficient strength and compactness (screened-vacuum thermal insulation). Moreover, the selection of the necessary coating is defined not only by its thermo-optical properties, but also by adhesion to the metal shell surface taking into account the high deformations of its surface during deployment, as well as by different rate on sublimation of materials under the conditions of space vacuum.

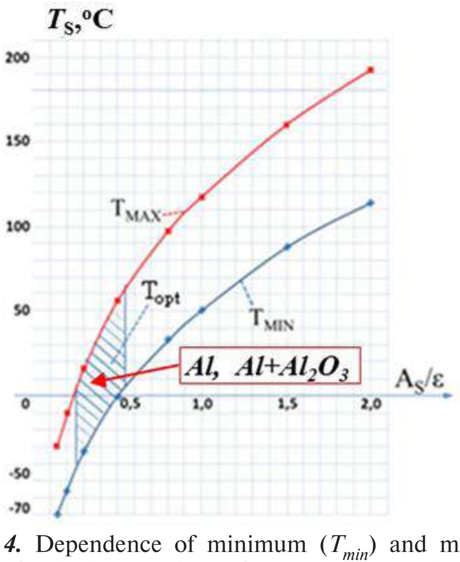

Fig. 4. Dependence of minimum (T_{min}) and maximum (T_{max}) of calculation values of temperatures at the surface of conical-type TVS on relation $A_{S/\varepsilon}$. T_{opt} – optimum range of surface temperatures

The preparation of optic surfaces of TVS after correction of rigidity can be realized by the electron beam spraying of thin coatings from metals and their compounds at proper relations $A_{S/\varepsilon}$. This method can provide the sufficient adhesion strength of coatings and effective control of their thickness. The required result was obtained in deposition of aluminium coating of 480 nm thickness on surface of shell of 0.175 mm thick steel AIS1321 with a further spraying of 45 nm thick Al_2O_3 layer on aluminium, that simulates the formation of an oxide film, which greatly increases the coefficient of absorption A_S. Measurements of integral semi-spherical thermoradiation characteristics of the mentioned coatings, carried out by using the calorimetric methods of investigation, confirmed their correspondence to the above calculation range of relations $A_{S/\varepsilon}$ [6].

Challenging tasks of application of multi-conical TVS as deployable systems and casing structures of orbital space modules [7] are connected with need of their further utilization, which requires updating the mechanism of reverse transformation, preserving the initial geometry. The capability of rigid shells of a transformable volume to reusable reproducing the stable geometric parameters is correlated with the bases of method of a regular isometric transformation. However, the real metal shell after the first repeated cycle of transformation acquires a wavy-like deformation in the inter-corrugation gaps, which proves a local buckling. The analysis of the mathematical model of movement of the test structure and results of carried out experiments on transformation of TVS elements, allowed making conclusion about the causes of conical shells buckling, which are subjected to the reverse transformation by the vacuum generation in the inner spacing. So, the direct shell transformation is going on successively, starting from a circular corrugation of the largest diameter, which is subjected to the highest loading under the condition of stable transformation pressure during the entire process. On the contrary, during the reverse transformation any of elements of the TVS deployable shell surface undergoes loading, which is equal approximately to a normal atmospheric pressure. Moreover, all the surface elements are beginning to move simultaneously. During the transformation process the local deformations increase in the vicinities of apexes of circular corrugations, the zones of their location are united, thus leading to a general buckling of the structure and significant distortions of its surface.

Conclusion about a local nature of bending deformation at the buckling boundary and appropriate deformations of a middle surface for the test thin shell is confirmed by the finite-element modelling of stresses and strains in the process of volume deformation. Thus, equivalent stresses on the face surfaces are located in a near-boundary zone of elasticity-plasticity, and at a neutral surface of the corrugation their values do not exceed 10...20 MPa. Basing on the given considerations it can be assumed that one of the possible variants of change in the transformation technology for realization of reusable change in shell shape can be decrease in a radius of rounding in apexes of matrix stiffeners. Here, the zones of maximum of elastic-plastic deformations are localized in vicinities of apexes of the corrugations, the number of transition zones of equivalent stresses is decreased, and a sinusoidal profile of the conical generating line is approaching the form of a lumpy-broken curve, which corresponds to the mathematical model of a mirror reflection of a truncated conical surface (see Fig. 1, *c*).

For experimental investigation of behaviour of TVS shell of diameters $D = 400$ mm, $d = 250$ mm, conicity angle $\alpha = 25^{\circ}$ and shell thickness of steel AISI321 $\delta = 0.175$ mm at a reverse transformation, a test specimen of structure of length $L = 1190$ mm from 7 sections with a ratio $r_C/\delta = 3.0$, were r_C is the rounding radius of apexes of the corrugations, was manufactured. Here, the basic criterion of approaching the isometric transformation, which consists in equality of length of initial and transformable region of a conical shell meridian, as well the ratio of thickness of its material δ to pitch size b, were not subjected to changes.

The process of direct, and also reverse transformation, realized in generation of vacuum in the inner volume of the test structure is given in Fig. 5, and the curve of pressure for stages (I-X) is presented in Fig. 6. The experiment confirmed the feasibility of repeated inter-axial folding of multi-sectional TVS up to state which allows making its required dismantling and utilization after finishing the term of exposition at the near-Earth orbit. It should be also noted that the increased circular rigidity of corrugations of a large radius in the region of contour of rigid fixation leads to appearance of "popping" effect of shell (see the stage of deployment "III" and corresponding to it stage "VIII", Fig. 5, *b*. In this case the reverse transformation is performed not strictly successively, starting from a large-radius fold, but from some free corrugation with a least circular rigidity, which can be caused by initial geometric imperfections of initial conical billet or deviations of the technological process of corrugating. As a result, a fragment of shell between the largest and first "folded" corrugation

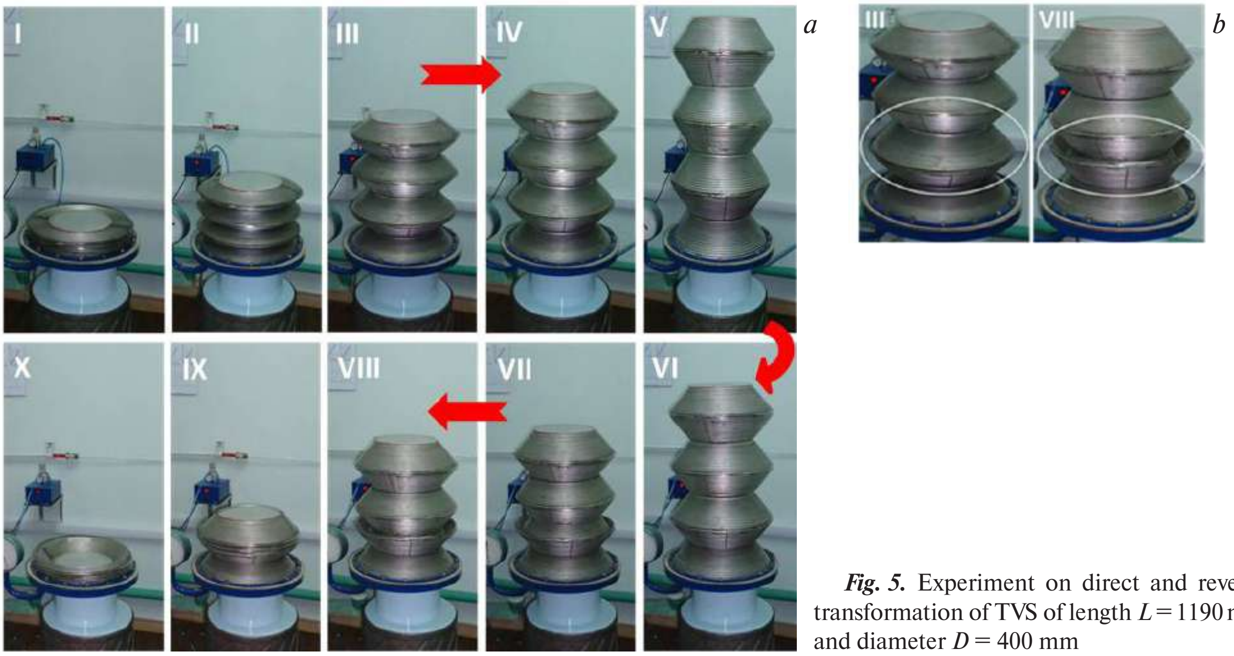

Fig. 5. Experiment on direct and reverse transformation of TVS of length $L = 1190$ mm and diameter $D = 400$ mm

remains untransformed, which has some negative effect on the final compactness of TVS (see Fig. 5, stage "I" and "X"). To avoid the appearance of such effect is possible by changing the radius of generating line of corrugations within small ranges with a decrease in their total radius. The determination of interrelations of geometric, strength and rigidity characteristics of TVS, which occur, may represent the subject of challenging investigations.

The presented results of development illustrate the feasibility of design and manufacture of load-carrying shell structures, which can be launch to the near-Earth orbit in a compact state and at minimum consumption of energy for transformation up to the design sizes. The application of the described structures in space engineering allows us to transfer to the new quality level in carrying out the research experiments, connected with the activity outside the spaceship, in manufacture of casing structures of the orbital station and, in future, can be used in building of long-term constructions [8] on the Moon surface.

Fig. 6. Pressure curve for stages N, (I – X)

REFERENCES

1. *Paton B.E., Lobanov L.M., Volkov V.S.* Metal transformable-volume structures // Avtomatich. Svarka. – 2011. – No. 12. – P. 30–40 (in Russian).

2. *Paton B.E., Lobanov L.M., Volkov V.S.* Metal transformable-volume structures for space engineering // Acta Astronautica. – 2015. – V. 110. – P. 50–57.

3. *Paton B.E., Lobanov L.M., Samilov V.N. et al.* Design and peculiarities of technology of manufacture of large-sized welded transformable-volume structure // Avtomatich. Svarka. – 2006. – No. 7. – P. 3–12 (in Russian).

4. *Lobanov L.M., Volkov V.S.* Development of technology of manufacture of double-wall welded transformable-volume structure // Avtomatich. Svarka. – 2012. – No. 10. – P. 37–42 (in Russian).

5. *Lobanov L.M., Volkov V.S.* Peculiarities of manufacture of thin-walled welded transformable-volume structures for space application // Avtomatich. Svarka 2015. – No. 1. – P. 33–39. (in Russian)

6. *Lobanov L.M., Volkov V.S., Yakimkin A.V., Savitsky V.V.* Functional characteristics improvement of metal transformable-volume structures for space applications // Journal of Aerospace Technology and Management. – 2016. – V. 8. – No. 1. – P. 55–62. DOI:10.5028/jatm.v8i1.529.

7. *Lobanov L.M., Volkov V.S.* Prospects for application of transformable-volume structure technologies in the designing of space vehicles / Proceedings of International Conference on Satellite & Space Missions, August 17-19, 2015, Houston, USA // Journal of Aeronautics & Aerospace Engineering. – 2015. – V. 3. – Iss. 3.

8. *Lobanov L.M., Volkov V.S.* Solution to the problem of combination of spatial rigidity, stability and compactness in load-carrying shells of challenging space habitats / Proceedings of International Conference on Satellite & Space Missions, July 21-23, 2016, Berlin, Germany // Journal of Aeronautics & Aerospace Engineering. – 2016. – V. 5. – Iss. 2.

DEVELOPMENT OF AN INTEGRATED UNIVERSAL NAVIGATION COMPLEX ON THE BASIS OF FIBER-OPTIC GYROSCOPES AND PENDULUM ACCELEROMETERS

O. Zlatkin, V. Chumachenko, S. Oliynik, Yu. Kuznyetsov
Research and Production Enterprise HARTRON-ARKOS LTD (RPE HARTRON-ARKOS LTD)

The navigation devices based on fiber-optic gyroscopes (FOG) and pendulum accelerometers (PA) for use in aircraft control systems of different types are being developed at the Research-Production Enterprise (RPE) HARTRON-ARKOS LTD (Kharkiv, Ukraine). The integrated universal navigation complex (UNC) is one such device. Fiber-optic gyroscopes become a serious alternative to mechanical, laser and other gyros. They have rather high accuracy of measurements, relatively small dimensions, mass, energy consumption and low readiness time [1]. That is what determined their use in the UNC.

Description of the device. In Fig. 1 the appearance of the prototype UNC (a) and its structural elements (*b*) are presented. The Fig. 2 shows the structural diagram of the device.

The basic set of UNC consists of an inertial measuring unit (IMU) and a navigation computer connected via the RS422 channel with the equipment of the consumer of the satellite navigation system (EC SNS). In addition, in navigation computer the additional links on the RS422 channels with radio- and baro- devices of measuring an altitude (RM and BM) and on-board computer control system (BC CS) are provided. The IMU consists of three FOGs (SFOS 501 type) and three PAs (A50-5 type), which operate in the mode of measurements of angle and speed, accordingly. FOG and accelerometers are installed on the base platform in accordance with the orthogonal scheme. The device is made in the form of a monoblock, and the EC SNS represents a separate construction.

The basic principle of functioning the UNC is the principle of a strapdown inertial navigation system (SINS), adjusted by external information sensors.

The goal of development. The goal is to create an accurate universal navigation device with stable precise characteristics that do not depend on the temperature of the environment and other factors, while the characteristics of these sensors are closer to the middle class precision sensors.

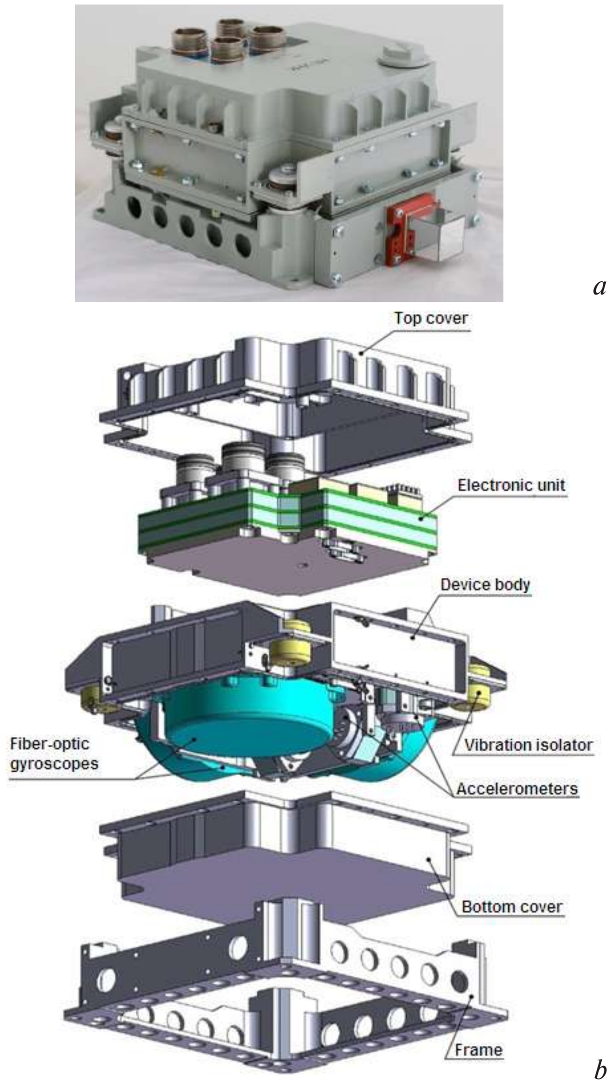

Fig. 1. The appearance of the prototype UNC and its structural elements

The applying FOG as an angular velocity meter has put a number of new tasks to the developers. The main ones are the problems of studying the influence of temperature, including the PA, the magnetic field and radiation, on the error of measurement of the FOG, as well as the question of improving the technology of testing and methodology

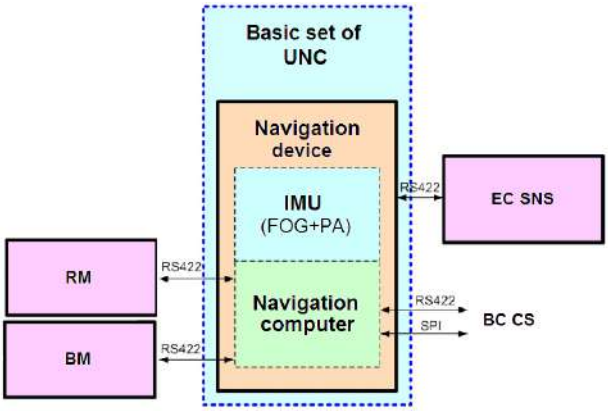

Fig. 2. The structural diagram of the UNC

for determining the technical characteristics, the development of mathematical models [2, 3].

To achieve the above-mentioned goal, the following tasks were set:

– study of the heat sensitivity of FOG and AK and the construction of a mathematical models of sensors temperature error;

– carrying out calibration works to determine the systematic errors of the FOG and PA, which are independent of the temperature factor, and technological errors in the manufacture of the IMU;

– assessment of the effectiveness of the developed methodology to achieve the exact characteristics of the device.

Solving set tasks. The step-by-step solution of the above-mentioned tasks is the technology of creating an integrated UNC based on a free-form inertial navigation system on FOG and PA.

It should be specially noted the follows. The enterprise has created technology of conducting thermal tests of separate sensors (FOG, PA) and technology of thermal testing of the device as a whole. Approximate polynomial mathematical models of thermal errors of FOG and PA (bias of zero, and scale factors) were constructed. These models allowed algorithmically compensate the thermal errors of sensors in the UNC. This ensured the stability of the exact characteristics of the device [4].

Mathematical model of thermal FOG drift:

$$\begin{gathered} W_T(T,G,t) = K_0^W + K_1^W T_{FOG}(t) + \\ + K_2^W G_{FOG}(t) + K_3^W T_{FOG}(t) G_{FOG}(t) + K_4^W G_{FOG}^2(t) + \\ + K_5^W T_{FOG}(t) G_{FOG}^2(t) + K_6^W G_{FOG}^3(t), \end{gathered}$$

Mathematical model of thermal PA errors:

$$\tau_T(T,t) = K_0^\tau + K_1^\tau T_{PA}(t) + K_2^\tau T_{PA}^2(t),$$

$$K_T(T,t) = K_0^K + K_1^K T_{PA}(t) + K_2^K T_{PA}^2(t) + K_3^K T_{PA}^3(t),$$

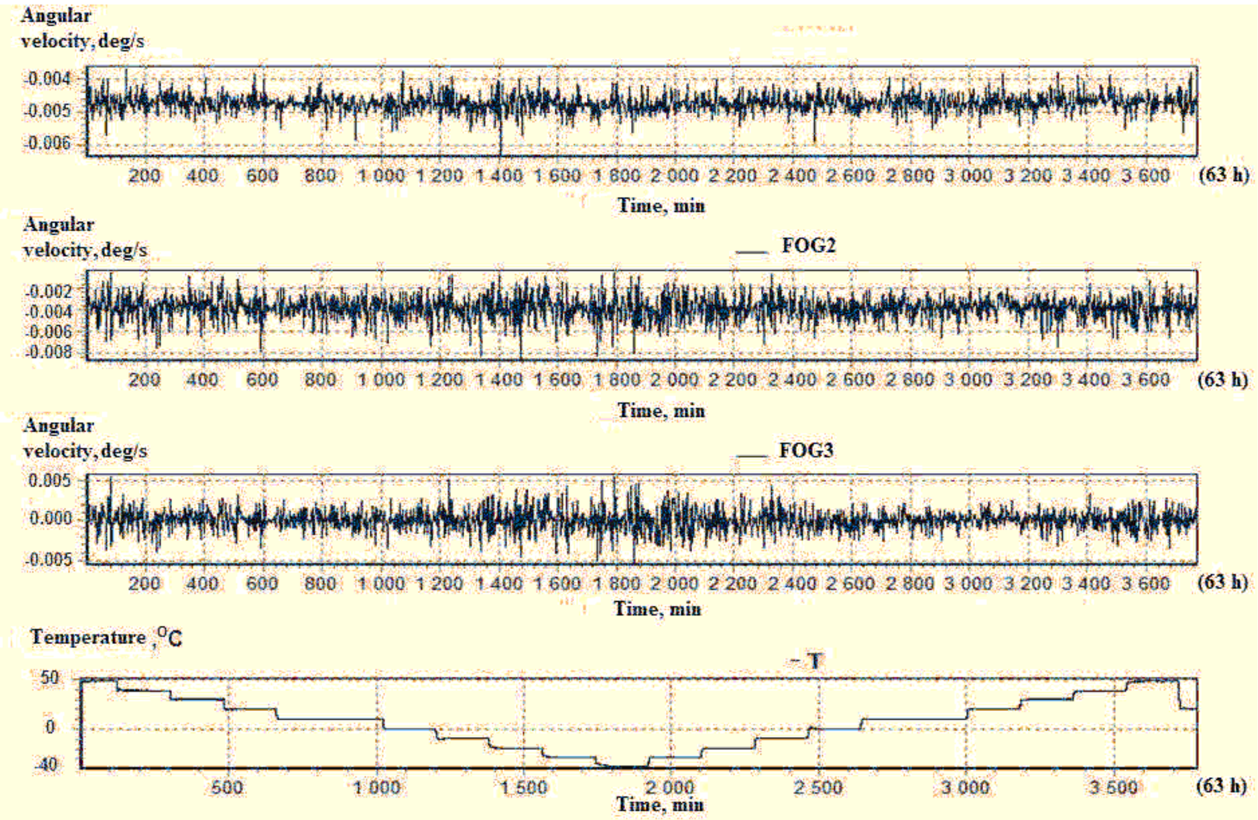

Fig. 3. Measurement of FOG as the part of the UNC

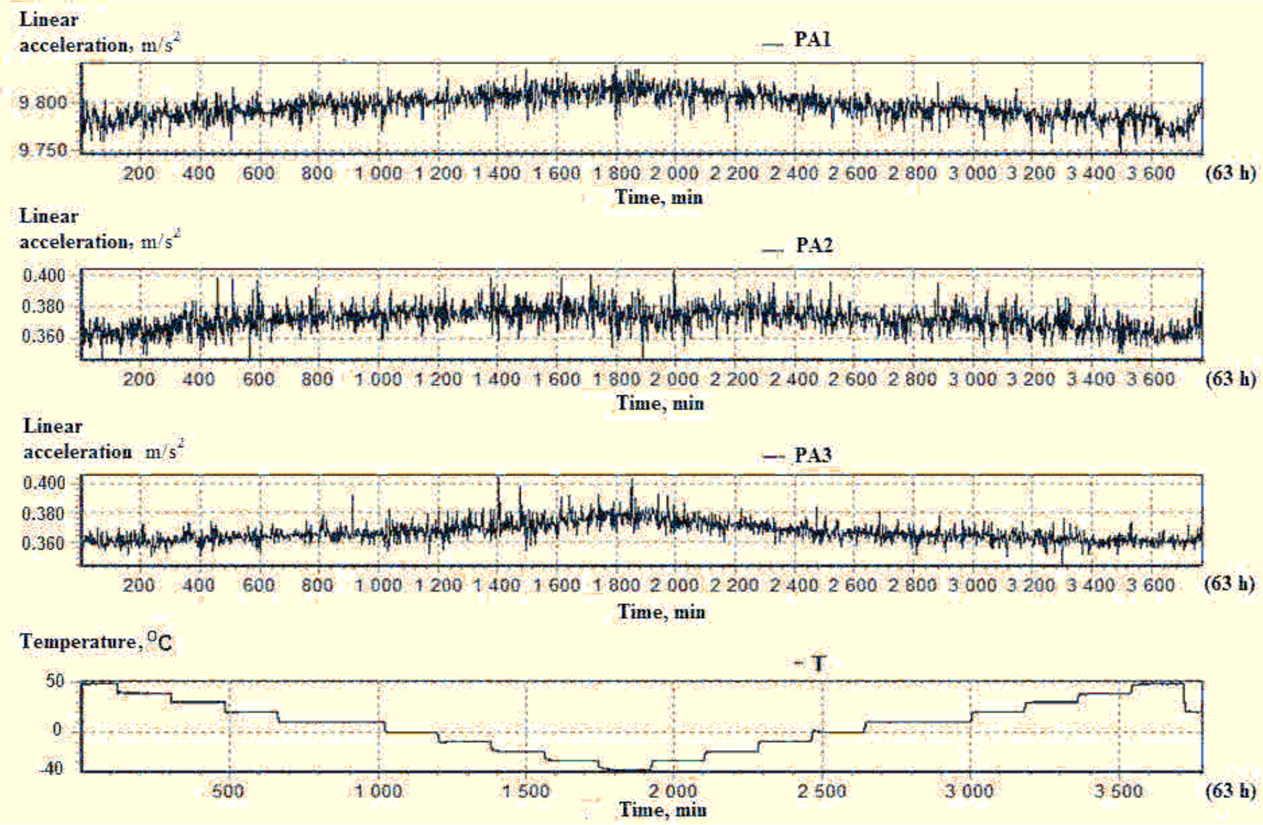

Fig. 4. Measurement of PA as the part of the UNC

where K_i^W, K_j^τ, K_k^K ($i,j,k=0,1,2,...$) – the parameters of mathematical models of thermal FOG drift, biase of zero and error of scale PA coefficients; $T_{FOG}(t)$, $G_{FOG}(t)$, $T_{PA}(t)$, $G_{PA}(t)$ – centered and normalized temperature and sensors temperature gradient.

Thermal tests require a lot of time. For its reduction, software was developed that allows automation of tests on the Acutronic stand and to carry them out continuously for 63 hours.

On graphs Fig. 3 and 4 are the output signals of the FOG and PA during their thermal tests in the UNC when the ambient temperature changes in the range –40 ... +50 °C and the base temperature +10 °C.

From these graphs it is clear that that the FOG of this party has small errors due to temperature changes of the device. The developer of FOG provides compensation for its programmatic errors in the controller of the most sensitive element. However, software in the computer of the UNC in the absence of such temperature self-compensating FOG (which took place for FOG previous party) allows its temperature compensation.

From the graphs shown in Fig. 4, it can be seen that that PAs have a marked thermal sensitivity. The Tables 1, 2 shows the thermal errors of PA and the results of the thermocompensation of PA as the part of the UNC.

Table 1

The thermal errors of PA as the part of the UNC

T, °C	The thermal errors of PA, m/s²					
	PA1		PA2		PA3	
	Reading	Error	Reading	Error	Reading	Error
50	9.7713	-0.0239	0.3627	-0.0102	0.3598	-0.0050
10	9.7932	0.0000	0.3719	0.0000	0.3643	0.0000
-40	9.8144	0.0192	0.3735	0.0006	0.3784	0.0136

Note. The reference value is 9.809965 m/s² (sensitivity axis of the PA1 directed along the axis of gravity of the Earth.

Table 2

The results of the thermal compensation PA as the part of the UNC

T, °C	The residual thermal errors of AK after of the thermal compensation, m/s^2					
	AK1		AK2		AK3	
	Reading	Error	Reading	Error	Reading	Error
50	9.8173	0.0021	0.0055	-0.0015	0.0025	0.0005
10	9.8128	0.0006	0.0046	0.0012	0.0025	0.0005
-40	9.8081	-0.0003	0.0082	0.0024	-0.0025	-0.0005

When carrying out the calibration of the device, the systematic errors of the sensors at the base temperature are determined:

- bias of zero FOG and PA;
- errors of scale factors;
- angles of actual orientation of the sensitivity axes of the FOG and PA after placement of them in the construct of the IMU.

The method of calibration is based on the direct measurements of the sensors and their comparison with the reference values. For the implementation of the method, the following data is required: measurement of sensors; value of the azimuth of the angle of the device; the value of the latitude of the place; reference value of the angular velocity of the platform for each gauge turn; reference value of the measured angle of the platform turn. The conditions for conducting experiments are as follows: horizontality of the axes of the IMU; absence of precession of the axis of rotation; high accuracy of the original exhibition of the IMU axes; high accuracy of fixing the time to reach the measured angle of the platform turn [5, 6].

Achieved basic characteristics. After calibration of the UNC and taking into account the systematic values of temperature compensation, an array of formular parameters that correspond to this device was formed. The key in evaluating the results of experimental research of the device is the conclusion that the random variances (3σ) correspond to the range ΔL and the side ΔB from the design values.

According to the results of the test of the navigation device on a triple stand after calibration, the systematic components of the deviations in the series of five test cycles at a given flight time of 500 s were the follows:

$\Delta L = 143$ m, $\Delta B = 44$ m – for static tests;

$\Delta L = 44$ m, $\Delta B = -126$ m – for dynamic tests.

At the same time, according to the statistical data processing of static and dynamic tests, the errors do not exceed the calculated marginal deviations:

$\Delta L = 55$ m, $\Delta B = 52$ m (marginal deflection of 260 m) – static tests;

$\Delta L = 120$ m (marginal deviation of 320 m),

$\Delta B = 108$ m (marginal deviation of 260 m) – dynamic test.

A test of the UNC on a vibrostend with a vertical table with vibro-loading on three instrumental axis x_I, y_I, z_I in series was performed. The volume of tests contained cycles with vibro loading and initial conditions without vibration loading. The cyclogram of vibro-loading was 350 s long with two sections of broadband random vibration: 9.1g – 50 s and 9.1g – 20 s.

The analysis of additional deviations ΔL and ΔB, arising from vibration loading, showed the presence of the following systematic shifts on three axes:

x_I: $\Delta L = -2$ m, $\Delta B = -29$ m;
y_I: $\Delta L = -80$ m, $\Delta B = 1$ m;
z_I: $\Delta L = 73$ m, $\Delta B = 4$ m.

As a result of the research, the following main characteristics of the UNC were obtained [6, 7]:

Range of measurement of angular velocity, degrees/s	+100
Range of measurement of linear acceleration, m/s^2	+85
Accuracy in the integrated (inertial-satellite) operating mode (3σ), m	15–16
Time of exact readiness, min	10
Period of updating of initial information, ms	1.25
Operating temperature range, °C	–40 ... +60
Power consumption, W	22.5
Reliability in flight	0.9983
Weight of the device, kg	3.6
Overall dimensions, mm	190 × 190 × 120

Conclusions. In the RPE HARTRON-ARKOS LTD the technology for the creation of integrated navigation devices based on the FOG and PA for use in the control systems of aircraft of various types was developed.

The research have shown that the navigation device – a universal navigation complex created with this technology – integrates with the satellite navigation system as well as in the autonomous inertial modes, provides characteristics that meet the requirements for modern control systems for rocket carriers, objects of aviation technic, unmanned aerial vehicles of medium and heavy class.

REFERENCES

1. *Zlatkin Yu.M., Oleynik S.V., Kuznyetsov Yu.A., Uspenskiy V.B., Bagmut I.A.* Technology and results of tests of the strap-down star-inertial unit for control systems of spacecrafts / Proceedings of 19th Saint Petersburg International Conference on Integrated Navigation Systems, May 28-30, 2012, Saint Petersburg, Russia. – P. 238–241.

2. *Zlatkin Yu.M., Oleynik S.V., Kuznyetsov Yu.A., Uspenskiy V.B.* Results of the study of the influence of the Earth's magnetic field on the measurement error of a fiber-optic gyroscope // Space Technique. Missile Weapons: Scientific-Technical Issue. – Dnepropetrovsk: SE "DB "Yuzhnoye". – 2011. – P. 122–132 (in Russian).

3. *Chumachenko A.V., Firsov S.N., Kuznyetsov Yu.A., Uspenskiy V.B., Golub E.Yu.* Methodology of determination and results of the tests of influence of the Earth's magnetic field on the operation of fiber-optic gyroscopes // Radio Electronics and Computer Systems. – 2012. – No. 2 (54). – P. 66–71 (in Russian).

4. *Kuznyetsov Yu.A., Oleynik S.V., Uspenskiy V.B., Khatsko N.E.* Development of drift models VOG OIUS 501 in the conditions of temperature changes of the sensor // Proceedings of the 25th International Scientific Conference "Mathematical Methods in Engineering and Technology – MMET-25": in 10 volumes. – V. 6. – Session 10. Volgograd: Volgograd State Technical University, 2012. – P. 82–84 (in Russian).

5. *Kuznyetsov Yu.A., Gudzenko A.V.* Development of algorithms for determining the error of mutual installation of the ARS and the AIU of the spacecraft control system // Proceedings of the 25th International Scientific Conference "Mathematical Methods in Engineering and Technology – MMET-25": in 10 volumes. – V. 6. – Session 10. Volgograd: Volgograd State Technical University, 2012. – P. 77–79 (in Russian).

6. *Zlatkin O.Yu., Oleynik S.V., Chumachenko A.V., Kuznyetsov Yu.A., Kozhuhov V.D., Uspensky V.B., Gudzenko A.V.* The development of a high-precision strapdown inertial system based on medium-accuracy fiber-optic gyroscopes for rocket and space applications / Proceedings of 21th Saint Petersburg International Conference on Integrated Navigation Systems, May 26-28, 2014, Saint Petersburg, Russia. – P. 272–287.

7. *Kuznyetsov Yu.A., Oleynik S.V., Uspenskiy V.B.* The experience of creating a strapdown and astroinertial unit based on fiber-optic gyroscopes for spacecraft control systems // Dynamics of Flight and Control: 50 years in KHPI. Monograph / Breslavskiy D.V., Uspenskiy V.B., Larin A.A., et al. Under the editorship of Breslavskiy D.V. – Kharkov: NTU "KhPI", 2014. – P. 295–322 (in Russian).

ON-EARTH RADIATION TESTING OF MATERIALS AND EQUIPMENT FOR SPACE APPLICATION: REQUIREMENTS AND PRACTICES

V. Maslyuk[1], M. Romanyuk[1], I. Hajnish[1], I. Megela[1], G. Pitchenko[1], O. Turhovskij[1], O. Docenko[2], V. Masley[2], S. Luniov[3]

[1] Institute of Electron Physics of NAS of Ukraine (IEP NASU)

[2] Yuzhnoye State Design Office

[3] Lutsk National Technical University

It is known that radiation factors are among the basic ones that determine the time and efficiency of the operation of spacecraft (SC) on orbits of the Earth. According to expert estimates, more than half of failures in the operation of the SC's equipment are due to the harmful effects of radiation factors in outer space. The influence of cosmic radiation can lead to a gradual degradation of the properties of materials and characteristics of onboard equipments and consequently – both the partial failure in the operation of the SC, or the complete failure of the onboard equipment during the time of their operation in open space. The world knowing practice of solving these sorts of problems is to carry out a complex of works on the creation of radiation-resistant equipment, the search for new materials/structures with the required characteristics [1–3], the choice of optimal modes of their work, and the creation of stand benches simulating the radiation factors of cosmic radiation.

The existence of such type of the radiation test benches solves many tasks of space engendering. There are the tasks to create a database about of real radiation resistance of well-knowing semiconductors/structures or some constructive materials and devices for space applications and to solve the functions of their radiation testing and to create the possibility of scientific and methodological works in this direction. The creation of such radiation test benches is an essential task of space engineering and can be realized only by available nuclear-physical installations [4]. In this work, the results of the organization of radiation tests of materials and devices of space designation by electronic accelerator microtron M-30 of the IEP NASU are presented.

Radiation factors of outer space and general requirements for on-earth radiation testings

Nuclear particles of the Earth's radiation bands (ERB), solar cosmic rays and galactic cosmic rays are the main components of cosmic ionizing radiation, which differ in origin, localization, and energy characteristics in the near-Earth space, where there is a vast majority of spacecraft. The characteristic values of the energy of nuclear particles of ERB lie in the range ~ 10^5–10^8 eV, and the density of their flows varies within 10^8–10^{12} $m^{-2}\cdot s^{-1}$. From the moment of opening ERB, they are divided into internal, the center of which is in the equatorial plane is at an altitude of about 3000 km, and the outer, with a center at an altitude of 15–20 thousand km. Significant efforts have been made in the world to develop standards for radiation factors that determine the electronic and proton components of outer space, implemented in NASA AE-8 (for electrons), AP-8 (for protons) models. These models are now the basis of practical calculations of radiation sustainability of SC in both the US and Europe. The specified characteristics determine the depth of permeability and the nature of radiation damage to materials SC, which should be reproduced during ground trials.

The nature of the influence of ERB factors on materials and equipment of the spacecraft is determined by the composition, energy, and the number of particles falling on the object being irradiated. For their description, the following parameters are used:

– ionizing particles flux – the ratio of the number of ionizing particles dN falling on this surface over time interval dt to this interval: $F = dN/dt$ [s^{-1}];

– fluence of ionizing particles - the ratio of the number of ionizing particles dN penetrating the volume of the elementary sphere to the cross-sectional area dS of this sphere: $\Phi = dN/dS$ [m^{-2}];

– ionizing particle flux density – the ratio of the flow of ionizing particles penetrating the volume of the elementary sphere to the cross-sectional area dS of this sphere: $\varphi = dF/dS$ [$m^{-2}\cdot s^{-1}$].

The universal measure of the effect of nuclear radiation on a substance is the absorbed dose of radiation – the ratio of the average energy transferred during irradiation to the mass of matter in this volume. The unit of the absorbed dose is Gray ($1\,\mathrm{Gy} = 1\,\mathrm{J} \cdot \mathrm{kg}^{-1}$). Although the absorbed dose is an indicator that indicates the radiation resistance of materials and devices of the SC, it is important to consider the conditions of their irradiation as well. There is the variety, the energy spectrum of nuclear particles of cosmic radiation, the temperature, the state of the vacuum, and especially the power absorbed dose (Fig. 1). The peculiarities of ground tests are that they are accelerated with a reduction in the duration of radiation in 10^3–10^8 times about the time of exploitation of materials and equipment in space. Often, the replacement of some types of cosmic radiation by others is also practiced. This action allows in many cases to replace ERB factors with electron fluxes or γ-quanta with fixed energy, adhering to the equality of absorbed doses. In many cases, radiation processes, depending on the total absorbed dose and dose rate, are interrelated.

When using accelerators, as radiation simulators, the radiation factors of the outer space of the radiation are usually carried out by streams of high-energy mono-energetic nuclear particles. The equivalence of imitation experiments and orbital conditions is achieved by performing the equality of the fluence of the particles falling on the surface of the samples in space and the simulato $\varphi_s t_s = \varphi_i t_i$, where φ_s, φ_i – the density of the flux of particles in space and the installation simulator, t_s – the duration of the orbital flight of the spacecraft, t_i – the time of exposure to the specimens.

On the basis of this equivalence condition, the obtained fluencies of the nuclear particles of the ERB in orbit and the time t_i of the irradiation of the samples in the simulator accelerator are calculated.

Thus, when researching the influence of cosmic radiation on the materials and elements of the SE equipment, it is necessary to achieve equalities of the conditions in which samples are found in space and ones under of simulating on-ground installations.

Metrological test bench based on the M-30 microtron for on-ground testing of materials and equipment for space designation

Laboratory's on-eath facilities used in the study of radiation resistance of materials and the equipment of SC, in particular, the elements of electronic equipment, can be divided into two classes:

– simulating installations in which ionizing radiation of the same physical nature as in outer space, i.e., the flows of electrons, protons and heavy ions, are created;

– simulating installations, in which the dominant radiation effects are observed in the studied objects, characteristic of the conditions of operation of objects in outer space, using factors of powerful X-ray radiation, gamma radiation, pulsed laser radiation, neutron flux, etc.

When choosing the type and characteristics of the radiation used in the settings of both classes, are guided by the general requirements and criteria discussed in the previous section.

Electronic accelerator microtron M-30 for radiation testing. Microtron M-30 is a cyclic

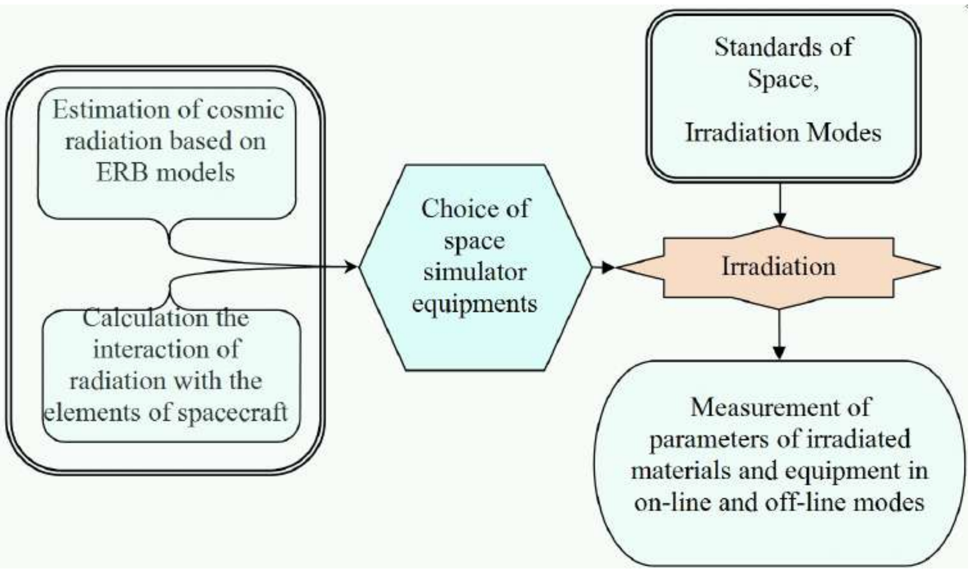

Fig. 1. Scheme of the organization of research on the influence of cosmic radiation

accelerator of relativistic electrons with a variable multiplicity of acceleration [5]. In the M-30, the accelerator module is a volumetric resonator excited by an impulse magnetron. The power plant of the microtron uses as a generator of microwave magnetron MI-262 with a pulse power of 9 MW, a generation frequency of 3200 MHz, an irradiation pulse duration of 0.2–0.3 μs, and a misspelength of 3300–5000. The pulse of the radiation of the microtron is a sequence of electron clusters that follow each other with a frequency of 3200 MHz and a duration of ~ 30 ps.

The efficiency of the electron output from the M-30 microtron reaches 80–100 %; the average electron beam current can vary from 0.01 to a maximum value of 50 μA ($3.12{\cdot}10^{14}$ el·s^{-1}). A bunch of electrons from an accelerator is output through a window of titanium thickness of 25 μm (11.3 mg·cm^{-2}); when passing through the titanium window electrons lose up to 30 keV of the initial energy. Time instability of electron flux density ≤ 14 %. The size of the electron beam at the exit of the accelerator M-30 has the form of an ellipse with diagonals that make up 10–12 mm horizontally and 3–4 mm vertically, the divergence of the output beam of electrons to the outlet window: in the vertical direction – $1.5{\cdot}10^{-3}$ radians, in the horizontal – $1.5{\cdot}10^{-2}$ radians. The efficiency of the electron output from the microtron M-30 reaches 80–98 %, the magnitude of the current of accelerated electrons on the radiation plane is measured by the Faraday cylinder (FC). The main parameters determining the magnitude of the current of accelerated electrons in the M-30 are the temperature of the cathode, the value of the accelerating voltage from the cathode, the efficiency of the capture of the modulator microwave field, the effectiveness of the electron output, and so on.

In the microtron M-30, for every passing of the electron beam through the resonator, the electron energy increases by 0.51 MeV, and they begin to move in the next higher orbit in the magnetic field. The number of orbits in the vacuum chamber M-30 is 29, the change of energy is smoothly within the range of 1–3 MeV from the microtron control panel and is stepped in the range from 1.4 to 24 MeV. A step change in energy takes 5–6 hours. The main parameters that determine the energy of accelerated electrons in the M-30 are the number of the orbit and the magnitude of the magnetic field of the vacuum chamber. The change in the energy of accelerated electrons may be carried out: step by step, within the range of 3–30 MeV in a 1.5 MeV step using the appropriate waveguide inserts located in the vacuum chamber; smoothly, due to the change in the value of the accelerating potential in the resonator and the subsequent change in the voltage of the conducting magnetic field.

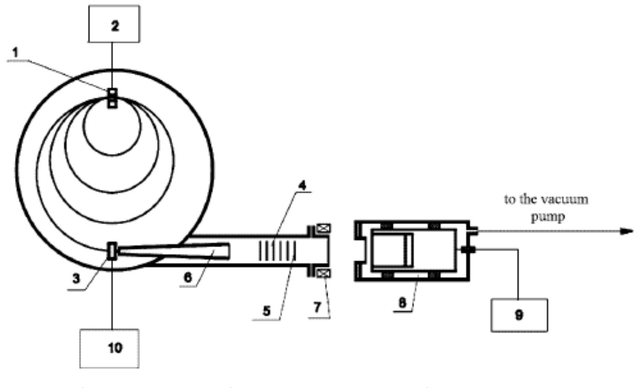

Fig. 2. The layout of the arrangement of microtron M-30 devices under irradiation

The microtron's management, control of accelerating parameters, its inclusion and exclusion are carried out remotely from the control panel, which is modernized for such tasks. In particular, the graphical interface, as well as the scheme of conjugation with the functional units of the microtron M-30 using the modules of the analog-digital converter (ADC) WAD–AIK–BUS (AKON produced), galvanically resolved incoming channels allow to implement a system of monitoring, statistical processing and archiving of parameters accelerator. The software part of the control panel contains a set of virtual panels, each of which real-time displays the value of the parameter M-30 or their functional dependencies. The number of sensors processing a program complex depends on the number of ADCs that are connected to one bus and allows the addressing of 127 modules, each of which has four channels for incoming signals.

The layout of the arrangement of devices M-30 is shown in Fig. 2, where 1 – resonator, 2 – ultrahigh frequency generator, 3 – electron collector; 4, 5 – monitor indicator; 6 – the node of the output of the beam; 7 – an induction sensor; 8 – FC; 9, 10 – current meters.

Metrological test bench based on microtron M-30 for radiation testing of materials and devices of space designation

As noted above, the global practice of such radiation tests is to create, by nuclear-physical installations, metrological radiation stands, which simulate the actual conditions of use of the equipment being studied. First of all, they carry out a reasonable choice of the type of ionizing radiation and its intensity, which depends on the degree of radiation degradation of materials and devices. By specifying their irradiation regimes, radiation effects are taken

Fig. 3. Microtron M-30 as a radiation stand:
a – control panel and *b* – metrological bench for radiation tests with FC and irradiation field shaper

into account, which depend on a number of factors, including exposure conditions (temperature, active/passive modes), power and integral value of the absorbed dose, as well as the predominant radiation-physical and radiation-chemical processes that determine deterioration of the operational parameters of the investigated object [6–8]. In complex systems, they try to identify the weakest link, which mainly determines their radiation resistance.

High monoenergetic beam (up to 0.02%), the ability to vary the energy and density of the stream of accelerated electrons in broad limits, makes the M-30 microtron attractive to create a stand for radiation testing, Fig. 3 [4–5]. To establish the metrological characteristics, it is necessary to periodically conduct studies on the parameters of the electron beam on the irradiation plane at various distances from the node of the M-30 output. For all types of measurement, the measurement error is determined by the formula $\delta_x = \theta_x + S_x$, where θ_x – is the non-excluded part of the systematic error of the measured values, S_x is the random error of the measured value. This activity allows guaranteeing the error of the installation of dosimetric characteristics when irradiated samples for the confidence probability $P = 0.95$. During the metrological certification of the M-30, some spatiotemporal and energy components of the electron beam of the microtron are established. There are such as its energy value, density, and distribution of the electron flux density on the irradiation field. The operational characteristics of the M-30 that affect the above attributes are used to determine the permissible deviations of the operating parameters that ensure the support of the electron energy, electron flux density and integral flow with a given error in the irradiation of the specimens. An essential characteristic of the M-30, which determines the characteristic dimensions of the tested apparatus, is the uniformity of the radiation field in the plane of the placement of samples. The system of diffusers and formers of the irradiation field to form a uniform flow density of electrons is used and control is performed in situ using a special radiation field scanner.

The starting date for determining the mode of operation of the microtron and the conditions of exposure are the establishment of some technical parameters. There are the real doses of irradiation, the geometric dimensions of the investigated object, the energy and the density of the electron flow in the irradiance area. These data allow us to establish: the distance from the test sample to the microtron output window, the required irregularity of irradiation, the maximum of the electron flux density in the irradiated area, and calibrate the current integrator to ensure the dose of radiation. The irradiation is suspended by the supervisor when the integrator is set up for a given radiation dose.

Measurement of the electron flux density. The density of the electron flux is measured with the help of a FC, which is an absolute device. The FC itself is a thick-walled glass of copper, on the bottom of which is fixed graphite plate $1.7\,g{\cdot}sm^2$, under which there is a ring ferrite magnet. The copper glass is inserted into a grounded steel vacuum chamber and is isolated from the last porcelain insulator. The geometric dimensions of the FC are selected so that it can measure the flows of accelerated electrons with energies up to 30 MeV. The current FC is determined by the voltage drop on the load resistance R_n (Fig. 4), which is measured by an analog-to-digital converter. To measure the density of the electron flux Φ_e, the FC is located in the center of the irradiation field.

Formation and measurement of the spatial distribution of electron flux density. To form a uniform electron flux density on an irradiation plane, a specially designed formwork, which consists of tantalum plates and a steel cone, reduces the density of the electron flux in the center of the beam and increases it on the periphery. The unevenness of the spatial distribution of the density of the electron flux is measured using a small-scale FC, which moves along the intersection of a beam of accelerated electrons in the horizontal and vertical directions. The area of the entrance window of a small-sized FC is 8 cm^2 and can be reduced to 1 cm^2, 2 cm^2, 5 cm^2 using additional collimators. The transfer of the FC is carried out remotely in the horizontal and vertical directions with a step of 1, 5, 10, 20, 40 mm, the maximum dimensions of the studied plane are 1000×1000 mm^2.

The scheme for measuring the density of the electron flux and the homogeneity of the irradiation field is shown in Fig. 4.

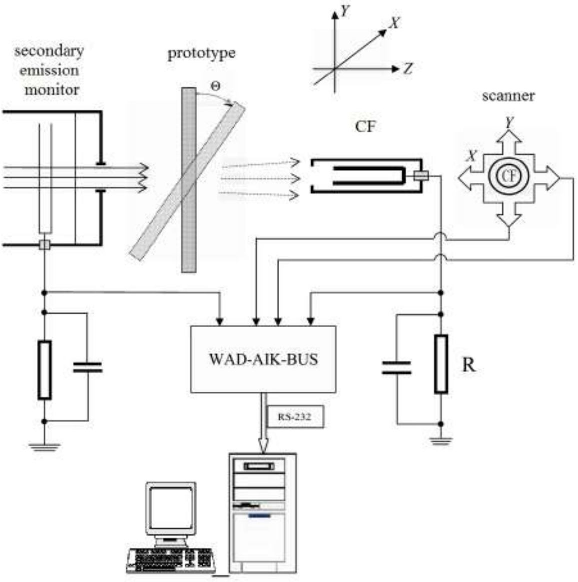

a

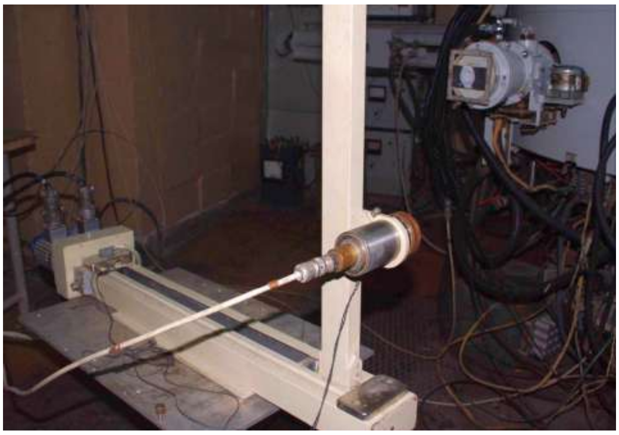

b

Fig. 4. *a* – a diagram of functional elements for studying the characteristics of the radiation field (current, homogeneity), *b* – the form of the scanner radiation field M-30

Determination of electron energy in the radiation field. In determining the nature of the interaction of the electron beam with the substance and the calculation of the absorbed dose, it is necessary to know their energy on the radiation plane, for example, E_{pe} – the most probable value of energy. The E_p value is calculated from the parameters that are determined from the absorption curve of the electron beam *N(R)*, depending on the thickness of the metal foil, in which we have chosen the aluminum plates. Fig. 5 shows the source data for finding E_p and an automated device that allows you to define *N(R)*.

The empirically established relationships of the most probable energy E_p and the average energy of the electron beam E_a on the input surface of the substance for the depths of penetration of R_p and R_{50} (Fig. 5, *a*):

$$E_p(MeV) = 0{,}22 + 1{,}98\,R_p + 0{,}0025\,R_p^2, \quad 1\,MeV < E_p < 50\,MeV,$$

$$E_a(MeV) = 2{,}33 \cdot R_{50}, \quad 5\,MeV < E_a < 35\,MeV.$$

Here, R_p and R_{50} are the extrapolated date and half-slack depth, respectively, expressed in cm. The analysis shows that this technique allows us to find not only the value of E_p, but also to evaluate the spectrum of the electron beam on the irradiation

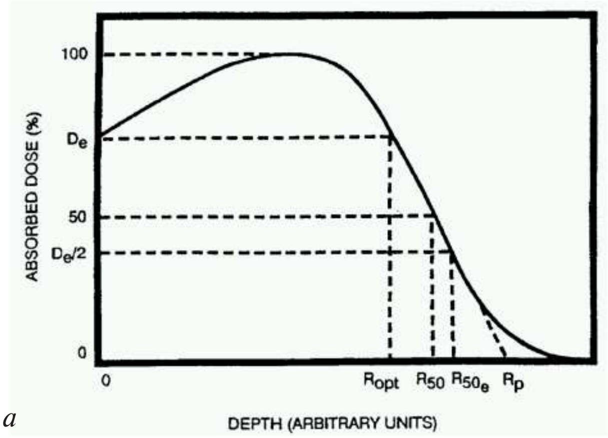

a

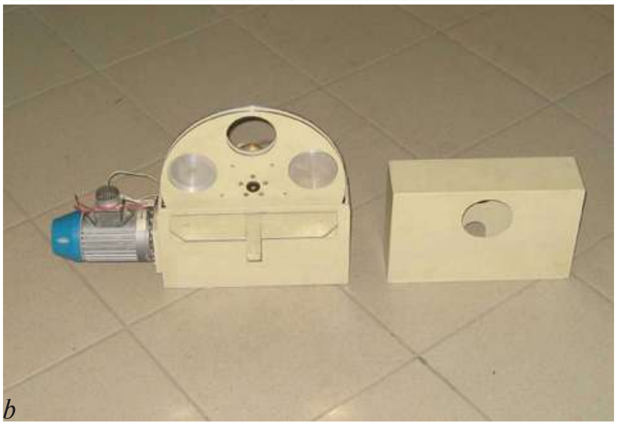

b

Fig. 5. *a* – is a typical distribution of the dose at a depth of matter under irradiation with a beam of electrons, *b* – is a device for constructing the dependencies N(R) for the M-30

area, according to the absorption curve. A radiation test bench based on the M30 also allows the creation and control of dosimetry of intense fields of gamma and neutron radiation, as well as mixed streams of gamma-neutron and gamma-electronic fields with a predetermined energy spectrum of nuclear particles [9].

Radiation experiments on the M-30 for space technology

In this section, some results are presented that characterize the microtron M-30 as a radiation stand and the results obtained there.

Passporting of radiation fields M-30. The attestation methodology allows one to determine the energy and spatial characteristics of a beam of accelerated electrons for a predetermined confidence probability *P* on different planes perpendicular to the electron beam for different distances ($d = 0–400$ cm) of the metrological bench from the node of the M-30 output. First of all, this applies to the characteristics of the M-30 microtron irradiation field for a beam of electrons having different energies and a distance *R*. In Fig. 6 gives an example of the study of the field of irradiation of the microtron M-30 for a beam of electrons having different energy and distance *R* with the use of a scanner, Fig. 5, *b*).

Radiation tests on the M-30 for space technology

Possibilities of a radiation test bench based on the microtron M-30 are used for regular ground tests to confirm whether the radiation resistance of materials and equipment of space technology is established [4]. In Fig. 7 shows the operational stages of radiation tests on the M-30 and some of the samples of space technology being studied.

Effect of radiation M-30 on the optical properties of space materials

An essential element of the systems of an orientation of the spacecraft is photoelectric devices, the input windows of these devices are made of different varieties of optical and electrovacuum glass (in particular, borosilicate, aluminum silicate, molybdenum, and tungsten group, quartz), as well as leucosapphire Al_2O_3 and LiF monocrystals. It is interesting to study the possibility of using in the conditions of cosmic radiation $Li_2B_4O_7$ crystals that have similar optical properties to Al_2O_3 and LiF monocrystals. Also, single crystals of leucosapphire are also used as substrates of electronic chips. On the microtron M-30 a number of investigations of the patterns of changes in the optical properties of both non-doped and doped niobium and iron Al_2O_3 crystals, as well as LiF, $Li_2B_4O_7$, and

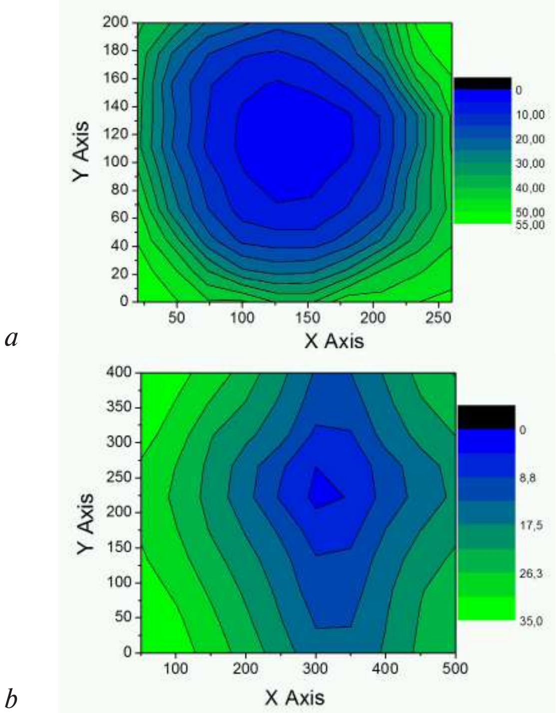

Fig. 6. *a* – the date of the homogeneity of the irradiation field M-30 investigation for a beam of electrons with an energy of 2 MeV at a distance of 1 m from the output node, *b* – the same diagram for energies 18 MeV and R = 3 m

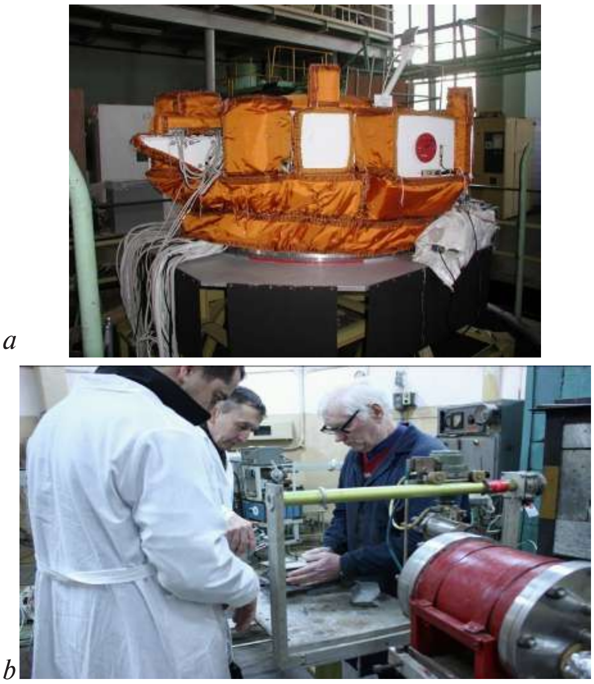

Fig. 7. *a* – STEP-F unit detector unit in the space complex «CORONAS-Photon» after radiation testing on M-30; *b* – stage of the test on the M-30 of the SIDRA device, produced in the framework of the international project Ukraine-Spain (project manager – prof. O. Dudnik)

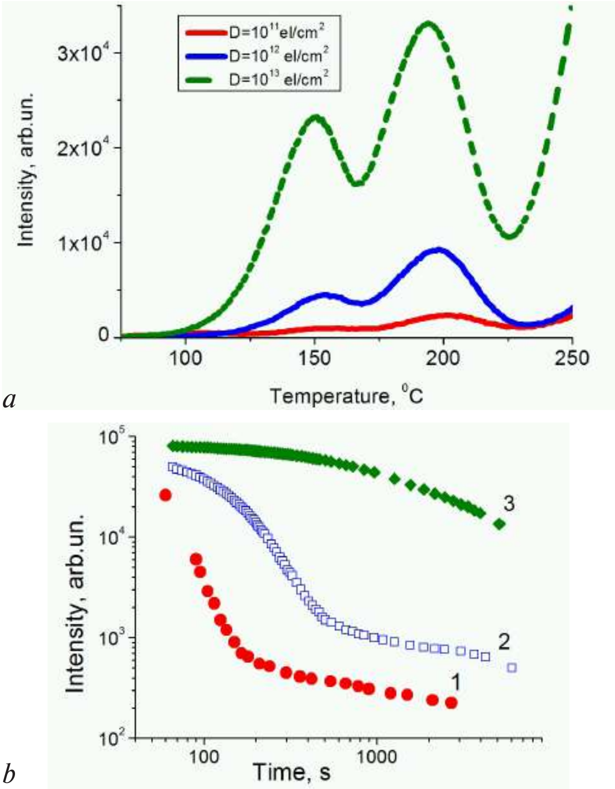

Fig. 8. *a* – the thermoluminescence curves of crystals of Al_2O_3, Al_2O_3: Nb, Al_2O_3: Fe, irradiated by gamma quanta created by braking radiation of electrons fluence 10^{11}–10^{14} e/cm^2; *b* – the phosphorescence curves of samples Al_2O_3, Al_2O_3: Nb, Al_2O_3: Fe irradiated by electrons at a dose of 10^{12} e/cm^2, with an intensity of $3 \cdot 10^9$ e/(cm^2·s)

doped $Li_2B_4O_7$: Cu, $Li_2B_4O_7$: Mn crystals under the irradiation of electron and gamma rays were carried out [10–12]. For samples of leucosapphire, the results of the studies are shown in Fig. 8.

Conclusion

The available methodological and hardware allows one on the base of the microtron M-30 with the possibility of generation of a monoenergetic beam of electrons (1–18 MeV), metrological equipment conducting regular radiation testing of materials and devices of space designation. The mentioned activity on the modernization of the radiation stand bench has created new possibilities of directed change of parameters of the radiation field, to carry out their control, statistical processing and data archiving. The availability of certified radiation fields allows us to conduct not only the regular certification work of materials and equipment CA but also promising researchers for space materials science, investigate the effectiveness of systems of passive CA protection and optimize the layout of spacecraft. Another class of tasks is to develop methods for simulating some radiation factors using others ones being based on the physics of radiation damage in the matter.

REFERENCES

1. *Luniov S.V., Zimych A.I., Maslyuk V.T., Khvyshchun M.V., Herasymiuk Yu.A.* The impact of uniaxial deformation and irradiation on the electrical properties of single crystals n-Ge / Luniov S.V. et al. – Vienna: «East West» Association for Advanced Studies and Higher Education GmbH, 2017. – 136 p.

2. *Luniov S.V., Zimych A.I., Nazarchuk P.F., Maslyuk V.T., Megela I.G.* Specific features of electron scattering in uniaxially deformed n-Ge single crystals in the presence of radiation defects //Radiation Effects and Defects in Solids. – 2016. – V. 171. – Iss. 11–12. – P. 855–868.

3. *Myroniuk D.V., Lashkarev G.V., Maslyuk V.T. et al.* Effect of High Energy Electron Irradiation on Structure and Optical Properties of ZnO Films // Acta physyca Polonica A. – 2013. –V. 124. –No. 5. – P. 981–985.

4. *Maslyuk V.T.* On the modern state and prospects of fundamental and applied research at the electron accelerator (microtron) M-30 // Visnyk of NAS of Ukraine. – 2016. – Iss. 11 – P. 46–55 (in Ukrainian).

5. *Maslyuk V., Shpenik O.* Microtron M-30 for Basic and Applied Studies for the Carpathian Euro-Region countries // Book of Abstracts. Intern. Conference «Integrating Access to Pan-European Research Infrastructures in Central and Eastern Europe» (INARIE), November 30 – December 02, 2015, Debrecen, Hungary. – P. 29.

6. *Luniov S.V., Zimych A.I., Nazarchuk P.F., Maslyuk V.T., Megela I.G.* Specific features of electron scattering in uniaxially deformed n-Ge single crystals in the presence of radiation defects //Radiation Effects and Defects in Solids. – 2016. – V. 171. – Iss. 11–12. – P. 855–868.

7. *Luniov S.V., Zimych A.I., Nazarchuk P.F., Maslyuk V.T., Megela I.G.* Radiation defects parameters determination in n-Ge single crystals irradiated by high-energy electrons // Nuclear physics and atomic energy. – 2016. – V. 17. –No. 1. – P. 47–52 (in Ukrainian).

8. *Luniov S.V., Zimych A.I., Nazarchuk P.F., Maslyuk V.T., Megela I.G.* The impact of radiation defects on the mechanisms of electron scattering in single crystals n-Ge// J. of physical studies. – 2015. – V. 19. – No. 4. – P. 4704–4711 (in Ukrainian).

9. *Parlah O.O., Masliuk V.T., Dovbnia A.M., Holovei V.M., Pylypchinets I.V., Lendel O.I., Simochko D.M.* Application of boron carbide B_4C for cleaning bremsstrahlung radiation beams of electron accelerators. Patent Ukraine. No. 96384. 10.02.2015 (in Ukrainian).

10. *Maslyuk V., Megela I., Okunieva T., Pekar J., Pekar V.* Specific features of the influence of high-current high-energy electron beams on the luminescent properties of undoped and Nb, Fe- doped Al_2O_3 crystals // Radiation Protection Dosimetry. – 2014. DOI: 10.1093/rpd/ncu213.

11. *Maslyuk V.T., Megela I.G., Obryk B. & Vieru-Vasilitsa T.O.* Luminescent properties of LiF: Mg, Cu, P detectors irradiated by the 10 MeV electrons // Radiation Effects and Defects in Solids. – 2017. – V. 172. – Iss. 11–12. – P. 1–8. Available at: https://doi.org/10.1080/10420150.2017.1393425).

12. *Maslyuk V.T., Megela I.G., Viyeru-Vasilitsa T.O., Roman I.Yu.* Study of influence of radiation defects on optical and luminescence properties of CaF_2 crystals // Nuclear physics and atomic energy. – 2016. – V. 17. – Iss. 1. – P. 53–58 (in Ukrainian).

DEVELOPMENT OF METAL AND CERAMIC HEAT PROTECTIVE COATINGS FOR REUSABLE SPACECRAFTS

G. Frolov, O. Grigoriev, V. Solntsev, Yu. Evdokimenko, V. Kisel, I. Neshpor

Frantsevich Institute for problems of materials science of NAS of Ukraine (IPM NASU)

Heat protection of the head parts of ballistic missiles, descent modules of manned crafts and automatic planetary stations, as a rule, is created on the basis of ablating heat-shielding materials [1, 2]. One of the most effective ablating heat-shielding materials is the Phenolic Impregnated Carbon Ablator (PICA-X), which is used for descended spacecraft protection which surface at an input speed of 7 km/s is heated to a temperature of 1850 °C. In this case, the heat flux impact on the heat-shielding coating is 10 times lower than when entering the atmosphere from the second space velocity. Although the PICA-X heat-shielding material is lighter than carbon phenolic, it is easy to show that for large reusable space shuttles (RSS) such as Space Shuttle and "Energia-Buran", the mass of such heat-shielding coating (HSC) would be tens of tons, although at a planning descent trajectory, the level of thermal loads in the RSS is an order of magnitude lower than for descent ballistic-type vehicles.

For heat protection, which was used on the RSS of "Shuttle"-type, lightweight carbon-carbon materials and super-light heat protection plates were used. The latter were made of light fiber-reinforced material based on quartz fibers with specific weight of 110–250 kg/m^3. However, it had low mechanical and thermoerosion characteristics and was often destroyed under the effect of solid particles and accidental impacts. For example, the mechanical destruction of the carbon-carbon coating of RSS Columbia led to a ship disaster. Therefore, when designing new heat shielding systems (HSS) of space systems under development, ceramic and metallic materials that have good mechanical strength and are more suitable for repairing at ground maintenance are widely used.

A rather complete list of HSS is presented in the review "European Directions for Hypersonic Thermal Protection Systems and Hot Structures 31st Annual Conference on Composites Materials and Structures Daytona Beach, FL January 22, 2007". In this paper it is shown that the great attention is paid to the use of metallic HPS developed in European countries.

HSS with a metal frame and of high-efficiency thermal insulation at manufacturing of forebodies and wing edges of ultra-high-temperature ceramics (UHTC) meet most requirements for thermal protection of RSS in practically the entire operating temperature range. A serious problem is the ceramic and metal elements of the HSS construction junction.

Metal thermal protection, as a rule, operates at temperatures of 1100–1200 °C, and UHTC is able to work for a long time in an oxidizing environment at temperatures up to 1700 °C and tens of hours up to 2000 °C.

For the production of metal thermal protection, operating in the temperature range up to 1100 °C, oxidation-resistant alloys with a specific weight of about 8000 kg/m^3 are used. In [3], a dispersion-reinforced alloy of UIPM based on nichrome was obtained. At its development a fundamentally new technology was applied, which made it possible to obtain a material with a density of 8.28 g/cm^3 with increased ductility and heat resistance. It has been life tested on the SSI-7 solar plant [1]. The metal plate made of the UIPM alloy of 100 × 100 × 1.7 mm, with an initial weight of 143.9 g., after 20 heating cycles at a temperature of 1100 °C for 20 minutes, increased its weight to 144 g. Thus, the experiments at the SSI-7 solar plant confirmed the working capacity of the developed alloy on samples with dimensions close to the conditions simulating the operational ones.

A semi-industrial production technology of elements of the flame tubes made of ZrB_2-SiC-$ZrSi_2$ and ZrB_2-$MoSi_2$ UHTC systems of pilot burners for coal air mixtures combustion at thermal power plants has been developed at IPMS of NAS of Ukraine.

Development of metallic nichrome heat protection

The laboratory technology of obtaining a dispersion-reinforced nichrome with a high aluminum content with a density of 7500 kg/m^3 by reactive sintering has been developed. The material possesses the necessary technological properties due to the fine-grained structure and is designed for operation at temperatures up to 1200 °C.

A carbonyl nickel powder with a particle size of less than 10 µm was chosen as the basis, which made it possible not to use the technology of the alloy mechanochemical synthesis. Moreover, the powders size of the main alloying components of chromium and aluminum were less than 40 µm, which accelerated the alloy homogenization.

The introduction of yttrium oxide was carried out by chemical precipitation of yttrium salts on a carbonyl nickel powder from aqueous solutions. To obtain a more uniform yttrium nanopowder, nickel oxide was introduced at co-precipitation. With this technology, Y_2O_3 nanoparticles did not coagulate and were evenly distributed on the surface of nickel particles. After that, the remaining components of the alloy were introduced into the mixture: aluminum and chromium. Mixing was carried out in an eccentric mixer for 8 hours.

The processes of powder metallic mixtures compaction in steel molds have been studied for real alloys in order to establish possible technological parameters, in particular, the compaction pressure and its effect on the preforms density. At the same time, the formability and compactability of the mixtures were determined. It is established that, due to the high plasticity of nickel, the mixtures based on the carbonyl powder with chromium and aluminum are well compacted (Fig. 1, *a*).

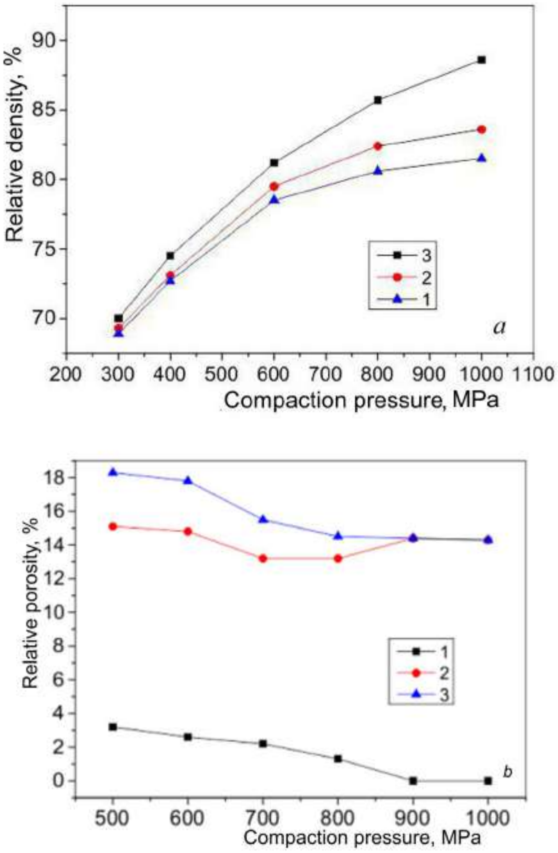

Fig. 1. The dependence of preforms relative density: 1 – Ni-20Cr; 2 – 1 Ni-20Cr-2Al; 3 – Ni-20Cr-6Al (*a*) and the nature of porosity of preforms from nichrome Ni-20Cr: 1 – open, 2 – closed, 3 – general (*b*) on the pressing pressure in steel molds with a two-way load application

With aluminum content increase in the mixture its compactability rises. At a pressure of 500 MPa, rather dense preforms are obtained. The increase in pressure makes it possible to improve their density, but this often leads to the massive preforms delamination and the failure of steel molds. In this regard, the specific pressure of compaction was limited to 500–600 MPa.

The nature of the open and closed porosity distribution, depending on the pressing pressure is of particular interest (Fig. 1, *b*). The obtained results indicate that at the compaction pressure range of 500–600 MPa the closed porosity prevails over the open porosity, which is less than 3 % and drops to zero with a pressure increase of more than 600 MPa. This reduces the requirements to the sintering medium as for the content of active gases – oxygen and nitrogen in it.

The study of the preforms compaction sintering regularities showed that shrinkage is observed in the alloy. The maximum relative density and shrinkage of preforms are reached at temperatures of 1275–1300 °C. Herewith, the relative density of compacts is 75.5–76.25 % (Fig. 2). After sintering, their density reaches 86.5 %. The obtained specimens with such a relative density have in their structure an insignificant amount of open and closed porosity.

To obtain preforms of the necessary density, as well as sheets of different thickness for the complex profile construction manufacturing, a rolling operation should be used.

The carried out researches have shown that the necessary parameters of the rolled samples are obtained during cold rolling with the reduction rate of not more than 10 % and subsequent removal of work hardening by annealing at a temperature of no less than 1200 °C. Annealing at the initial stage in the presence of open porosity in the material must be carried out in a protective atmosphere (inert gases or vacuum). In subsequent stages it is also possible to conduct annealing in the air. The samples after cooling in air have a black color due to the formation of a spinel on the surface, which prevents further rolling. Since the spinel disintegrates and pure chromium oxide remains on the surface in vacuum under heating, it is advisable to use annealing in a vacuum furnace at all stages of rolling. After three cycles of cold rolling with intermediate annealing at 1200 °C, the porosity decreases to 7.3–7.4 %. In subsequent rolling cycles, the porosity further

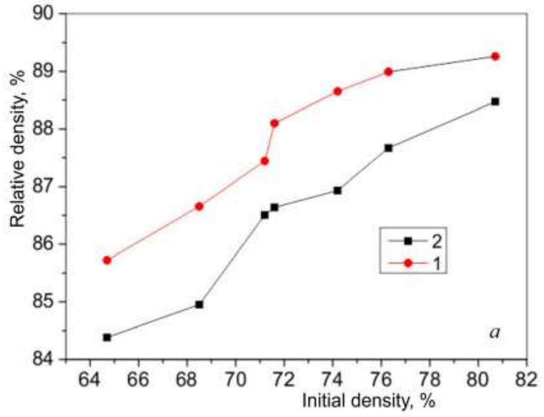

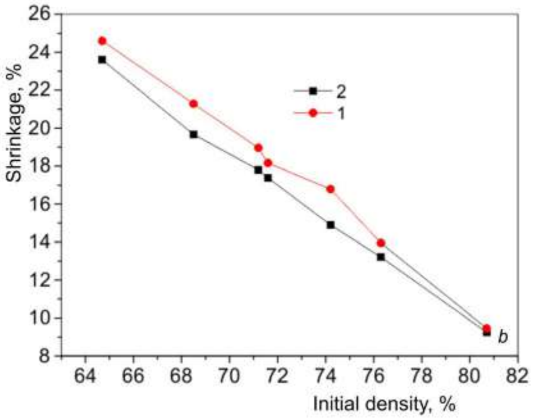

Fig. 2. The dependence of relative density (*a*) and nichrome preforms shrinkage with 6 % Al (*b*) on the initial density of preforms at sintering temperatures: 1 – 1300 °C, 2 – 1275 °C

reduces, and the necessary porosity of less than 3 % is achieved after the fifth cycle. The density of the alloy is 7450–7500 kg/m^3 [4].

The investigation of the cyclic heat resistance of the obtained nichrome was studied by placing the samples in a heated oven at 1200 °C without a protective medium. One cycle of isothermal holding was 20 minutes followed by cooling in an air atmosphere. The results obtained indicate a high heat resistance of the developed nichrome (Fig. 3).

A dense protective film is formed during 5–6 cycles, after that the weight gain is not practically observed, which indicates that there is no interaction of atmospheric oxygen and nitrogen with it.

A HSS mockup has been made of the obtained rolled sheets. It was tested at the gas dynamic stand of the Institute problem strength NAS of Ukraine under the HSS operation program [4].

Development of niobium metallic heat protection

The niobium-based alloy obtaining is described in [5]. In this paper, the tests of an alloy sample at convective heating in kerosene-air combustion products is considered [6].

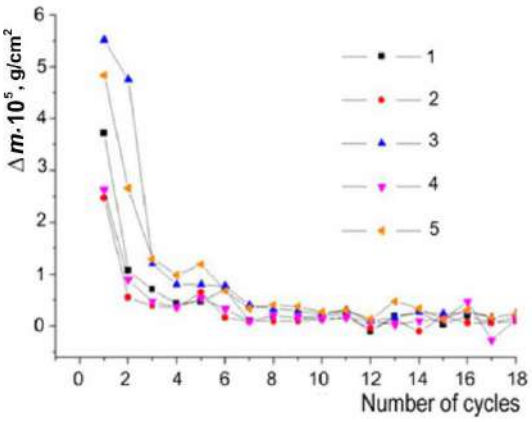

Fig. 3. The cycles heat resistance of the dispersion-reinforced nichrome with the thickness of: 1 – 0.1 mm, 2 – 0.06 mm, 3 – 1 mm, 4 – 0.05 mm, 5 – 0.5 mm

The aim of the tests was to determine the stability of the niobium based alloy sample, by determining the dynamics through the sample mass and the morphology of its surface transformational changes as a result of the thermal-erosive and oxidative influence of the supersonic flow at the surface temperature of 1200 °C.

A sample of a powder niobium alloy obtained by sintering and rolling in the shape of a plate with dimensions of 38 × 11 × 3 mm and an initial mass of 6.738 g (density: 5.4 g/cm^3) has been tested. The alloy is intended for the manufacturing of metallic heat protection for a reusable hypersonic aircraft.

The samples tests were carried out in a supersonic flow of kerosene in air combustion products that flow from a GVO-2M supersonic air-liquid-fuel burner with a diameter of the critical section of the nozzle of 11 mm, an output section of 15.4 mm. The pressure in the combustion chamber (CC) of the burner in all tests was 0.7 MPa, which provided an outflow at a mode close to the nozzle rated conditions. The oxidizer excess ratio, calculated from the kerosene flow rate, was about $\alpha = 1.4$, which corresponds to the temperature in the CC and the flow stagnation temperature is 1697 °C. At the testing, the sample surface temperature remained of 1200 °C, by changing the temperature of the flowing stream with fine adjusting of the fuel (kerosene) supply. The flow velocity in the outlet section of the nozzle was 1408 m/s (2.1 M).

The sample was placed in a distance of 40 mm from the nozzle cutoff, the stagnation pressure on its surface at the tests was 0.47 MPa. The calculated volume content of molecular and atomic oxygen on the surface at this pressure is $C_{O2} = 1.45 \cdot 10^{18}$ cm^{-3} and $C_O = 2.2 \cdot 10^{14}$ cm^{-3}.

Table 1

Conditions and results of thermal-erosion tests of a niobium alloy sample

Test number / number of heating cycles	Time, c	Temperature, °C			Change in mass of the sample in the test, mg	Rate of change in mass, g/(min·m^2)	Emissivity
		Average	Max.	Min.			
Nb-1 / 1	1200	1202	1305	1099	12.75	2.318	0.78–0.83
Nb-2 / 1	1073	1198	1313	1103	36.60	7.442	0.87–0.87
Nb-3 / 1	1196	1188	1303	1028	–3.70	–0.675	0.80–0.87
Nb-4 / 1	1199	1192	1262	1093	–0.10	–0.018	0.77–0.79
Nb-5 / 1	431	1199	1348	1107	0.00	0.000	0.79–0.86
Nb-6 / 1	1172	1198	1281	1123	–14.66	–2.729	0.83–0.80
Nb-7 / 1	1500	1199	1251	1148	–21.50	–3.127	0.83–0.85
Nb-8 / 1	1498	1205	1266	1153	–10.39	–1.513	0.83–0.88
Nb-9 / 1	1381	1208	1285	1147	–9.74	–1.539	0.87–0.90
Nb-10 / 1	1199	1205	1260	1154	–3.89	–0.708	0.92–0.91
Nb-11 / 1	1201	1208	1266	1120	–2.47	–0.449	0.95–0.93
Nb-12 / 1	1200	1203	1281	1056	–2.39	–0.435	0.88–0.89
Nb-13 / 1	1201	1200	1288	1083	0.89	0.162	0.91–0.89
Nb-14 / 2	2398	1204	1277	1094	–0.21	–0.019	0.91–0.95
Nb-15 /17	1017	1215	1302	1106	3.48	0.747	0.82–0.91
Nb-16 /23	1408	1208	1275	1121	0.08	0.012	0.87–0.95
Nb-17 /22	1303	1204	1334	1079	–1.85	–0.310	0.75–0.92
Nb-18 /23	1893	1214	1267	1121	0.35	0.040	0.94–0.96

The sample is exposed in the flow at a length of 25 mm and thus the heating area is 275 mm^2.

The tests consisted in exposing the sample in the flow for a certain time, the counting of which was started from the moment the surface reached a temperature of 1200°C, measured by laser-guided pyrometers: 1) INFRATHERM Converter IGA 100 (IMPAC Electronic Gmb, Germany) and 2) IMPAC ISQ 5-LO MB-30 (LumaSense Technologies, USA).

Measurements of the surface temperature-brightness $T_{w\ pyr}$ (pyrometer IGA 100) and true T_w (pyrometer ISQ 5-LO MB-30) – were carried out at a frequency of 1 s^{-1}, the obtained data were recorded by the regular program INFRATHERM on a PC. Based on the data obtained, the values of the emissivity of the niobium alloy at the surface temperature were calculated from the formula:

$$\varepsilon = \exp[C_2(1/T_1 - 1/T_2)]$$

(T_1 is the true temperature; T_2 is the brightness temperature; $C_2 = 8449\ \text{K}^{-1}$ is pyrometric constant of a pyrometer with an average wavelength of $\lambda = 1.63\ \mu\text{m}$).

As temperature T_1 and T_2, the average integral temperatures T_w and $T_{w\ pyr}$ were taken, respectively, for 60–100 seconds in areas with a relatively steady surface temperature. Recording of the pyrometers readings in the Nb-1 test (test No. 1 of the niobium alloy sample) with the results of calculation the emissivity values based on 450–550 seconds and 1050–1150 seconds of the test is shown in Fig. 4. Fig. 4, *b* shows the variation of the niobium alloy sample emissivity during a multicycle test of Nb-17.

The sample was weighed on a laboratory scale VLR-200 with an accuracy of 0.05 mg before and after each test.

The total duration of 18 tests was 23570 s (393 minutes or 6.5 hours) in 100 cycles with an average surface temperature of 1203 °C. The conditions and results of the tests are given in Table 1.

The change in the sample mass during the test is shown in Fig. 5. The largest weight gain of the sample occurs in the first 40 minutes of heating (49.4 mg), when the oxide film forms and grows, then for two hours there is an equally intense loss of mass, after which the process of mass change gradually stabilizes. During the last three hours of testing, the sample has both a weight gain and its loss, and the total sample weight change in the last eight tests (90 heating cycles with a total duration of 194 minutes) is only 2.12 g/m^2 (loss). The total change in the mass

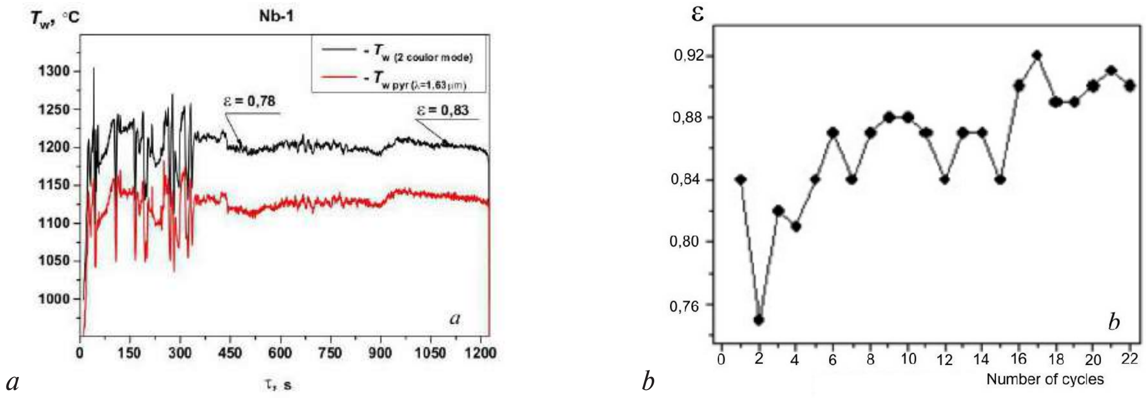

Fig. 4. Surface temperature of the Nb-based alloy sample in the heating spot during the Nb-1 (*a*) test and the change in the emissivity during the test Nb-17 (*b*)

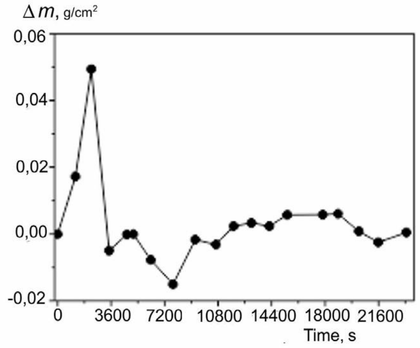

Fig. 5. Change in mass of a niobium alloy sample during thermal-erosion testing at a surface temperature of 1200 °C

of the sample for 6.5 hours of testing was 16.7 mg (loss), which corresponds to a loss of 61 g/m^2, and for a sheet 0.5 mm thick it is less than 2.3 % of the original mass.

Figure 6 shows the image of the Nb alloy sample after thermal erosion tests of Nb-12, Nb-16 and Nb-18. After the Nb-2 test, the surface of the sample in the heating zone got black, and during the following ten tests its morphology changed insignificantly: after the Nb-12 test (total 228 minutes of heating in twelve cycles), the surface had no significant defects, the oxide film retained its continuity, in the zone of action of the jet core, where its thermal-erosion action is maximal, the roughness of the surface is noticeably less than at the edge of the sample (Fig. 7, *a*). In subsequent tests, the surface of the sample loses uniformity in the heat spot, defects appear as transverse (relatively long side of the specimen) parallel cracks, which after some time are transformed into intumescence. Under the further thermal-erosive effect of the flow, these intumescences are smoothed out and the surface becomes relatively homogeneous again.

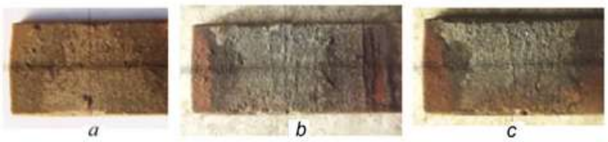

Fig. 6. The image of the sample of the Nb alloy after thermoerosion tests: *a* – after the Nb-12 test; *b* – after the Nb-16 test; *c* – after the Nb-18 test

Fig. 6, *b* shows the surface of the sample after the Nb-16 test (total 326 minutes of heating in 55 cycles) – defects in the form of cracks transformed into intumescences are seen on the upper edge of the image near the central part of the specimen, which near it are largely blurred. Almost the same picture is on the opposite (lower) edge of the sample. In Fig. 5, *c*, where the surface is shown after the final test of Nb-18 (total 391 minutes of heating in a hundred cycles), it can be seen that a significant part of the defects is completely smoothened, i.e. there occurred their complete "healing".

At the same time, a newly formed defect of 0.75 × 0.3 mm in size can be seen on the place of the previous one (enlarged in Fig. 7, *a*) resembling a fallen out seal. At the same time, the formation of the defect shown in Fig. 7, *a*, represents that "oxide fillings" under certain conditions (most likely, as a result of thermal cycling) can be fragmentarily chipped out.

In the upper and lower (in the image) parts of the defect, one can see the formation of two more fragments, the chipping of which will lead to the further crack elongation. Since the oxide filling of the initial crack is formed by the material of its

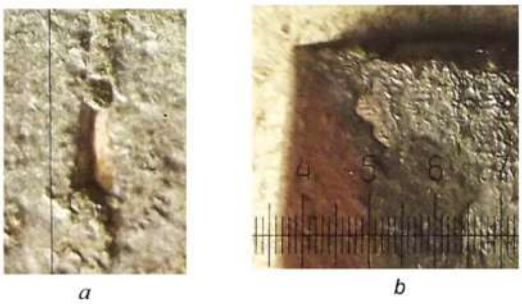

Fig. 7. Defects on the surface of Nb-based alloy sample after the thermal-erosion tests: *a* – the exposed section of the «healed crack; *b* – detachment of the oxide film

walls, its removal inevitably leads to an expansion and deepening of the crack. Then one of the possible mechanisms of thermal-erosion destruction of the niobium alloy surface under test can be represented as an increase in the size of its defects during the alternation of cycles of their healing by "oxide fillings" and their subsequent chipping. Thus, self-healing of cracks, as well as other surface defects, for example, potholes, formed during high-speed impact with dust particles in a gas stream occurs.

Life tests of UHTC front edge elements under conditions simulating hypersonic flight

The aim of the tests: the determination of operational properties of sharp leading blades models of a hypersonic aircraft made of ultrahigh-temperature ceramics of various compositions, under conditions of the supersonic flow of a fuel-air mixture of combustion products.

UHTC Sharp blades models produced by IPMS NAS of Ukraine of the following compositions: № 1 – ZrB_2-15$MoSi_2$; № 2 – ZrB_2-15SiC-5CrB_2; № 3 – ZrB_2-15$MoSi_2$-5CrB_2 have been tested.

The tests have been carried out with the use of a supersonic air-fuel burner GVI-13 with regenerative air cooling. Kerosene RT grade has been used as the fuel. For testing models in the shape of a wedge, the burner was equipped with a flat nozzle with the critical and output cross-sections of 26× 5 mm and 26 × 8 mm, respectively (Fig. 8, *a*) [7, 8, 9].

The model was attached to the manipulator of the stand by a clamp consisting two plates cooled by water. The model was thermally insulated with asbestos plates of 1 mm thick. The length of the fixed part of the model was 24 mm.

The model was positioned exactly at the center of the slit nozzle so that their symmetry axes coincided, the distance from the cut of the nozzle to the leading edge of the model in tests No. 2, No. 3 was 7 mm, in tests No. 1 – 15 mm. Insertion of the model into the flow was carried out with the short side forward.

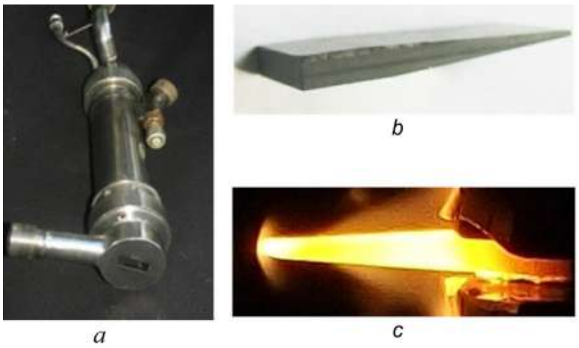

Fig. 8. The test of UHTC sharp blades model of a hypersonic aircraft on UTS test bench: *a* – burner with a flat nozzle, *b* – the model before testing, *c* – the model under testing

The tests were carried out at a pressure of 0.5 MPa in the burner combustion chamber, the flow temperature was regulated by the fuel consumption, changing the values of the oxidizer excess ratio (OER) in the fuel-air mixture. The test started at the minimal temperature reached by deep throttling of the burner, then it was smoothly raised to the maximum achievable in the combustion chamber with the OER $\alpha = 1.0$. At the end of the test, the flow temperature was gradually reduced to a minimum, after that the model was withdrawn from the stream. The braking pressure of the flow at the leading edge in the tests of models No. 1 was $P_o = 0.38$ MPa, on the No. 2 and No. 3 – $P_o = 0{,}43$ MPa. At the testing, the temperature of the model in the region adjacent to its leading edge was measured by laser-guided pyrometers.

The model before and under testing is shown in Fig. 8, *b*, *c*.

When calculating the true UHTC temperature of ZrB_2-15$MoSi_2$ composition, the previously obtained most probable value of its emissivity in the unoxidized state of $\varepsilon = 0.72$, and the maximum and minimum fixed values of its emissivity in this state of $\varepsilon = 0.77$ and $\varepsilon = 0.68$, respectively have been used. For UHTC of other compositions, the value of the emissivity was assumed to be $\varepsilon = 0.7$.

In the tests, the change in the mass of the models has been controlled by weighing on a laboratory scale VLR-200G with an accuracy of 0.05 mg.

Test results

Models No. 2 and No. 3, except Model No. 1, were fractured at the first cycle of thermal-erosion tests. Apparently, this is due to the uneven flow: the nozzle had a size of 26 mm, and these models ~ 24 mm, and also by a higher value of the braking pressure on the surface (0.43 MPa).

At the same time model No. 1 was 2 mm narrower (22 mm) and, consequently, the temperature distribution along the sharp edge of the model was more uniform, and the braking pressure on its surface was 0.38 MPa.

Model No. 1 was tested in four tests (No. 1-1, No. 1-2, No. 1-3, No. 1-4), after which it retained its integrity. Tabl. 2 shows the conditions and test results.

The wiev of model No. 1 after tests No. 1–2 is shown in Fig. 9, *a*. After test No. 1–3, the roughness of the edge increased significantly due to numerous microdefects in the form of dying. After testing No. 1-4, most of the surface of the leading edge crumbled to a depth of 0.18–0.22 mm. However, in this case its shape was preserved (Fig. 9, *b*), which allows us to state that the model remains operational.

Table 2

Results of thermal-erosion tests of Model No. 1

Test number	Test duration, s	Test duration at operating mode, c	The average integral temperature at the operating mode at the measuring point, °C	Change in the model mass, Δm, mg	The calculated mean integral temperature of the leading edge at $\varepsilon = 0.72$, °C
No. 1-1	1241	839	1489	−1.95	1774
No. 1-2	1601	1202	1513	9.55	1831
No. 1-3	826	250	1519	32.45	1845
No. 1-4 (all)	1719	945	1485	40.4	1765
No. 1-4	mode 1	385	1462	–	1715
No. 1-4	mode 2	560	1501	–	1802

Weight loss of the model for the entire test period was 80.45 mg. Fig. 10 shows the change in mass during the test.

Despite the fact that there is practically no free oxygen in the combustion products flowing around the model during operation, after the first test, its mass increased, indicating the UHTC oxidation. At the further tests, the formation of an oxide film occurred on the surface of the model, especially intensively on the part which is the farthest from the edge (Fig. 10, *b*). Probably, the oxidation of the model surface occurred during the operating mode reaching process and cooling after it, when there was air excess in the fuel-air mixture.

Conclusions

1. Nb-based alloys samples tests at a temperature of 1200 °C under conditions of convective heating by combustion products on the UTS test bench revealed their sufficient heat resistance for these alloys use in metallic thermal shielding systems for reusable space vehicles. X-ray diffraction analysis showed that the high efficiency of the developed alloys is provided by the formation of protective films on the surface.

2. Thermal-erosion tests of sharp leading blades models of a hypersonic aircraft made of ultra-high-temperature ceramics of various compositions under conditions of supersonic flow with a stream of chemically neutral combustion products of a stoichiometric fuel-air mixture at surface temperatures in the flowing zone of 1650–1850 °C have been carried out. ZrB_2-15$MoSi_2$ model has been tested at the leading edge temperatures of 1715–1845 °C under four heating cycles with a total duration of 3236 seconds at a braking pressure of 0.38 MPa. The leading edge average integral temperature over the entire testing time was 1800 ± 40 °C, the model weight loss during the test period was 80.45 mg, the linear drift was about 0.2 mm. According to the tests, model No. 1 has fully retained its operability. It allows to recommend ZrB_2-15$MoSi_2$ ceramics for sharp leading blades of a hypersonic aircraft thermal shielding application. The compositions of ZrB_2-15SiC-5CrB_2 and ZrB_2-15$MoSi_2$-5CrB_2 require additional studies.

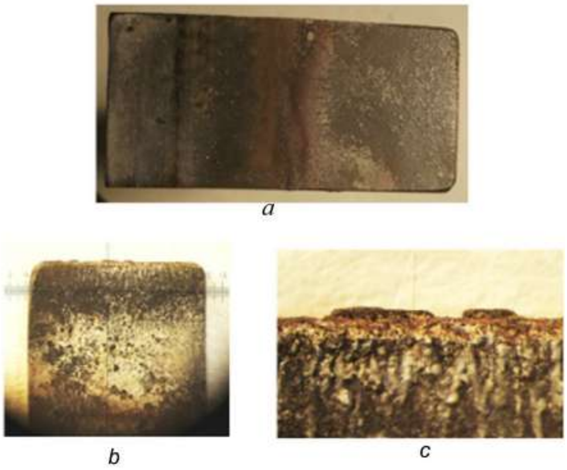

Fig. 9. Image of No. 1 model after thermal-erosion testing: *a* – after No. 1-2 test; *b* – after No. 1-4 test; *c* – the same as *b* with an enlarged edge (the division value is 54 μm)

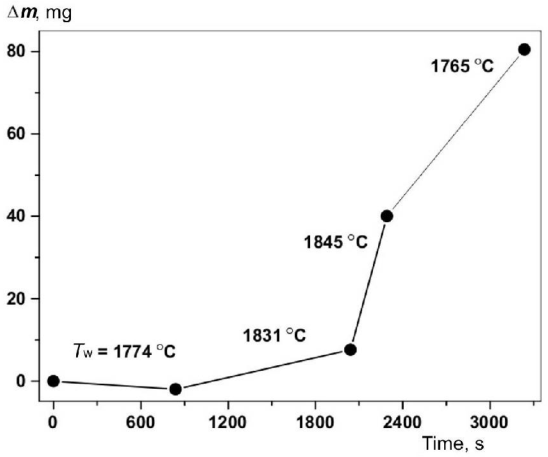

Fig. 10. Change in the mass of No. 1 model at thermal-erosion tests

REFERENCES

1. *Polezhaev Yu.V., Frolov G.A.* Thermal destruction of materials / Eds. V. Skorokhod (Academician of NASU). – Kiev: Akademperiodyka, 2006. – 354 p. (in Russian).

2. *Frolov G.A., Tykhyy V.G. and Potapov A.M.* Criteria of thermal destruction for the estimation of quality of heat-protective materials in various heating conditions // Acta Astronautica. – 2009. – V. 64. – Iss. 1. – P. 41–48.

3. F*rolov G.A., Solntsev V.P., Solonin S.M., Buchakov S.V., Evdokimenko Yu.I., Kisel V.M., Potapov A.M.., Tikhyy V.G.* High-temperature tests of metallic thermal protection for rocket and space technology // Aerospace Engineering and Technology. – 2008. – No. 10/57. – P. 62–65 (in Russian).

4. *Solntsev V., Frolov G., Kravchuk L., Nazarenko V., Bilan I., Petrash K., Husarova I., Potapov A.* Development of rolling modes for samples made from nichrome powder alloy and their testing at operating temperatures // International journal for science, techics and innovations for the industry. – 2017. – Iss. 5. – P. 254–257.

5. *Solntsev V.P., Skorokhod V.V., Frolov G.A., Petrash K.N., Solntseva T.A., Potapov A.M., Gusarove I.A.* Development of a heat-resistant alloy based on niobium for thermal protection of rocket-space equipment // Visnyk dvigunobuduvannya. – 2016. – No. 2. – P. 198–206 (in Russian).

6. *Evdokimenko Yu.I., Kisel V.M., Frolov G.A., Buchakov S.V.* Burner device of a two-stage configuration for high-speed air-fuel spraying with liquid fuel // Visnyk dvigunobuduvannya. – 2015. – No. 2. – P. 143–148 (in Russian).

7. *Evdokimenko Yu.I., Frolov G.A., Kissel V.M.* Thermal testing of front edge materials of hypersonic aircraft. // Naukovi notatki. Interacademic collected papers. – Lutsk: Publishing house of Lutsk National Technical. Un-t, 2017. – Iss. 58. – P. 145–152 (in Russian).

8. *Evdokimenko Yu.I., Frolov G.A., Kisel V.M., Kolotilo A.D., Buchakov S.V., Grigoryev O.N., Neshpor I.P.* Equipment and test results of materials based on zirconium diboride for heat-stressed elements of hypersonic aircraft / Abstracts of the 17th Ukrainian Conference on Space Research, August 21–25, 2017, Odesa, Ukraine. – P. 109 (in Russian).

9. E*vdokimenko Yu.I., Frolov G.A., Kisel V.M.* Method of thermal testing of materials of sharp front edges of hypersonic aircraft // Materials of the 7th Belarusian Space Congress, October 24-26, 2017, Minsk, Belarus. Minsk: OIPI NAS of Belarus, 2017. – V. 1. – P. 63–66 (in Russian).

SUPERLIGHT-WEIGHT THERMAL PROTECTION SYSTEM: CONCEPTION, METHODS, AND MODELING

V. Yatsenko[1], Iu. Falchenko[2], L. Petrushynets[2]

[1] Space Research Institute of NAS of Ukraine and SSA of Ukraine (SRI NASU-SSAU)

[2] E.O. Paton Electric Welding Institute of NAS of Ukraine (EWI NASU)

A space system (SS) at the all fly stages has a big number of negative factors, which can be destroyed a thermal protection system [1–8]. On the surface of the orbital system influences extremely high temperature. The thermal protection system of a reusable rocket should allow the possibility of a multiple use. She also must be easy and inexpensive. The vehicle also required low vulnerability to orbital debris and minimal thermal conductivity. Designers should to bond the thermal protection system directly to its aluminum skin, which presented an additional challenge. This system should have an additional structural stability during start and after returning from orbit. The costs associated with the development of TPS often exceed 25 % of the total costs of a spacecraft.

TPS of the head parts of ballistic missiles, manned re-entry vehicles and automatic planetary stations is usually created on the basis of destroyable (ablative) thermal protection materials. One of the most effective ablative heat shield materials is Phenolic Impregnated Carbon Ablator (PICA-X), applied for protection of the re-entry vehicle SpaceX's Dragon [1–8].

In active systems liquid or gas cooler is used, which allows extracting heat from the inner surface or from the volume of filtration through physicochemical transformations. Active thermal protection systems are generally more technically complicated and heavier than passives. Cooler tanks, pipes, pumps or pressure accumulators and other assistive devices reduce their mass-geometric efficiency.

The article is devoted to the review of the main results obtained in the implementation of the project, the concept, modeling results and the problem of risk assessment of the influence of space factors on materials, elements and system of thermal protection of spacecraft, and a comparative analysis of the results of numerical simulation and experimental studies in the diffusion welding of the heat-shielding panel.

Conception of TPS modelling

In the frame of the EU project «Superlight-weight thermal protection system for space application (LIGHT-TPS)» [1–3] the research was carried out on the basis of simulation of a prototype model of the thermal protection system of spacecrafts for multiple use with a specific gravity of no more than 10 kg/m^3. The bottom line is an analysis of influence of the free space environment on the superlight-weight thermal protection system (TPS). This paper concentrates on new methods that based on the following approaches: synergetic, optimization, probabilistic, physical, and computational.

Our approach concerns the self-organized synthesis of structures and the creation of technologies on the principles of self-organization in conjunction with the creation of materials with new functional properties.

The first concerns the synergetic approach. The synergetic approach to the solution of problems of self-controlled synthesis of structures and creation of self-organizing technologies is considered in connection with the super-problem of materials creation with new functional properties. Synergetics methods and mathematical design are considered according to actual problems of material science.

The second approach describes how the optimization methods can be used to determine material microstructures with optimized or targeted properties. This technique enables one to find unexpected microstructures with exotic behavior (e.g., negative thermal expansion coefficients).

The third approach concerns the dynamic probabilistic risk analysis of TPS elements with complex characterizations for damages using a physical model of TPS system and a predictable level of ionizing radiation and space weather. Focusing is given mainly on the TPS model, mathematical models for dynamic probabilistic risk assessment and software for the modeling and prediction of the influence of the free space environment [11]. The probabilistic risk assessment method for TPS is presented considering some deterministic and stochastic factors.

The forth approach concerns results of experimental research of the temperature distribution on the surface of the honeycomb sandwich panel size 150 × 150 × 20 mm at the diffusion welding in vacuum are considered. An equipment, which provides alignment of temperature fields in a product for the formation of equal strength of welded joints is considered. Many tasks in computational materials science can be posed as optimization problems. This technique enables one to find unexpected microstructures with exotic behavior (e.g., negative thermal expansion coefficients).

The last approach is concerned with the generation of realizations of materials with specified but limited microstructural information: an intriguing inverse problem of both fundamental and practical importance. Computational models based upon the theories of molecular dynamics or quantum mechanics would enable the prediction and modification of fundamental materials properties. This problem is solved using deterministic and stochastic optimization techniques. The main optimization approaches in the frame of the EU project "Superlight-weight thermal protection system for space application" are discussed. Optimization approach to the alloys for obtaining materials with required properties using modeling techniques and experimental data will be also considered. This report is supported by the EU project "Superlight-weight thermal protection system for space application (LIGHT-TPS)".

A Novel Approach to Risk Analysis

We have analysed state-of-the-art approaches to measure effects of the ionizing radiation influence on materials, elements, and TPS system. The bottom line of our research is that the basic tenets of risk assessment have always been applied to TPS system safety using statistical methods. However, risk analysis must also consider aspects of the human behaviours.

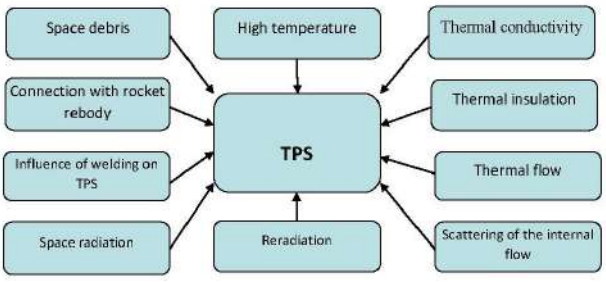

Fig. 1. Influence of space factors on the thermal protection system

The basic principles of risk assessment can be applied to TPS using statistical and optimization methods. Risk analysis should also take into account aspects of the developer's human behavior. Therefore, we proposed the following set of risk methods assessment: (*a*) statistical; (*b*) reliability assessment; (*c*) optimization methods; (*d*) accelerated TPS simulation; (*e*) nonlinear mathematical models.

The study of radiation effects on spacecraft has become increasingly important in recent years [11]. It is well known that electrical systems are sensitive to the radiation. Recent studies have shown that mechanical devices may also be exposed to radiation-induced damage. Especially sensitive to radiation devices that control by electric fields through insulators, i.e. (electrostatically located) cantilever beams, the location of which causes electrostatic interaction). Since insulators can collapse in the case of dielectric rupture, there is a high probability that these devices will have reduced performance in the space environment. Another difficulty is that the radiation can cause damage to the TPS material grid. Despite the long history of the TPS system, it is very important to study the effect of ionizing radiation on TPS in a specific TPS system. This problem was repeatedly considered by researchers to provide reliable and practical TTS for space flight. This approach allows to use the methods for assessing the risk of the influence of space factors to evaluate possible damage TPS components. The functional model of risk analysis is shown on Fig. 2.

Numerical modeling and experimental research

We have carried out a comparative analysis of the results of experimental studies and numerical simulation and obtained dependencies between the temperature of the heating of the material on the basis of nickel and the porosity of the material (Fig. 3).

A group of curves on Fig. 3 shows the evolution of temperature inside the material from porous nickel when placed in a furnace with a temperature of 2400 °C. Curves correspond to different geometric porosity distribution in the material. The small deviation in the behavior of these curves (Fig. 3, *a*, *d*) shows that the configuration of the metal component of this material at low and high porosity does not significantly affect the processes of heat transfer

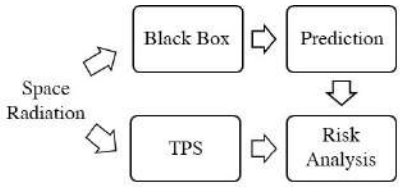

Fig. 2. Functional model of risk analysis

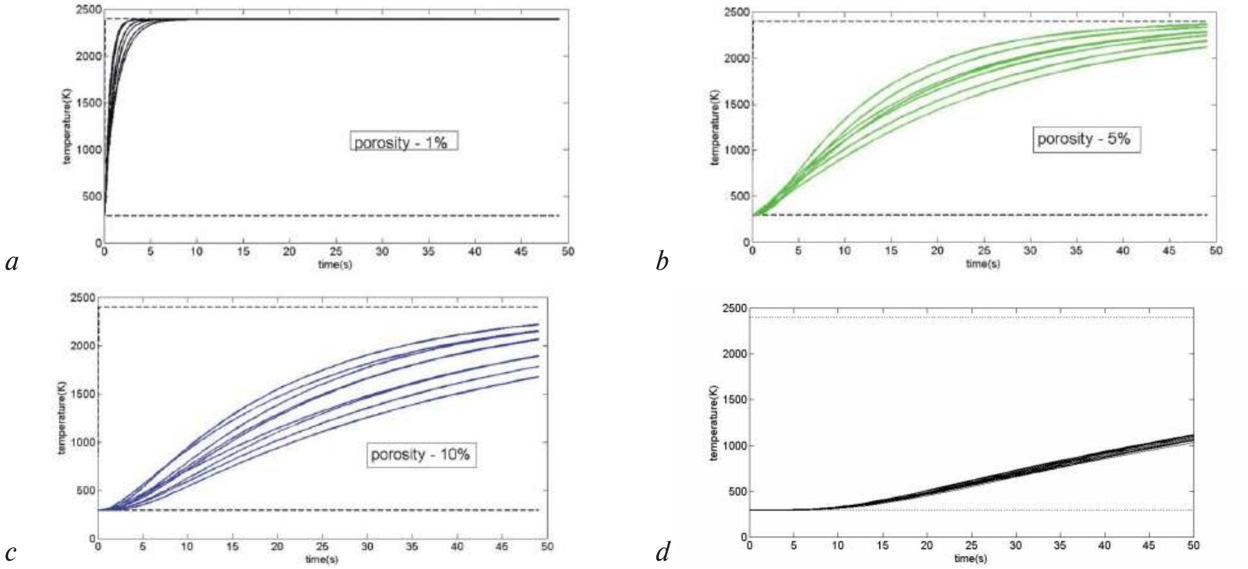

Fig. 3. Distribution of the temperature in the center of the sample from nickel, depending on its porosity: *a* – porosity of the material 1 %, *b* – 5 %, *c* – 50 %, *d* – 90 %

and the temperature distribution of the material. Also, it is noteworthy that when the porosity of the material increases, the speed of its heating is changed. On Figure 3, *a* at porosity 1 %, the heating rate is greatest, and with the porosity of 90 % (Fig. 3, *d*) – the smallest.

The presented results are important both for taking into account the influence of the space factors of space on reducing the risk of uneven heating of the TPS, as well as when receiving welded joints. In the process of welding, it is necessary to ensure the uniformity of the heating of the welding surfaces.

TSP design

Structurally, the TPS consists of the thermal protection panels (TPP), which therefore consist of honeycomb core, top and bottom covers.

The weight of an TPP welded from a honeycomb core with dimensions 150 × 150 × 16 mm with a wall thickness of 0.03 mm, an upper and a lower cover of a thickness of 0.5 mm and 0.1 mm is approximately 120 ... 130 grams. The light weight of a three-layer panel is caused by the presence of hollow cells and powder alloy based on nichrome – YUIPM-1200 which was used as a material. Calculation shows that the weight of the corresponding volume of metal from the Ni-Cr alloy is 2880 grams. So the «conventional» porosity of the TPP panel is about 95 %.

Optimization of the heating conditions of the TPP during diffusion welding in vacuum

In the case of diffusion welding, it is important to ensure homogeneity of the heating of the surfaces of the product, and to determine the consistency of the properties of the welded joint. Therefore, in the case of diffusion welding of products with a developed surface, it is necessary to control the character of the heating of various parts of products. Analysis of TPP structure and design of working chamber of diffusion welding unit shows that the conditions for uniform heating of three-layer panel are not favourable (Fig. 4).

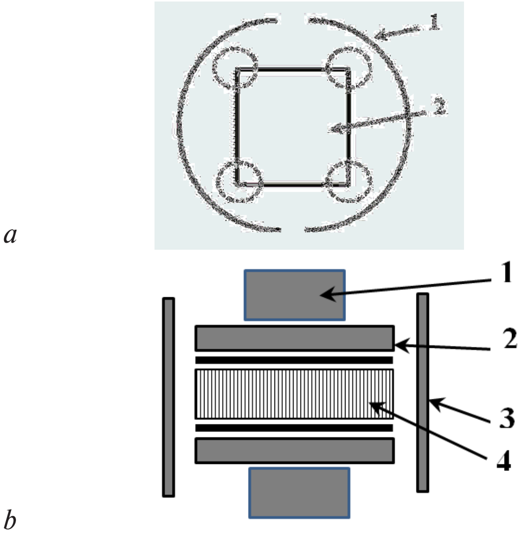

Fig. 4. Scheme of heating of TPP under conditions of diffusion welding: *a* – top view: 1 – heaters from molybdenum, 2 – TPP; *b* – side view: 1 – upper and lower rod, 2 – upper and lower flanges, 3 – heaters, 4 – TPP

Non-uniform heating of the three-layer panel is due to its rectangular shape and cylindrical shape of molybdenum heaters (Fig. 4, *a*), that promotes predominant heating of panel corners and the side surface of the panel. Small height of the panel and its considerable area can also be regarded as the conditions, which do not promote uniform heating of the panel (Fig. 4, *b*). The area of the panel is 225 cm^2, and its height is 1.6 cm.

Heating system of TPP during welding analyzed using analytical and numerical models. In particular, the numerical model was implemented using the finite element method. The theoretical results were compared with the experimental data in terms of the temperature difference, showing the significant reliability of both analytical and numerical models. After testing the finite element model, a sensitivity analysis was performed to study the effect of some variables.

Chromel-alumel (ChA) thermocouples which were fixed on honeycomb core and face cover surface, were applied for temperature measurement. Visual control of temperature was conducted with application of multichannel thermocontroller (EPA C1-IT-4УН), and signal recoding in digital format was performed in DATA LOGGER (DT-171T).

We also investigated the effect of various heating conditions on the temperature distribution on the surface of the TPP. In the first variant, the panel was installed between the upper and lower rods and was heated directly. In the second variant, the technological equipment, which consisted of an upper and lower flange and a bushing, was used to heat the TPP. This device was supposed to redistribute the heat flow from the heaters from the lateral surface of the TPP to its end surfaces.

Heating TPP without using technological equipment

TPP was set between the upper and lower rods, whose diameter was less than the area of the covers and was 90 mm. Heater height was 200 mm. Thermocouples were fixed on the end face of honeycomb core, in the corner and center of face cover. Temperature in control points was studied simultaneously. TPP heating rate was equal to $V = 5$ °C/min. As shown by the conducted studies, the most intensive heating is observed on honeycomb core. During the control measurement time, its temperature was equal to 900 °C. In the corner of panel face cover maximum heating temperature was equal to 800 °C, and in its center – to 650 °C. This leads to the conclusion that a considerable temperature gradient is observed in different panel sections (Fig. 5, *a*, *c*).

In the TPP, the honeycomb core and corners of the covers are heated most intensively at a temperature of 900 °C and 800 °C accordingly, and the heating of the central part of the covers is slowed down to – 650 °C.

It should be noted that in diffusion welding of items with a developed surface, such a technique as welding in forming devices is widely used [12]. Application of protective fixtures allows equalizing the temperature in different sections of the part to be welded, and smoother adjustment of welding pressure.

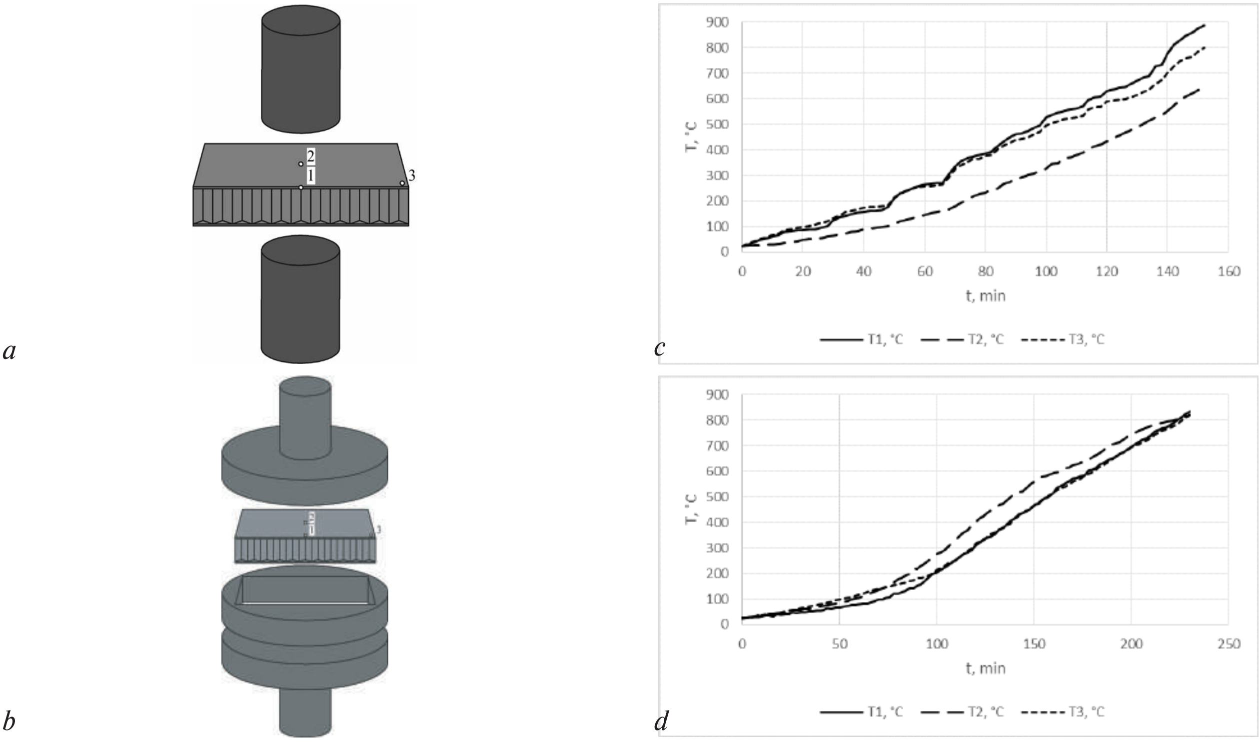

Fig. 5. Arrangement of the TPP in the chamber of the equipment: between the upper and lower rods (*a*) and the heating graphs of the various sections on the surface of the TPP (*c*) in the process equipment (*b*) and the heating curves of the various sections on the surface of the TPP (*d*). Points 1 to 3 indicate locations for fixing thermocouples

Fig. 6. Side view of a sample of a three-layer panel after compression tests

Heating of the TPP in the technological equipment

For this purpose, the technological equipment is used to get steadier heating of the entire panel (Fig. 5, *b*). A flange of 50 mm height was made, in the middle of which an area for honeycomb core of 150 × 150 mm size was cut out. Above and below the TPP, massive flanges were also installed. Thermocouples were fixed in the middle of the end face and in the corner and center of face cover. The results obtained are shown in Fig. 5, *d*.

The analysis of the received graphs shows, application of protective flanges at TPP heating allows equalizing the temperature on the surface of TPP. Temperature is approximately the same in all the points and is equal to 800 °C.

Tests of tensile specimens were performed to evaluate the strength of the joints, as well the compression tests of samples that was cut from TPP. Individual elements corresponding to hexagonal cells were cut out with an abrasive disc from of three-layer panel of 150 × 150 mm size. Dimensions of honeycomb core cells were 10 × 10 mm.

Investigations were performed using digital pressure controller of "KOLI" Company, XK3118T1 model and pressure sensor of "CAS" Company, MNC-1 model with working range from 0 up to1000 kg.

Fig. 7. Thermal protection panel's layout obtained by diffusion welding in vacuum

Appearance of a three-layer panel sample after compression tests is shown in Fig. 6. As is seen from the Figure deformation of honeycomb core walls takes place at compression without destruction of the areas of welding the honeycomb core to panel covers.

Based on the results of the research, three-layer cellular panels made of heat-resisting powder Ni-Cr alloy were obtained (Fig. 7).

Conclusions

The influence of space environment factors on the thermal protection system of space vehicles was analyzed. A new concept for modeling the TPS is proposed, which is based on the following principles: synergistic, physical and computational.

Algorithmic and software for simulation of the system of thermal protection of space vehicles and calculation of the magnitude of risk have been developed. Also, the dependence of the magnitude of the risk of space factors was obtained. It is established that among more than 22 factors affecting the state of TPS, the welding technique occupies an important place.

Nature of thermal protection panels heating was studied under the conditions, which correspond to the process of vacuum diffusion welding. It is shown that the nature of panel heating is essentially influenced by a number of factors, namely: geometrical – rectangular shape of three-layer panel, cylindrical shape of heaters, small panel height and its considerable area.

It is found that heating of the panel without fixture application prevailing heating of honeycomb core and face plate corner to 900 °C and 800 °C, respectively, is observed in it at slower heating of the central part of face plate (650 °C). The use of technological equipment provides more steady heating of the entire panel.

REFERENCES

1. *Johnson S.M.* Thermal Protection Materials and Systems: An Overview // Engineered Ceramics: Current Status and Future Prospects. – Hoboken, New Jersey: John Wiley & Sons, Inc., 2016. – P. 224–243.

2. *Agrawal Parul, Prabhu Dinesh.* Investigation of Performance Envelope for Phenolic Impregnated Carbon Ablator (PICA) // 54th AIAA Aerospace Sciences Meeting, January 4–8, 2016, San Diego, California, USA. – P. 1–16.

3. *Hsi-Wu Wong, Jay Peck, James Assif et al.* Detailed analysis of species production from the pyrolysis of the Phenolic Impregnated Carbon Ablator // Journal of Analytical and Applied Pyrolysis. – 2016. – V. 122. – Iss. 11. – P. 258–267.

4. *Demonis I.M., Petrova A.P.* (2011). VIAM Materials in Space Technology // All materials. Encyclopedic Guide. – 2011. – No. 6. – P. 2–9 (in Russian).

5. *Lozino-Lozinskii G.N., Bratukhin A.G.* Aerospace Systems. – Moscow: MAI, 1997. – 416 p. (in Russian).

6. Elements (types) of thermal protection «Buran». Available at: http://www.buran.ru/htm/tersaf4.htm (in Russian).

7. *Donald M. Curry.* Space Shuttle Orbiter thermal protection system design and flight experience / First ESA/ESTEC Workshop on Thermal Protection Systems, May 5–7, 1993, Noordwijk, Netherlands.

8. *Pate-Cornell M.E., Fischbeck P.S.* Safety of the thermal protection system of the space shuttle orbiter: Quantitative analysis and organizational factors. Phase 1: Risk-based priority scale and preliminary observations. – Langle: National Aeronautics and Space Administration Scientific and Technical, 1990. – 110 p.

9. *Yatsenko V.* Optimization methods in material science: synergetics, dynamical models, and optimization problems / Abstracts of the 3rd International Scientific conference "Nonlinear analysis and applications", May 15, 2015, Kyiv, Ukraine. – P. 79.

10. Y*atsenko V., Girenko A., Husarova I. et al.* Superlight-weight thermal protection systems for space applications: conception, methods, and applications / Abstracts of the 6th European Conference for Aeronautic and Space Sciences (EUCAS 2015), June 29– July 3, 2015, Krakow, Poland. – P. 169.

11. Y*atsenko V., Pardalos M., Boyko N., Rebennack S.* Space weather influence on power systems: prediction, risk analysis, and modeling // Energy Systems. – 2010. – V. 1. – No. 2. – P. 197–207.

12. *Gusarova I., Parko M., Potapov A. et al.* Evaluation of high temperature resistance of three-layer honeycomb panel produced from YuIPM-1200 alloy by vacuum diffusion welding // Avtomaticheskaya Svarka. – 2016. – No. 12. – P. 29–33 (in Russian).

13. *Falchenko Yu., Petrushynets L., Ustinov A. et al.* Diffusion welding in vacuum thin sheet of nickel alloy // Technical sciences and technologies. – 2016. – No. 4. – P. 87–96 (in Ukrainian).

OXIDATION PROCESSES INVESTIGATIONS OF ZRB2- BASED PLASMA COATING ON CARBON-CARBON SUBSTRATES IN THE HIGH-TEMPERATURE FLOWS OF COMBUSTION PRODUCTS

O. Grigoriev[1], I. Podcherniaeva[1], G. Frolov[1], M. Parco[2], I. Neshpor[1], Yu. Evdokimenko[1], D. Vedel[1], M. Kuetemeyer[3]

[1] Frantsevich Institute for problems of materials science of NAS of Ukraine (IPM NASU)
[2] Industry and Transport Division (TECNALIA), Spain
[3] Deutsches Zentrum fur Luft- und Raumfahrt (DLR), Germany

For thermal, erosion and corrosion protection of new generation of supersonic reusable space aircrafts the materials with improved properties are in need. Sharp leading edges and nose cones are subjected to high temperatures in severe thermal cycling conditions in both neutral and oxidative environments, as well as the erosive impact of gas streams and particles. For these extreme operating conditions, materials with high resistance to oxidation, erosion, low creep and high resistance to thermal shock are of great demand. Existing heat-shielding materials based on ZrO_2 and rare-earth element oxides do not meet such requirements at temperatures of ~2000 °C. The most promising materials for this purpose are composites with ceramic matrix, ultra-high temperature ceramics (UHTC) and carbon-carbon composite materials (CCCM) with coatings, resistant to high-temperature oxidation (HTO), for example from silica carbide.

UHTC based on ZrB_2 has a unique combination of high melting point, high mechanical properties and erosion resistance in combination with a relatively low density (6 g/sm^3). UHTC based on zirconium diboride of ZrB_2-SiC system [1–3] attracts special interest of the researchers concerning its high resistance to high-temperature oxidation (HTO), which is provided by the formation of a protective SiO_2 glass-like film on the scale surface.

During a long period of time the attention of researchers is paid to the ZrB_2-$MoSi_2$ system [4–7]. The increased resistance of these ceramics to HTO is caused by the formation of a borosilicate glass film based on β-SiO_2 (cristobalite) which covers the silicide phases of molybdenum at oxidation [4]. Taking into account the dependence of the thermal conductivity of zirconium dioxide on porosity (0.5–2 W/(m·K)), we can expect an increased heat-shielding ability of a porous oxidized plasma coating based on ZrB_2. However, the studies of heat-shielding capacity of the ZrB_2-$MoSi_2$ system for compact materials are limited, and as for ZrB_2-$MoSi_2$ system coatings on substrates of CCCM, there is practically no information. It is known, the ZrB_2-$MoSi_2$ system two-layer coating applied on pyrolytic graphite by a slip laser method [4], although, for plasma coatings such studies are absent.

The aim of this work is to investigate the processes of high-temperature oxidation of a plasma $ZrB_2 + 15\%$ $MoSi_2$ UHTC coating on a CCCM substrate under the impact of supersonic streams of combustion products of fuel mixtures with various free oxygen content.

Materials for UHTC coatings and methods of their research

Raw materials characteristics: ZrB_2 powder manufactured by Shtark, Germany, grain size of 1.0 µm, 98.7% purity, with the main impurity of O: 0.8% and C: 0.3%. Molybdenum disilicide ($MoSi_2$) manufactured by Shtark, Germany, grain size 1.0–3.0 µm, 98.5% purity, the main impurity O: 1.2% and Fe: 0.3%.

Composite powders (CP) of ZrB_2-15 vol.% $MoSi_2$ UHTC for coating were obtained by mixing the raw components in a planetary mill followed by granulation. The particle size of the CP was 40–60 µm (Fig. 1).

The coating was deposited by plasma method using an installation consisting of a commercial plasma gun F4 and a spray system for supplying an inert gas. At the front of the F4 plasma gun, a special frame was attached (Fig. 2), in the shape of a tubular extender with an inert gas injection system, to create

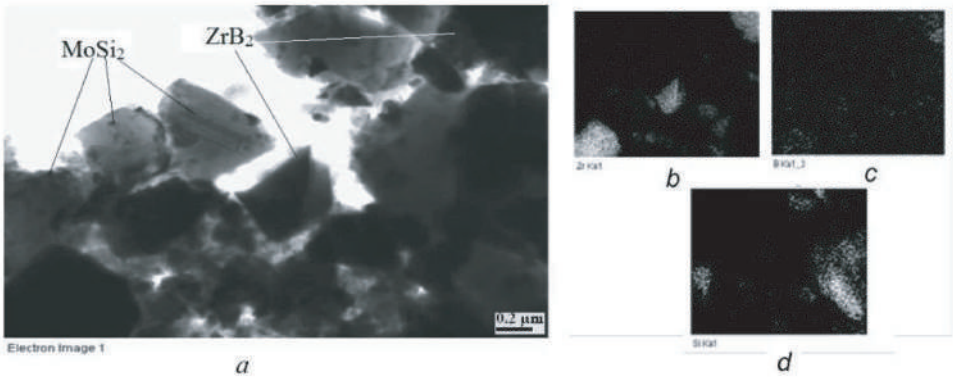

Fig. 1. Raw powder particles of the charge (*a*) in the characteristic radiation: Zr (*b*), B (*c*), and Si (*d*)

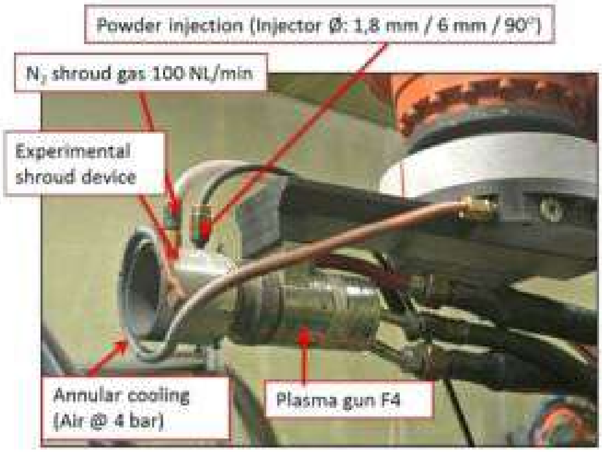

Fig. 2. General view of the plasma torch

a protective atmosphere around the plasma flaw. Cooling of the carcass was carried out by blowout with nitrogen. Parameters of plasma deposition: plasma forming gas: Ar (40 l/min) + H_2 (10 l/min), current strength 600 A, voltage 60 V.

The substrate is a composite C/C material with silicon film on the fiber surface of the DLR production (Germany). Its microstructure and the local chemical analysis, are shown in Fig. 3.

To determine the erosion resistance of the coating in a gas jet of a supersonic burner, two testing modes were used [6]. In the first mode, the surface of the plasma coating was subjected to gas erosion in a two-phase jet of an air-kerosene burner GVO-2M with a nozzle critical diameter of 11 mm and an output nozzle of 15 mm. The excess oxidizer coefficient in this case was $\alpha = 0.95 \ldots 1.1$. Calculations show that the thermal-gas-dynamic conditions of the thermal-erosion effect in the tests (stagnation temperature

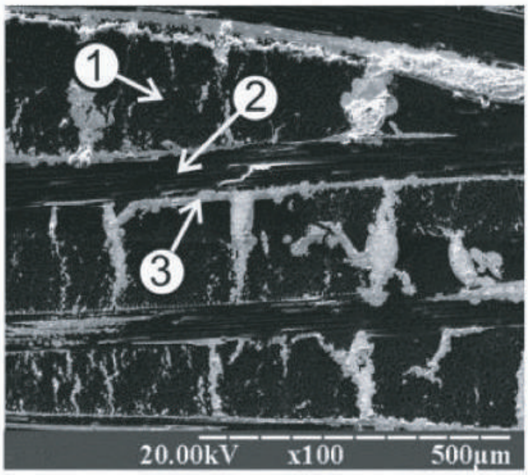

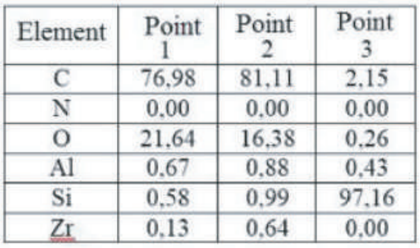

Element	Point 1	Point 2	Point 3
C	76,98	81,11	2,15
N	0,00	0,00	0,00
O	21,64	16,38	0,26
Al	0,67	0,88	0,43
Si	0,58	0,99	97,16
Zr	0,13	0,64	0,00

Fig. 3. The microstructure of the C/C substrate cross-section and its chemical local analysis where 1, 2 – fiber, 3 – Si coating on the fiber

Table 1

Parameters of the combustion products flow of kerosene in air in the output section of the nozzle dependently on the excess oxidizer coefficient (α) at a pressure in the combustion chamber (CC) of 0.8 MPa

Excess oxidizer coefficient, α	Temperature, °C		The flow rate, m/s	Content O + O_2, % (wt.)
	stagnation	in flow		
0.9	2095	1282	1540	$3.07 \cdot 10^{-3}$
1.0	2106	1322	1541	0.28
1.1	2013	1235	1501	1.9

Table 2

Parameters of the flow of combustion products of kerosene in oxygen in the outlet section of the nozzle dependently on the excess oxidizer coefficient (α) at a pressure in the combustion chamber of 0.8 MPa

Excess oxidizer coefficient, α	Temperature, °C		The flow rate, m/s	Content $O + O_2$, % (wt.)
	stagnation	in flow		
2	2669	1868	1709	44.16
2.5	2475	1690	1622	53.58
3	2285	1514	1545	60.58

of 2050 °C and stagnation pressure of 0.45 MPa) approximately correspond to the flight conditions of a hypersonic aircraft at an altitude of 18 km at a speed of 1920 m/s (6.5M) – naturally, without accounting for the oxidative effects of air oxygen and completely simulate the conditions in the supersonic part of the solid propellant rocket engine nozzle. Table 1 shows the parameters of the combustion products at these values of α.

In the second mode, the tests were carried out in a stream of oxygen-kerosene burner KKR-6. The distance from the cut of the nozzle to the surface of the sample was 40 mm, the inflow of the stream was at an angle of 80° to the surface. The excess oxidizer coefficient in this case was $\alpha = 2.3–2.5$ or more dependently on temperature [7]. Table 2 shows the flow parameters and oxygen content in the combustion products of the KKR-6 burner.

Thus, under thermal-erosion tests in the combustion products of the oxygen-fuel mixture, the oxidative effect of the flow, determined by the concentration of oxygen in all its modifications on the oxidized surface, is at least tens of times greater than the effect of hypersonic air flow in real conditions – the volume concentration of atomic oxygen (the most chemically active form of oxygen) is 22 times higher, molecular oxygen by 7 orders of magnitude. The distance from the cut of the nozzle to the surface of the specimen in both modes was 40 mm, the inleakage of flow was under the angle of 80° to the surface. Samples fixed on the linear manipulator holder were introduced into flow at a speed of 30 mm/s.

During the test, the surface temperature in the center of the heating spot was measured with two laser-guided pyrometers:

1) INFRATHERM Converter IGA 100 (IMPAC Electronic Gmb, FRG) pyrometer with a range of measured temperatures of 350…1800 °C and a wavelength of $\lambda = 1.45 \ldots 1.8$ μm.

2) IMPAC ISQ 5-LO MB-30 pyrometer (LumaSense Technologies, USA) with a range of measured temperatures of 1000…3000 °C operating in two-color mode at wavelengths of $\lambda = 0.9$ μm (channel No. 1) and $\lambda = 1.05$ μm

The microstructure of the surface was studied on an electron microscope of REM 106I, XRD – on a DRON-3 installation in CuKα-radiation. Microhardness was measured on an optical durometer of PMT-3 at a load of 0.5 N.

Results and discussion

A plasma coating of ~350 μm thick is formed without pores and cracks, well adjacent to the base and is characterized by the absence of lamellas (Fig. 4, *a*). The absence of pores in the coating indicates, according to [7], the reduced thermal conductivity of the ZrO_2 phase. The composition of the original coating corresponds to the composition of the sprayed composite powder (Fig. 5, *a*). The phase composition of the coating subjected to gas thermo-erosion by air and oxygen-containing streams characterized by different contents of the active phase of oxygen in the jet is shown in Fig. 5, *b, c*. In both cases, in

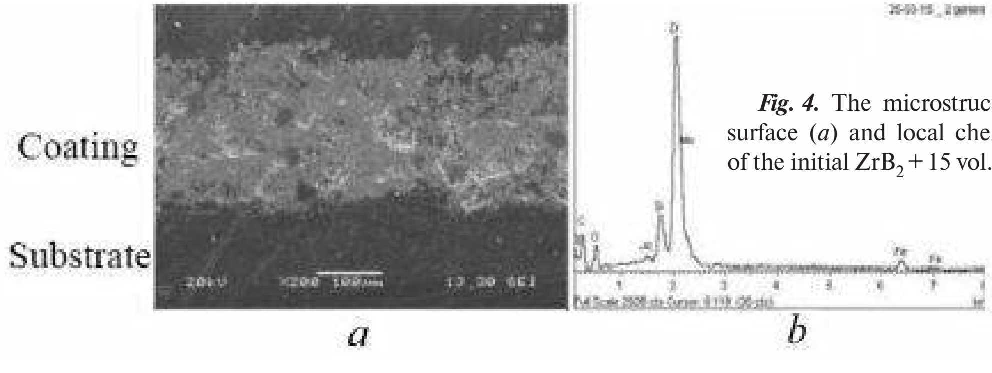

Fig. 4. The microstructure of the cross-section surface (*a*) and local chemical analysis at point 1 of the initial $ZrB_2 + 15$ vol. % $MoSi_2$ coating (*b*)

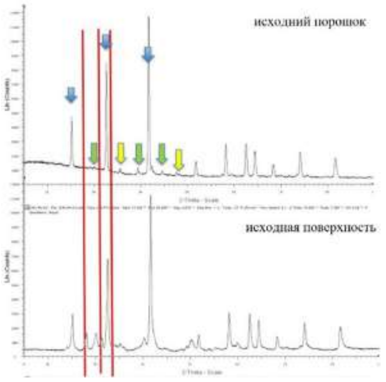

a

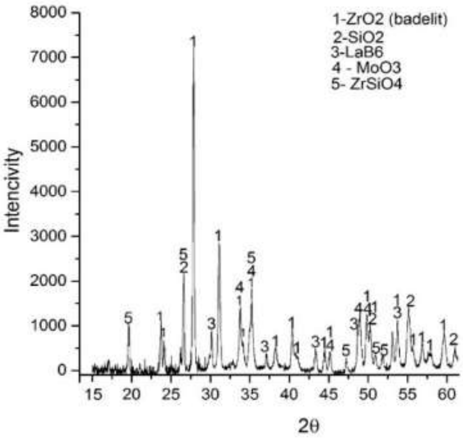

b

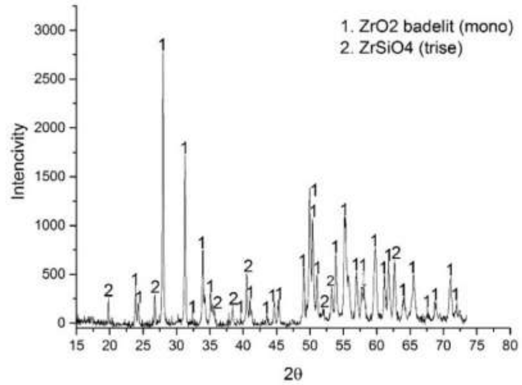

c

Fig. 5. XRD from the surface of the ZrB_2+15 vol.% $MoSi_2$ plasma coating: *a* – a raw powder and a surface; *b*, *c* – after thermal-erosion in air-containing (*b*) and in oxygen-containing (*c*) stream

accordance with (1)–(4) reactions, the main phase of the surface is the light phase of ZrO_2 (mon) with a small addition of the dark phase of zircon distributed in the shape of separate inclusions. However, in the case of a higher-temperature oxygen-containing jet, the amount of zircon is naturally larger, and the absence of additional oxide phases (MoO_3, SiO_2) is due to their evaporation.

The ZrB_2+15$MoSi_2$ coating material is oxidized by the following reactions:

(1) $ZrB_2 + 2{,}5O_{2(g)} = ZrO_2 + B_2O_3$,
(2) $5MoSi_2 + 7O_{2(g)} = Mo_5Si_3 + 7SiO_2$,
(3) $Mo_5Si_3 + 7{,}5O_{2(g)} = 5MoO_3 + 3SiO_2$,
(4) $ZrO_2 + SiO_2 = ZrSiO_4$.

The attention is drawn to the fact that in an oxygen-containing jet, the coating is oxidized to the entire thickness of ~318 µm (Fig. 6, *b*), whereas in the air containing jet during the test time only a thin layer with a thickness of ~56 µm is oxidized (Fig. 6, *a*), as a result of a lower oxygen content in the gas stream represented in the atomic form as a result of the dissociation of the triatomic molecules of the combustion products. Therefore, considering the low thermal conductivity of zirconia, we can expect a lower thermal conductivity of the fully oxidized coating and, accordingly, the maximal protection of the CCCM substrate from the high-temperature impact of the gas jet. Due to the complete oxidation of the coating over its entire thickness, an effective thermal protection of the substrate is formed due to the light phase of zirconia (88 %) with inclusions of the dark phase of zircon (11.5 %) with an average size of 7.9 µm (Fig. 7 *b*, *c*). These inclusions inhibit the propagation of cracks, which explains their absence in both the coating and the interphase boundary (Fig. 7, *b*)

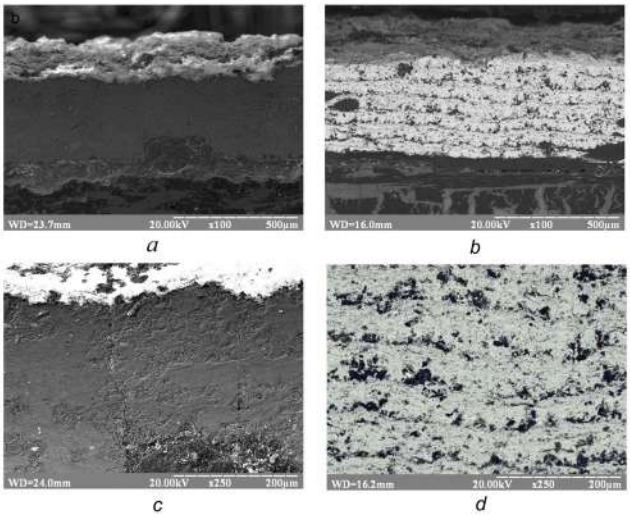

a *b* *c* *d*

Fig. 6. Microstructure of the cross-section of the plasma coating after thermal erosion in jets of combustion products of air-fuel (a, b × 500) and oxygen-fuel mixtures (c, d × 200)

When exposing by an air-containing jet, the structure of the unoxidized part of the coating adjacent to the substrate is distorted by intense thermal action, cracks are formed (Fig. 6, *c*). Cracks on the interface "coating-substrate" contribute to the penetration of the coating material into the substrate (Fig. 7, *a*). The thickness of this defect zone is ~100 µm. In case of oxygen containing jet, there are no defects on the interphase boundary (Fig. 7, *b*) resulting from the effective thermal

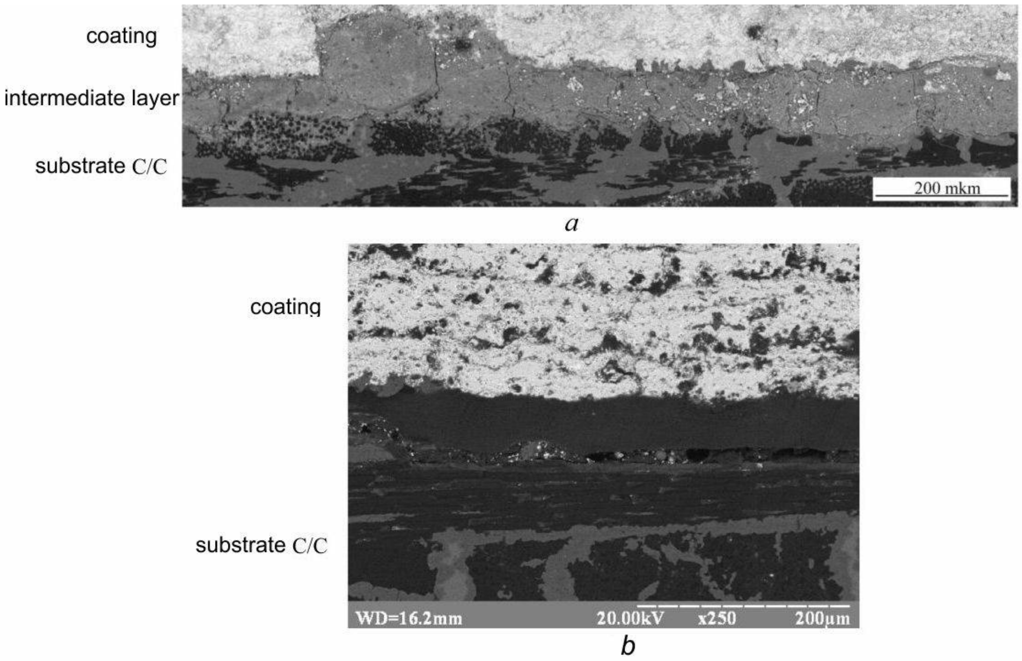

Fig. 7. The microstructure of the cross-section of the interface between the «coating» substrate in the air-containing (*a*) and oxygen-containing (*b*) jet

protection of the coating, which is oxidized over the entire thickness.

Thus, the higher the oxygen content in the high-temperature gas jet acting on the surface of the ZrB_2-based plasma coating, the thermal protection effect of the carbon substrate is better.

The microhardness of the coatings is close to the microhardness of zirconia and is 22 ± 2 GPa after testing in an air-containing jet, and 26 ± 2 GPa in an oxygen-containing jet. The reduced value of the microhardness of the coating is caused by the presence of softer phases – MoO_3 and SiO_2 (Fig. 5).

The increased oxidation rate of the coating (Tabl. 1) in an oxygen-containing gas jet leads to the effective thermal protection of a C/C composite (substrate)

The data of Tabl. 3 show that effective thermal protection of a C/C composite can be achieved by oxidation of a plasma UHTC coating based on ZrB_2 with a thickness of > 100 µm under conditions of thermal-erosive exposure of an oxygen-containing gas jet or the initial phase of operation.

However, herewith, the oxide components (MoO_3, SiO_2) responsible for the corrosion resistance are evaporated. The solution of the problem is in combining high-temperature thermal and corrosion protection of C/C composite by applying a ZrB_2-based two-layer UHTC coating, in which the oxidized part of the coating adjacent to the base is combined with the non-oxidized outer coating layer of ZrB_2 UHTC, responsible for HTO resistance. The development of such coatings will be the subject of our further research.

Besides the mentioned above studies, life tests of $ZrB_2 + 15$ vol.% $MoSi_2$ UHTC coatings on CCCM substrate has been carried out. They showed that in comparison with an unprotected CCCM substrate,

Table 3

The dependence of the ZrB_2+15 об.% $MoSi_2$ plasma coating oxidation rate on the regimes of the erosive gas jet impact

The jet composition	The excess of oxidant coefficient, α	The determining surface temperature, °C	Stagnation pressure, MPa	Holding time, c	Oxidized layer thickness, µm	Oxidation rate, µm /s	Defects in the coating
Combustion products of air-fuel mixtures	0.95–1.1	1573	0.45	513	55.7	0.11	Cracks, coating material penetration into the substrate
Combustion products of oxygen-fuel mixtures	2.3–2.5	1606	0.38	600	317.5	0.53	No

the coating protects the substrate in a supersonic jet of combustion products of the air-fuel mixture before the beginning of fracture for at least not less than 18.5 minutes, and in the oxygen-fuel jet – not less than 10 minutes. Herewith, it should be noted that the temperature of the surface of the coated sample in the jet of combustion products of the air-fuel mixture was more than 1500 °C, and in the oxygen-fuel jet was more than 1600 °C.

The work has been implemented within the framework of the European project FP-7.

Conclusions

1. A plasma coating based on the UHTC of $ZrB_2 + 15\% MoSi_2$ system with a thickness of 350 μm was obtained on a carbon-carbon composite material. A coating of 350 μm thick without pores and cracks closely adjacent to the base is characterized by the absence of lamellas.

2. The oxidation rate of the coating subjected to thermal erosion impact of combustion products in the air-containing jet is 0.11 μm/s, microhardness of the oxidized layer is 22±2 GPa, in the oxygen-containing stream – 0.53 μm/s and 26±2 GPa, respectively.

3. It is established that as a result of thermal-erosive impact of supersonic flows of air- and oxygen-containing gas mixtures under the test conditions, in the first case, an oxide layer of 56 microns thick is formed in the coating, and in the second, the coating is oxidized to its full depth.

4. An oxidized coating layer with a thickness of more 100 μm provides effective thermal and corrosive protection of the CCCM substrate, preventing its destruction as a result of thermal-erosive impact of high-speed gas stream.

REFERENCES

1. *Neshpor I.P., Mosina T.V., Grigoriev O.N., Panasyuk A.D., Pasichnyi V.V., Frolov G.A., Koroteev A.V.* The investigation of ZrB_2 based UHTCs corrosion resistance under concentrated solar radiation impact // Powder metallurgy. – 2015. – No. 3/4. – P. 77–83.

2. *Podcherniaeva I., Grigoriev O., Panasijuk A., Evdokimenko Yu., Kisel V., Jurechko D.* ZrB_2 based HVAF high-temperature coating on metallic alloys // Powder metallurgy. – 2016. – No. 11/12. – P. 110–115.

3. *Lavrenko V., Panasijuk A., Grigoriev O., et al.* The regularities of the high-temperature oxidation process of ZrB_2-$MoSi_2$ system materials // Powder Metallurgy. – 2012. – No. 01/02. – P. 131–137 (in Ukrainian).

4. P*odcherniaeva I., Grigoriev O., Panasijuk A., Yurechko D.* Hightemperature laser coatings of ZrB_2-$MoSi_2$ system on graphite // Superhard materials. – 2016. – No. 5. – P. 50–62 (in Russian).

5. *Grigoriev O., Neshpor I., Mosina T., Vinokurov V., Koroteev A., Vedel D.* The influence of ZrB_2-based UHTC production technology on its corrosion resistance// Naukovi notatki. Interacademic collected papers. – Lutsk: Publishing house of Lutsk National Technical. Un-t, 2017. – Iss. 58 – P. 94–99 (in Ukrainian).

6. *Evdokimenko Yu., Kisel V., Frolov G, Buchakov S.* Two-stage configuration burner for high-speed air-fuel spraying with liquid fuel // Bulletin of engine building. – 2015. – No. 2. – P. 143–148 (in Russian).

7. *Yevdokimenko Yu., Frolov G., Kisel V.* Thermal testing of front edge materials of a hypersonic aircraft. – Lutsk: Publishing house of Lutsk National Technical. Un., 2017. – Iss. 58. – P. 153–161.

APPLICATIONS OF THE DIRECT LYAPUNOV METHOD AND ALGORITHMS OF ELLIPSOIDAL ESTIMATION IN PROBLEMS OF SPACECRAFT CONTROL

V. Kuntsevich, V. Volosov, V. Shevchenko

Space Research Institute of NAS of Ukraine and SSA of Ukraine (SRI NASU-SSAU)

In 2016–2017, the Space Research Institute of the National Academy of Sciences of Ukraine and the National Space Agency of Ukraine performed a series of investigations in the field of a further improvement of the efficiency of control of small spacecrafts designed to solve a wide range of functional problems including the tasks of video overview or Earth remote sensing in the territory of Ukraine.

The content of these studies was aimed at applying the latest achievements and developments of the general theory of control of dynamic systems (DS) to obtaining new effective methods that generalize and improve the known techniques for solving a wider class of typical functional problems of attitude control of up-to-date and prospective small spacecrafts.

Among such achievements, there are the well-known generalizations of the theorems of Lyapunov direct method concerning the stability of individual solutions of ordinary differential equations (ODEs) and their difference analogues to the study of the stability of invariant sets in the phase space of the corresponding equations of DS motion made by V.I. Zubov and N.N. Krasovskii. These performed researches were also based on new methods of the DS control theory under uncertainty, namely those using the set-theoretic interpretation of uncontrolled parametric and structural (external) perturbations of their mathematical models (MM). In contrast to the known methods and, above all, the Kalman filter based on the use of the probabilistic properties of the indicated perturbations-uncertainties, only the assumption of their boundness on norm is used. It is worth noting that the indicated perturbations can have other probabilistic properties in addition to boundness, but they are not used in the corresponding methods. The approach to DS control based on the use of the boundness of uncontrolled disturbances was called guaranteed or (synonymous) game. Within the framework of this approach, two methods of mathematical description of bounded sets were formed called polyhedron and ellipsoidal methods. The performed studies used the methods of ellipsoidal approximation of compact sets in the corresponding spaces – DS phase space for the synthesis of small spacecraft control and parameter space in the problem of estimating its parameters. Here, the small spacecraft parameters are the elements of the inertia matrix in the dynamic Euler equation, its mass, and coordinates of its center of mass.

Problem statement

To formulate the problem statement, let us introduce the following right orthogonal reference frames (RF):

– body reference frame (BRF) $Oxyz$ with an origin in O – the center of mass of a small spacecraft;

– orbital reference frame (ORF) $Ox_oy_oz_o$ whose axis Oy_o id directed along the current radius-vector of the small spacecraft with an origin in the center of the Earth, while axis Ox_o is located in the plane of the orbit with a positive direction towards the orbital motion of the small spacecraft;

– inertial reference frame (IRF) $Ox_Iy_Iz_I$. As an IRF, one can use the ORF «stopped» at some point in time. Without a fundamental loss of accuracy, one can also take an IRF whose coordinate axes are parallel to those of the geocentric second equatorial RF used in spherical astronomy.

In the general case, the equations of controlled angular motion of a small spacecraft (considered as a solid) relative to the center of mass represent a nonlinear system of ordinary differential equations (ODE), which splits into two systems called kinematic and dynamic equation systems (KES and DES correspondingly). The KES determines the variation of the BRF orientation parameters relative to some basic RF (in this case, relative to the ORF or IRF) as a function of the angular velocity, more specifically – the vector $\omega^T = (\omega_1, \omega_2, \omega_3)$ of the projections of the small spacecraft absolute angular velocity on the BRF axes. The DES determines the time evolution of the angular velocity vector depending on the control and perturbing moments. In this case, the ODE system can be presented in the form

$$\dot{\Lambda} = F(\Lambda, \omega, \omega_o) \qquad (1),$$

$$J\dot{\omega} = f(\omega, J, m_C, m_P) \qquad (2),$$

where Λ stands for the vector of orientation parameters, ω_o is the orbital angular velocity, J is the matrix of the small spacecraft parameters (inertia tensor), m_C is the vector of control moments specified by the projections on the BRF, m_P is the summary vector of disturbing moments – aerodynamic, gravitation, solar pressure forces, etc. that meets the condition $\|m_P\| \le c_P$, where c_P is some specified constant. At ω_o^T=(0,00), system of equations (1), (2) determines the orientation of the BRF relative to the IRF, while at ω_o^T=$(0,0,-2\pi/T)$, where T is the small spacecraft circulation period, – the orientation relative to the ORF. The specific form of the functions $F(.)$ and $f(.)$ is given for example in [1–4]. The orientation parameters in Eq. (1) can be chosen as the Euler-Krylov angles. In this case, the components of the vector are the angles of roll, heading, and pitch $\Lambda^T = (\gamma, \psi, \vartheta)$. However, if the value of one of these angles is equal to $\pi/2$, the right-hand side of the corresponding equation (1) breaks and becomes infinite, which prevents them from being used in the mathematical software for control systems of maneuverable small spacecrafts.

The control systems of up-to-date small spacecrafts include strap-down inertial orientation systems, with mathematical software algorithms using orientation parameters in the form of the vector $\Lambda^T = (\lambda_o, \lambda^T)$, $\lambda^T = (\lambda_1, \lambda_2, \lambda_3)$ consisting of normalized quaternion components and more specifically Rodrig-Hamilton (RG) parameters. In essence, they were also proposed by Euler and, in the case of angular motion, determine the unit vector of the instantaneous axis of rotation of the BRF relative to the basic RF and the angle of rotation with respect to the latter. In this case, the right-hand sides of the ODE have no singular points and do not contain trigonometric functions. Therefore, the integration of such ODEs in an on-board computer is performed much faster than that of the ODE with Krylov-Euler angles $\Lambda^T = (\gamma, \psi, \vartheta)$.

The general trend of creation of up-to-date and prospective spacecrafts is both the complication as well as expansion of the range of tasks to be solved and the toughening of the requirements to the quality of attitude control processes in accuracy, speed, and stability under non-stationary flight conditions.

The inertial parameters of mathematical models of a spacecraft, determined by its inertia tensor, mass, and the coordinates of its center of mass, can change during flight, which is not always accurately predictable. These changes can lead to the loss of the properties of optimality, speed, and quality of transient processes that the control system was supposed to have, as well as the violation of its functional operation. It is specific of not only large spacecrafts, but also small spacecrafts with mobile structural elements, in particular, those equipped with manipulators. Therefore, it is highly important to develop methods and algorithms for obtaining current values of estimates of inertial parameters of a spacecraft under flight conditions with their direct use for adaptation of control systems. A large number of studies is devoted to solving these problems [4]. Here we propose a single methodological approach based on the formation of systems of equations and inequalities in a regular flight and their solution with the use of the previously developed robust algorithm for the method of ellipsoids.

Control synthesis for the angular motion of a spacecraft

An inherent functional requirement to mathematical software is to ensure the stability of the attitude control system. Therefore, a synthesis of attitude control algorithms focused on the stability criterion is considered in an almost limitless number of publications. However, most of these publications do not specify, at least explicitly, two specific properties of such systems. To be more precise, these are the properties of the solutions of ODE systems used to describe the angular motion of a small spacecraft.

The first of them is as follows. As was noted above, the ODE system consists of the KES and DES. Moreover, the norm of the state vector (SV) of the KES is an integral of motion. It retains its value equal to the norm of the initial state vector during the evolution of the system. In the case where the SV components are the Rodrig-Hamilton parameters, which is actually of interest, its norm is identically equal to unity $\|\Lambda(t)\|^2 = \Lambda^T(t)\Lambda(t) \equiv 1$. In this case, the motion of the representative point in the phase space of system (1), (2) is realized along the integral manifold $M = \{\Lambda, \omega{:}\Lambda^T\Lambda = 1, \omega^T\omega < \infty\}$. It is obvious that in this case any solution of the KES, i.e. a solution with a norm equal to unity, cannot be asymptotically Lyapunov stable by definition. It can only have the form of stability, which is called Lyapunov conditional asymptotic stability or stability on manifolds mentioned in Lyapunov's studies.

That is why the problem of control synthesis with the use of Rodrig-Hamilton parameters is correctly formulated not as a synthesis problem by the criterion of asymptotic stability, but the synthesis problem by the criterion of conditional asymptotic stability.

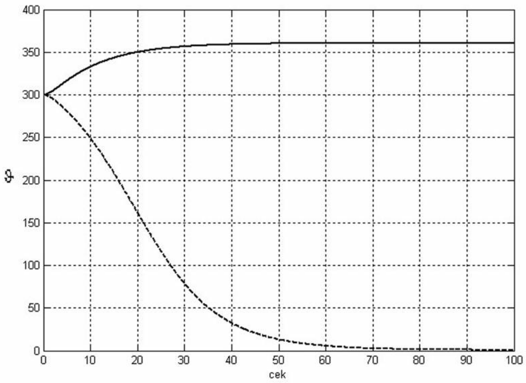

Fig. 1. Transient processes of orientation

Despite its simplicity, this methodological result appears to be quite important. The ignoring of the considered property of the KES in a number of works leads not only to an incorrect interpretation of the obtained results, but also to making incorrect conclusions.

The second result is as follows. As is known, the same steady-state physical orientation of a small spacecraft can be described by two sets of Rodrig-Hamilton parameters that differ from each other in sign. In particular, a two-point set $M=\{\Lambda_S, \omega_S{:}\Lambda_S^T=(\pm 1,0.0,0), \quad \omega_S^T=(0,0,0)\}$ corresponds to the steady-state alignment of the BRF with the IRF in the phase space of system (1), (2). Thus, the required orientation correlates with two VS values or two KES solutions. Therefore, the attitude control should be synthesized using well-known generalizations of the Lyapunov method to the study of the stability of bounded sets in the phase space of ODE rather than the direct Lyapunov method for investigating the stability of isolated solutions of ODE. To solve the problem of control synthesis, we propose an original non-smooth «piecewise-quadratic» Lyapunov function positively defined with respect to the set M_S. The effectiveness of the obtained control algorithm is illustrated for clarity in Fig. 1 by an example of a plane rotation of a small spacecraft relative to the axis Oz_o in the problem of alignment of the BRF and IRF. Such motion of the small spacecraft corresponds to the values of the Rodrig-Hamilton parameters $\lambda_1=\lambda_2=0$ and the angular velocities $\omega_1=\omega_2=0$, $\omega_3\neq 0$. In this case, $\lambda_0(t)=cos(\theta(t)/2)$, $\lambda_3(t)=sin(\theta(t)/2)$, $\Lambda^T(t)\Lambda(t)=\lambda_0^2+\lambda_3^2\equiv 1$.

Figure 1 shows the transient processes of alignment of the BRF and IRF axes at an initial mismatch characterized by the angle of mismatch between the same axes $\theta=300°$. The solid curve corresponds to the obtained algorithm using the proposed piecewise quadratic Lyapunov function $V_1(\Lambda,\omega)$, while the dotted curve corresponds to the known algorithm obtained if choosing the «classical» Lyapunov function – the quadratic form $V_0(\Lambda,\omega)$ positively defined with respect to the isolated solution of system (1), (2) $\Lambda_S^T=(+1,0,0,0)$, $\omega_S^T=(0,0,0)$. One can see from Fig. 1 that the proposed algorithm provides the alignment of the RFs by the shortest path due to the rotation up to $\theta=360°$, i.e. at the angle $\Delta\theta=60°$. The existing algorithm provides the rotation at the angle $\Delta\theta=300°$. The intersections of the manifold M by the plane $\omega_3=0$ that correspond to this example and the LF level lines $V_j(\Lambda,\omega), j=1,2$ are shown in Fig. 2 by blue and green lines, respectively. The arrows show the directions of the motion of the representing point along the manifold M corresponding to decreasing LF $c_j<c_{j+1}$.

We also obtained an algorithm for controlling the orientation of a small spacecraft relative to the ORF. In this case, a well-known method of decomposition of the general problem of orientation into the kinematic and dynamic

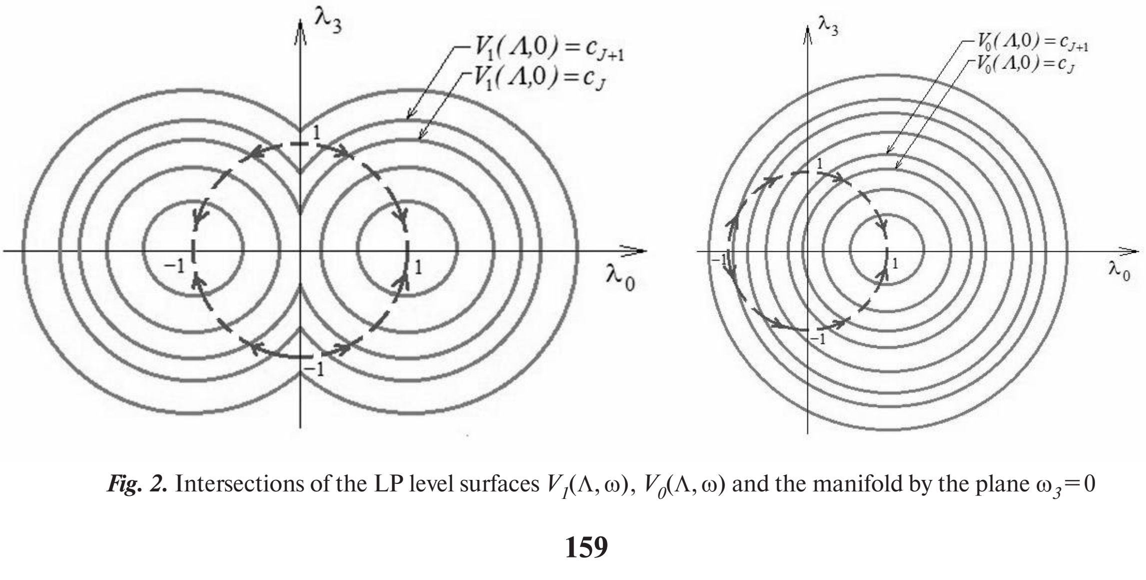

Fig. 2. Intersections of the LP level surfaces $V_1(\Lambda,\omega)$, $V_0(\Lambda,\omega)$ and the manifold by the plane $\omega_3=0$

problems for KES and DES and two Lyapunov functions was used [1].

Method for estimating the inertial parameters of a small spacecraft in flight

Algorithm for estimating the matrix of inertia. Let us obtain a recurrent algorithm for estimating the matrix J at discrete time moments t_k, $t_{k+1}-t_k=T$, where T is the specified discrete interval. It is supposed that the vectors $\Lambda(t)$, $\omega(t)$ can be measured by standard on-board instruments (for example an astrosensor and an angular-velocity sensor) at discrete time intervals and the control momentum is created by systems of control power gyroscopes (gyrodines and/or flywheels) $m_u=\varphi(\omega,\dot{G},G)$ [4]. Here, $G=(G_1,G_2,G_3)^T$ is the measurable vector of the summary kinetic momentum of all power gyroscopes determined by its projections G_j on the BRF. The control itself is the derivative $\dot{G}$ of the kinetic momentum G depen-ding on the speed of precession of the gyrodines or the rotational acceleration of the flywheels. The required value of $\dot{G}$ can be derived from the equation $\varphi(\omega,\dot{G},G)=m_C$, where the momentum m_C is determined according to the control synthesis method described above. The integration of the both sides of equation (2) at the time interval $t\in[t_k,t_{k+1}]$ with the use of the available measurements of the current values of the functions $\omega(t)$ and $G(t)$ as well as the boundness of the perturbation moments m_P provides the following system of linear inequalities for determination of the matrix J

$$y_k=h_k^T x+\xi_k,\quad \|\xi_k\|\leq \mathrm{c},\quad k=0,1,\ldots \quad (3),$$

whose set of solutions is guaranteed to include the required six-dimensional vector $x=x_*$ composed of the elements of the symmetric (3×3)-matrix J. The formulas for calculation of the vectors y_k and the (3×6) matrix h_k^T are given in [4]. To obtain the estimates $\hat{x}_k$ of the vector x_*, we used the previously developed recurrent robust algorithm for calculation of the centers $\hat{x}_k$ and matrices $H_k=H_k^T>0$ of ellipsoids of the form

$$E_k=E[\hat{x}_k,H_k]=\{x\in R^6:\sigma(x,\hat{x}_k,H_k)\leq 1\},$$
$$\sigma(x,\hat{x}_k,H_k)=(x-\hat{x}_k)^T H_k^{-1}(x-\hat{x}_k) \quad (4),$$

for which the condition $x_*\in E_k$ implies that $x_*\in E_{k+1}$. The formulas of this algorithm adapted to the specifics of the considered problem are given in [4]. If the indicated inclusion appears violated at some $k=\tilde{k}$ and $x_*\notin E_{\tilde{k}}$ (for example the matrix J changes due to a separation of a part of the small spacecraft) then the property of robustness of the algorithm according to L.S. Pontryagin and A.A. Andronov will induce «expansions» of the ellipsoids, for which $x_*\in E_k$ at $k\geq\tilde{k}_*\geq\tilde{k}$. It is obvious that, for a convergent algorithm, $SpH_k\to 0$ and $\|x_*-\hat{x}_k\|\to 0$, i.e. the estimation will be accurate. Under the real conditions, the accurate estimation cannot be achieved due to the finiteness of measurement noise $\|\xi_k\|\leq c$, $c\neq 0$ and ellipsoid (4) will asymptotically reach a steady state for which the inclusion $x_*\in E[\hat{x}_\infty,H_\infty]$ holds true.

To estimate the effectiveness of the proposed algorithm, a series of computational experiments was performed in an attitude control closed loop. We analyzed the graphs of the matrix trace SpH_k, the estimation accuracy $\delta J_k=\|x_*-\hat{x}_k\|$ and the indicator function (the membership function) $\sigma_k=\sigma(x_*,\hat{x}_k,H_k)$. It is obvious that $x_*\in E[\hat{x}_k,H_k]$ at $\sigma_k\leq 1$ and $x_*\notin E[\hat{x}_k,H_k]$ at $\sigma_k>1$. The experiments used the adaptive control principle – the control moments m_C were calculated applying the algorithm obtained for control synthesis in section 1 with the matrix of inertia J replaced by its current estimate $\hat{J}_k$. The synthesized control was aimed at the alignment of the BRF and ORF. Fig. 3 shows the results of experiment 1 under the membership condition $\sigma_0<1$ (an a priori assumption) satisfied for the initial ellipsoid. Fig. 4 demonstrates the results of experiment 2, in which the membership condition $\sigma_k>1$ was violated at $k=15$ by imitating an abrupt change of the elements x_* of the matrix of inertia. As was expected, at any $k\geq 0$ in experiment 1, the indicator function $\sigma_k<1$. In experiment 2, the violation of the condition $x_*\in E[\hat{x}_k,H_k]$ resulted in an abrupt change of the indicator function $\sigma_k\gg 1$ and an increase of the trace function SpH_k ("inflation" of the ellipsoids) until the ellipsoid "absorbed" the point x_* – the indicator function assumed the value $\sigma_k<1$; the estimation error also decreased $\delta J_k\to 0$.

The both experiments have demonstrated a successful attitude control, i.e. the alignment of the BRF and ORF, for which $\lambda_0(k)\to 1$, $\lambda_j(k)\to 0$, $j=1,2,3$ (see Fig. 5).

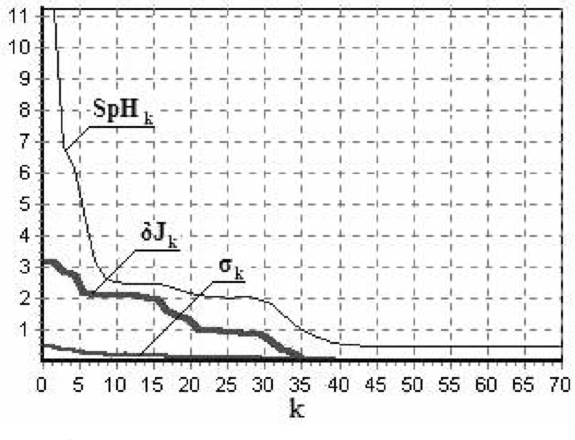

Fig. 3. Experiment results at $\sigma_0<1$

Method for estimating the coordinates of the center of mass inside a spacecraft. To solve the problem of estimating the coordinates of the center of mass, the RFs introduced above are supplemented with one more building reference frame $Px_by_bz_b$ associated with the spacecraft having the origin at some point P of the spacecraft chosen in a definite way. The coordinates axes $Px_by_bz_b$ are parallel to the corresponding axes of the BRF. In the building RF, one specifies the coordinates of the installation and direction of the sensitivity axes of various spacecraft devices and payload. The relative position of the coordinates is illustrated in Fig. 6.

It is supposed that a three-component newtonometer is installed at the point A measuring the projections of the apparent acceleration vector on the axes of the building RF $Px_by_bz_b$ coinciding with its projections on the BRF. The vector of the coordinates $d=(x_b, y_b, z_b)^T$ of the newtonometer in the building frame $Px_by_bz_b$ is assumed to be known. The same way as was described above, it is assumed that the angular velocity vector ω is measured. The problem of estimating the vector of p-coordinates of the center of mass of the small spacecraft in the building RF $Px_by_bz_b$ is solved. The solution is based on the use of theorems of theoretical mechanics on the motion of a free solid body. Namely, the acceleration of an arbitrary point is represented in the form of the acceleration of the center of mass and that caused by the rotation with respect to the center of mass. We also use the theorem stating that the center of mass of a system of material points (small spacecraft) moves as a material point with a mass equal to the mass of the entire system under the action of the force equal to the sum of all the external forces. It is assumed that the norm of the vector of non-gravitational forces is restricted by some known constant. Similarly to the determination of the inertia tensor by integrating the readings of a newtonometer and angular velocity sensors at the time intervals $[t_k, t_{k+1}]$, we obtain systems of inequalities of the form (3), whose set of solutions includes the required vector $x_*=r$ (see Fig. 6). The latter can be solved using the robust algorithm of the method of ellipsoids for the calculation of the centers $\hat{x}_k=\hat{r}_k$ and matrices H_k of ellipsoids of the form (4). The vector of the estimated coordinates of the center of mass can be found by the formula $\hat{p}_k=d-\hat{r}_k$.

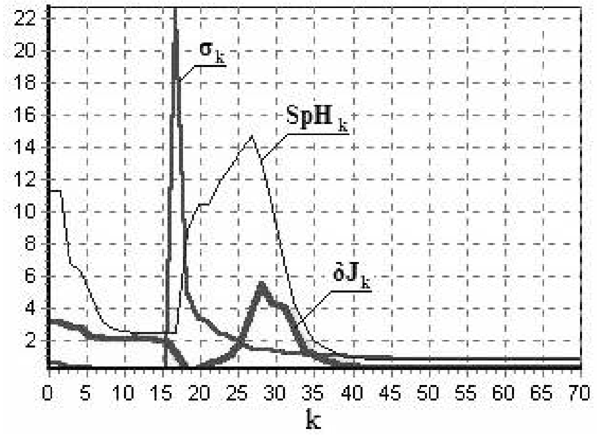

Fig. 4. Experiment results at $\sigma_{15}>1$

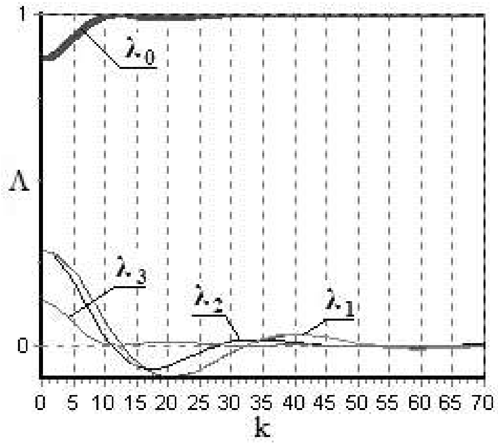

Fig. 5. Transient processes of orientation

Conclusions

1. The problem of synthesis of small spacecraft attitude control is for the first time correctly formulated as a problem of stability on a manifold in the space of Rodrig-Hamilton parameters. Methods for the synthesis of small spacecraft attitude control based on generalizations of the direct Lyapunov method for investigating the stability of individual solutions of differential equations to the study of the stability of invariant sets in their phase space are proposed. Their direct use provided a number of new algorithms for small spacecraft attitude control, whose particular cases are both well-known algorithms and the solution of a wider class of attitude control problems. The computer simulation has illustrated the effectiveness of the proposed algorithms and their advantages as compared to the existing ones.

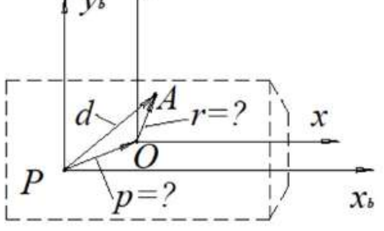

Fig. 6. Relative position of the building RF $Px_by_bz_b$ and BRF $Oxyz$

2. The existing problem statements for autonomous estimation of small spacecraft dynamic parameters under flight conditions are analyzed together with the methods of their solution using standard up-to-date on-board sensors and control devices. Among the latter, there are positional orientation sensors, angular velocity sensors, linear acceleration sensors, and gyro-force control systems (gyrodines and/or flywheels) of arbitrary structure with measurable kinetic moments. The small spacecraft dynamic parameters are the inertia tensor and the coordinates of the center of mass in the spacecraft or, more specifically, in its building frame. Based on the performed analysis, it is established that the existing problem statements are reduced to the formation of systems of linear equations or inequalities using the results of discrete measurements. A unified methodological approach to the formation of such systems is proposed. The recurrent robust algorithm of the ellipsoid method developed at the Space Research Institute of the National Academy of Sciences of Ukraine and the National Space Agency of Ukraine is adapted to solving the obtained systems. The effectiveness of using the proposed algorithm for estimating the inertia tensor is illustrated by computer simulation of the adaptive attitude control of a small spacecraft. In this case, the control moments were formed using the proposed attitude control algorithm with the actual matrix of inertia replaced by its current estimate.

REFERENCES

1. *Volosov V.V., Shevchenko V.N.* Synthesis of algorithms for spacecraft attitude control based on generalizations of the direct Lyapunov method // Journal of Automation and Information Sciences. – 2017. – No. 5. – P. 106–117 (in Ukrainian).

2. *Volosov V.V., Shevchenko V.N.* Synthesis of algorithms for attitude control of a spacecraft based on generalizations of Lyapunov direct method // Abstracts of the XXIV International Conference on Automated Control "Automatics–2017", September 13–15, 2017, Kyiv, Ukraine. – P. 55 (in Russian).

3. *Victor V. Voloso*v Attitude Control of a Spacecraft in the Orbital Coordinate System Using Ellipsoidal Estimates of its State Vector // Journal of Automation and Information Sciences. – 1999. – V. 31. – Iss. 4–5. – P. 24-32.

4. Report of the Space Research Institute of the National Academy of Sciences of Ukraine and the National Space Agency of Ukraine "Methods and algorithms of precision robust control of small spacecrafts and their realization on problem-oriented processors". Available at: http://www.ikd.kiev.ua/phocadownload/userupload/space_reports_2016/report2.pdf (in Ukrainian).

LIST OF IMPLEMENTING ORGANIZATIONS

No.	Organization	Acronym	E-mail
1	ARSENAL Special Device Production State Enterprise	ARSENAL SDP SE	info@arsenalcdb.com.ua
2	Bogolyubov Institute for Theoretical Physics of NAS of Ukraine	BITP NASU	itp@bitp.kiev.ua
3	G.V. Karpenko Physico-Mechanical Institute of NAS of Ukraine	PMI NASU	pminasu@ipm.lviv.ua
4	Institute of a hydrobiology of NAS of Ukraine	IH NASU	post_mail@hydrobio.kiev.ua
5	I.M. Frantsevich Institute for Problems of Materials Science of NAS of Ukraine	IPMS NASU	dir@ipms.kiev.ua
6	Institute of Electron Physics of NAS of Ukraine	IEP NASU	nanu.iep@gmail.com
7	Institute of Food Biotechnology and Genomics NAS of Ukraine	IFBG NASU	office.ifbg@nas.gov.ua
8	Institute of Ionosphere of NAS and MES of Ukraine	IION NASU and MESU	iion@kpi.kharkov.ua
9	Institute of Molecular Biology and Genetics of NAS of Ukraine	IMBG NASU	inform@imbg.org.ua
10	Institute of Telecommunication and Global Information Space of NAS of Ukraine	ITGIS NASU	itelua@kv.ukrtel.net
11	Institute of Radio Astronomy of NAS of Ukraine	IRA NASU	rai@ri.kharkov.ua
12	Lviv Center of Space Research Institute of NAS and SSA of Ukraine	LC SRI NASU-SSAU	vakor@isr.lviv.ua
13	LTD RPI (Research and Production Enterprise) HARTRON-ARKOS	LTD RPI HARTRON-ARKOS	centr@hartron.com.ua
14	Lutsk National Technical University	LNTU	vkt@lntu.edu.ua
15	Main Center of the Special Monitoring, NSFCTC, SSA	MCSM NSFCTC SSA	oper@gcsk.gov.ua
16	M.G. Kholodny Institute of Botany of NAS of Ukraine	IB NASU	inst@botany.kiev.ua
17	National Technical University of Ukraine "Kyiv Polytechnic Institute"	NTUU «KPI»	mail@kpi.ua
18	O.V. Palladin Institute of Biochemistry of NAS of Ukraine	IBCH NASU	secretar@biochem.kiev.ua
19	Paton Electric Welding Institute of NAS of Ukraine	PEWI NASU	office@paton.kiev.ua
20	Space Research Institute of NAS and SSA of Ukraine	SRI NASU-SSAU	ikd@ikd.kiev.ua
21	State Institution "Scientific Centre for Aerospace Research of the Earth" of Institute of Geological Sciences of NAS of Ukraine	CASRE IGS NASU	casre@casre.kiev.ua
22	Taras Shevchenko National University of Kyiv	KNU	genmilinevsky@gmail.com
23	V.N. Karazin Kharkiv National University of MES of Ukraine	KhNU MESU	info@karazin.ua
24	Yuzhnoye State Design Office	Yuzhnoye SDO	info@yuzhnoye.com

NATIONAL ACADEMY OF SCIENCES OF UKRAINE
STATE SPACE AGENCY OF UKRAINE

SPACE RESEARCH IN UKRAINE 2016—2018

**The report was prepared
by Space Research Institute
of NAS of Ukraine and SSA of Ukraine**

in English

Scientific editor
FEDOROV Oleg

Compiler
SAMOYLENKO Lyudmyla

Computer layout
T. Skorokhod